THE UNIVERSITY OF HULL

Modelling the Chemical Evolution of the Milky Way: Short-lived Radioactive Isotopes from AGB Stars and the impact of SNe Ia

A Thesis submitted in fulfillment of the requirements

for the Degree of Doctor of Philosophy

E. A. Milne Centre for Astrophysics

School of Mathematics and Physical Sciences

by

Thomas Christopher Lewis Trueman

July 2023

Acknowledgements

Despite the many difficult times, I will look back on the years spent as a PhD student with great fondness because of the people that I interacted with along the way – friends, family, work colleagues, and housemates have all supported me, in one way or another, during the writing of this thesis. Listed below are the names of only some of these people, and I must apologise for the many more names that have been omitted for the sake of brevity.

First, I could not have asked for a more supportive, understanding, and humorous supervisor than Marco – he always remained upbeat and positive, a global pandemic notwithstanding. His seemingly unending knowledge of all things nucleosynthesis is as worrying as it is impressive. Second, I was incredibly lucky to work alongside Maria Lugaro and her team based at Konkoly Observatory for large parts of my research. Her kindness and expertise helped me in equal measure, and I always looked forward to our meetings together because they were so often filled with laughter. Third, I would like to thank Brad Gibson, for welcoming and supporting me in the E.A. Milne Centre since my arrival.

A better term than “work colleagues" would be “friends" to describe those with whom I have shared an office with – be it in Hull or Budapest. These friends are far more than just a list of names, and I can only apologise to each that I do not have the space to write here a personal message of thanks to them all. To this end, I am fortunate to have worked alongside Kate, James, Gareth, Richard, Matt, Lawrence, David, Kevin, Laura, Ryan, Oliver, Claire, Umberto, and many others in Hull; as well as Andrés, Benoit, Jacqueline, Benjamin, Hannah, Bori, Blanka, Benjámin, Marika, Claire, and Fernando in Budapest. In particular, I must single out Benoit Côté, whose GCE code `OMEGA+` is used to conduct the work done in this thesis and who was always happy to offer me help and advice, especially when I was just learning to use said code. Naturally, there are also a few friends that deserve a special mention. Iraj, Liv, Mikkel, and Roberta your hospitality, kindness, and friendship have kept me going through the good times and the bad – you provided me a home away from home,

and our times together in Farndale and Hull were some of my happiest memories of the last few years. Leah, our kitchen chats were the highlight of my ‘working’ day, and you are still the only person I know who can make the sound of a fish. Kiri, for the many hours we spent questioning our life decisions in the Spar. Lastly my good friend Tom, thank you for putting up with me as a roommate during our time in Budapest; the board games were one of the only things keeping me sane during the pandemic.

Finally, this work could not have been achieved without the love and support of my family. Mum, Dad, and Charlotte could not have done any more to look after me and offer me moral support, even when I was stuck in another country. Whilst working from home, I could not have asked for a better office companion than Bramble – even when he wasn’t feeling his best, he could never fail to brighten up my day. My grandmothers, aunts, uncles, and cousins have always showed interest in my work, and they have collectively contributed in making my time as a PhD student so much more enjoyable.

Declaration of Originality

This thesis is submitted in partial fulfilment of the degree of Doctor of Philosophy from the University of Hull. I declare that the work undertaken in this thesis is original and my own and was carried out under the supervision of Dr Marco Pignatari and Professor Brad Gibson. Any work that was done while in candidature for a research degree at this University that has been previously published, or that has been submitted with the intent of publication, is clearly stated in the relevant Chapter's prologue. Where work, results, or ideas have been taken from other sources, those sources are explicitly referenced.

Candidate signature: Thomas Trueman

Date: 06/07/2023

Abstract

This thesis demonstrates how Galactic Chemical Evolution (GCE) models of the Milky Way can be used to constrain the processes that have shaped our home in the cosmos. In Chapter 1, the observational evidence for GCE is reviewed. The fundamental ingredients for building chemical models and their parameterization are then described in Chapter 2. These ingredients are discussed within the context of the `OMEGA+` GCE code that is used to run the simulations at the core of this research project. Thereafter, GCE predicted abundance ratios calculated using several different stellar yield sets are qualitatively compared to observational data for elements from C to Pb. In Chapter 3, GCE models are used to follow the radioactive-to-stable abundance ratios for three short-lived radionuclides (SLRs), namely ^{107}Pd, ^{135}Cs, and ^{182}Hf, in the interstellar medium up until the time of the Solar System formation. The time taken for the GCE predicted ratios to decay to early Solar System ratios (ESS) derived from meteorites can be used to infer timescales relevant to the birth of Sun. The constraining potential of these calculations depend on several uncertainties, including the production of the SLRs in stellar nucleosynthesis models, observational limits of GCE parameters, and the average time between successive enrichment events, γ. For this reason, the GCE framework is calibrated for each of two sets of low- and intermediate-mass stellar yields and three different GCE parameterizations. Furthermore, two different values of γ are also considered. Taking into account these uncertainties, self-consistent isolation times are found for all three SLRs. In Chapter 4, GCE predicted abundance ratios calculated for four different Type Ia supernova (SN Ia) explosion mechanisms are quantitatively compared to observational data for the Fe-peak elements in order to help constrain SN Ia progenitor in the Galaxy. A statistical test is used to determine the fraction of sub-Chandrasekhar mass SNe Ia ($f_{\rm sub}$) that best fit the observational data. It is found that different values of $f_{\rm sub}$ are obtained using different sets of massive star yields. Finally, in Chapter 5 the main results of the thesis are summarised and potential future avenues of research are considered.

Contents

List of Figures

List of Tables

Dedicated to my faithful companion, Bramble

1. Introduction

The intrinsic beauty of our Galaxy has captivated the minds of mankind for millennia. And yet, despite all of its grandeur and glory, it is humbling to acknowledge that the Milky Way is entirely unremarkable from other galaxies in the Local Group. That our home in the cosmos is so normal, however, means that we can be more certain that our models of galaxy evolution based on the Milky Way are translatable to galaxies beyond our own.

Theories of galaxy evolution can be tested and refined by comparing model predictions to observations made across a broad spectrum of wavelengths. To this end, observations of absorption and emission lines can be used to directly measure the chemical abundance patterns in stars of different ages; these measurements have afforded us a unique insight into the elemental abundances in the Galaxy at different epochs in its past. The aim of Galactic Chemical Evolution (GCE) is to, by way of combining the disciplines of stellar and galaxy evolution, disentangle the information from spectroscopic observations in order to construct a complete timeline of the chemical and dynamical processes that have shaped the Galaxy we see today.

The vast majority of elements heavier than Li can only be formed in stars. The chemical evolution of a galaxy is therefore inextricably linked to its star formation history, which is itself regulated by dynamical gas flow processes. Indeed, a galaxy is very much a chemodynamical system on a scale which is impossible to fully resolve using numerical models. For this reason, it is necessary for GCE models to introduce a number of free parameters where complex processes are not yet understood, or where a complete treatment is unfeasible given computational costs. Nevertheless, the successes of GCE models are numerous and ever-growing, and from them we have began to better understand our "astrochemical heritage" (Caselli & Ceccarelli, 2012).

1.1 Cosmic abundances

1.1.1 Abundance measuring techniques

Following the construction of the Periodic Table by Dmitri Mendeleev in 1869, and the subsequent classification of elements based on their atomic numbers by Henry Moseley in 1913, it became apparent that elements with odd atomic numbers were less abundant than their even counterparts (Oddo, 1914; Harkins, 1917). This paved the way for a new scientific discipline called *cosmochemistry*, which concerns itself with the explanation for the origin and distribution of the elements in the Universe. The pioneering work in this regard was conducted by Victor Moritz Goldschmidt, who in 1938 published his final in a series of nine monographs detailing his 'Geochemical Laws' of the rare earth elements. In fact, the table of the 66 elemental abundances contained in Goldschmidt (1938) was built using an amalgamation of terrestrial and meteoritic data and so, claimed Goldschmidt on the grounds of the latter, they represented the *cosmic abundances*. It was later argued by Urey (1954) that, due to the heating of the Earth during its formation process, the meteoritic abundances offer a more robust measurement of the protosolar composition than the terrestrial abundances since they have undergone less fractionation. Erstwhile to the work of Goldschmidt, the solar abundances had already been calculated based on spectral line measurements of the solar photosphere (Russell, 1929), a technique that was later applied to measure abundances in other stars (Berman, 1935). However, as noted by Suess & Urey (1956), spectral line intensities are subject to several sources of line broadening and depend on (at the time) fairly poorly understood physical conditions in stellar interiors, whilst meteorites suffer some amount of processing that chemically alters the composition from that of the original solar system matter. This meant there were large discrepancies between the meteoritic and photospheric abundances for some elements, such as Al, P, S, Cl, and the even elements from Cu to Zn. Since these early studies, refinements to measuring techniques combined with more realistic solar models have narrowed the gap between the two disciplines (widely used solar abundance compilations used in GCE models include Anders & Grevesse, 1989; Grevesse & Noels, 1993; Lodders, 2003; Asplund et al., 2009; Lodders, 2019). Figure 1.1 shows that the current disagreement between solar photospheric and meteoritic abundance measurements is

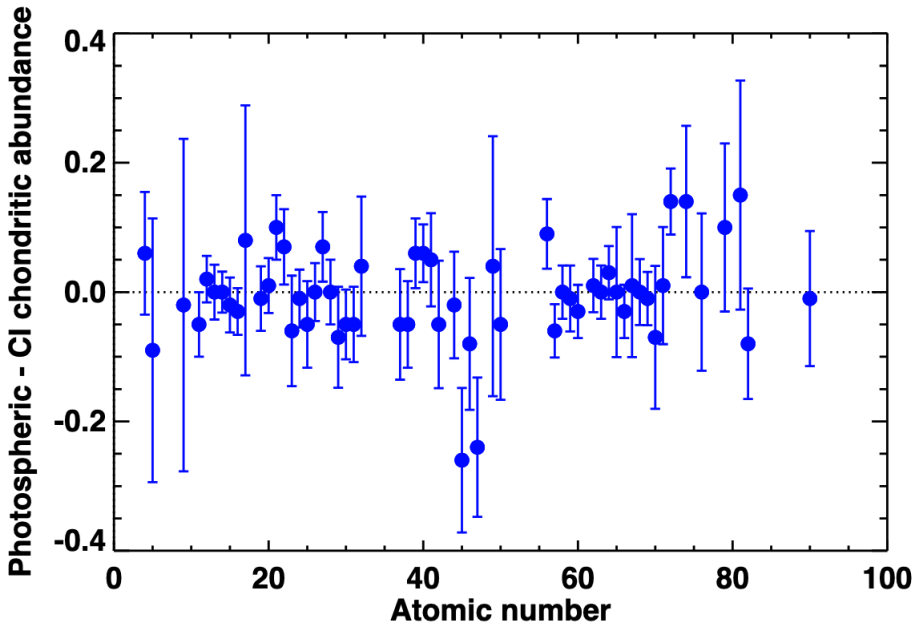

Figure 1.1: Differences in the solar abundances for photospheric and meteoritic data, with the exceptions of the volatile elements and Li. Data and Figure are from Asplund et al. (2021).

generally limited to less than 0.2 decimal exponent (dex) for the majority of elements. Notable exceptions are H, C, N, O, and the noble gases which are volatile and so are incompletely condensed in meteorites, as well as the fragile He and Li which are destroyed in stars (these are omitted from the Figure). Notwithstanding those exceptions, that both measurement techniques show remarkable agreement for the solar abundances is reassuring, especially given the prominence of the solar data as a reference for extrasolar abundances. An overview of these techniques is given below – for a comprehensive review of meteoritic and photospheric abundance measurements in the literature, the reader is referred to Palme et al. (2014).

1.1.1.1 Photospheric abundances

In her 1925 Thesis, Cecilia Payne explained how the abundances of elements on the surface of a star of known temperature could be inferred through quantum mechanical principles (Payne, 1925). This work was groundbreaking, and it led to the discovery that the Sun was mostly made of H and He, rather than predominantly Fe like the Earth (Russell, 1929). However, in order to quantitatively derive the abundances of elements at the stellar surface, it is necessary to compare the observed absorption and emission lines to a theoretical emission spectrum

based on a model atmosphere. The accuracy of photospheric abundance measurements are limited by stellar modeling uncertainties, rather than spectral line measurements (Hill, 2001; Asplund et al., 2021). In particular, the transition from 1D model atmospheres to 3D hydrodynamical simulations have allowed a more thorough treatment of radiative and collisional processes. Also, it is becoming more apparent that for some elements the assumption of local thermodynamic equilibrium – that is, atomic particles are described by a population distribution according to the Boltzmann and Saha relations – is not valid. In general, 3D NLTE models have led to a decrease in the derived abundances of all but the lightest elements in the Sun. In the case of oxygen, the abundance derived using 3D NLTE atmosphere models by Allende Prieto et al. (2001) was a factor of two lower than previously measured by Grevesse & Noels (1993), consequently bringing it closer to the value measured in the ISM and hot stars.

1.1.1.2 Meteoritic abundances

The three main groups of meteorites, categorized based predominantly on their composition, are irons, stony-irons, and stones. Of these, the stones can be roughly grouped into achondrites, which have undergone some amount of chemical alteration due to melting, and chondrites, which are undifferentiated having never reached melting temperatures. Chondrites are comprised of several different components which were formed by different processes and, as such, their chemical composition has been altered to varying degrees; these components include:

- *chondrules*: millimetre-sized solidified melt droplets that cooled over short timescales. Typically contain some amount of olivine (Mg_2SiO_4 and Fe_2SiO_4) and Fe-Ni metals.
- *refractory inclusions*: so-called because they are rich in refractory trace elements, the calcium-aluminium-rich inclusions (CAIs) are believed to be some of the earliest forming solids in the early solar system.
- *matrix*: an assortment of fine-grained minerals and presolar grains, matrix has similar chemical composition to chondrites but with lower levels of depletion of the volatile elements.

There are a large variety of methods by which one can determine the chemical composition of meteorites, including wet chemical analysis, neutron activation analysis, electron microscopes, and mass spectrometry (for a description of these techniques and many more, we refer the reader to McSween & Huss, 2010). From these, a small group of meteorites called CI chondrites were identified as having compositions that most closely resemble that of the material from which the solar system was born. High-precision spectrometry allows the measurement of isotopic abundances, which led to the identification of excesses of ^{26}Mg in the CAIs of the Allende meteorite (Gray, 1974). Later, these isotopic anomalies were attributed to the decay of the radioisotope ^{26}Al (Lee et al., 1977), which was incorporated into the inclusions while still alive. Since ^{26}Al has a half-life of ~ 0.7 Myr, the ^{26}Al/^{26}Mg ratio is as an accurate *cosmochronometer*[1] that can be used to date events in first few million years of the solar systems history (Lugaro et al., 2018).

1.1.2 Stellar nucleosynthesis

The first attempt to understand the origin of the cosmic[2] abundances was pioneered by Hoyle (1946), who proposed that all the elements heavier than helium in the solar system were the products of fusion reactions inside stars. The presence of technetium in the atmospheres of S-type stars later confirmed that stars were actively undergoing some sort of heavy-element synthesis (Merrill, 1952); this is because the isotopes of technetium are radioactive, with half-lives much shorter than the stellar lifetimes (the longest lived isotope has a half-life of $< 10^7$ years). The theory of Hoyle (1946) was developed upon in the seminal papers on nucleosynthesis by Burbidge et al. 1957 (hereafter B^{2}FH) and Cameron (1957), who attempted to uncover the origin of the cosmic abundance curve (plotting the relative abundance as a function of atomic mass). Based on a combination of nuclear theory and the shape of the aforementioned distribution, B^{2}FH outlined seven different nuclear burning processes by which elements could be made in stellar interiors.

The cosmic abundance curve for the solar atmosphere shown in Figure 1.2 has changed

[1]Derived from "cosmo" (pertaining to the Universe) and "chronology" (ordering of events by their age).

[2]In reality, it was based solely on measurements of the solar composition which was thought to be universal in its application

little from the one constructed by B^2FH. The general trend is a decrease in abundance with increasing atomic weight (A), however, there are clear peaks at Fe, and for species close to the *magic* number nuclei at $A = 50, 82, 126$. The peak at Fe is due to the fact that ^{56}Fe has the highest binding energy per nucleon[3], thus the fusion of heavier nuclei results in a net energy loss from the system. The most abundant elements by far are H and He, which make up 74% and 24% of the total mass of the Sun. These, together with trace amounts of Li, were created long before even the formation of the Galaxy at the start of the Universe, during Big Bang nucleosynthesis (Cyburt et al., 2016). There is a large drop of $\sim$ 10 dex between the He ($A = 4$) and Li ($A = 7$) abundances, where the last is in the region marked by an **x** in the bottom left of the Figure. This is in part due to the fact that no stable isotope exists with $A = 5$, but also because of the relative ease with which Li is destroyed in stars. The elements Be ($A = 9$) and B ($A = 10, 11$) are also not readily produced by stellar nucleosynthesis and B^2FH proposed that they were formed instead by some unknown x-process, later identified to be cosmic ray spallation (Reeves et al., 1970; Meneguzzi et al., 1971). The remaining elements with $A \geq 12$ can all be made inside stars by a combination of different nucleosynthesis processes that correspond to the labels in Figure 1.2. The processes are briefly described below (we refer the reader to Iliadis 2007 for more detail), and in Section 2.3 we discuss in more detail the types of stellar enrichment event that each are synonymous with.

1.1.2.1 Hydrostatic burning processes

If the internal pressure of a star is balanced against its self gravitation, then it is said to be in a state of hydrostatic equilibrium. In this state, the interior structure and composition of the star evolves according to sequential thermonuclear burning stages, where the ashes of the previous stage form the fuel for the subsequent two-body charged-particle reactions. All stars begin by burning hydrogen, since it is the element with the lowest charge and thus has the lowest energy threshold to initiate nuclear fusion.

Hydrogen burning: Whilst on the main sequence, a star will fuse together four ^{1}H nuclei into ^{4}He via one of two mechanisms: (1) *proton-proton chains* or (2) the *CNO* cycle (Wiescher

[3]This is not strictly true as ^{62}Ni has the highest binding energy per nucleon, but is destroyed by photodisintegration in stellar interiors

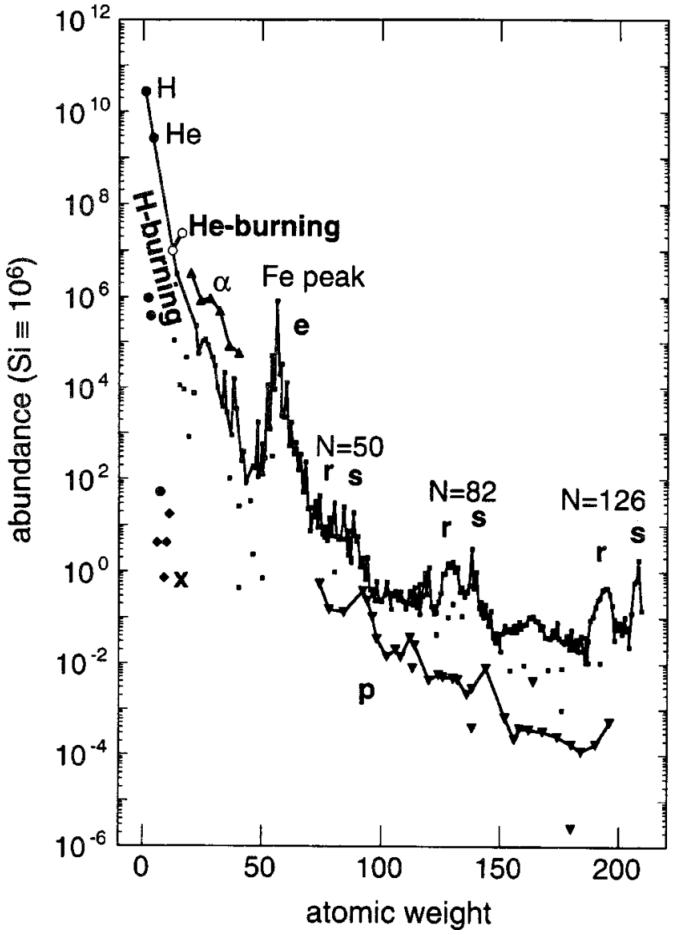

Figure 1.2: The cosmic abundances for the solar photosphere normalized to $\log(N_{\mathrm{Si}}) = 6$. The annotations indicate the respective nucleosynthesis process that produces each isotope. Figure from Ireland (1996).

et al., 2010). For stars with initial compositions close to primordial (i.e., almost exclusively H and He), (1) will always dominate. However, if there are sufficient amounts of C, N, and O in the star then (1) and (2) compete for energy generation, with (2) dominating in stars with core temperatures of $T \gtrsim 20 \times 10^6$ K that are ~ 1.5 times more massive than the Sun (Iliadis, 2007). Proton captures onto seed nuclei with $A = 20 - 40$ can also alter the abundances of Ne, Na, Mg, and Al. Of relevance in this thesis (see Section 2.5 and Chapter 3), hydrogen-burning is one of the main stellar processes responsible for the production of the short-lived radioisotope ^{26}Al, which is made by proton capture on ^{25}Mg, and is ejected by the winds of very massive stars ($M \geq 35 M_\odot$) during the Wolf-Rayet phase of evolution, or by binary interactions in stars of $10 - 35 M_\odot$ (Brinkman et al., 2019).

Helium burning: Following the cessation of hydrostatic H burning, the core of the star contracts and the temperature rises sufficiently to ignite core He burning, with H burning continuing in a layer surrounding the core. In this stage of stellar evolution ^{4}He is converted into ^{12}C via the triple-α process, so called because it involves the fusing of three ^{4}He nuclei (Salpeter, 1952). Some amount of this C, depending on the temperature and density in the star, can capture a further α-particle to become ^{16}O. The carbon-to-oxygen ratio in the core at the end of He burning depends sensitively on the competition between the triple-α and ^{12}C(α,γ)^{16}O reactions, with higher C/O ratios being favoured in stars of lower mass (Woosley et al., 2002). Irrespective of the central density, only a very small amount of ^{16}O will be destroyed via α-captures in to ^{20}Ne; therefore the primary products of He-burning are ^{12}C and ^{16}O. During core He-burning in massive stars ($M_\star \gtrsim 10 M_\odot$; see Section 2.3.2), ^{22}Ne is produced via the reaction chain ^{14}N(α,γ)^{18}F(e$^+$)^{18}O(α,γ)^{22}Ne using the ^{14}N produced by CNO cycling during H-burning. The ^{22}Ne(α,n)^{25}Mg reaction is the primary neutron source reaction for the weak *s*-process (see Section 1.1.2.3; Couch et al., 1974; Lamb et al., 1977) in massive stars, producing nuclei between Fe and Sr (Pignatari et al., 2010).

1.1.2.1.1 Advanced burning processes

Whilst all stars undergo H- and He-burning[4], due to the high Coulomb barriers involved in heavy-ion fusion reactions, only those much more massive than the Sun ($M \gtrsim 11 M_{\odot}$; Siess, 2006; Aliotta et al., 2022) will evolve through a series of advanced burning stages at their centre. Stars in the mass range $7 M_{\odot} \lesssim M \lesssim 10 M_{\odot}$ will instead ignite C off-centre under degenerate conditions, and upon depletion of C in the core will experience no further hydrostatic burning processes (see, e.g. Jones et al., 2013; Doherty et al., 2017; Jones et al., 2019a). During these advanced burning processes, the star evolves rapidly since neutrino emission dominates over energy loss by radiation and convection for temperatures $\gtrsim 0.5$ GK (Fowler & Hoyle, 1964). The higher temperatures reached during these later processes, together with the preponderance of trace species produced during earlier burning stages, allow for increasingly more complex and vibrant nuclear reaction networks.

Carbon-burning: The fusion of two ^{12}C nuclei can predominantly proceed through three different channels at astrophysical temperatures, producing either ^{23}Na, ^{20}Ne, or ^{23}Mg via the decay of the highly excited ^{24}Mg compound nucleus. The two most important channels for energy generation are ^{12}C(^{12}C, α)^{20}Ne and ^{12}C(^{12}C, p)^{23}Na, with most of the ^{23}Na being subsequently destroyed via ^{23}Na(p, α)^{20}Ne and ^{23}Na(p, γ)^{24}Mg (Arnett & Thielemann, 1985). This stage of hydrostatic burning has a crucial role in determining the neutronization degree of the C-O core of an intermediate-mass star, and thus the nucleosynthesis products from supernovae (Aliotta et al., 2022). Furthermore, the protons and α particles released by the ^{12}C+^{12}C fusion allow for efficient activation of proton- and α-capture reactions (Pignatari et al., 2013). In particular, the ^{22}Ne(α, n)^{25}Mg reaction can be reactivated during carbon-shell burning with higher neutron densities but lower overall neutron exposures (i.e., neutron density integrated over time; Seeger et al., 1965) than He-shell burning, leading to an s-process signature with enhanced productions of the isotopes ^{70}Zn, ^{86}Kr and ^{80}Se compared to the s-processing during core He-burning (Raiteri et al., 1991; Bennett et al., 2012). Following C-burning, the core consists primarily of ^{16}O (leftover from He-burning), ^{20}Ne, and ^{24}Mg.

[4]Actually, astrophysical objects below $\sim 0.5\ M_{\odot}$ will evolve straight to a He white dwarf upon depletion of their H fuel (Karakas & Lattanzio, 2014).

Neon-burning: Although the Coulomb barrier for ^{20}Ne is higher than for ^{16}O, the endothermic photodisintegration reaction ^{20}Ne(γ,α)^{16}O has a lower temperature threshold than oxygen fusion. The α-particle released from this disintegration fuses with ^{16}O to make ^{20}Ne, and the photodisintegration and α-capture reactions compete until eventually an equilibrium abundance of ^{20}Ne is established (Woosley et al., 2002). The ^{20}Ne can then capture a liberated α-particle to produce ^{24}Mg, such that the net change in the core abundances during Ne-burning can be described as 2 ^{20}Ne $\rightarrow$ ^{16}O + ^{24}Mg. The α-capture chain can continue up to ^{32}S, with some amount of ^{29}Si and ^{30}Si also produced by neutron captures onto ^{28}Si (Chieffi et al., 1998). The ^{23}Na produced during C-burning is also efficiently destroyed by proton and α-captures producing ^{20}Ne and ^{26}Mg, respectively (Thielemann & Arnett, 1985). At the end of Ne-burning, the most abundant species in the core are ^{16}O, ^{24}Mg, and ^{28}Si, as well as small amounts of the neutron rich isotopes of Mg, Al, and Si.

Oxygen-burning: At temperatures of $T \sim 2 \times 10^9$ K oxygen burning is ignited, with the fusion of two ^{16}O producing the ^{32}S* compound nucleus, which may decay into (from most probable to least) ^{31}P, ^{28}Si, ^{30}P, and ^{31}S (Woosley et al., 2002). The ^{31}P is efficiently turned into ^{32}S and ^{28}Si via proton captures, whereas the short-lived ^{31}S is turned into ^{30}P and ^{31}P via photodisintegration and radioactive decay, respectively. The α-chain can continue beyond ^{32}S, resulting in large increases in the abundances of ^{36}Ar and ^{40}Ca by the time the oxygen fuel is completely consumed, with more massive stars ($\gtrsim 15 M_\odot$) also producing supersolar amounts of ^{42}Ca and ^{46}Ti (Thielemann & Arnett, 1985). The temperatures are also high enough to destroy via photodisintegration reactions the *s*-process nuclei produced during core He- and shell C-burning, converting them instead into the iron group (Woosley et al., 2002). At the cessation of core O-burning, the most abundant species are ^{28,30}Si, ^{34}S, and ^{38}Ar.

Silicon-burning: The final hydrostatic burning process that can take place in stars is Si-burning – it is also the most complex. The net effect can be considered as the fusion of two ^{28}Si to form ^{56}Fe, although a vast number of reactions and nuclei are involved in the process (Chieffi et al., 1998). During this stage of stellar evolution, nucleosynthesis proceeds via the capture of protons, neutrons, and α-particles produced by photodissociation reactions of ^{28}Si and ^{32}S, rather than the fusion of two heavy nuclides (Thielemann & Arnett, 1985). Equilbira

between the reactions responsible for the production and destruction of nuclei is eventually reached, and the system is said to be in a state of nuclear statistical equilibrium (NSE). The relative abundances of nuclei in NSE depend on the number of neutrons compared to protons, or the neutron excess. The mass of the predominantly Fe core, which is now supported by electron degeneracy pressure, continues to grow until it approaches the Chandrasekhar mass ($M_{\rm Ch} \sim 1.4 M_{\odot}$). At which point, the core cannot support itself from gravitational collapse and the star explodes as a core-collapse supernova.

1.1.2.2 Explosive Nucleosynthesis

A supernova (plural supernovae) is the spectacular explosion of a dying star. These super-luminous events occur when a massive star is unable to support itself from self-gravitation (core-collapse supernova; CC-SN), or in a binary system in which thermonuclear runaway is triggered in the primary star by mass accretion from its companion (Type Ia supernova; SN Ia). During a SN, the ashes of past hydrostatic burning processes in the progenitor are incinerated by the outwardly propagating shock wave or thermonuclear flame, such that explosive nucleosynthesis is characterised by burning at high temperatures and densities over short enough timescales (sometimes only fractions of a second) that weak interactions are generally too slow to be consequential (Arnett, 1996). The ejecta from SNe have a layered structure reflecting successive explosive burning stages of the preprocessed fuel, and contains also some of the heavy elements synthesised during the previous hydrostatic burning processes (Woosley & Weaver, 1995; Thielemann et al., 1996; Woosley et al., 2002; Nomoto et al., 2013). Some of the most important explosive nucleosynthesis processes are summarised below.

Carbon- and neon-burning: Explosive C- and Ne-burning share many similarities with each other, including the fact that they are relatively well described by a steady-state approximation[5] (Arnett, 1996). During these processes, the material reaches peak temperatures of $\sim 2-3$ GK and produces mainly the $N \approx Z$ isotopes of O, Ne, Na, Mg, and Si (Maeda, 2022). Additionally, some rare neutron-rich nuclei in the mass range $36 \leq A \leq 88$ can also be made using the neutrons liberated by (α, n) reactions on ^{22}Ne and ^{25,26}Mg (Howard et al.,

[5]A species reaches a steady-state abundance when its production rate is balanced by its rate of destruction.

1972). Of significance for γ-ray astronomy is the production of ^{26}Al via proton captures onto the ^{25}Mg made during C and Ne-burning (Limongi & Chieffi, 2006).

Oxygen-burning: Typical peak temperatures during explosive O-burning are $3 - 4$ GK, which is sufficiently high for heavy elements ($Z > 28$) to photodissociate (Arnett, 1996). Equlibria is established between the forward and reverse rates of individual reactions, and clusters of nuclei form which are governed by local thermodynamic properties (Magkotsios et al., 2010). The abundances of species in clusters approach an intra-cluster equilibrium, however, since inter-cluster interactions are weak the plasma is said to be in a state of quasistatic equilibrium (QSE). A state of QSE is reached during O-burning – the abundances of the IMEs are described relatively well by NSE, with the element Ca acting as a bottleneck between the Si-Ca and Fe-peak clusters due to its magic proton number ($Z = 20$) (Arnett, 1996). Most of the ^{16}O is therefore converted into the α-elements ^{28}Si, ^{32}S, ^{36}Ar, and ^{40}Ca, with the production of heavier species beyond Ca strongly inhibited due to the elements high nuclear stability.

Silicon-burning: For peak temperatures and central densities above ~ 5 GK and $\sim 10^7$ g cm^{-3} respectively, the explosive Si-burning goes to completion and the abundances of species follow an NSE (Jerkstrand et al., 2015). Since the process takes place on sufficiently short timescales for weak reaction rates to be negligible, the proton and neutron numbers remain fixed at $N_n \approx N_p$, resulting in the production of large amounts of ^{56}Ni at the time of freeze-out (Maeda, 2022). At lower densities the Si burning is still complete, however, the triple-α reaction drops out of equilibrium and so the nuclei beyond $A = 12$ are unable to remain in an NSE. The result is an "α-rich freeze-out" leaving much larger quantities of He in the plasma at later times; this allows efficient α-captures to build Fe-peak nuclei, such as ^{44}Ti and ^{48}Ti, that are not normally produced during Si-burning (Woosley et al., 2002). Incomplete Si-burning occurs at temperatures below ~ 5 GK, and in this regime the IMEs and Fe-peak elements are in two separate QSE clusters (Jerkstrand et al., 2015). The products of incomplete Si-burning much more closely reflect those of hydrostatic Si-burning, with appreciable amounts of the α-elements (i.e., ^{28}Si, ^{32}S, ^{36}Ar, and ^{40}Ca) as well as the Fe-peak elements.

Electron captures: A key difference between the yields of CC-SNe and SNe Ia is that

only in the last are the central most regions ejected during the explosion (a neutron star or black hole remnant remains following a CC-SN). In particular, the central density of the WD progenitor can significantly alter the chemical composition of the ejecta, because weak interactions become relevant at high densities (see, e.g. Hillebrandt et al., 2013). In SNe Ia progenitor with central densities $\gtrsim 10^9$ g cm^{-3} the electron fraction (Y_e) can drop below 0.5, which is necessary for the production of ^{55}Mn (Leung & Nomoto, 2021). This means that in general WDs near the Chandrasekhar mass ($M_{\rm Ch} \sim 1.4 M_\odot$) produce significantly more Mn than those WD below $M_{\rm Ch}$. In addition, lower Y_e conditions favour the production of the neutron-rich Fe-peak elements, such as ^{58}Ni (Thielemann et al., 1986; Maeda, 2022).

1.1.2.3 Neutron capture processes

The solar system abundances of nuclides with $A > 60$ could not have been formed by charged-particle reactions because of the large Coulomb barriers involved. Instead, the elements beyond iron were mostly formed by a series of neutron captures onto seed nuclei to produce successively heavier isotopes. As more neutrons are captured the nucleus becomes unstable and can decay by spontaneous radioactive disintegration by transforming a neutron into a proton and, in so doing, forming a new element.

The slow neutron capture (s)-process: If the neutron capture rate is *slow* compared to the competing β-decay rate of radioactive nuclei, then the reaction pathway progresses close to the *valley of stability* – the narrow interconnected section of the chart of the nuclides that is occupied by stable isotopes. The *s*-process takes place in stellar environments with neutron densities in the range of $10^7 - 10^{12}$cm^{-3}. The dominant *s*-process neutron source reactions in stars are (i) the ^{13}C(α,n)^{16}O reaction that operates in the He burning layers of low-mass, asymptotic giant branch stars (e.g., Straniero et al., 1995; Gallino et al., 1998; Herwig, 2005; Karakas & Lattanzio, 2014); and (ii) the ^{22}Ne(α,n)^{25}Mg reaction during He and C shell burning in massive stars (e.g., Raiteri et al., 1991; Kaeppeler et al., 1994; The et al., 2000; Pignatari et al., 2010). The *s*-isotope distribution can be relatively well reproduced by assuming a simplified stellar environment with constant temperature and density, wherein *s* elements form via a series of successive neutron captures on Fe seed nuclei. In this so-called

classical model, abundance peaks naturally form at isotopes with magic neutron numbers ($A = 88, 140, 208$) that have energetically favourable shell configurations (Kaeppeler et al., 1990). Between these natural bottlenecks, the neutron capture flow is a smooth function of mass number, and the solar *s* distribution for $A > 90$ (*main* component) is fit well by this simplified approach (see, e.g., Figure 2 in Käppeler et al., 2011). However, below $A = 90$ the classical model underproduces the *s* distribution relative to solar, such that an additional *weak s* process component must be considered. An important metric that determines the relative abundances of *s*-isotopes is the neutron-to-seed ratio. As discussed previously, the ^{22}Ne neutron source is produced using the ^{14}N ashes from CNO cycling and therefore relies on some amount of heavy elements being already in the star during core H-burning. Thus in massive stars the neutron-to-seed ratio, and therefore the weak *s*-abundance pattern of the ejecta, is metallicity invariant (though the absolute yields scale with metallicity). On the other hand, the primary production of ^{13}C during He shell burning in low- and intermediate mass stars means that the neutron-to-seed ratio increases at lower metallicities – this has the effect of shifting the *s*-abundance pattern toward higher mass numbers (Cristallo et al., 2009). The *s*-distribution is also be affected by the number density of neutron poison isotopes in the region, such as ^{14}N, which have high neutron capture cross sections and so remove some amount of the neutron flux that would otherwise be captured on Fe-seed nuclei (Lugaro et al., 2003).

The rapid neutron capture (r)-process: Whilst the *s*-process is responsible for about half of the elements heavier than Fe in Nature, the remainder can be attributed to the *r*-process. Typical neutron densities for activation of the *r*-process are $N_n \gtrsim 10^{20}\text{cm}^{-3}$, which operates over timescales of a few hundred to several thousands of years (Cowan et al., 2021). Since the neutron density is high, the rate of neutron capture is *rapid* in comparison to the rate of radioactive decay, thus allowing the reaction pathway to proceed all the way to the neutron-drip line. Sufficiently high neutron densities require burning under explosive conditions, such that the neutron capture and reverse photodissociation rates are in equilibrium. Maxima in the neutron flux from the *r*-process reaction pathway are found at neutron shell closures $N = 50, 182, 126$ for nuclei along the neutron-drip line. After successive β-decays toward stability (recall that β-decay changes only the nuclear structure of the nucleus and not its

atomic mass number), the r-distribution has abundance peaks at the corresponding A (Cowan et al., 2021). The result is that the maxima in the r-distribution are shifted to lower A compared to the s-distribution. The r-distribution is also smoother than its s counterpart. Akin to the s-distribution, there is strong evidence to suggest that at least two different r-process components – termed the *main* and *weak* components – are at work in the Galaxy (see, e.g. Côté et al., 2019a, and discussion in Section 2.4.7). Potential astrophysical sites of the r-process are discussed in greater detail towards the end of the following Chapter.

1.1.3 Stellar abundance notation

It is important to note that the chemical abundances measured in the solar photosphere by high-resolution spectroscopy are not the products of nucleosynthesis taking place in the innermost regions of the Sun. Instead, they were inherited by the Sun inside the gas from which it formed $\sim$ 4.6 billion years ago, and so offer a direct probe of the stellar enrichment events that polluted the local interstellar medium (ISM) preceding its birth. The solar abundances are often used as a measuring stick by which the abundances in other stars are compared, with the most common way of expressing stellar abundances being the square bracket notation,

$$[\mathrm{X/H}]_\star = \log(\mathrm{X/H})_\star - \log(\mathrm{X/H})_\odot, \tag{1.1}$$

where $[\mathrm{X/H}]_\star$ is the ratio of the abundance (either by number or mass) of element X to that of hydrogen measured in a star, expressed in dex. The subscript $\odot$ denotes the solar ratio, such that for any element $[\mathrm{X/H}]_\odot = 0$. Historically, the [Fe/H] ratio has been used as a proxy for the amount of heavy elements in a star, however, the true *metallicity* (Z) is calculated by summing the fractional contribution toward the total mass from all elements with $A \geq 12$. Chamberlain & Aller (1951) provided the first evidence that the 'cosmic' abundances were in fact unique only to the Sun, wherein they found that the spectra of two F-type subdwarfs (long-lived, low-mass stars) had *"abnormally small amounts of Ca and Fe"*. It is now well established that stars of different ages and at different locations in the Galaxy will have different metallacities. Indeed, as we will come to discover in the next Section, stars with similar physical properties can be grouped into populations, and members of a given

population typically also share characteristic abundance signatures that reflect the larger scale processes that drive galaxy formation and evolution.

1.2 Formation and large scale structure of the Milky Way

It was first realised by Baade (1944) that the brightest stars in the Andromeda galaxy (originally called nebula) and its elliptical neighbours were markedly less luminous than those in our own Galaxy. He conceptualised that stars in galaxies could be grouped into one of two distinct stellar populations based on their age, luminosity, location, and kinematic properties. Population I consisted of mostly bright O- and B-type stars found in the spiral arms of galaxies, whereas Population II stars were older and less luminous and associated with the spheroidal components (i.e., halos and bulges) of spiral type galaxies and ellipticals. Thereafter, Baade (1946) first identified Population II stars in our own Galaxy, belonging to the NGC 6522 globular cluster in the Sagittarius cloud - this was the first evidence for the Galactic Bulge component of the Galaxy.

The spiral structure of the Galaxy's arms was first discovered by Morgan et al. (1952), who noticed that the spatial distribution of ionized hydrogen (HII) traced out a similar arm structure to those of the Andromeda spiral galaxy. Radio astronomy measurements of the 21-cm line of neutral hydrogen confirmed that interstellar gas is concentrated in the spiral arms of the Galaxy (see Oort et al., 1958, and reference therein). However, due to our location in the Galaxy, situated on one of the spiral arms within a layer of Galactic dust, observations in the optical wavebands are limited and so mapping the exact spiral structure has proved difficult (see, e.g. the discussion in Hou & Han, 2014).

In combination with HI (Caswell & Haynes, 1987) and HII mapping (Georgelin & Georgelin, 1976), extensive sky surveys in the near-infrared (Blitz & Spergel, 1991; Weiland et al., 1994; Binney et al., 1997) and of molecular clouds (Dame et al., 2001), have unravelled the large-scale structures of the Galaxy. The Milky Way is a barred spiral galaxy of SBbc morphological type in the Hubble classification. It consists of four distinct stellar populations, namely the thin and thick disk, spheroidal stellar halo, and bulge which are indicated on the schematic diagram of the Galaxy in Figure 1.3. Recent simulations of the

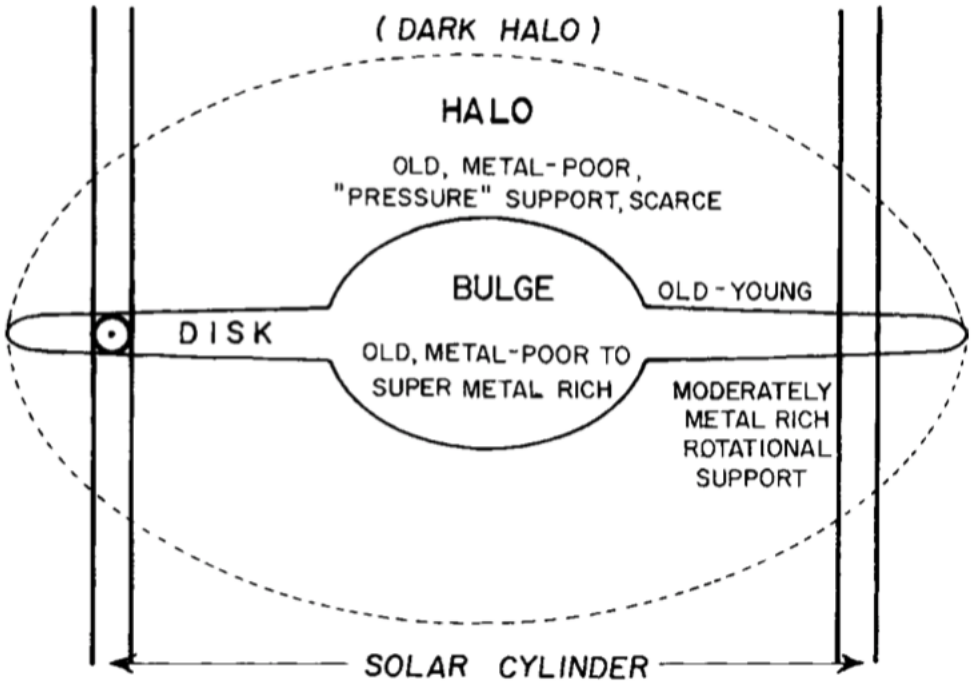

Figure 1.3: Schematic diagram of the Milky Way. The location of the Solar System is marked by the $\odot$ symbol in the disk. Figure from Pagel (2009).

Galaxy based on rotation curve data suggest these populations constitute a stellar mass of $\sim 5 \times 10^{10} M_{\odot}$ (Cautun et al., 2020), though the total mass of the Milky Way is dominated by the dark matter halo within which the baryonic matter is embedded.

Most agree a unified formation theory of the Milky Way can be achieved by individually solving the formation histories of its components. Two competing formation theories are the *Monollithic Collapse Model* and the *Hierarchical Clustering Model*. Originally proposed by Eggen et al. (1962) due to the perceived correlation between a star's eccentricity and its metal-deficiency (measured in terms of its ultraviolet excess), the Monollithic Collapse Model suggests that the Milky Way formed from a giant protogalactic gas cloud that collapsed rapidly (of the order 10^8 years), during which time the first-generation stars were born in globular clusters that would later reside in the halo. The angular momentum of the gas eventually prevented further collapse in the radial direction, but in the axial direction the Galaxy flattened to form a disk. This model could explain why younger, more metal-rich stars had less eccentric orbits since they resided in the disk and were born from material that had been pre-enriched by the first-generation stars. In the Hierarchical Clustering Model

proposed by Searle & Zinn (1978), it was instead argued that the large age distribution of clusters in the outer halo was evidence that they were accreted into the Galaxy over a much longer timescale via a series of merger events, with the disk forming gradually from the gas that was ejected by these primordial stellar populations. Furthermore, they claimed that the correlation between kinematics and abundances for halo stars found by Eggen et al. (1962) was an artifact of the selection bias for their data. Following the emergence of the Lambda cold dark matter (ΛCDM) model and the discovery that galaxies have dark matter halos, the paradigm has increasingly shifted more towards the last as the preferred mechanism for the Milky Way's formation (see, e.g. White & Rees, 1978; Blumenthal et al., 1984; Bullock et al., 2001).

In recent years, extensive spectroscopic surveys such as The Sloan Extension for Galactic Understanding and Exploration Survey (SEGUE Yanny et al., 2009), Gaia-ESO (Gilmore et al., 2012), the Abundances and Radial velocity Galactic Origins Survey (ARGOS Freeman et al., 2013), Apache Point Observatory Galactic Evolution Experiment (APOGEE Majewski et al., 2017), GIRAFFE Inner Bulge Survey (GIBS Zoccali et al., 2014), and the Radial Velocity Experiment (RAVE Steinmetz et al., 2006), have provided detailed abundance and kinematic data for a vast number of stars in the Galaxy. These have unravelled some of the more complex structures that exist in the stellar populations of the Milky Way, as well as providing a clearer picture of the evolutionary processes that form them.

1.2.1 The stellar halo

Despite the fact it makes up only a few percent of the total stellar mass in the Galaxy ($1.4 \pm 0.4 \times 10^9 M_\odot$; Deason et al., 2019), the stellar halo is perhaps the most important component of our Galaxy when it comes to understanding its formation; the reason for this is twofold. First, it has a long dynamical time-scale, so retains the memory of past merger events, and second it potentially contains some of the oldest and most metal-poor stars in the Galaxy.

As remarked by Hartwick (1987), the spatial distribution of stars in the halo trace out the shapes of two distinct components – an inner flattened component and a spherical outer component. Indeed, there is now strong evidence that the stars in the halo are bifurcated

into an inner and outer halo, grouped based on their chemistry and kinematics (*c.f.* Schönrich et al., 2011). Inner halo stars are characterised by mostly prograde orbits and a metallicity distribution function that peaks at [Fe/H] ≈ -1.6, whereas outer halo stars have net retrograde orbits and metallicities that peak at [Fe/H] ≈ -2.2 (Carollo et al., 2007, 2010; Nissen & Schuster, 2010; Schuster et al., 2012). The inner versus outer dichotomy has only become more clear following the data releases from the Gaia and APOGEE missions (see, e.g. Hayes et al., 2018; Haywood et al., 2018; Mackereth et al., 2019). In particular, Hayes et al. (2018) found two chemically distinct stellar populations, exhibiting either high- or low-[α/Fe] (labelled LMg and HMg, repsectively), that also exhibit different directions of orbital motion. They proposed that stars in the inner halo (LMg) could likely have been captured in a merger event during an earlier formative epoch of the Milky Way's past, whereas the HMg population had abundances and orbits similar to disk stars, so likely had origins that related somehow to the thick disk.

Using data from the *Gaia* mission, it was inferred that much of the inner halo and thick disk was formed during a major merger event with a dwarf galaxy named *Gaia*-Sausage-Enceladus (hereafter GSE; Helmi et al., 2018; Belokurov et al., 2018) that occurred 10 Gyr ago, or equivalently at $z \sim 2$ (where z here is the redshift, not metallicity). This is not the only major merger event for which there is strong chemical and/or kinematic evidence, with other notable mergers including the Helmi streams (Helmi et al., 1999), and the dwarf galaxies Sagittarius (Ibata et al., 1994), Sequoia (Myeong et al., 2019), and Thamnos (Koppelman et al., 2019), among others (see the recent review by Helmi, 2020). In particular, the GSE merger is thought to be responsible for the majority (up to $\sim 66\%$) of stars in the local halo with [Fe/H] $\lesssim -1.3$ and low [Mg, Al, Ni/Fe] (Mackereth et al., 2019). Instead, the high-metallicity halo stars (sometimes referred to as the *in situ* halo) are thought to be the result of the "Splash", a merger event that kicked stars from the proto-disk into high eccentricity orbits (see, e.g. Belokurov et al., 2020). Four new substructures were identified by Naidu et al. (2020) which they claimed, together with those substructures previously discovered, could account for the origin of $\gtrsim 95\%$ of giants in the halo up to 50 kiloparsecs from the Galactic centre. For the more local halo, Ruiz-Lara et al. (2022) used a best-fitting algorithm to group halo globular clusters into substructures based on their metallicity distribution function, position in space,

and age and find that at least 20% can be strongly identified with substructures. For a complete list of known globular clusters and their likely origin scenario, whether that be from a specific merger event or formed *in situ*, we refer the reader to Massari et al. (2019).

1.2.2 The Galactic thin disk

The thin disk contains most of the stellar mass in the Galaxy ($\sim 3.5 \pm 1 \times 10^{10} M_{\odot}$; Bland-Hawthorn & Gerhard, 2016), and is responsible for its distinctive shape in the night sky. It is in this component that most of the Galaxy's star formation takes place, with a predicted star formation rate of $1.65 \pm 0.19 M_{\odot} \mathrm{yr}^{-1}$ for a Kroupa initial mass function (Licquia & Newman, 2015). As its name would suggest, the thin disk reaches only a scale height of ~ 0.3 kpc above the midplane of the Galaxy (Jurić et al., 2008), with an exponentially decreasing vertical stellar density profile both above and below the plane (Gilmore & Reid, 1983). The thin disk extends further radially with a scale length of ~ 3 kpc[6] (McMillan, 2011), however, some argue this is unusually short when compared to analogue galaxies of similar star formation rate and mass (Boardman et al., 2020). Unlike in the axial direction, the radial density distribution is best fitted by two separate exponential profiles (Bovy et al., 2016; Mackereth et al., 2017), however, the reason for this "broken" density profile is unclear (Lian et al., 2022). Stars in this component have low eccentricity orbits, with older stars having in general more random and less circular orbits (Bird et al., 2013).

The presence of super metal-rich dwarf stars ([Fe/H] $\gtrsim 0.25$ dex) in the solar neighbourhood (see, e.g. Feltzing & Gonzalez, 2001) has been interpreted as evidence for radial migration in the disk (Sellwood & Binney, 2002; Roškar et al., 2008; Kubryk et al., 2015). These stars that were presumably born in the inner disk were kicked into orbits at larger Galactocentric radii by interactions with other disk substructure (i.e., spiral arms, molecular clouds; Minchev et al., 2018) or via perturbations from merger events (Carr et al., 2022). Further evidence of disk phase mixing was revealed following the second Data Release of the Gaia mission, where several substructures and morphologies were identified in the phase space distribution of disk stars (Antoja et al., 2018).

[6]For comparison, the Sun resides at a Galactocentric radius of 8 kpc

1.2.2.1 Abundance gradients in the thin disk

In terms of chemical features, the stars in the thin disk display a clear negative abundance gradient - that is, there is a general trend of decreasing metallicity at larger Galactocentric distances (seminal works in the field include: Searle & Zinn, 1978; Peimbert, 1979; Shaver et al., 1983). Observations of HII regions (Rudolph et al., 2006; Esteban & García-Rojas, 2018; Arellano-Córdova et al., 2020), classical Cepheids (Luck, 2018), open clusters (Janes, 1979; Donor et al., 2020; Sales-Silva et al., 2022), and planetary nebula (Maciel et al., 2003; Stanghellini & Haywood, 2018), are amongst the wealth of evidence that confirm this anti-correlation (see Arellano-Córdova et al., 2021, for a recent comparison of results obtained by these techniques). In particular, planetary nebula and open clusters offer an important probe of the spatial and temporal evolution of the oxygen and global metallicity abundance gradients, respectively. However, they are not without potentially large kinematic uncertainties (Mollá et al., 2019). Measurements of forbidden lines in extragalactic HII regions have also been used to confirm radial abundance gradients in galaxies beyond our own (McCall et al., 1985; Garnett et al., 1997; Sánchez et al., 2012, 2014; Ho et al., 2015).

The radial metallicity gradient in the Milky Way for three different age bands of F and G dwarf stars from the Geneva-Copenhagen Survey is shown in Figure 1.4. For stars less than 6 Gyr old, the slope of the best-fitting lines is between ~ -0.08 and -0.1 dex/kpc, whereas the gradient for the oldest stars is both shallow and positive, +0.028 dex/kpc. A re-analysis of the data by Casagrande et al. (2011) using more accurate effective temperature and metallicity measurements also confirmed a flattening of the gradient with lookback time, however, the exact slope is strongly dependent on the choice of kinematic and/or metallicity cuts for the bins. Recent results by Anders et al. (2017) and Stanghellini & Haywood (2018) also confirm a flattening of the gradient with age in populations of red-giant stars and PNe, respectively. Furthermore, using data from the SDSS-II APOGEE experiment Hayden et al. (2014) find that the magnitude of the slope flattens i) at Galactocentric radii $R < 6$, ii) with increasing elevation above the disk plane, iii) in stars with higher $[\alpha/\mathrm{M}]$. Recently, measurements from mono-abundance stellar populations show a flattening of the gradient with increasing age, at a rate of 0.003 dex kpc^{-1} Gyr^{-1} (Vickers et al., 2021). This flattening is generally considered

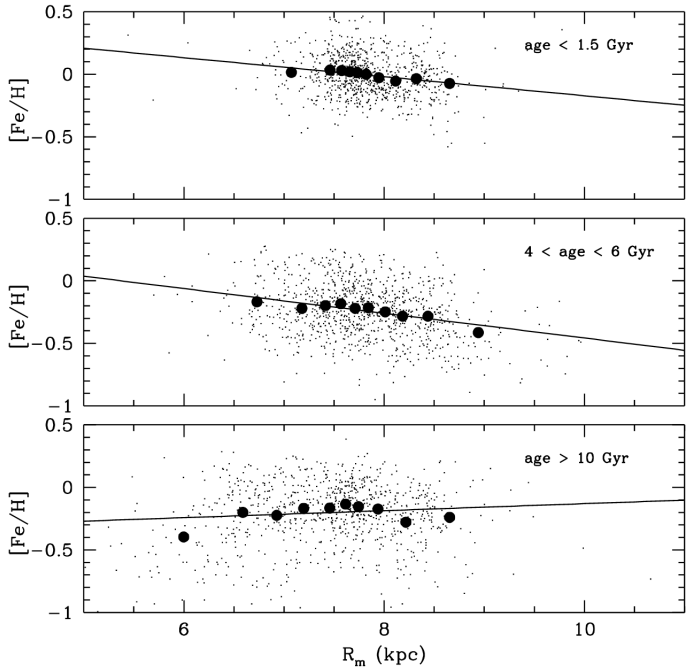

Figure 1.4: Metallicity (measured in terms of [Fe/H]) as a function of mean radius (R_m) for disk stars from the Geneva-Copenhagen survey, binned by age. Figure from Nordström et al. (2004).

to be the result of radial migration (Magrini et al., 2016).

In order to produce a radial abundance gradient in GCE models it is necessary to assume that the disk forms inside-out, whereby the inner regions of the disk form on a much shorter timescale than those at larger radii (Chiosi, 1980; Tosi, 1982; Lacey & Fall, 1985; Matteucci & Francois, 1989; Chiappini et al., 1997). However, this formation scenario alone is insufficient to reproduce the slope of the observed abundance gradients (Grisoni et al., 2018; Palla et al., 2020). This can be solved by assuming additional physical mechanisms such as a variable star formation efficiency that is a function of galactocentric radius (Colavitti et al., 2009; Belfiore et al., 2019), a threshold in the gas density for the star formation rate (Chiappini et al., 2001), radial gas inflows induced by material falling onto the disk (Portinari & Chiosi, 2000; Spitoni & Matteucci, 2011; Spitoni et al., 2013), or the effect of stellar migration (Spitoni et al., 2015; Schönrich & McMillan, 2017; Vincenzo & Kobayashi, 2020). However, it is not yet clear the extent to which each of these processes contributed toward the radial gradients observed in the Galactic thin disk. There is also a general consensus from cosmological simulations that the metallicity gradient generally steepens over time (Gibson et al., 2013; Vincenzo &

Kobayashi, 2018; Bellardini et al., 2021).

1.2.3 The Galactic thick disk

The thick disk is comparatively less massive than its thin counterpart ($M_\star = 6 \pm 3 \times 10^9 M_\odot$; Bland-Hawthorn & Gerhard 2016) and was first identified by virtue of its vertical density profile (Gilmore & Reid, 1983). This component has also been observed in other spiral galaxies (Dalcanton & Bernstein, 2002). Stars in the thick disk are typically older (Silva Aguirre et al., 2018) and are enhanced in [α/Fe] relative to thin disk stars of the same metallicity (Fuhrmann, 1998; Lee et al., 2011; Haywood et al., 2013; Hayden et al., 2014). The metallicity distribution function for the thick disk is also uniform at all radii, and peaks at around [Fe/H] ~ -0.4 (Hayden et al., 2015), with an extended low-metallicity tail down to [Fe/H] $\lesssim -1.6$ (Beers et al., 2002). There is strong evidence to suggest that thin and thick disk stars can be resolved into separate stellar populations based purely on their chemistry alone (Lee et al., 2011; Adibekyan et al., 2011; Anders et al., 2014). However, Bovy et al. (2012) argue that the Milky Way's disk is instead comprised of various stellar sub-populations, which follow a single smooth distribution in morphological parameters. Figure 1.5 shows the [α/M] versus [M/H] distribution of stars in the Gold sample[7] from APOGEE data, with a clear disparity (or "gap") in the data along the dashed line which denotes the chemical boundary suggested by Anders et al. (2014) that separates thick disk (blue) from thin (red). A similar binarity of sequences in the [α/Fe] versus [Fe/H] plane for the solar neighbourhood was also found by Hayden et al. (2015); one sequence remains relatively flat at solar-[α/Fe] and the other (high-[α/Fe]) exhibits a clear downward trend with metallicity, with both eventually merging to solar-[α/Fe] at super-solar metallicity. However, at larger galactocentric distances no high-[α/Fe] stars are observed, which indicates that the thick disk is more centrally bound than its thin counterpart, with a scale length of between $\sim$ 1.8 kpc (Cheng et al., 2012) and $\sim$ 2.2 kpc (Bovy et al., 2016). There is a clear increase in scaleheight with radius for the solar-[α/Fe] sequence due to disk flaring (Minchev et al., 2017); this has been interpreted by some to mean that the thin and thick disk have a different dynamical origin (Robin et al.,

[7] A subset of $\sim$ 4000 stars in the solar neighbourhood (1-2 kpc from the Sun) for which precise distance ($\sigma(d)/d < 0.2$) and proper motions are available. The cuts are applied by Anders et al. (2014).

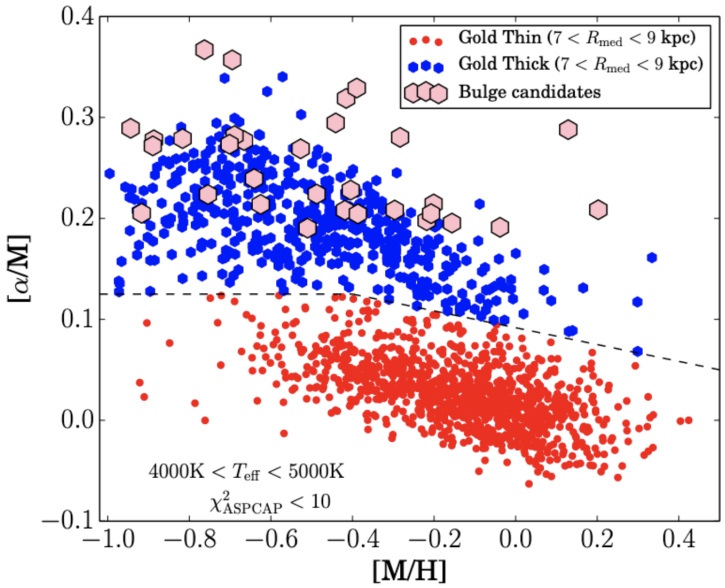

Figure 1.5: Distinction of thin and thick disk stars in the Gold sample of the APOGEE data based on their location in the [α/M]-[M/H] diagram. Figure from Anders et al. (2014).

2022).

Stars in the thick disk are kinematically hotter than their thin disk counterparts, with larger velocity dispersions and generally less well defined orbital paths (Chiba & Beers, 2000). Due to the fact that the thick disk shares some kinematic and chemical properties with both the thin disk and halo, it has been suggested that its formation may be inextricably linked to one of these two components (see Section 1.1.in Cheng et al. 2012 and Section 5.2 in Helmi 2020 for a discussion of these). Based on a purely chemical study of the thick disk and halo stellar populations, Bland-Hawthorn et al. (2019) found no discernible distinction between the two components for abundance ratios of several α, Fe-peak (Mn, Ni), and light elements, suggesting they likely formed from similar gas. There is also mounting evidence for a bimodal distribution of the age-metallicity relation for stars in the solar neighbourhood (Nissen et al., 2020; Miglio et al., 2021). This coincides with a discontinuity in the age-velocity dispersion relation, and is strong evidence that the thick and thin disk formed from two separate episodes of gas accretion, with an interim period of quenched star formation between them. In the so-called two-infall model initially proposed by Chiappini et al. (1997, 2001), the thick disk forms during the initial infall over a short timescale, whereas the thin disk forms inside-out

over a long timescale during the second infall. This leads to a doubly peaked star formation history, with maxima corresponding to the formation of the thick and thin disks (e.g. Snaith et al., 2015; Mor et al., 2019). In order to fit observational data from the AMBRE project (de Laverny et al., 2013), the timescales for accretion of the thin and thick disk in the revised infall model of Grisoni et al. (2017) are 7 Gyr and 0.1 Gyr respectively, with a gap in the star formation between infall episodes that lasts $\sim$ 700 Myr. Alternatively, they find the data can be fit by assuming that the thin and thick disk form in parallel; that is, they evolve entirely independently from each other, but the onset of formation for the thin disk is not delayed with respect to the thick disk in variance with the two-infall model. However, Spitoni et al. (2019, 2020) propose that a revised two-infall model with a long delay time ($\sim$ 4.5 Gyr) between the first and second infall episodes is a requirement for predicting the age-metallicity relation in the observed data of Silva Aguirre et al. (2018). A similar timescale for quenching of star formation is found by Spitoni et al. (2021), who use Bayesian analysis to constrain a multi-zone GCE model to APOGEE DR16 data.

1.2.4 The Galactic Bulge

The morphology and structure of the Galactic bulge has been extensively mapped out using red clump giants (see, e.g. Stanek et al., 1994, 1997). These have revealed that the majority of stars in the most central component of the Galaxy reside in a triaxial bar-like structure (Rattenbury et al., 2007), with a length of $\sim$ 4.5 kpc (Cabrera-Lavers et al., 2007). Measurements of two red clump stellar population peaks observed in the bulge suggest the bulge's morphology cannot be simply described as a tilted bar (McWilliam & Zoccali, 2010; Nataf et al., 2010). These observations can instead be understood if the bar is more of a funnel shape, thus coining the term boxy/peanut (b/p) bulges to describe such a morphology (López-Corredoira et al., 2005). The b/p shape is not unique to the Milky Way, as nearly half of all disk galaxies which are viewed edge-on also contain this structure (Lütticke et al., 2000). N-body simulations show that a b/p shape is indicative that initially the bulge formed similarly to a disk but, due to instabilities, it collapsed forming a bar-like structure at its centre (Athanassoula, 2005; Di Matteo et al., 2014). The bulge has been estimated to constitute about one fifth of the total mass in the Galaxy (Zoccali & Valenti, 2016), with a stellar mass of $\sim 2.0 \times 10^{10} M_{\odot}$ (Sofue

et al., 2009; Valenti et al., 2016; Portail et al., 2017).

The Galactic bulge has a broad metallicity distribution $-1.5 \lesssim$ [Fe/H] $\lesssim 0.5$ (Zoccali et al., 2008; Barbuy et al., 2018), however, it is still unclear whether the global metallicity distribution is best fit with double Gaussians at [Fe/H] $\approx +0.3$ and [Fe/H] ≈ -0.3 (i.e. a bimodal distribution; Rojas-Arriagada et al., 2014; Gonzalez et al., 2015; Zoccali et al., 2017) or whether it has several peaks (Ness et al., 2013; Bensby et al., 2017). It is evident also from the kinematics of the stars that the bulge is comprised of at least two stellar populations, a result that had been previously predicted by chemodynamical models (Samland et al., 1997). In particular, stars in the bar are metal-poor and α-rich, which suggests it formed quickly (Bovy et al., 2019), perhaps collapsing in a timescale of $\lesssim 1$ Gyr (Matteucci & Brocato, 1990; Cavichia et al., 2014; Friaça & Barbuy, 2017). Using the ARGOS and APOGEE surveys, Wylie et al. (2021) found that [Fe/H] increases and [Mg/Fe] decreases in bulge stars with increasing Galactocentric distance. Furthermore, there is a clear bimodal distribution in the [Fe/H] versus [Mg/Fe] plane along the bar, with two maxima that are '[Fe/H] rich-[Mg/Fe] poor' and '[Fe/H] poor-[Mg/Fe] rich', each with unique kinematics (Johnson et al., 2022). This is strong evidence that the bulge contains stars that formerly belonged to the thin and thick disk populations, suggesting it forms as a composite system. This formation scenario is also supported by the fact that the bulge has a distinct vertical metallicity gradient (Zoccali et al., 2008; Rojas-Arriagada et al., 2020), which is reminisce of a classical bulge formed via mergers. On the other hand, the b/p shape is characteristic of a collapsing disk population, and thus suggests a more *in situ* origin (Ness & Lang, 2016).

1.3 Metallicity scaling relations

1.3.1 Age-abundance relations

The relationship between stellar age and metallicity, hereafter the age-[Fe/H] relation, provides a fossil record of the stellar enrichment history of the Galaxy and is therefore a strong observational constraint for Galactic simulations and chemical evolution models. Observations of dwarf stars in the solar vicinity have established a clear decrease in [Fe/H] in older stars (Twarog, 1980). However, due to the substantial scatter in [Fe/H] for disk stars (Edvardsson

et al., 1993; Haywood et al., 2013; Rebassa-Mansergas et al., 2016), field stars (Pancino et al., 2010), and open clusters (Netopil et al., 2016) in a given age bin, the existence of an ubiquitous age-[Fe/H] correlation has been questioned (Feltzing & Gonzalez, 2001). In particular, it appears that beyond the solar vicinity the age-[Fe/H] relation is relatively flat in young and intermediate age stars ($0 - 8$ Gyr), with a decrease in [Fe/H] only observed in older stars (Bergemann et al., 2014; Rebassa-Mansergas et al., 2016; Sahlholdt et al., 2022). The scatter can be somewhat reconciled when one considers that the uncertainties associated with individual stellar age measurements can be significant (as much as $20 - 50\%$ depending on the technique used; Soderblom, 2010), nevertheless, the wide metallicity distribution in the solar neighbourhood suggests that some amount of radial migration has also taken place (Francois & Matteucci, 1993; Feuillet et al., 2018).

A tight correlation in the age-[α/Fe] relation is observed in thin disk stars, which suggests that α-elements and Fe produced by supernovae are well homogenized in the ISM, whereas accretion of pristine gas into the disk can lead to a more stochastic distribution of H (Edvardsson et al., 1993; Nissen, 2015). The small scatter in the age-[X/Fe] relations of some elements means that chemical abundances can be used as precise chemical clocks to extrapolate the age of stars (Delgado Mena et al., 2019). By introducing also a metallicity dependency, Bedell et al. (2018) and Ness et al. (2019) demonstrated the existence of an [X/Fe]-age-[Fe/H] relation – that is, stars of a given age and [Fe/H] also have very similar abundance patterns – in solar twin stars and stars belonging to the low-α disk population, respectively. As discussed in Section 1.2.2.1 and shown in Figure 1.4, for stars of similar age [Fe/H] is a strong indicator of birth radius ($R_{\rm birth}$), and so the [X/Fe]-age-$R_{\rm birth}$ relation can be used to probe the smoothness (i.e., whether it is bursty or steady) of the Galaxy's star formation history over the whole disk (Carrillo et al., 2023). Furthermore, the [X/Fe]-age-$R_{\rm birth}$ relation can be used to determine more precise ages for some stellar types than can be achieved with current methods (Hayden et al., 2020). Using data from the GALAH survey, Sharma et al. (2022) found that elements can be grouped based on the slope of their abundance gradient in the age-[Fe/H] plane, where the members of a group share a common nucleosynthetic production site. However, whilst the scatter in the elemental abundances are still too large to pinpoint stars to a specific cluster (i.e., strong *chemical tagging*; Freeman & Bland-Hawthorn, 2002), the scatter is sufficiently small

to provide enough spatial resolution for tagging stars to birth radii (weak chemical tagging). This last means that the [X/Fe]-age-$R_{\rm birth}$ relation can help improve our understanding of dynamical processes that drive stars away from their birth place, such as radial migration.

1.3.2 The mass-metallicity relation

Although the work in this thesis concerns the chemical evolution of the Milky Way, it is imperative for our understanding of galaxy evolution that we do not 'fine tune' parameters in our GCE models so as to only be able to reproduce the abundance distributions in our own Galaxy. To this end, a fundamental property of galaxies is the relationship between their stellar mass ($M_\star$) and the metal content of the gas-phase of the ISM, where this last is typically measured in terms of the O/H ratio in the gas. The so-called mass-metallicity relation (MZR; Lequeux et al., 1979) provides constraints for several key parameters in GCE models, such as the gas accretion history, star formation rate, and gas outflow rate (Finlator & Davé, 2008; Mannucci et al., 2010; Maiolino & Mannucci, 2019). Early observations of a small number of elliptical galaxies established a correlation between their stellar mass-to-light ratio and the global metallicity (McClure & van den Bergh, 1968; Rood, 1969; Faber, 1973; Visvanathan & Sandage, 1977). This relationship was later tightened using much larger sample sizes of star-forming galaxies observed by large-scale sky mapping, such as the Sloan Digital Sky Survey (SDSS; see, e.g. Tremonti et al., 2004; Kewley & Ellison, 2008). It is now clear that within the range $10^7 M_\odot \lesssim M_\star \lesssim 10^{12} M_\odot$, more massive galaxies are also more metal rich. The exact nature of the MZR varies as a function of $M_\star$, although the general form is of a power-law slope at low masses ($M_\star \lesssim 10^{10} M_\odot$) out to $z \sim 3$, which asymptotes to a constant metallicity above some turnover mass (Sanders et al., 2021). That the MZR decreases in galaxies of lower mass could be due to their shallower potential wells, which makes them more susceptible to lose metals via supernova driven winds (Spitoni et al., 2010; Davé et al., 2011; Feldmann, 2015; Chisholm et al., 2015; Spitoni et al., 2017); this effect can also be reproduced by considering a time-dependent metal outflow, where winds are more metal-enhanced at larger redshifts (Lian et al., 2018; Sanders et al., 2021). An alternative interpretation is that more massive systems are enriched on faster timescales, either due to higher star formation efficiencies (Calura et al., 2009), or a positive correlation between $M_\star$

and the high mass cutoff of the initial mass function (Köppen et al., 2007; Vincenzo et al., 2016a).

The MZR is also a function of a galaxy's star formation rate (SFR), such that metallicity decreases with increasing SFR for fixed $M_\star$ (Ellison et al., 2008) – this is known as the Fundamental Metallicity Relation (FMR; Mannucci et al., 2010). Most studies find that the FMR is invariant with redshift out to $z \sim 2.5$ (Mannucci et al., 2010; Sanders et al., 2018), but that at very high redshifts there is large scatter relative to the FMR (Onodera et al., 2016). Recently, an analysis of three $z \sim 8$ galaxies observed by the *James Webb Space Telescope* found that the lowest mass galaxy was severely metal-deficient compared to the predicted FMR at this redshift (Curti et al., 2023); this suggests that galaxies at early epochs undergo rapid, turbulent growth – a departure from the steady secular growth of galaxies via steady gas flows at higher redshifts.

2. GCE models

Section 2.5 of this Chapter contains a written review of the evolution of ^{26}Al in the Galaxy, which was submitted as part of Laird et al. 2022 to J.Phys.G. This paper is a large collaborative effort, but the work contained herein is entirely my own. Feedback for this review was given by Benoit Côté and Maria Lugaro.

The first attempt to describe analytically how the metallicity of a system with stellar enrichment evolves as a function of time was made by van den Bergh (1958) and Schmidt (1959, 1963). This so-called *Simple Model* made several underlying assumptions, chiefly that the solar neighbourhood can be modeled as a "closed-box" system with no circulation or mixing of gas with other parts of the Galaxy, which led to vast overpredictions of the number of low-metallicity stars compared to observations. The favoured solution was to allow pristine gas to flow into the system, thereby diluting the Galactic disk which would continue to grow as it accreted more material (Larson, 1972). It quickly became evident that the Galaxy is very much a chemodynamical system (see, e.g. Larson, 1976). Not only is metal-poor gas accreted from the intergalactic medium (IGM), but the energetic feedback from the violent deaths of stars as supernovae can eject metal-rich gas from the Galaxy in superwinds (Heckman et al., 1990; Veilleux et al., 2005; Shen et al., 2010) which can, depending on the ratio of the kinetic energy of the outflowing material to the size of the potential well of the halo, potentially be re-accreted later as 'galactic fountains' (Shapiro & Field, 1976; Oppenheimer & Davé, 2008). It is clear then that a closed-box model is an inadequate oversimplification of the gas flow mechanisms that drive galaxy formation and evolution. However, the Simple Model is nonetheless worthy of discussion because of its historical importance in the context of GCE, and because its predictions still serve as an important measuring stick for modern semi-analytical and numerical models (see, e.g. Côté et al., 2016).

2.1 The Simple Model

In this Section, we derive the solution to the Simple Model following the formalism of Pagel & Patchett (1975). The basic assumptions used in the derivation are as follows:

1. The gas evolves inside a “closed-box" system with no gas inflows or outflows. The system, which is assumed to represent the solar neighbourhood if it were chemically isolated from the rest of the Galaxy, is described by a cylindrical shell perpendicular to the plane of the Galaxy and centred on the Sun extending radially ~ 1 kpc.

2. The star formation rate is proportional to the total mass of gas in the system raised to some power.

3. The gas is initially devoid of all metals and contains no stars, such that the *primordial* composition of the gas contains only those isotopes that were produced during the Big Bang.

4. At all times the chemical composition of the gas is homogeneous, and stars born from the gas inherit the chemical composition of the gas at that time.

5. The initial mass function is constant in time. Stars with lifetimes of the order of ~ 10 Gyrs or that leave behind a compact remnant serve to lock-up some fraction of gas, α, in each generation of stars. Therefore, the total mass of gas in the system decreases with time.

6. Stellar ejecta is instantaneously recycled into the ISM.

To arrive at the solution for $Z(t)$, we first define the metallicity as the fraction of metals in the gas, per unit mass

$$Z = \frac{M_Z}{M_g}, \tag{2.1}$$

where M_Z and M_g are the mass of all metals (i.e., $A \geq 12$) and the total mass of all elements (i.e., including H and He) in the parcel of gas, respectively. Since the gas is initially of primordial composition, $M_Z = 0$ at time $t = 0$. Consider now the change in metallicity, δZ,

for some small time interval t to $t + \delta t$. Since Z is a function of M_Z and M_g, the differential of Z with respect to time is

$$\frac{\mathrm{d}Z}{\mathrm{d}t} = \frac{\delta Z}{\delta M_Z}\frac{\mathrm{d}M_Z}{\mathrm{d}t} + \frac{\delta Z}{\delta M_g}\frac{\mathrm{d}M_g}{\mathrm{d}t}. \tag{2.2}$$

To get the partial derivatives on the right hand side, we differentiate Equation 2.1 to get $\delta Z/\delta M_Z = 1/M_g$ and $\delta Z/\delta M_g = -M_Z/M_g^2 = Z/M_g$, so that Equation 2.2 becomes

$$\frac{\mathrm{d}Z}{\mathrm{d}t} = \frac{1}{M_g}\frac{\mathrm{d}M_Z}{\mathrm{d}t} - \frac{Z}{M_g}\frac{\mathrm{d}M_g}{\mathrm{d}t} \tag{2.3}$$

which, for a small time interval δt, can be expressed as

$$\delta Z = \frac{\delta M_Z}{M_g} - Z\frac{\delta M_g}{M_g}. \tag{2.4}$$

To get an equation in terms of only Z and M_g we have to solve for δM_Z. From assumption (2), we know that in a given time interval the mass of stars $\delta M_\star$ that are born in the system is proportional to the mass of gas in the system. Therefore, according to assumption (4), the amount of metals that are incorporated into these stars is $Z\delta M_\star$, and the mass of newly synthesised metals ejected by stars is proportional to the mass of gas that forms them (assumption 5). This constant of proportionality, called the *yield* (Searle & Sargent, 1972), is the ratio of the mass of metals ejected by a population of stars, to the mass of metals locked-up in stars per unit mass. Thus, the rate of increase in M_Z due to stellar ejecta is $p\delta M_\star$, where p is the newly defined population-level stellar yield. It then follows that the change in mass of metals in the gas in time interval δt is

$$\delta M_Z = p\delta M_\star - Z\delta M_\star. \tag{2.5}$$

Since the system is a closed-box, the total mass of baryonic matter must be conserved, so any change in the mass of gas in δt must be due to star formation, thus $\delta M_g = -\delta M_\star$. Substituting this into Equation 2.5 gives

$$\delta M_Z = Z\delta M_g - p\delta M_g, \tag{2.6}$$

and upon substituting the above expression for δM_Z into Equation 2.4, we have that

$$\delta Z = \frac{Z\delta M_g - p\delta M_g}{M_g} - Z\frac{\delta M_g}{M_g} = -p\frac{\delta M_g}{M_g}. \tag{2.7}$$

This can be solved by converting to a differential equation and integrating from time 0 to t, where we make use of assumption (3) that $Z(t = 0) = 0$,

$$\int_0^{Z(t)} \mathrm{d}Z' = \int_{M_g(0)}^{M_g(t)} p\frac{\mathrm{d}M_g'}{M_g'}. \tag{2.8}$$

According to (5), the stellar yield $p = p'/\alpha$ is assumed to be constant in time, where p' is the mass of newly synthesised heavy elements (i.e, those metals that were not already present in the gas that formed the stellar population) and we remind that α is the fraction of gas per unit mass of stars formed that is permanently locked into long-lived stars (Pagel & Patchett, 1975). Following integration, Equation 2.8 becomes

$$\begin{aligned} Z(t) - 0 &= -p\left[\ln M_g'\right]_{M_g(0)}^{M_g(t)} \\ Z(t) &= -p\ln\left(\frac{M_g(t)}{M_g(0)}\right) \\ &= -p\ln\mu, \end{aligned} \tag{2.9}$$

as derived by (Talbot & Arnett, 1971; Searle & Sargent, 1972), where $\mu \equiv M_g(t)/M_g(0)$ is the gas fraction at time t. Equation 2.9 tells us that the metallicity increases as the gas fraction decreases, or more specifically, that the increase in Z is more rapid as more baryonic matter is in the form of stars. We can also derive an expression for $Z(t)$ in terms of the mass of stars, starting with Equation 2.4 and the previously used relation $\delta M_g = -\delta M_\star$, we have that

$$\delta Z = p\frac{\delta M_\star}{M_g(0) - M_\star(t)}, \tag{2.10}$$

which can be integrated over as in Equation 2.8, such that

$$\begin{aligned} \int_0^{Z(t)} \mathrm{d}Z' &= p\int_0^{M_\star(t)} \frac{\mathrm{d}M_\star'}{M_g(0) - M_\star'} \\ Z(t) &= -p\ln\left(\frac{M_g(0) - M_\star(t)}{M_g(0)}\right) \end{aligned} \tag{2.11}$$

which after taking the exponential gives,

$$\frac{M_\star(t)}{M_g(0)} = 1 - \mathrm{e}^{-Z(t)/p}. \tag{2.12}$$

Equation 2.12 tells us the fraction of baryonic matter in the form of stars as a function of the gas metallicity. Since at each timestep some fraction of long-lived stars are born and remain in the system indefinitely, $M_\star(t)$ is cumulative and is proportional to the total number of stars in the system with $Z \leq Z(t)$, such that

$$S(\leq Z) \propto M_\star(t) = M_g(0)\left(1 - \mathrm{e}^{-Z/p}\right), \tag{2.13}$$

where $S(Z')$ is the total number of stars at time t' and gas metallicity $Z(t') = Z'$. Since stellar metallicities are given in terms of $\log_{10}(Z/Z_\odot)$, the metallicity distribution function (MDF) as it appears in Pagel (1997) is

$$\begin{aligned}
\frac{\mathrm{d}S}{\mathrm{d}\log Z} &\equiv \frac{\mathrm{d}S}{\mathrm{d}U} \quad ; \quad U(Z) = \log(Z) \\
&= \frac{\mathrm{d}Z}{\mathrm{d}U} \times \frac{\mathrm{d}S}{\mathrm{d}Z} \\
&= \left(\frac{\mathrm{d}U}{\mathrm{d}Z}\right)^{-1} \times \frac{\mathrm{d}S}{\mathrm{d}Z} \\
&\propto Z\mathrm{e}^{-Z/p}.
\end{aligned} \tag{2.14}$$

This distribution therefore depends on the gas metallicity and the stellar yield. This last we can estimate using Equation 2.9 and present day values for the solar metallicity $Z_\odot = 0.014$ (Asplund et al., 2009), which we assume to be a good representation of the solar neighbourhood average (Esteban et al., 2022), and the gas mass fraction of the Galaxy $\mu_\odot \lesssim 10\%$ (Wiklind et al., 2019), such that $Z_\odot = 0.014 = -p \ln 0.1$, giving $p \approx 0.006$. The normalised distributions for Equation 2.14 with $p = 0.006$ and $p = 0.03$ (a more realistic estimate from nucleosynthesis models weighted over an IMF) are plotted in Figure 2.1. For comparison, we plot also a histogram of observational data from nearby F and G dwarf stars in bins of $[\mathrm{Mg/H}] = \log_{10}\left(\frac{N_{Mg}}{N_H}\right)_\star - \log_{10}\left(\frac{N_{Mg}}{N_H}\right)_\odot$. Although the derivation for the Simple Model uses Z to represent the metal fraction of the gas summed for all elements except H and He, it is analogous to compare it to, for example the Mg abundance observed in long-lived stars because it is an α-element and so is produced predominantly by short-lived massive stars; this means the amount of Mg locked in long-lived low mass stars in the Simple Model

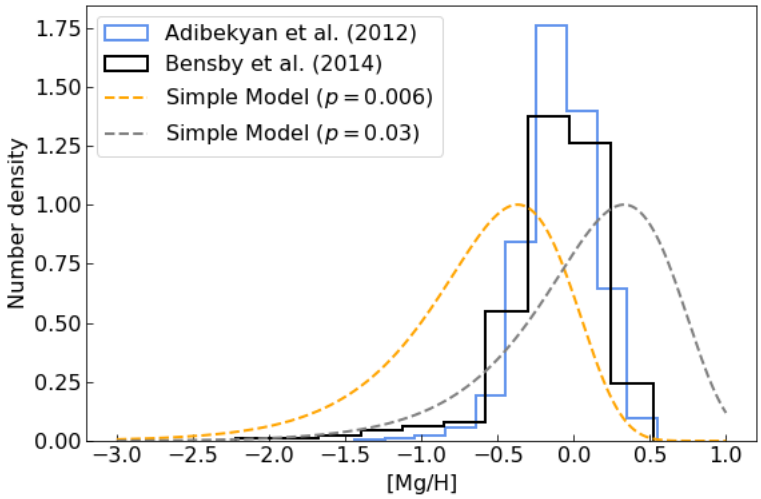

Figure 2.1: Metallicity distribution function for Simple Model with $p = 0.006$ (orange dashed line) and $p = 0.03$ (grey dashed line), where the first value is calculated using Equation 2.9 for $Z_\odot = 0.014$ and $\mu = 01$. Binned observational data of [Mg/H] for F and G dwarfs is taken from Adibekyan et al. (2012) and Bensby et al. (2014).

is negligible. The Z and [Mg/H] equivalence would cease to be true, however, if we were to relax the instantaneous recycling approximation and instead take into account the mass and metallicity dependent yields for a variety of stellar sources that enrich the ISM over different timescales.

Finally, we recall assumption (2), that the star formation rate $\delta M_\star(t) \propto \mu^n(t)$, or equivalently

$$\tau_\star = \frac{M_g}{\delta M_\star} = -\frac{M_g}{\delta M_g}, \tag{2.15}$$

where we have assumed $n = 1$ (Schmidt, 1959), and the constant τ is the 'turnover time' for the efficiency with which gas is converted into stars. Converting to a differential equation and integrating from time 0 to t, we have that

$$\int_{M_g(0)}^{M_g(t)} \frac{1}{M_g'} \mathrm{d}M_g' = -\tau_\star \int_0^t \mathrm{d}t', \tag{2.16}$$

leading to,

$$\frac{M_g(t)}{M_g(0)} = \mathrm{e}^{-t/\tau_\star}, \tag{2.17}$$

and finally using Equation 2.9 we arrive at an expression for the metallicity as a function of time:

$$Z(t) = p\frac{t}{\tau_\star}. \tag{2.18}$$

Recall that, since the instantaneous recycling approximation is assumed, an element like Mg will evolve according to $Z(t)$ and thus the Simple Model predicts a linear increase in the abundance with time. This prediction provides a relatively good fit for the stellar populations in the Galactic bulge (Rich, 1990; Zoccali et al., 2003) and the halo (Pagel, 1992), however, as seen in Figure 2.1, it overpredicts the number of low metallicity stars compared to long-lived stars in the solar neighbourhood.

That a large number of low-metallicity stars are born in the Simple Model is unsurprising when one considers that the metallicity evolves according to Equation 2.9. Since the reservoir of available gas decreases from its initial maximum at $t = 0$ due to star formation, the population-level stellar yield p (assumed to be constant) is diluted by an ever decreasing gas supply. Since the star formation rate is proportional to the mass of gas, the mass of stars born per stellar generation decreases with time, so more stars are born at early time from the low metallicity gas. The abundances of elements in the photospheres of long-lived stars are assumed to remain unchanged over their lifetime, and refelct the metallicity of the gas at the time of birth. That so few G dwarf stars have a low metallicity presented a problem for the Simple Model.

2.1.1 The G dwarf problem

The *G-dwarf Problem* was the term coined to describe the paucity of low-metallicity, long-lived G-dwarf stars in the MDF compared to Simple Model predictions. This inconsistency was first realised by van den Bergh (1962) and Schmidt (1963), who argued that the stellar birth rate function must not be time-independent, but instead the function must have been biased more toward stars with initial masses $\gtrsim 1 M_\odot$ at early Galactic times. In addition to the variable initial mass function first proposed by Schmidt (1963), other potential solutions to the G-dwarf problem included: a prompt enrichment from low-metallicty, high-mass stars with

very short lifetimes which pre-enriched the pristine gas with metals prior to the birth of the first stellar population (Truran & Cameron, 1971); a relaxation of the assumption that elements are distributed homogeneously in the Galaxy, and that the increased density in pockets of metal-rich gas can accelerate star formation locally (Talbot & Arnett, 1973; Talbot, 1974); and dilution of the gas via the inflow of pristine material from outside the Galaxy (Larson, 1972; Quirk & Tinsley, 1973). The pros and cons of each were reviewed by Pagel & Patchett (1975), who argued that deviations from the “closed-box" assumption of the Simple Model must also be accompanied by a revision of the star formation function in order to solve the G-dwarf problem. Observations of high-velocity clouds of neutral hydrogen gave credence to the theory that the Milky Way is still actively accreting intergalactic gas (Oort, 1970). By the time Beatrice Tinsley wrote her seminal paper on GCE, it was well established that the influx of metal-poor gas into the Galaxy would have profound effects on its chemical evolution, and this had been proven to be an elegant solution to the G-dwarf problem (Tinsley, 1980).

2.2 GCE beyond the Simple Model and the OMEGA+ code

The G-dwarf problem highlighted a clear failing of the Simple Model: that it did not include a proper treatment of the gas flows in and out of the Galaxy. The first attempt to address this issue was made by Larson (1972), who suggested that the accretion of pristine material into the disk occurs at the same rate at which gas is removed due to star formation. Later, using a hydrodynamcial model, Larson (1976) proposed that the disk of Milky Way-like galaxies could have formed inside-out - that is, the central parts of the disk formed when the gas inflow rate was at a maximum, with a declining accretion rate at larger Galactocentric distances. In the ‘inside-out’ scenario, the ratio between the star formation rate and the infall rate in the disk decreases with increasing distance from the Galaxy centre; this is a potential explanation for the observed negative abundance gradients in the thin disk (Matteucci & Francois, 1989). To model this last, it was also necessary to consider a spatial distribution of elements in the disk, which could be achieved in a numerical context by assuming the disk to be formed of concentric rings of gas (or annuli), where the surface mass density is a function of Galactocentric distance (e.g. Smith, 1975; Chiosi, 1980; Tosi, 1982).

Another challenge for GCE models was to be able to explain the observed overabundance of [O/Fe] in metal-poor (i.e., [Fe/H] $\lesssim -1.0$) stars (see, e.g. Sneden et al., 1979; Clegg et al., 1981). Tinsley (1979) argued that such anomalies in the abundance ratios of "common primary elements" pointed to the requirement of a better treatment of the delay-times[1] associated with their progenitors. She suggested that the overabundance of [O/Fe] in halo stars could be explained if Type Ia supernovae (SNe Ia) had delay-times of $\lesssim 10^8$ years, and that these events should contribute a significant fraction of the Galaxy's Fe. This last had also been proposed by Chevalier (1976), who considered that the Fe enrichment from SNe Ia could be delayed with respect to massive stars. Numerical models that relaxed the instantaneous recycling approximation for low-mass stars had already been established, and these made it possible to follow the chemical contribution from different stellar enrichment sources (Schramm & Tinsley, 1974; Vigroux et al., 1976). Assuming the binary SNe Ia model of Whelan & Iben (1973), Greggio & Renzini (1983) reproduced the [O/Fe] versus [Fe/H] trend by considering a delayed enrichment of Fe from SNe Ia. The following year, Nomoto et al. (1984) calculated nucleosynthesis yields for a carbon deflagration SNe Ia model (W7 model), the yields of which were used by Matteucci & Greggio (1986) to follow for the first time the GCE of the solar neighbourhood by considering the time-delayed contributions from low- and intermediate-mass stars, massive stars, and SNe Ia separately. They also predicted the same metallicity trends for the evolution of Mg and Si as for O, arguing that if these former were also produced by massive stars then overabundances should be observed in older halo stars compared to disk stars. This prediction was later confirmed by observation (Francois, 1986) and with it, so too was the instantaneous approximation dropped in favour of the *time-delay model*.

GCE models continued to evolve away from the confinements imposed by the closed-box. Fueled by a combination of refinements to experimental techniques (see Clayton, 1982, for a review of the techniques) used to determine more precise meteoritic abundance data (Anders & Grevesse, 1989), a wealth of new abundance measurements for both metal-poor (e.g. Gratton & Sneden, 1988) and disk stars (e.g. Edvardsson et al., 1993), and the leap in

[1]The timescale of a particular stellar enrichment event, measured from the time of birth for the progenitor star (usually a function of initial stellar mass).

computational capabilities at the end of the 1980s, new chemodynamical GCE models were developed (Burkert & Hensler, 1988; Theis et al., 1992; Timmes et al., 1995). However, the large number of free parameters introduced by the coupling of chemical and dynamical effects exacerbated the uncertainties when compared to their more simple analytical and numerical counterparts.

The efficacy of GCE models are limited by uncertainties associated with stellar nucleosynthesis modeling, the dynamical behaviour of a galaxy's baryonic and non-baryonic matter, and limitations regarding present day observables, among other things. These uncertainties are further supplemented by restrictions regarding the temporal and spatial resolution of the system imposed by computational limitations. However, computational demands can be reduced substantially, for example, by making use of pre-calculated yield tables for a range of initial stellar metallicities and masses; this circumvents the problem of needing a GCE model that has to resolve at the scale of both stellar and galactic evolution. The coupling of chemical and dynamical effects in hydrodynamical simulations is also computationally intensive. An alternative are semi-analytical GCE models which sacrifice a thorough treatment of dynamical processes in favour of being able to explore a larger parameter space of initial conditions for significantly less computational resources. Despite their differences in approach, there are several ingredients that are shared by both chemodynamical and semi-analytical GCE models. In this Section, we describe these ingredients, with particular emphasis on how each is treated by the `OMEGA+` (One Zone Model for the Evolution of GAlaxies; Côté et al., 2017) GCE model that is used for the work in this thesis. This open-source code is part of the NuGrid Python Chemical Evolution Environment (NuPyCEE, `https://nugrid.github.io/NuPyCEE/overview.html`) which, together with its one-zone extension JINApyCEE (`https://github.com/becot85/JINAPyCEE`), forms the JINA-NuGrid chemical evolution pipeline. These packages allow to track separately the stable and radioactive species ejected by multiple stellar sources, and the decay module can account for radioisotopes that have more than one possible decay channel.

2.2.1 Gas flows

In the ΛCDM paradigm, galaxies are expected to grow via a series of mergers. Since this hierarchical dark matter growth is decoupled from baryonic physics, it is a relatively straightforward process to model with N-body simulations (Davis et al., 1985) and analytical techniques (White & Frenk, 1991). Within this cosmological framework, the gas and stars that make up the baryonic matter in galaxies are embedded inside the virial mass of the dark matter halo (Vogelsberger et al., 2014). Gas from the intergalactic medium (IGM) is also accreted into the Galaxy, causing it to grow and allowing it to sustain star formation over billions of years (Chiappini et al., 2001; Sancisi et al., 2008). Cosmological, hydrodynamical simulations have shown that for Milky Way-like galaxies the majority of gas is accreted in the form of smooth streams, rather than through mergers (van de Voort et al., 2011). Gas can also be expelled from the ISM through outflows driven by stellar feedback and active galactic nuclei, and the complex interplay between inflows and outflows of gas has – and will continue to have – a crucial role in the evolution of the Galaxy, chemically or otherwise (Fox, 2017).

For semi-analytical models such as `OMEGA+`, large-scale structure formation via gravitational coalescence is extracted from halo merger trees for N-body simulations of dark matter (for a review of this technique, see Somerville & Davé, 2015). The evolution of baryonic matter within this hierarchical growth framework is described using a set of ordinary differential equations that solve for physical processes such as star formation efficiency and stellar feedback. The virial mass at the end-point of a merger tree contains the whole galaxy object simulated by `OMEGA+`, and is defined as (Côté et al., 2018)

$$M_{\rm vir} = \frac{V_{\rm vir}^2 R_{\rm vir}}{G}, \tag{2.19}$$

where G is the gravitational constant and $V_{\rm vir}$ and $R_{\rm vir}$ are the virial velocity and radius, respectively. The cold- and hot-gas reservoirs of the respective star-forming and CGM components are modelled separately by `OMEGA+`. The change in the mass of gas in the central star forming region (henceforth called the galaxy) in timestep δt due to gas flow processes is given by

$$\delta M_{\rm gas} = \delta M_{\rm g,\,in} + \delta M_{\rm ej} - \delta M_{\star} - \delta M_{\rm g,\,out}, \tag{2.20}$$

where gas is added to the galaxy by inflows from the CGM ($\delta M_{\rm g,\,in}$) and stellar ejecta ($\delta M_{\rm ej}$), and depleted by star formation ($\delta M_{\star}$) and feedback driven outflows into the CGM ($\delta M_{\rm g,\,out}$). The CGM acts as the medium between which gas must pass in order to enter or leave the virialized system described by Equation 2.19. The change in mass of the CGM gas reservoir per timestep is given by the following equation,

$$\delta M_{\rm CGM} = \delta M_{\rm CGM,in} + \delta M_{\rm g,\,out} - \delta M_{\rm g,in} - \delta M_{\rm CGM,\,out}, \tag{2.21}$$

where $\delta M_{\rm CGM,in}$ and $\delta M_{\rm CGM,out}$ are the accretion and outflow rates of gas from and to the IGM, respectively. In this section we describe in more detail gas flows between the ISM, CGM, and IGM and look at how these are parameterised in semi-analytical models of GCE.

2.2.1.1 Inflows

From a theoretical standpoint, the accretion of primordial gas from the IGM is required to sustain star formation in the Galaxy (Tinsley, 1981; Tosi, 1988; Larson, 1991), as without a fresh supply of gas into the disk the Milky Way's gas depletion timescale is much shorter than the Hubble timescale, particularly at high redshift ($Z > 1$) (Genzel et al., 2010; Lilly et al., 2013). Furthermore, the influx of low-metallicity gas into the Galaxy has long been known to provide a solution to the G-dwarf problem (Lynden-Bell, 1975), and has also been shown to account for the overabundance of deuterium in the local ISM compared to GCE predictions (Romano et al., 2006; Steigman et al., 2007). Inflowing gas is also the main driver of cosmic star formation (Schaye et al., 2010).

It was first proposed by Oort (1966), that the high velocity (HVCs; $|V_{\rm lsr}| \gtrsim 80$ kms^{-}1) gas clouds of neutral hydrogen (HI) that had been observed by the Dwingeloo radio telescopes could likely be of extragalactic origin. However, this theory was later revised to account for the correlation of velocities for HI emission and Ca II absorption lines[2] in intermediate velocity clouds (IVCs; $|V_{\rm lsr}| \sim 40 - 100$ kms^{-1}), which were estimated to be at a height of no

[2]The presence of absorption lines in the gas indicated that the cloud was between the observer and the background stars of known scale height.

more than 1.5 kpc from the Galactic plane (Oort, 1970). This finding suggested that at least some of the clouds originate within the virial radius of the Galaxy itself. Instead, HI clouds with very high velocities (VHVCs; $|V_{\rm lsr}| \sim 230$ kms^{-1}) were thought to be of extragalactic origin due to the fact they were travelling at speeds exceeding those allowed by differential Galactic rotation (Wakker et al., 1999). From these, the rate of gas accretion into the Galaxy was estimated at $\gtrsim 0.2\ M_{\odot}{\rm yr}^{-1}$ (Mirabel & Morras, 1984), and it was proposed that the ubiquity of the VHVCs negative line of sight velocity reflected the movement of the Milky Way through the Local Group (Hulsbosch, 1978).

More recently, it has become apparent that HVCs and IVCs differ too in their distance and metallicity, supporting the idea that they have different origin scenarios. Most of the IVCs lie close to the Galactic plane with scale heights $\lesssim 2.5$ kpc (Wakker, 2001; Lehner et al., 2022), and typically have metallicities $\gtrsim 0.5\ Z_{\odot}$ (Wakker, 2001; Hayakawa & Fukui, 2022). For these reasons, IVCs are thought to originate inside the Galaxy itself, being ejected from the disk as hot gas due to stellar feedback and active galactic nuclei, and after cooling falling back onto the disk as neutral clouds – the so-called 'galactic fountain' cycle (Shapiro & Field, 1976). On the other hand, HVCs are typically less metal-rich ($0.1 - 1.0\ Z_{\odot}$) and are located at much larger distances from the plane of the disk $\gtrsim 10$ kpc (van Woerden & Wakker, 2004), and are therefore thought to be of mostly extragalactic origin (see Marasco et al., 2022, and references therein). For larger galaxies ($\gtrsim 10^{11} M_{\odot}$) at low redshift, the gas is predominantly shock-heated to the virial temperature during accretion ('hot mode' accretion; Nelson et al., 2013), whereas at greater lookback times and for galaxies below this mass threshold 'cold mode' accretion of gas can take place (Kereš et al., 2005, 2009; Dekel et al., 2009). Since the gas must first be sufficiently cooled, the timescale for gas to reach the disk during hot mode accretion is much longer than for cold mode accretion, and so the star-formation rate of high-mass galaxies peaks at higher redshifts (Behroozi et al., 2013).

Whilst the evidence from both observations and cosmological simulations point to a clear picture of gas accretion in the Milk Way, a complete dynamical treatment of gas infall remains elusive. For this reason, there is no consensus on how best to parameterise gas inflow in semi-analytical GCE models. The most simplistic approach is to assume that the rate of gas depletion via star formation is equal to the summation of the infall rate and the stellar

enrichment rate (e.g. Larson, 1972; Tinsley, 1980), such that

$$\delta M_\star = \delta M_{\mathrm{g,\,in}} + \delta M_{\mathrm{ej}}. \tag{2.22}$$

In this regime, the total baryonic mass increases whilst the mass of gas remains unchanged from its initial value. Since the gas is assumed to be of primordial composition, it no longer holds that $\delta M_g = -\delta M_\star$ as was the case in the closed-box model (since $\delta M_g = 0$ and star formation is still occuring), and as such with accretion the metallicity evolves according to

$$\delta Z = (p - Z)\frac{\delta M_\star}{M_g}, \tag{2.23}$$

where we have made use of Equations 2.4 and 2.5, and the assumption that $\delta M_g / M_g = 0$. We can eliminate the time dependency by introducing a new independent variable, $M = M_g + M_\star$ where M is the total baryonic mass in the galaxy. It follows that the only change in M is due to star formation, thus $\delta M = \delta M_\star$ and $\mathrm{d}Z/\mathrm{d}M = \delta Z/\delta M_\star$, and therefore Equation 2.23 becomes

$$M_g \frac{\mathrm{d}Z}{\mathrm{d}M} = p - Z. \tag{2.24}$$

The solution to this inhomogenous equation can be solved by first finding the general solution to the complementary equation (i.e., with $p = 0$),

$$\begin{aligned} -\int \frac{1}{Z} dZ &= \frac{1}{M_g}\int dM \\ -\ln(Z) + A &= \frac{M}{M_g} + B \\ Z &= C\exp\left(-\frac{M}{M_g}\right), \end{aligned} \tag{2.25}$$

where the constant C arises because the indefinite integrals lead to integration constants A and B. A particular solution to Equation 2.24 is $\mathrm{d}Z/\mathrm{d}M = 0$ for $Z = p$. Conceptually this makes sense, as there will be no change in the metallicity per unit mass if the population level yield has the same chemical composition as the gas already in the system. Therefore, the general solution to Equation 2.24 is

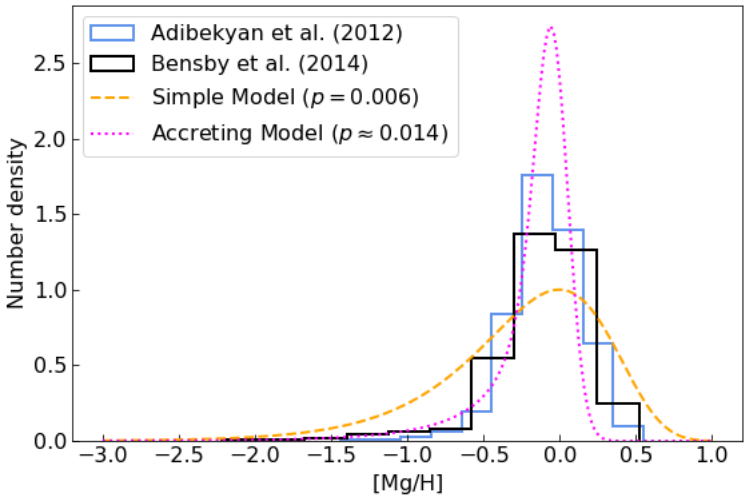

Figure 2.2: Same as Figure 2.1, but for MDF predictions using the Simple Model with $p = 0.006$ (orange dashed line) and Accreting Model with $p \approx 0.014$ (pink dotted line).

$$Z = p + C \exp\left(-\frac{M}{M_g}\right). \tag{2.26}$$

Assuming the same initial conditions as for the closed-box, we have that $M = M_g$ and $Z = 0$, thus $C = -p/\exp(-1)$ and so Equation 2.26 has the solution (Tinsley, 1980)

$$Z = p\left(1 - \exp\left(1 - \frac{M}{M_g}\right)\right). \tag{2.27}$$

Since the mass of gas in the system remains constant, eventually the mass of stars in the system will come to dominate the total mass, such that $Z \to p$ as $M/M_g \to \infty$. This means that the metallicity of the system will asymptotically approach p, and the resulting MDF will be extremely narrow, with nearly all stars having $Z = p$ (see Figure 8 in Tinsley, 1980). However, a more realistic distribution function can be approximated by taking into account the uncertainties associated with stellar abundance measurements, and assuming a fixed uncertainty value (arbitrarily chosen here as 0.1 dex) by fitting a Gaussian over the distribution (see, e.g. Bovy, 2015); a distribution of this form is shown in Figure 2.2, assuming $p \approx 0.014$ so as the peak of the distribution converges at $Z_\odot$. Compared to the MDF for the Simple Model, the 'Accreting Model' predicts far fewer low-metallicity stars, and as such provides an elegant solution to the G dwarf problem.

Despite its relative success in overcoming the failings of the Simple Model, as pointed out by Chiosi (1980), there is no physical reason why the rate of inflow should remain constant (*c.f.* Naab & Ostriker, 2006). In particular, in the dynamical model of Larson (1976), the main features of the disk could be replicated by assuming that the Galaxy's spheroidal components form on much shorter timescales than the outer regions of the disk. Therefore, Chiosi (1980) proposed an exponential law for the infall rate that is a function of both Galactocentric radius (r) and time, such that the surface density (σ), of an annulus in the Galaxy evolves according to

$$\delta\sigma(r,t) = A(r)\exp(-t/\tau), \tag{2.28}$$

where τ is the timescale of collapse for the slow gas inflow that builds the disk from inside-out. Later, in order to explain the dichotomy in [α/Fe] between thin- and thick-disk stars, Chiappini et al. (1997) introduced a second 'delayed' infall to account for the younger population of stars in the thin disk. In this two-infall regime, the rate of mass accretion in a given annulus is given by

$$\delta M_{\mathrm{g,\,in}}(t,r) = A_1(r)\exp\left(\frac{-t}{\tau_1}\right) + A_2(r)\exp\left(\frac{t_{\mathrm{max}}-t}{\tau_2(R)}\right), \tag{2.29}$$

where t_{max} is the time of maximum accretion of gas onto the disk, and τ_1 and $\tau_2(R)$ are the timescales for formation of the thick- and thin-disk[3], respectively. Since its conception, the two-infall law has been widely used in semi-analytical GCE models, with the majority adopting values of $t_{\mathrm{max}} \approx 1$ Gyr, $\tau_1 \approx 0.8$ Gyr and $\tau_2(R = R_\odot) \approx 7$ Gyr (Chiappini et al., 2001; Cescutti et al., 2007; Romano et al., 2010; Spitoni et al., 2019).

All GCE models in this thesis are based on the two-infall model, however, since the Galaxy component in `OMEGA+` is modelled as a single zone, the radial dependency of the inflow rate in Equation 2.29 is omitted. The normalisation constants A_1 and A_2 are free parameters that determine the magnitude of the first and second infall, respectively. They take different values throughout this thesis, and are used to calibrate the rate of the inflow so as to reproduce the

[3]In multi-zone GCE models, the timescale of accretion for the second infall is a function of Galactocentric radius based on the assumption that the thin-disk forms inside-out (see, e.g. Romano et al., 2000).

observed stellar and gas masses in the disk.

2.2.1.2 Outflows

The dearth of interstellar gas and presence of high-energy, outwardly flowing radio clouds from a high percentage of elliptical galaxies provided strong evidence of supernova driven galactic winds (Mathews & Baker, 1971). This mechanism of gas loss was shown to be particularly effective in lower mass galaxies with shallower potential wells, leading to them having lower average metal contents than more massive galaxies (Larson, 1974; Tremonti et al., 2004; Lilly et al., 2013). The high iron content of intracluster gas as measured by X-ray emissions indicates that the galaxies in these clusters should lose a significant fraction $\sim 10\%$ of their ISM at earlier epochs (De Young, 1978). However, not all outflows will expel gas beyond the virial radius of the galaxy, in which case, the gas can cool and sink back into the disk as inwardly propagating galactic fountains (Davé et al., 2011). Cosmological, hydrodynamical simulations show that this re-accreted material can come to dominate the infall rate for galaxies at low redshift ($z < 1$; Oppenheimer et al., 2010). At high redshift, the stellar feedback for massive galaxies is thought to be be inefficient due to high gas surface densities (since energy is more efficiently radiated away at high gas density; Matteucci, 2012), which results in fast gas consumption and rapid evolution of the metallicity (Bassini et al., 2022).

In this thesis, we assume that all outflows are due to stellar feedback, however, in reality at least some of the outflowing gas is driven by active galactic nucleus feedback (Fabian, 2012), particularly in galaxies with dark matter halos $M_{\rm vir} \gtrsim 10^{12}\ M_{\odot}$ (Mitchell et al., 2020). Given this assumption, it becomes trivial to parameterise the outflow rate as proportional to the rate of star formation, such that

$$\delta M_{\rm outflow} = \eta\ \delta M_{\star} \tag{2.30}$$

where the constant of proportionality, η, is the mass loading factor that determines the ratio of the outflow rate to the star formation rate (e.g. Murray et al., 2005; Muratov et al., 2015). Herein, the metallicity of the outflowing gas is assumed to be identical to that of the ISM,

although some simulations predict that SNe may preferentially accelerate ejected metals rather than the surrounding gas, leading to metal-enhanced outflows (Pilyugin, 1993; Marconi et al., 1994; Mac Low & Ferrara, 1999; Scannapieco et al., 2006). However, this so-called metal-loading factor has been shown to be more efficient in galaxies less massive than the Milky Way (Chisholm et al., 2018; Berg et al., 2019). For all models in this thesis, we adopt a value of $\eta \sim 0.5$ in order to regulate the evolution of the metallicity and reproduce present day values for the stellar and gas masses in the Galaxy. This value is comparable to those estimated from observations (Fox, 2017; Calabrò et al., 2022) and cosmological simulations that include AGN feedback (Davé et al., 2011; Somerville & Davé, 2015; Pandya et al., 2021). Herein, η is assumed to remain constant with Galactic time, however, Finlator & Davé (2008) and Peeples & Shankar (2011) find that the observed MZR is best reproduced in GCE models where the mass loading factor scales with the slope of the MZR for $\eta >> 1$, but is constant otherwise. From Equation 2.30, the evolution of the mass of gas in the Simple Model with only outflows is

$$\begin{aligned} \delta M_g &= -\delta M_\star - \delta M_{\text{outflow}} \\ &= -(1+\eta)\ \delta M_\star, \end{aligned} \tag{2.31}$$

and it follows from Equation 2.5 that the mass of metals in the gas now becomes

$$\begin{aligned} \delta M_Z &= (p - Z)\delta M_\star - Z\delta M_{\text{outflow}} \\ &= (p - Z - \eta Z)\ \delta M_\star, \end{aligned} \tag{2.32}$$

and upon substitution of δM_g from Equation 2.31,

$$\delta M_Z = -\frac{(p - Z - \eta Z)}{(1+\eta)}\ \delta M_g. \tag{2.33}$$

Finally, we can get an expression for the time evolution of Z by substituting Equation 2.33 into Equation 2.2, to get

$$\begin{aligned}\delta Z &= \frac{Z+\eta Z-p}{1+\eta}\,\frac{\delta M_g}{M_g} - Z\frac{\delta M_g}{M_g} \\ &= \frac{Z+\eta Z-p}{1+\eta}\,\frac{\delta M_g}{M_g} - \left(Z\frac{\delta M_g}{M_g}\times\frac{1+\eta}{1+\eta}\right) \\ &= -\frac{p}{1+\eta}\frac{\delta M_g}{M_g},\end{aligned} \tag{2.34}$$

which, after integration using the same boundary conditions as for Equation 2.8, gives

$$Z(t) = -p'\ln\left(\frac{M_g(t)}{M_g(0)},\right) \tag{2.35}$$

where $p' = p/(1+\eta)$ is the effective yield. Comparing Equation 2.35 for a Simple Model with outflows but no inflows, to Equation 2.9 which is the equivalent expression but for a closed box model, we can see that $p' < p$, always (Edmunds, 1990).

2.2.2 The stellar birthrate

The stellar birthrate function, $B(m,t)$ describes the number of stars born as function of initial mass, per unit time. In GCE models, it is often expressed as the product of the star formation rate, $\delta M_\star(t)$, and the initial mass function, $\phi(m)$, such that (Matteucci, 2012):

$$B(m,t) = \delta M_\star(t)\phi(m). \tag{2.36}$$

The star formation rate and initial mass function are described in more detail below.

2.2.2.1 Star formation rate

The star formation rate (SFR) describes the rate at which the reservoir of molecular interstellar gas in a galaxy is converted into stars. This process is understood to take place in the overdense regions of giant molecular clouds that are in a state of virial balance (McKee & Ostriker, 2007). Unfortunately, the physical processes that take place inside these gas clouds are poorly understood because they cannot be observed in galaxies outside our own (Kennicutt & Evans, 2012). For this reason, the SFR is typically parameterized in GCE models as a gas-density power law of the form originally proposed by Schmidt (1959),

$$\delta M_\star(t) = \tau_\star \Sigma_g^N, \tag{2.37}$$

where Σ_g is the surface gas density, and the SFR has units $M_\odot$ yr^{-1} kpc^{-2}. For star-forming galaxies, there is a strong correlation between the disk-averaged SFR, $\Sigma_{\rm SFR}$, and the total (i.e., atomic + molecular) gas density for exponent $N = 1.4$ (Kennicutt, 1998, see Figure 2.3) – this is known as the Schmidt-Kennicutt law. We remind that the constant of proportionality in Equation 2.37, $\tau_\star$ with units of [yr^{-1}], is the star formation timescale (or equivalently the gas consumption timescale) which, when averaged over a given region, is given by Equation 2.15. Therefore, an equivalent expression for the SFR in terms of $\tau_\star$ is

$$\delta M_\star(t) \equiv \epsilon_\star \frac{M_g(t)}{\tau_\star}, \tag{2.38}$$

which is the widely used form of the SFR used in many semi-analytical models (Somerville & Davé, 2015). The constant, $\epsilon_\star$, is the dimensionless star-formation efficiency, and its value is determined by `OMEGA+` based on a recurrence formula to derive a suitable gas-to-stellar mass ratio at the end of the simulation (Côté et al., 2016). Its value is somewhat trivial however, as cosmological simulations suggest that irrespective of the gas consumption timescale the SFR in galaxies is self-regulating, and is sensitive to the gas accretion rate (Schaye et al., 2010).

2.2.2.2 Initial mass function

The initial mass function (IMF) describes the number density of stars born in a given stellar population as a function of their mass. The IMF, $\phi(m)$, is typically determined by obtaining a *present-day mass function* for a given stellar population (usually clusters or field stars) by applying the theoretical mass-luminosity relation for main sequence stars to the observed luminosity function. The IMF is then derived based on the lifetimes of the respective stars (see derivations in Prantzos, 2008). Since more than 50% of stars are in binary and higher-order system, it is important to consider corrections to the luminosity function due to unresolved binaries. Furthermore, as pointed out by Kroupa et al. (2013), there are inherent biases in the distribution of masses in a given population which mean that it is not possible to observe the complete spectrum of stellar masses in a coeval group. If the cluster is young, low-mass stars may have not yet evolved onto the main sequence, whereas in older clusters there may be a dearth of higher mass stars due to them being preferentially ejected from the cluster core

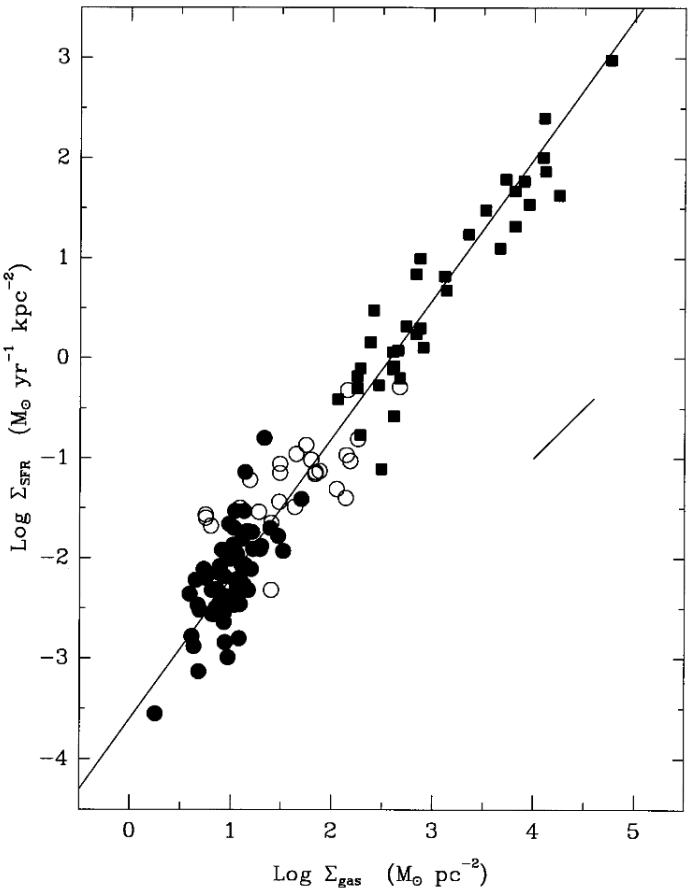

Figure 2.3: SFR as a function of gas density in star-forming disk galaxies (circles) and starburst galaxies (squares). The best-fitting line to the data has index $N = 1.40$, and the short line to its right indicates the slope if the scaling radius were changed by a factor of 2. Figure from Kennicutt (1998).

(Banerjee & Kroupa, 2012; Oh & Kroupa, 2016). Finally, it is common practice to normalise the function to unity, such that the total mass in stars is given by

$$\int_{m_{\rm low}}^{m_{\rm up}} m\phi(m)dm = 1, \tag{2.39}$$

where $m_{\rm up}$ and $m_{\rm low}$ are the upper and lower mass limits over which the IMF is considered.

The seminal work in this field was conducted by Salpeter (1955), who was the first to measure the IMF of the solar neighbourhood based on the observed luminosity function. He concluded that the mass distribution was consistent with a power-law of the form

$$\phi_{\rm Salpeter}(m) \propto m^{-\alpha}, \tag{2.40}$$

with power-law index $\alpha = +2.5$[4]. Due to the uncertainties associated with measuring the luminosity of more massive stars at the time, Salpeter was unsure of the form of the IMF outside the mass range $-0.4 < \log(m/M_\odot) < 1$. In the years following, it became evident via derivations of the luminosity function from field stars, that there was a clear flattening of the trend at absolute magnitudes of $M_v \approx 15$ (Luyten, 1968; Wielen, 1974), corresponding to a lower mass limit for the power-law at $M \approx 0.5M_\odot$ (see, e.g. Reid et al., 1999, 2002) with $\alpha \approx 1 - 1.3$. Motivated by this discovery, Miller & Scalo (1979) conceptualised a lognormal distribution of the form $\mathrm{d}\log\xi(\log M)/\mathrm{d}\log M = -(1 + \log M)$, which has a steepening slope with increasing M. On the other hand, Salpeter (1955) cautiously underestimated the upper mass limit to which a power-law IMF can seemingly be applied, with subsequent measurements adopting an IMF of this form even in excess of $100M_\odot$ (Scalo, 1986; Kroupa et al., 1993; Chabrier, 2003). Among these, we bring particular attention to the IMF of the form derived by Kroupa et al. (1993), the revised version[5] of which (Kroupa, 2001) is adopted in the remainder of this thesis. The IMF takes the form of a broken (or multi-part) power-law

[4]Herein, we adopt the nomenclature of e.g. Audouze & Tinsley (1976) and Tinsley (1977) – that is, the negative sign is part of the equation and so the the index parameter is positive. For further discussion of IMF conventions and language usage, we refer the reader to Hopkins (2018)

[5]The slope of the power-law in Kroupa et al. (1993) is shallower at higher masses and comprises three rather than four components as in Kroupa (2001), where the last includes a separate power-law index for substellar masses ($M < 0.08M_\odot$).

distribution, where the power-law index is mass-dependent and given by:

$$\begin{aligned} \alpha_0 &= +0.3 \pm 0.7, & 0.01 \leq M/M_\odot < 0.08, \\ \alpha_1 &= +1.3 \pm 0.5, & 0.08 \leq M/M_\odot < 0.50, \\ \alpha_2 &= +2.3 \pm 0.3, & 0.50 \leq M/M_\odot < 1.00, \\ \alpha_3 &= +2.3 \pm 0.7, & 1.00 \leq M/M_\odot. \end{aligned} \tag{2.41}$$

For the GCE models of Mollá et al. (2015), the Kroupa IMF[6] provides the best-fit to the observational data of the Milky Way's disk. In a similar vein, Romano et al. (2005) conclude that multi-slope IMFs are necessary in order to reproduce the key properties of the solar vicinity, and Muñoz-Mateos et al. (2011) find excellent agreement between their spectro-photometric models with Kroupa type IMF and multi-wavelength observations of spiral galaxies. Another frequently used multi-slope IMF in GCE models is that of Chabrier (2003), which takes a lognormal form below $1M_\odot$ with a peak mass at $\approx 0.2M_\odot$, and a Salpeter power-law form otherwise. A comparison of the multi-slope IMFs normalized to the Salpeter IMF is shown in Figure 2.4. As can be seen, the IMFs of Kroupa (2001) and Chabrier (2005) predict more short-lived massive stars per stellar population than Salpeter (1955), and thus a faster evolution of the global metallicity when used in GCE models. The choice of IMF and the upper mass cutoff ($M_{\rm up}$) are a major source of uncertainty in GCE models that assume the instantaneous recycling approximation, with Vincenzo et al. (2016a) finding variations in the population-level oxygen yield of more than a factor of 10 between Chabrier (2005) and Kroupa et al. (1993) IMFs for different values of the upper mass cutoff.

The universality of the high mass end of the IMF has been well demonstrated through its continued successful application to local stellar clusters (Bastian et al., 2010; Offner et al., 2014), although questions remain regarding its exact nature at lower masses, particular in the substellar domain (Thies & Kroupa, 2007; Jeffries, 2012; Kroupa et al., 2013). The determination of this last may seem unimportant for GCE studies, given that low-mass stars have lifetimes longer than the age of the Universe, however, the shape of the IMF at lower masses influences the fraction of massive stars born in a given stellar population, and thus indirectly influences the population-level yield.

[6]When corrected for unresolved binaries, such that $\alpha_3 = 2.7$ (Kroupa, 2002).

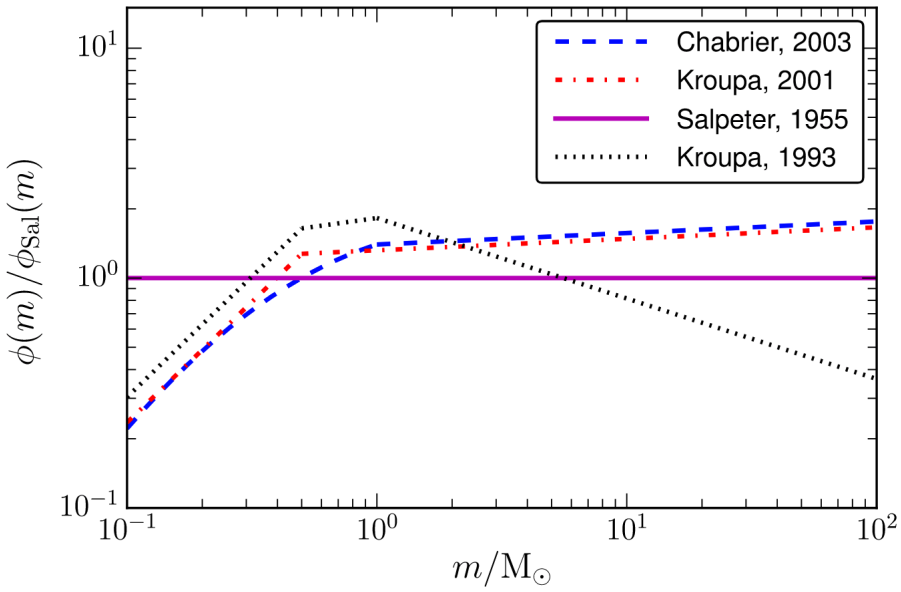

Figure 2.4: Comparison of selected multi-slope IMFs to the mass invariant power-law IMF of Salpeter (1955). Figure from Vincenzo et al. (2016a).

There is also the question as to whether or not the IMF is invariant (see, e.g. Kroupa et al., 2013), such that it can be represented by a so-called *canonical* IMF (Kroupa, 2001). Recent evidence suggests this is not the case. In particular, it appears as though the IMF becomes "top-heavy" (i.e., relatively more high mass stars are born per stellar population) in regions with high star formation rates (Schneider et al., 2018; Zhang et al., 2018; Pouteau et al., 2022), and "bottom-light" in high density clusters at low metallicities (Marks et al., 2012; Jeřábková et al., 2018). Furthermore, the IMF appears also to be metallicity dependent, with the thermodynamic behaviour of low-metallicity gas favouring a top-heavy IMF (Sharda & Krumholz, 2022); this means that the Population III IMF was dominated by very massive, short-lived stars (Bromm & Larson, 2004; Susa et al., 2014).

2.3 Stellar yields

Following the Big Bang, the Universe's baryonic matter consisted almost entirely of H ($\sim$ 75% by mass) and He ($\sim$ 25%), with trace amounts of Li. It is therefore crucial that GCE models accurately simulate the enrichment of the gas by stellar ejecta, in order to reproduce the distribution of metals we see in the Galaxy today. The most important ingredient for GCE in

this regard are the yields calculated from stellar nucleosynthesis models, ideally spanning a large range of initial masses and metallicities. The mass of a star at zero age main sequence (ZAMS) ultimately determines its evolution through the Hertzsprung-Russel diagram and hence the nucleosynthesis processes it will undergo, although the binarity of a star can also have a profound impact on its late stage evolution.

So far, we have considered only a simplified model, whereby the mass of elements ejected by a stellar population is described by a time-invariant population-level yield, p. In practice, this means that the ratio between the abundances of any two metals remains constant over the lifetime of the Galaxy. However, in reality we know this is not the case. In order to accurately predict the abundance ratios in the Galaxy, it is necessary to consider separately the mass- and metallicity-dependent yields for different enrichment events, that eject over different timescales. Assuming then a time-delay model for stellar enrichment, the yield of element i ejected per enrichment event for a star of mass m and lifetime τ_m, is given by (Prantzos, 1998):

$$p_i(m) = p_i^0(m) + p_i(m), \tag{2.42}$$

where $p_i^0(m) = X_i^0 \cdot (m - m_{\rm rem})$ is recycled material that was already present in the star at birth; the initial mass fraction of element i in the gas is X_i^0, and the remnant mass following the enrichment event is $m_{\rm rem}$. The term $p_i(m)$ is the *net yield*, and is the mass of newly synthesised element i ejected by the star, given by (Matteucci, 2012)

$$p_i(m) = \int_0^{\tau_m} \dot{M}_{\rm lost} \cdot \left[X_i - X_i^0\right] \, dt, \tag{2.43}$$

where $\dot{M}_{\rm lost}$ is the mass loss rate of the star, and the integral is taken over its lifetime.

In general, all GCE models include the yields for low- and intermediate-mass stars (LIMS), massive stars, and Type Ia supernovae. For some elements, such as those produced predominantly by the r-process, additional enrichment events with unique delay-time distributions must also be considered. However, the yields calculated by different stellar evolution groups are not always consistent, to the extent that the uncertainties associated with stellar nucleosynthesis dominate the total GCE uncertainty for some elements (Côté et al., 2017). It is therefore

essential that GCE predictions are calculated using yield sets from different stellar evolution codes, so that the conclusions drawn are robust for different choices of the input physics (see, e.g. Romano et al., 2010; Mollá et al., 2015; Prantzos et al., 2018; Kobayashi et al., 2020b).

In this Section, we give an overview of the different types of stellar enrichment events that are included in GCE models. The yield sets used in this thesis are compared in Figures A.1, A.2, A.3, A.4 in Appendix A.

2.3.1 Low- and intermediate-mass stars (LIMS)

$0.8 \leq M_\star/M_\odot \lesssim 8$: Owing to the range of ZAMS masses they cover, these stars form the bulk of the stellar population in the Galaxy (excluding those stars with lifetimes in excess of the Hubble time). Those on the lower mass end ($M_\star \lesssim 2M_\odot$) have lifetimes spanning several Gyrs, compared to just several Myrs for stars with $M_\star \sim 8M_\odot$ that are close to the *transition mass* (Karakas & Lattanzio, 2014). The transition mass tentatively delimitates between intermediate-mass stars and massive stars, where in the last all the burning stages are assumed to begin centrally. However, several modeling uncertainties affect the evolution of stars in the transition mass range (Jones et al., 2013), and inevitably different groups reach different conclusions depending on the choice of input physics. For this reason, the transition mass is a free parameter in GCE models, and its value throughout this thesis is fixed at $M_{\rm trans} = 8M_\odot$.

From a GCE perspective, the most important stages of stellar evolution for LIMS are the ascent of the giant branches following the cessation of core H-burning. In particular, during the late stages of evolution along the asymptotic giant branch (AGB), successive thermal pulses create convective instabilities which dredge-up C, He-burning ashes, and *s*-isotopes from the core to the surface of the star. These are then expelled from the star into the ISM via stellar winds. In this thesis, we make use of the mass- and metallicity dependent yields for LIMS from the FRUITY database[7] (Cristallo et al., 2008, 2009, 2011, 2015a, hereafter C15) and the Monash group (Karakas et al., 2012; Fishlock et al., 2014; Karakas & Lugaro, 2016; Karakas et al., 2018, hereafter K18). In addition, the yields from the NuGrid

[7] fruity.oa-abruzzo.inaf.it

collaboration[8] (Pignatari et al., 2016; Ritter et al., 2018b; Battino et al., 2019, 2021) and S-process NUcleosynthesis Post-Processing code for ATon (`SNUPPAT`; Yagüe López et al., 2021a) are also considered, however, due to the more limited range of metallicities (compared to C15) and masses (compared to K18) computed for these yield sets, we do not include them in our analysis.

2.3.2 Massive stars

$M_\star \gtrsim 10 M_\odot$: Less numerous than their LIMS counterparts, these stars are nevertheless responsible for the majority of α-elements, several Fe-group elements, as well as a significant contribution of the light s-isotopes ($A < 90$) in the Galaxy. Since massive stars evolve quickly, they played an instrumental role in the early development of the Galaxy, both chemically and kinematically, predominantly due to the release of large amounts of both material and energy during their eventual explosion. Unlike LIMS stars, massive stars undergo all the hydrostatic burning processes described in Section 1.1.2, as well as explosive He, C, Ne, O, and Si burning following the gravitationally induced CC-SNe. For those elements produced during the presupernova evolution, the yields are sensitive to parameters such as the mass loss rates, mixing treatment, and convection, whereas, for the elements beyond iron the yields depend on the mechanism for initiating the explosion and the position of the mass cut (Romano, 2022).

Herein, we make use of massive star yields from the NuGrid database (see references in previous Section), the Japanese team headed by Ken'ichi Nomoto (Nomoto et al., 2006; Kobayashi et al., 2006; Kobayashi & Nakasato, 2011; Nomoto et al., 2013, hereafter N13), and from Limongi & Chieffi 2018 (hereafter LC18). The yield tables take into account mass loss by stellar winds during the presupernova evolution, and the composition of the ejecta following explosive nucleosynthesis. The stellar grid for NuGrid massive star models includes yields for $M/M_\odot = 12, 15, 20, 25$ at $Z = 1 \times 10^{-4}, 0.001, 0.006, 0.01, 0.02$ where the initial composition is scaled to solar, assuming $Z_\odot = 0.02$ from Grevesse & Noels (1993) and an isotopic distribution given by Lodders (2003). For N13, yields are taken from stars with $M/M_\odot = 13, 15, 18, 20, 25, 30, 40$ at $Z = 0.001, 0.004, 0.008, 0.02, 0.05$, where the $Z = 0.008$ yields are interpolated using the $Z = 0.004$ and $Z = 0.02$ models

[8] https://nugrid.github.io/

- the abundance pattern is not scaled to solar. The yields for hypernovae (with deposited energy $E = 10^{52}$ erg) are also included for stars with $M/M_{\odot} \geq 20$, which are assumed to occur in 50% of stars above this threshold mass. Finally, the massive star models of LC18 are calculated for $M/M_{\odot} = 13, 15, 20, 25, 30, 40, 60, 80, 120$ at $Z = 3.24 \times 10^{-5}, 3.24 \times 10^{-4}, 0.0032, 0.0135$ which correspond to [Fe/H] $= -3, -2, -1, 0$, respectively, assuming an initial solar composition given by Asplund et al. (2009). For LC18, the yields from the presupernova evolution are calculated including the effects of rotation. However, since the LC18 yields are not calculated for [Fe/H] > 0, a level of inaccuracy is introduced in the GCE calculations when the ISM reaches super-solar metallicities, due to the necessary extrapolation of the solar-metallicity stellar grid in this regime.

2.3.3 Type Ia SNe

The majority of stars are born in binary and higher order systems. Binary systems in which a WD (primary) grows in mass via accretion of material from its stellar companion (secondary) can lead to thermonuclear runaway under electron-degenerate conditions; this is the canonical origin scenario for SNe Ia (Hoyle & Fowler, 1960). They contribute significantly towards the Fe-peak elements in the disk, and also to a lesser extent produce some of the α-elements like Si, Ca, and Ti. Despite these clues, the identity of the secondary star and mass of the primary at the time of explosion are still unclear – this is the so-called “progenitor problem" (Maoz & Mannucci, 2012). Since central density affects the electron fraction in the WD core (see discussion of electron fraction in Section 1.1.2.2), it is possible to discriminate between different masses of the primary based on the chemical signature of SNe Ia ejecta. In particular, both the [Mn/Fe] and [Ni/Fe] ratios can only be made in supersolar quantities if the WD progenitor is near to $M_{\rm Ch}$ (Seitenzahl et al., 2013b; Blondin et al., 2022). By comparing GCE predictions to spectroscopic abundance measurements, these ratios can help to constrain the relative fraction of SNe Ia in the Galaxy from either a sub-$M_{\rm Ch}$ or near-$M_{\rm Ch}$ progenitor (see Chapter 4 and references therein). In addition to the mass of the primary, the speed of propagation of the flame front through the fuel, position of the initial C-ignition, and accretion of an He-rich layer onto the progenitor’s surface can all affect the SN Ia yield (see, e.g. Hillebrandt et al., 2013). Therefore, nucleosynthesis calculations covering a large number

of SNe Ia explosion mechanisms have been explored in the literature and are available for use in GCE models (e.g., Iwamoto et al., 1999; Fink et al., 2010; Kromer et al., 2017; Leung & Nomoto, 2018, 2020; Lach et al., 2020; Gronow et al., 2021a; Keegans, 2022). In Chapter 3 of this thesis the SNe Ia yields of Thielemann et al. (1986) are adopted (this Chapter concerns the GCE of several radioactive *s*-isotopes which are not produced by SNe Ia), whereas yields from a variety of metallicity-dependent sub- and near-$M_{\rm Ch}$ explosion mechanisms are included in the GCE investigation of the Fe-peak elements in Chapter 4.

In regards to the identity of the secondary star, two main channels have been proposed: (i) the single-degenerate scenario (Whelan & Iben, 1973), where the companion is a non-degenerate star such as a main sequence or He-burning star; and (ii) the double-degenerate scenario (Iben & Tutukov, 1984), where the companion is another WD. Whilst it is not possible to retroactively identify the degeneracy of the secondary based on the chemical signature of the explosion, there is a chance that, in the case of a non-degenerate companion, the pre-explosion system can be directly observed if the donor is sufficiently bright (McCully et al., 2014). Alternatively, if the secondary is itself a degenerate star, space-based gravitational wave detectors could be able to observe WD-WD mergers directly (see, e.g. discussion in Kinugawa et al., 2022). From a GCE perspective, the identity of the secondary can have profound implications on the delay time of the progenitor system, and thus determines the time at which SNe Ia begin contributing to the chemical enrichment of the Galaxy (Matteucci et al., 2009; Côté et al., 2016).

2.3.3.1 The SNe Ia rate

For CC-SNe, the length of time between the birth of the progenitor star and the eventual explosion, the so-called *delay-time*, is a strict function of stellar mass. This means that the delay-time distribution (DTD) of CC-SNe following a burst of star formation is fairly simple to calculate from the IMF. However, deriving a DTD for SNe Ia is more complicated because of the many different binary star configurations from which they could potentially arise. One such potential progenitor system is the violent of merger of two sub-$M_{\rm Ch}$ CO WDs following angular momentum loss due to gravitational wave radiation (see, e.g. Pakmor et al., 2012),

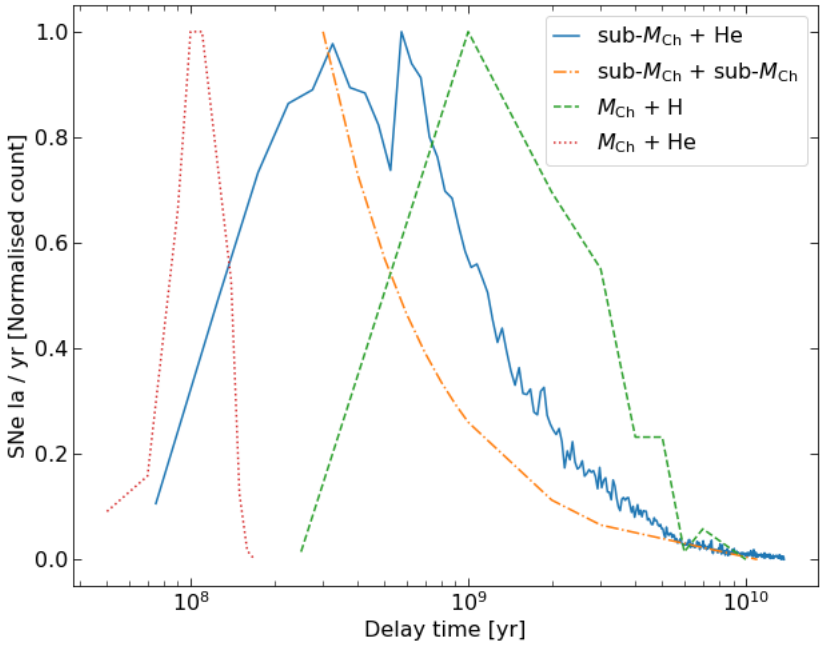

Figure 2.5: Delay time distributions (DTDs) for four different SNe Ia binary star configurations: (i) solid blue line – sub-M_{Ch} WD accreting He-rich material from either a He-burning star (first peak in DTD) or WD with He-shell (second peak), as calculated by Ruiter et al. (2014) and Gronow et al. (2021b), respectively; (ii) dotted-dashed orange line – violent merger of two sub-M_{Ch} due to gravitational wave radiation (power law DTD with exponent ≈ -1 as in, e.g., Maoz & Mannucci, 2012); (iii) dashed green line – M_{Ch} WD accreting H-rich material from non-degenerate companion, as calculated by Ruiter et al. (2009); (iv) dotted red line – M_{Ch} WD accreting He-rich material from He-burning star, as calculated by Liu et al. (2015).

which is expected to follow a power law DTD function of the form $\phi(t) \propto t^{-1}$ (see explanation in Ruiter et al., 2009). A power law DTD with exponent ≈ -1 has also been found to have the best fit to the observed SNe Ia rate in Nature (Totani et al., 2008; Maoz et al., 2012). However, there is strong evidence to suggest that the cosmic SNe Ia rate is not 'universal', but instead depends on the physical properties of the host galaxy (e.g., stellar mass, SFR, morphology; Mannucci et al., 2005; Scannapieco & Bildsten, 2005). In particular, it has been suggested that the SNe Ia DTD is comprised of two components: the t^{-1} power law describes a dominant population of 'prompt' progenitors in younger star-forming galaxies, whereas the lower SNe Ia rate in older quiescent galaxies is the result of a 'tardy' progenitor population (Li et al., 2011; Childress et al., 2014).

The SNe Ia DTDs for four different binary star configurations are shown in Figure 2.5, including the t^{-1} power law DTD from violent mergers of CO WD (sub-$M_{\rm Ch}$ + sub-$M_{\rm Ch}$). The DTDs for the other progenitor scenarios are extracted from binary population synthesis (BPS) codes that simulate the dynamical interactions between stars in a SSP (Han et al., 2020). Whilst BPS studies are a useful tool for constraining potential SNe Ia progenitor channels, they must make concessions when in comes to simulating many physical processes in order to remain computationally feasible. These simplifying assumptions can lead to substantial differences in the predicted SNe Ia rate when comparing results from various BPS codes (Toonen et al., 2014). Due to the large variations in DTDs in the literature, in this thesis the following simplifying assumption is made: all SNe Ia follow a power law DTD function, $\phi(t)$, such that the number of SNe Ia per unit of stellar mass formed in timestep δt is given by (Wiersma et al., 2009):

$$N_{\rm Ia} = A_{\rm Ia} \int_{t}^{t+\delta t} f_{\rm WD}(t)\phi(t)dt, \tag{2.44}$$

where $A_{\rm Ia}$ is a normalisation parameter, and the integrand is given by the product of the DTD and the fraction of progenitor stars that have become WDs by time t, $f_{\rm WD}(t)$. This last is a function of the lifetimes of stars in the mass range $3-8\ M_{\odot}$ and the IMF. The normalisation constant, $A_{\rm Ia}$, determines the total number of SNe Ia that explode per SSP across the Hubble time, and its value must be inferred based on only a limited number of observations or through BPS modeling. At present, observations predict SNe Ia to explode at a rate roughly an order of magnitude higher than BPS models (Maoz et al., 2014). Furthermore, it has recently been suggested that binary systems may preferentially form in lower-metallicity stars (Moe et al., 2019), which implicates the need for a metallicity-dependency for $A_{\rm Ia}$ (Gandhi et al., 2022). In this thesis, the value of $A_{\rm Ia}$ is tentatively chosen so that $\sim 10^{-3}$ SNe Ia explode per $M_{\odot}$, which is to the same order of magnitude as rates derived from observations (for comparison, a compilation of observed SNe Ia rates are given in Table 5 of Côté et al., 2016).

2.3.4 Additional stellar enrichment sources

GCE models that include the three stellar sources above are able to predict the bulk of the observed trends for the temporal evolution of the most common elements in the ISM. However, for some species additional stellar enrichment sources must be considered. A non-exhaustive list of additional sites include:

- *Classical Novae*: Analogous to SNe Ia, classical novae occur in binary systems due to mass transfer of material from a main sequence or red giant star onto the surface of a CO or ONe WD (see, e.g. Denissenkov et al., 2014, and references therein). The accreted material forms a shell around the WD, until it becomes massive enough to trigger thermonuclear runaway at the WD-shell interface. The material that is ejected in each outburst is rich in light radionuclides, such as ^{7}Be, ^{22}Na, and ^{26}Al (José & Hernanz, 1998; José et al., 2004; Vasini et al., 2022). In particular, classical novae have been considered a potential solution to the systematic underproduction of Li in GCE models – the so-called, *cosmic lithium problem* (D'Antona & Matteucci, 1991). However, there exists large discrepancies between the ^{7}Li yields derived via stellar nucleosynthesis models and observations, with the observationally derived yields providing a better fit to the protosolar Li abundance (Grisoni et al., 2019; Molaro et al., 2020; Kemp et al., 2022).

- *Super-AGB stars* ($7 \lesssim M_{\star}/M_{\odot} \lesssim 10$): Due to the computational demands that are required to fully evolve stars through the super-AGB evolutionary phase, only relatively recently have super-AGB yield sets been calculated using an adequate nuclear network for a range of initial metallicities (see, e.g. Doherty et al., 2017). In the years proceeding, it was therefore necessary that GCE models circumvent this missing mass range, either by extrapolation of LIMS yields to higher masses, interpolating the yields of LIMS and massive stars, or excluding these masses entirely from the initial mass function. Nevertheless, it seems as though for most isotopes the contribution from super-AGB stars toward the Galactic inventory is small (Kobayashi et al., 2020b).

- *Electron-capture supernovae* ($M_\star \gtrsim 25 M_\odot$): For stars close to the threshold mass between intermediate and massive stars, Ne is ignited off centre and the core of the star can suffer an electron-capture-induced collapse leading to either a neutron star or WD remnant (Nomoto & Leung, 2017). Such events have been proposed as potential sites for the r-process (Kobayashi et al., 2020b) and the intermediate (i)-neutron capture process (Jones et al., 2016), and they could help explain the GCE of several neutron-rich isotopes (Jones et al., 2019b) and Zn (Hirai et al., 2018).

- *Wolf-Rayet stars* ($10 \lesssim M_\star/M_\odot \lesssim 30$): Massive stars lose mass via stellar winds. Typically, the mass-loss rate is assumed to be a function of the star's luminosity, temperature and metallicity, with more bright and metal-rich stars experiencing more severe mass-loss. Wolf-Rayet stars are thought to be massive stars that have have lost their H-rich envelopes via mass-loss or mass transfer with a close binary companion, and they experience stellar winds that are an order of magnitude denser than other massive stars (Crowther, 2007; Brinkman et al., 2019). Historically, they have been considered important contributors to the Galactic budget of ^{19}F (Meynet & Arnould, 2000; Spitoni et al., 2018), however, this was recently challenged by Womack et al. (2023).

- *Faint supernovae* ($15 \lesssim M_\star/M_\odot \lesssim$?): Beyond some minimum mass (cautiously stated here as $15 M_\odot$ based on the massive star models of Ritter et al. 2018a), a fraction of SNe will have insufficient energy to completely overcome the gravitational well of the compact core and will collapse back in on themselves as a black hole. In this case, only the outer layers of the star will be ejected and the resultant SNe will be observationally faint as large amounts of ^{56}Ni will fall back onto the core (Heger et al., 2003). Since the inner regions of the star are not ejected (i.e., the yields are Fe-poor), and black hole-neutron star mergers are a potential site of the r-process, stars that die as failed SNe could be important for enhancing [r/Fe] in the Galaxy (Wehmeyer et al., 2019). Furthermore, faint SNe could lead to enhancements of [Mg/Si] and intermediate-mass elements relative to Fe-group elements, which could have important implications for the formation of rocky planets (Pignatari et al. 2023; submitted).

- *Neutron star mergers*: The electromagnetic emission produced by the radioactive decay of r-process ejecta in the wake of the GW170817 neutron star merger (NSM) event supported the long-held belief that these astrophysical sites could be major producers of the r-process elements in the Galaxy (Rosswog et al., 2018). The DTD for NSMs is expected to be somewhat analogous to that of the violent merger progenitor system for SNe Ia, where we remind that due to loss of angular momentum the DTD has a power law shape proportional to t^{-1}. However, since neutron stars are the remnants of CC-SNe that are the endpoints of massive stars, the peak of the DTD is shifted to earlier times than for SNe Ia (see, e.g., Dominik et al., 2012).

2.4 Evolution of abundance ratios in the disk

Since different stars eject different amounts of elements over different timescales, the elemental abundance ratios in the ISM provide a cosmological fingerprint of the environment's enrichment history. Studying these abundance patterns can enable us to constrain models of stellar and chemical evolution theories. For this reason, a concerted effort has been made in recent years to accurately measure the chemical and kinematic properties of the Galaxy's stellar populations using Galaxy-wide surveys (see discussion in Section 1.2).

In this Section, we show the predicted evolution of [X/Fe] versus [Fe/H][9] calculated using `OMEGA+` for the three different stellar grids of LIMS + massive star yields that are used in this thesis: i) C15 + N13, ii) C15 + LC18, & iii) K18 + NuGrid. The GCE predictions are compared to abundance ratios derived from stellar spectroscopy, and the best-fitting models are identified qualitatively for elements produced by the different nucleosynthesis processes described in Section 1.1.2. For SNe Ia, we assume a 50% contribution from each of the sub- and near-$M_{\rm Ch}$ WD progenitor channels; the yields are from Keegans (2022) and are based on post-processing of the Shen et al. (2018) and Townsley et al. (2016) models for each channel, respectively. For all GCE models in this Section, we include also the r-process yields for NSMs from Rosswog et al. (2014) assuming a DTD function as in Dominik et al. (2012). The [X/Fe] for the reference yields are show in Figures A.1, A.2, A.3 & A.4. For each of the

[9]Historically, iron has been favoured as a tracer element for the star formation history because it is one of the more abundant metals in the ISM and its transitions are in the visible range of the electromagnetic spectrum.

three yield sets, the OMEGA+ GCE model is calibrated to reproduce present day observables for the Galactic disk (see Figure A.5). The parameterization of the model is as described in the previous Sections of this Chapter, where we remind that a Kroupa type IMF is assumed and pristine material flows into the Galaxy according to the two-infall model. The first infall that is responsible for building the thick disk is characterised by a rapid accretion of gas prior to $\tau_1 = 0.8$ Gyr, as shown in the top right panel of Figure A.5. Thereafter, the thin disk is built over a longer timescale with a steadily decreasing inflow rate after $t_{\rm max} = 1$ Gyr. The star formation ($\dot{M}_\star$) peaks when the mass of available gas reaches a maximum, according to Equation 2.38. Herein, we do not consider a density threshold below which star formation ceases and therefore there is no 'gap' in the star formation history (for comparison, see Figure 3 in Chiappini et al. 2001 where a threshold is included).

Figure 2.6 (Figure 2.7) shows the evolution of [X/Fe] versus [Fe/H] for elements from C to Zn (Sr to Pb) for each of the three GCE models. The spectroscopic abundance data for the Milky Way's halo and thick and thin disks are a subset of the available abundance data from the STELLAB (STELLar ABundances) module[10]; the references are given in the Figure caption. Most of the data show large scatter at low-metallicities, particularly for those elements heavier than Zn, which could be due to how the abundance ratios are derived – either because of neglected NLTE effects which are most dominant at low-metallicities, or systematic differences in the data analysis techniques. Alternatively, the stellar compositions could reflect the stochastic nature of enrichment from single "bursts" of primordial supernovae activity, which would lead to an inhomogeneous dispersion of some heavy elements in the early Galaxy (Cayrel et al., 2004; Cescutti & Chiappini, 2013). For each GCE model, Figure 2.8 shows the predicted solar elemental distribution normalized to the solar abundances of Asplund et al. (2009); the contribution from each of the stellar sources toward each element is shown separately.

2.4.1 The CNO elements

Carbon, nitrogen, and oxygen (hereafter collectively referred to as CNO) have received much attention in the literature because they are the three most abundant metals in the Universe,

[10]See https://github.com/NuGrid/NuPyCEE for more information

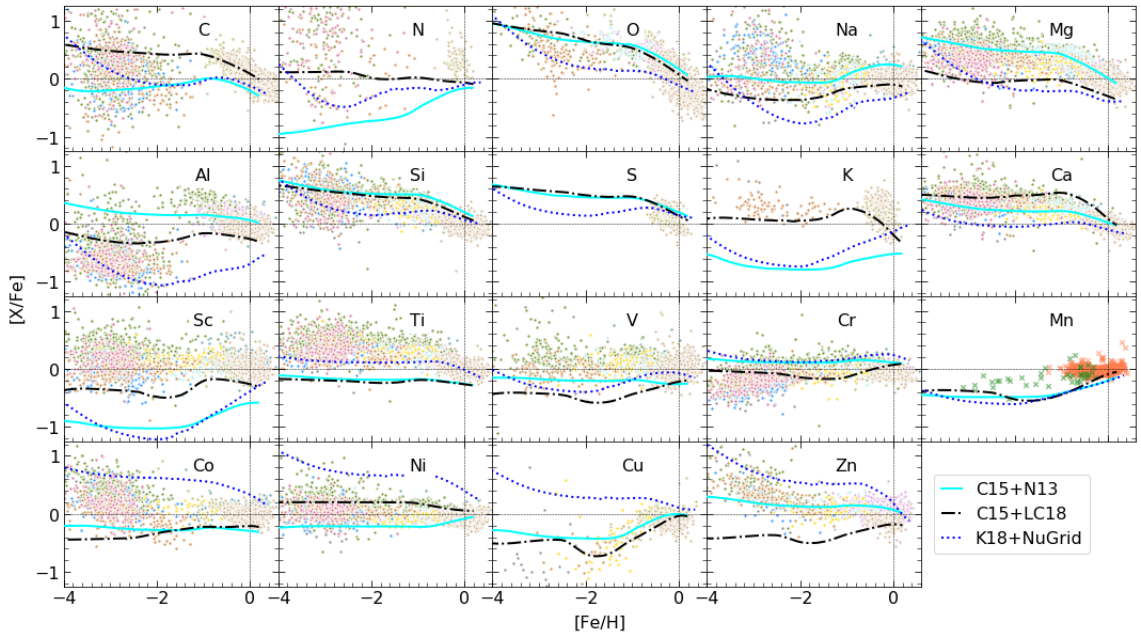

Figure 2.6: Evolution of [X/Fe] versus [Fe/H] for elements from C to Zn for the three GCE predictions. Observational data are: blue-grey (Adibekyan et al., 2012), khaki (Reddy et al., 2003, 2006), pink (Bensby et al., 2014), grey (Cohen et al., 2013, with CEMP stars removed), olive (Frebel et al., 2010), pale turquoise (Gratton et al., 2003), tan (Hinkel et al., 2014), gold (Ishigaki et al., 2012, 2013), blue (Jacobson et al., 2015), light brown (Roederer et al., 2014), red-violet (Yong et al., 2013), green crosses (NLTE data from Eitner et al., 2020), red crosses (NLTE data from Bensby et al., 2014; Battistini & Bensby, 2015). The intersecting dashed horizontal and vertical lines indicate the solar abundances measured by Asplund et al. (2009).

and because they appear to be a necessary component in the building blocks of life (Romano et al., 2020; Romano, 2022).

Carbon: The GCE predictions in Figure 2.6 have variations of $\sim$ 0.8 dex at very low metallicities, but converge to within $\approx$ 0.2 dex by [Fe/H]. A similar level of variation is seen in the low-metallicity regime for the GCE models with different yields in Romano et al. (2010). At [Fe/H] $\lesssim -1$, the [C/Fe] ratio for the two GCE models with C15 LIMS yields remain relatively flat, whereas for K18+NuGrid there is a sharp decrease in [C/Fe] from $\sim$ 1 to the solar value. At [Fe/H] ≈ -1.5 (equivalently, $\sim$ 0.1 Gyr), there is a shallow rise in [C/Fe] to the solar value for C15+N13 and K18+NuGrid due to the contribution from AGB stars with $M \lesssim 4M_{\odot}$ after this time (Kobayashi et al., 2020b). After [Fe/H] = -1, all GCE tracks decrease due to the Fe enrichment from SNe Ia. Both the C15+N13 and K18+NuGrid models with non-rotating massive star yields underproduce [C/Fe] relative to solar, however, the C15+LC18 model slightly overproduces. From examining Figure 2.8, we can see that the LC18 massive star yields contribute significantly more C than the non-rotating yields by the time the Sun is born. Interestingly, using the exact same LIMS + massive star yield combination, Prantzos et al. (2018) underproduce [C/Fe] relative to solar. This difference is most likely because they assume just one exponential infall episode to build the disk, and a Salpeter IMF with a steeper slope (α = +2.35) than that for massive stars in the Kroupa IMF. A good match with local (i.e., $d \leq 60$ pc) stars from Delgado Mena et al. (2021) is found for the GCE model of Romano et al. (2020) using the revised two-infall model of Spitoni et al. (2019) and the LC18 massive star yields but with LIMS yields from Ventura et al. (2013). Therefore, it appears that yields from rotating massive stars and a two-infall model are requirements for reproducing the solar abundance of C. The LIMS yields of K18 also lead to approximately 1.5 times as much C as the C15 yields, contributing $\sim$ 40% of the total solar abundance.

Nitrogen: Due to internal mixing and structural changes, low-metallicity massive star models that include rotation are prolific primary producers of ^{14}N (Meynet & Arnould, 2000; Chiappini et al., 2006; Hirschi, 2007; Maeder et al., 2009, and see the 15 & 20$M_{\odot}$, $Z = Z_{\rm min}$ models of LC18 in Figure A.2). This means that the C15+LC18 model has the highest [N/Fe]

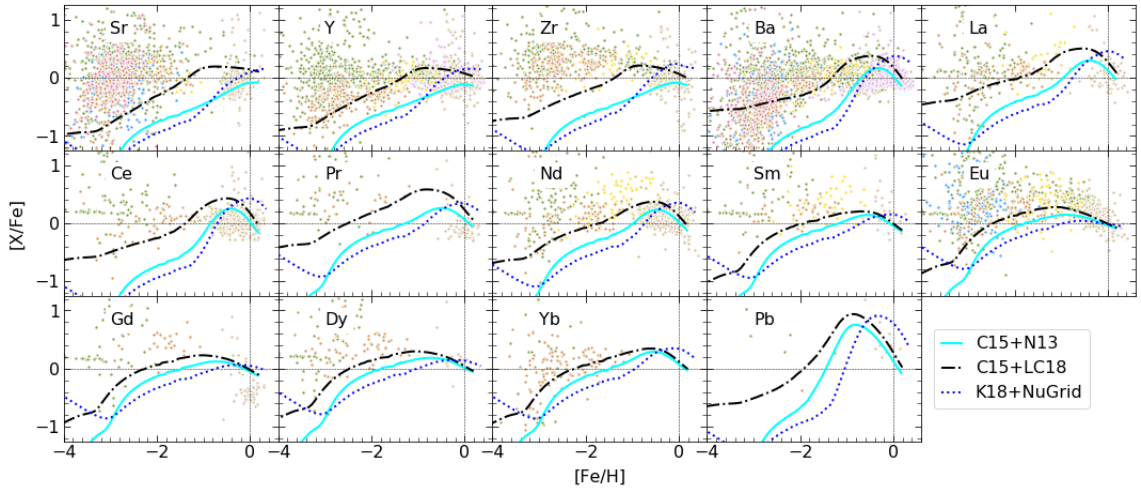

Figure 2.7: Same as Figure 2.6, but for elements from Sr to Pb.

at low metallicities[11]. From Figure 2.8 we can see that the K18 LIMS models produce more N than their C15 counterparts, by more than a factor of two. However, this GCE model does not overproduce [N/Fe] relative to solar due to the low contribution from the NuGrid massive star models. Our results are in good agreement with Prantzos et al. (2018), who also find with rotating massive stars that the evolution of [N/Fe] is mostly flat across all metallicities, but is highly sub-solar in the low metallicity regime when non-rotating massive star yields are used. Without a primary source of N from massive stars, the N abundance increases gradually with metallicity due to the increased secondary production of N at higher metallicities in higher mass AGB stars due to conversion of C and O into N via CNO cycling (Vincenzo et al., 2016b).

Oxygen: As O is predominantly produced by massive stars over short timescales, and is the most abundant metal in the Galaxy, its evolution is both relatively simple to model and approximates well the global metallicity evolution in the Galaxy. In fact, since the first time-delay models of Matteucci & Greggio (1986) the general features of [O/Fe] versus [Fe/H] have been well reproduced by GCE. All models in Figure 2.6 have [O/Fe] ≈ 1 at [Fe/H] ≈ -4, however, whilst in the C15 models the GCE tracks gradually decrease almost linearly until [Fe/H] ≈ -1, the K18+NuGrid model has a steeper decline at low metallicities.

[11] In fact, at [Fe/H] ≈ -4 the K18+NuGrid model has the highest [N/Fe] due to the large overproduction of N in the lowest metallicity $25 M_{\odot}$ NuGrid model (see bottom left panel of Figure A.2).

This is because the lowest metallicity $15M_{\odot}$ and $20M_{\odot}$ models in the NuGrid stellar grid produce much more Fe than the contemporaneous models of N13 and LC18, however, at higher metallicities the Fe yield is comparable between all models – thus, the [O/Fe] trend for K18+NuGrid flattens after [Fe/H] ≈ -2. All GCE predictions agree within 0.2 dex by solar – the C15 models have supersolar [O/Fe] and the K18+NuGrid model has subsolar. From Figure 2.8, the contribution from LIMS is less than 10% of the solar abundance for both C15 and K18. However, there are large variations in the contribution from massive stars, with N13 overproducing the solar abundance by ~ 1.5 times, whereas using NuGrid yields the O abundance is underproduced relative to solar.

2.4.2 The α-elements

Magnesium: It is well known that the evolution of [Mg/Fe] is not well reproduced by the majority of GCE models (see, e.g. Goswami & Prantzos, 2000; François et al., 2004; Prantzos et al., 2018), except those that assume some fraction of hypernovae in their massive star yields (see, e.g. Romano et al., 2010; Nomoto et al., 2013; Kobayashi et al., 2020b)[12]. This is also confirmed by our GCE models in Figure 2.6 – both C15+LC18 and K18+NuGrid are consistent with the systematic underproduction of Mg across all metallicities predicted by GCE models that include no contribution from hypernovae. However, the C15+N13 model provides a good fit to the observational data and the solar abundance. From Figure 2.8, the Mg contribution from both C15 and K18 AGB yields toward the solar abundance is small ($\sim 10\%$), and negligible from SNe Ia.

Silicon and Sulfur: For Si and S, the C15 models qualitatively show the same behaviour – a gradual decrease in the abundances relative to Fe until [Fe/H] ≈ -1, thereafter SNe Ia begin contributing significantly to the Galactic Fe budget creating a "knee" in the [α/Fe]-[Fe/H] diagram. The knee is clearly present in the observational data, and it delineates the older halo population from the younger disk stars. The location of the knee is sensitive to the star formation efficiency and the mass-loading parameter (Andrews et al., 2017), and because

[12]However, see also the predictions of Bisterzo et al. (2014) in Figure 5 of Mishenina et al. (2017) as an example of a GCE model that can reproduce [Mg/Fe] data without including hypernovae.

the mass-loading parameter is higher for the K18+NuGrid model[13] the position of the knee is shifted to higher metallicities ([Fe/H] ≈ -0.5). Furthermore, as for O, the [α/Fe] for K18+NuGrid has a faster evolution toward the solar value at low metallicities than in the C15 models due to the increased Fe production from the NuGrid massive star models in this regime. The evolution of Si and S for C15+N13 and C15+LC18 are nearly identical, which brings us to the same conclusion as in Prantzos et al. (2018) – that rotation in massive stars does not affect the well established [α/Fe]-[Fe/H] trends.

Calcium: Whilst all GCE tracks have a clear SNe Ia knee as for Si and S, there are much larger differences quantitatively between the three models. In particular, the effect of including rotation in the massive star yields increases the [Ca/Fe] ratio by ~ 0.4 dex at [Fe/H] ≈ -1, relative to C15+N13. For C15+LC18, the [Ca/Fe] increases with metallicity until [Ca/Fe] ≈ 0.6 at [Fe/H] ≈ -1, which is higher than any observational data at the same metallicity. The evolution of [Ca/Fe] in the K18+NuGrid model is also somewhat peculiar for an α-element, as [Ca/Fe] plateaus at the solar value from [Fe/H] ≈ -3 to [Fe/H] ≈ -1, rather than decreasing gradually as expected. In Romano et al. (2010), the Kobayashi et al. (2006) yields with a hypernovae fraction $\epsilon_{\rm HN} = 0$ have ≈ 0.2 dex higher [Ca/Fe] at [Fe/H] $= -1$ than for $\epsilon_{\rm HN} = 1$; herein we adopt $\epsilon_{\rm HN} = 0.5$ and find that this intermediate value provides the best fit to the [Ca/Fe] data. Whilst we find large differences in [Ca/Fe] for different yield sets, recently, using a three-infall model (with $t_{\rm max} = 4$ Gyr as in the revised two-infall model of Spitoni et al. 2019), Spitoni et al. (2022) demonstrated that the nucleosynthesis yields suggested by François et al. (2004) and Romano et al. 2010 (assuming $\epsilon_{\rm HN} = 1$ in this last) provide goods fits to spectroscopic data from Gaia Data Release 3 (Recio-Blanco et al., 2022) for [Ca/Fe]. In Kobayashi et al. (2020b), it is found that $\sim 40\%$ of solar Ca is produced by SNe Ia (assuming 100% of SNe Ia are from near-$M_{\rm Ch}$ WD progenitor), however, this value is closer to $\sim 20\%$ in all our GCE models; this results in a shallower slope after [Fe/H] ≈ -1 in Figure 2.6 for C15+N13 than in their Figure 16 with the same massive star yields.

[13]We remind that the mass-loading parameter is calibrated to reproduce the observed bulk properties of the Milky Way's disk, and since for K18+NuGrid the SFR is higher in order to reproduce the global metallicity evolution, the mass-loading factor must be higher so as to remove enough gas that the total mass of gas is within the observationally derived limits (see Figure A.5).

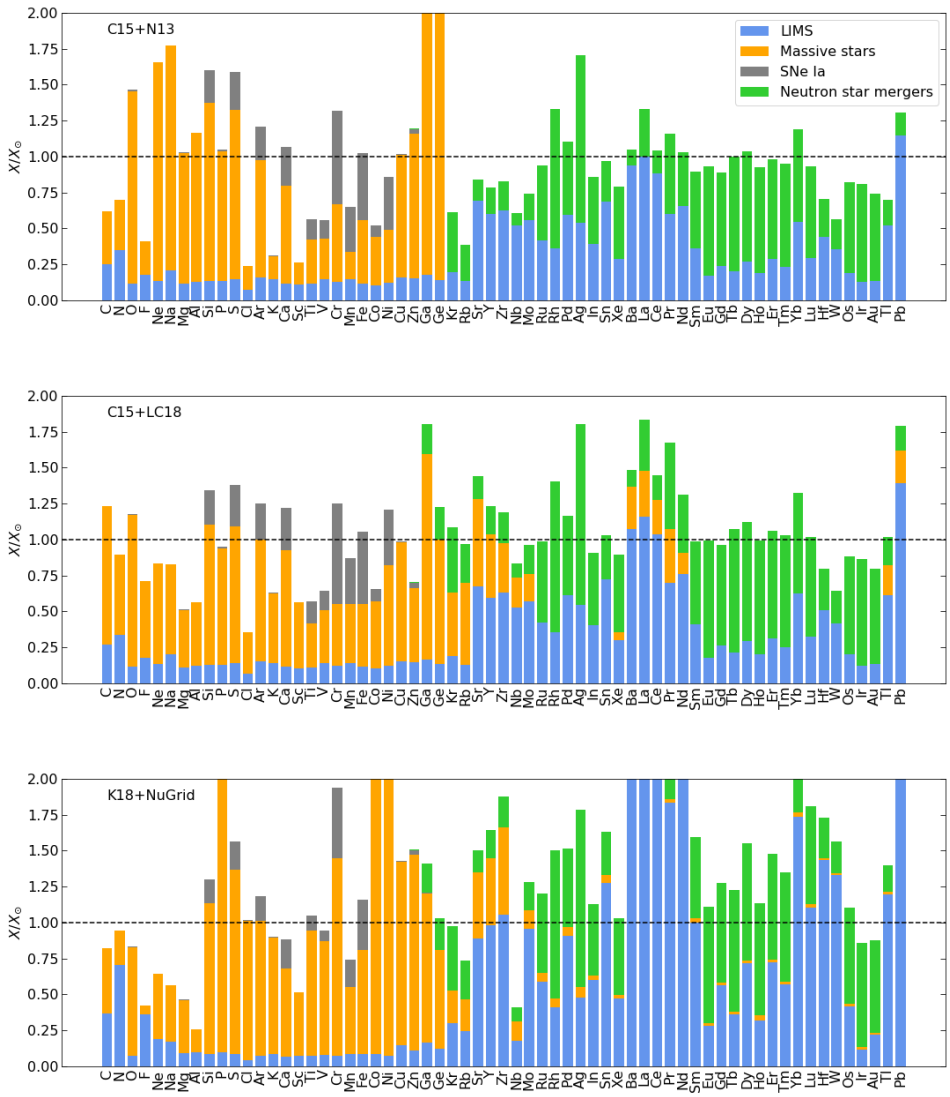

Figure 2.8: Contribution to each element from low- and intermediate-mass stars (blue), massive stars (orange), SNe Ia (grey), and neutron star mergers (green) in the Galaxy at the time of the birth of the Sun, $t_{\odot}$, for each of the three GCE models. Abundances are shown relative to solar, where the horizontal dashed-line indicates the solar value.

2.4.3 The odd-Z elements

Sodium: From Figure 2.6, it is apparent that the evolution of [Na/Fe] is not dependent on the implementation of rotation in the massive star yields, as the C15+LC18 model has an [Al/Fe] ratio between that of the C15+N13 and K18+NuGrid models at all metallicities. For the C15 models, the [Na/Fe] ratios is mostly flat until [Fe/H] ~ -1.5 with [Na/Fe] ≈ 0 and ~ -0.2 for N13 and LC18 massive star yields, respectively. During this time, ^{23}Na is predominantly produced by primary reactions during C-burning, and the increase in Na after [Fe/H] ~ -1.5 is from NeNa chain proton captures in LIMS models without hot bottom burning (see Figure 6 in Karakas, 2010). This increase is steepest in the K18+NuGrid model, because NuGrid massive stars produce less Na than N13 and LC18, and so the contribution from LIMS is more significant ($\sim 30\%$ of the total at [Fe/H] = 0).

Aluminium: As can be seen from Figure 2.6, the [Al/Fe] evolution is highly dependent on the choice of stellar yields. It is also highly affected by NLTE effects, which results in an average shift upwards of $\gtrsim +0.2$ dex in the LTE data for [Fe/H] $\lesssim -1$, such that the NLTE data in this low metallicity regime has a plateau (i.e., a slope of ≈ 0) at [Al/Fe] ~ -0.2 (Reggiani et al., 2017). For C15+N13, the [Al/Fe]-[Fe/H] evolution is comparable to [α/Fe]-[Fe/H], even though it is predominantly produced by secondary reactions during hydrostatic C-burning (Iliadis, 2007). For C15+LC18, the prediction fails to reproduce the [Al/Fe] data in the young disk stars. For K18+NuGrid, the GCE prediction underproduces [Al/Fe] relative to the observational data at all metallicities. It is evident from Figure 2.6 that the Al yield is sensitive to the choice of massive star yields, and this is also true for the short-lived radioisotope ^{26}Al. Understanding the evolution of the abundance of ^{26}Al in the ISM demands significant interest because i) it is ejected by many astrophysical sites, ii) it is a probe for recent stellar nucleosynthesis, and iii) its daughter isotope ^{26}Mg is found in excess in primitive meteorite samples. We briefly review the current picture of in Section 2.5

Potassium and Scandium: The evolution of these elements is not well fit by any of the GCE models. A potential solution could be convective C-O shell mergers, which have been shown to produce large increases in the yields of the odd-Z elements (Ritter et al., 2018b). Also, it is clear that rotation enhances the K and Sc yields (see also Prantzos et al., 2018), except

at high metallicities. Comparing between models in Figure 2.8, we see that for C15+LC18 and K18+NuGrid the solar abundance of K and Sc is mostly from massive stars, however, the LIMS contribution for these elements at [Fe/H] = 0 is comparable to that of massive stars in the C15+N13 model.

2.4.4 The Fe-peak elements

A brief discussion of the Fe-peak elements (in reference to Ti, V, Cr, Mn, Co, and Ni as a collective) is given here, however, we refer the reader to Chapter 4 for a more in-depth discussion of the GCE of these elements taking into account different SNe Ia explosion scenarios.

Titanium, Vanadium and Chromium: We note that Ti is often classified as an α-element (see, e.g. Romano et al., 2010) based on the atomic mass of its most abundant isotope, ^{48}Ti, and the similarity of the trends between the [Ti/Fe]-[Fe/H] and [α/Fe]-[Fe/H] observational data, rather than on nucleosynthetic principles. Both Ti and V are known to be underproduced by GCE models (Timmes et al., 1995; François et al., 2004; Romano et al., 2010; Prantzos et al., 2018; Kobayashi et al., 2020b), however, the K18+NuGrid model provides a good fit with the [Ti/Fe] data due to the large overproduction factor in the $15M_{\odot}$ NuGrid massive star models (see Figure A.2). The [V/Fe] evolution is not well reproduced by any of the GCE models at low metallicities, although the K18+NuGrid model again provides the best fit to the data at [Fe/H] = 0. The C15+N13 model qualitatively reproduces the plateau in the [V/Fe] data, however, it is $\sim$ 0.2 dex too low compared to observations. As for V, the Cr data is scattered around [Cr/Fe] $\approx$ 0 at all metallicities, with the models with non-rotating yields providing a better match than the C15+LC18 model. For Cr, all yields produce a flat trend with the metallicity until increasing after [Fe/H] ≈ -1 due to the contribution from SNe Ia – Figure 2.8 shows that Cr is the element that receives the largest relative contribution from SNe Ia toward the solar abundance. The NuGrid yields produce more than twice as much Cr by [Fe/H] = 0 than the N13 and LC18 yields.

Manganese: NLTE corrections are necessary for determining the Mn abundance from measurements of Mn I lines, especially at low metallicities. For this reason, we include only NLTE corrected data for this element. Compared to LTE data, the NLTE corrections do not

show a steep rise in [Mn/Fe] after [Fe/H] ~ -1, and instead the trend is relatively flat over the complete metallicity range (Eitner et al., 2020). In Figure 2.6, the GCE predictions all exhibit different behaviour: the C15+N13 model remains relatively flat until [Fe/H] ~ -1, and steadily increases thereafter; C15+LC18 is initially flat at [Mn/Fe] ≈ -0.2 between [Fe/H] ~ -4 and [Fe/H] ~ -3 before decreasing to [Mn/Fe] ≈ -0.3, the trend then turns upwards at [Fe/H] ~ -2 and begins to flatten after [Fe/H] = 0; K18+NuGrid decreases until [Fe/H] ~ -2, and then increases. No model is able to replicate the relatively flat trend seen in the data. The increase after [Fe/H] ~ -1 is due to the delayed enrichment from SNe Ia, however, [Mn/Fe] is still underproduced in all models. This could be alleviated by having a higher relative fraction of near-$M_{\rm Ch}$ SNe Ia (see Chapter 4). We note that the SNe Ia yields used in this analysis are metallicity dependent (see Figure A.3), and that the Mn yield has a clear upward trend with metallicity, particularly in the case of the sub-$M_{\rm Ch}$ channel. This metallicity dependency has long been considered a requirement for simultaneously reproducing the [Mn/Fe] evolution in the different Galactic components (McWilliam et al., 2003; Cescutti et al., 2008), however, this appears secondary in importance to the relative fraction of SNe Ia from WD progenitor of different masses (see Chapter 4).

Cobalt, and Nickel: Both the C15+N13 and C15+LC18 models are relatively flat for [Co/Fe] at all metallicities, but the K18+NuGrid model significantly overproduces with respect to the observational data. It is not clear what causes the increase in [Co/Fe] at very low metallicities, however, HNe have been proposed as a potential solution (Grimmett et al., 2020). For [Ni/Fe], the K18+NuGrid model has a similar trend as it does for [Co/Fe]. The C15+N13 and C15+LC18 models have opposite trends in the evolution of [Ni/Fe] after [Fe/H] ~ -1, increasing and decreasing, respectively. This is due to the fact that the low-metallicity rotating massive star models of LC18 produce more Ni than the N13 models (see also the relative contribution of massive stars in these models in Figure 2.8).

2.4.5 Copper and Zinc

Copper: The increase in Cu after [Fe/H] ~ -2 is not from SNe Ia enrichment (Figure 2.8 shows there is no contribution toward Cu from SNe Ia), but instead because the Cu yield scales according to metallicity in massive star models, due to the nature of its secondary production

by *s*-process neutron captures during He-core burning (Pignatari et al., 2010). The C15+N13 and C15+LC18 models fit the data relatively well, however, the NuGrid yields significantly overproduce [Cu/Fe] at subsolar metallicities.

Zinc: The data for [Zn/Fe] shows an α-element like behaviour, decreasing with increasing metallicity. Only the C15+N13 model provides a good fit to the data, except at very low metallicities. However, the astrophysical sites responsible for production of Zn are not well known, although both EC-SNe and HNe have both been considered as potential candidates (Hirai et al., 2018; Kobayashi et al., 2020b). With this in mind, we find that the C15+N13 yields with $\epsilon_{\rm HN} = 0.5$ provide the best fit to the [Zn/Fe] data, in agreement with Kobayashi et al. (2020b).

2.4.6 The *s*-process elements

We remind that the solar abundance distribution beyond Fe has three peaks corresponding to the magic neutron numbers. These peaks represent natural bottlenecks in the *s*-process flow, where the weak, main, and strong *s*-process components are responsible for the production of isotopes associated with the first, second, and third peaks, respectively. The weak *s*-component has been shown to predominantly operate in massive stars ($M_\star > 10 M_\odot$) during core He and convective shell C burning (Lamb et al., 1977; Arnett & Thielemann, 1985; Raiteri et al., 1991). However, some GCE models tend to underproduce elements at and around the first peak (see, e.g. Travaglio et al., 2004; Bisterzo et al., 2014), which can be mitigated by including yields from either rotating massive stars (Prantzos et al., 2018) due to mixing leading to a higher production of ^{14}N and consequently the neutron source ^{22}Ne (Meynet et al., 2006; Hirschi, 2007; Pignatari et al., 2008), or from ECSNe (Kobayashi et al., 2020b), both of which lead to an enhanced *s*-process contribution at low metallicities. The main component takes place in the periods of intermittent He-shell burning in thermally pulsing AGB stars via the activation of the primary neutron source reaction ^{13}C(α,n)^{16}O (Busso et al., 1999). Since the ^{13}C source in AGB stars is primary, the number of neutrons per Fe-seed nuclei (secondary elements) scales inversely with increasing metallicity. Therefore, at lower initial metallicities the neutron irradiation is higher, which results in a greater relative production of heavy (second peak) to light (first peak) *s*-elements, such that [hs/ls] versus

[Fe/H] is predicted to decrease as AGB stars begin contributing to the Galactic *s*-element budget (see, e.g. Busso et al., 2001; Bisterzo et al., 2011; de Castro et al., 2016). Finally, the production of large amounts of ^{208}Pb occurs via the strong component, which takes place in low-mass and low-metallicity AGB stars (Gallino et al., 1998; Travaglio et al., 2001).

The first s-process peak (Sr, Y, Zr): As expected, the C15+LC18 model best reproduces the data at subsolar metallicities due to the enhanced production of these elements in the rotating massive star yields. Even so, the prediction is still underproduced compared to the majority of observational data in this metallicity range, which could indicate the neglecting of a secondary 'weak' *r*-process component that is required to produce the light trans Fe elements with delay times shorter than those for neutron star mergers[14]; a potential candidate that fits this criterion are magnetorotationally driven supernovae (MRD SNe; Wehmeyer et al., 2015; Nishimura et al., 2017; Côté et al., 2019a). For comparison, the model of Prantzos et al. (2018) that assumes *r*-process yields from CCSN, whilst unphysical in its treatment, provides a much better fit to the observations at low-metallicities than their equivalent GCE model with no *r*-process contribution (see their Figure 16). This suggests that in extremely metal-deficient stars the observed enhancements in Sr, Y, and Zr are the result of a prompt *r*-process component, with only a marginal *s*-process contribution from massive stars at early Galactic times – this conjecture was first realised by Truran (1981), on the grounds that the evolution of [Sr, Y, Zr/Fe] do not behave as expected for secondary elements. The epoch of *r*-process domination for the first peak elemental abundances is short-lived, as the ratios [Y/Fe] and [Y/Mg] have both been shown to decrease with stellar age, which is strong evidence for a substantial contribution of Y from long-lived low-mass AGB stars (Nissen et al., 2017). The evolution of C15+N13 and K18+NuGrid are comparable for the first peak elements, with slight under- and over-productions relative to solar at [Fe/H] = 0 for the two models respectively. As can be seen in Figure 2.8, the N13 models do not produce any *s*-elements, hence the lower overall contribution by $t_\odot$. Figure 2.8 shows there is a significant contribution to the first peak elements at $t_\odot$ from the K18 AGB models, which causes an upward turn in K18+NuGrid in Figure 2.7 after [Fe/H] $\gtrsim -1$. Finally, we note that at $t_\odot$, the *r*-process

[14]Alternatively, it has been suggested that a so-called *lighter element primary process* could be responsible for $\sim 10\%$ contribution of the first *s*-peak elements in the Galaxy (see discussion in Section 3.3.3).

contribution to the first peak elements is $\sim$ 15% of solar.

The second s-process peak (Ba, La, Ce, Pr, Nd, Sm): As for the first peak elements, the best-fitting GCE model to the data at low metallicities is C15+LC18 due to the enhanced enrichment of *s*-elements over short timescales from rotating massive stars. However, as for the first peak elements, there is a clear underestimation in all models compared with the observational data. Using the same set of low-mass and massive star yields as in the C15+LC18 model, Rizzuti et al. (2019) were able to well reproduce the very low-metallicity data in the [Ba/Fe] versus [Fe/H] diagram by considering MRD SNe as the *r*-process source. Conversely, they also find that neutron star mergers with delay-times comparable to those of MRD SNe (i.e., $\tau \sim 1$ Myr, rather than a power law distribution which peaks at ~ 10 Myr as assumed in this work) can also provide a good fit to the observational data (see their Figure 10). For Ba, La, and Ce there is a clear upward turn in the GCE tracks after [Fe/H] ~ -1 as AGB stellar enrichment begins. This upward turn, whilst still present in the GCE tracks of Pr, Nd, and Sm, is less noticeable due to the higher abundance ratios in the metallicity interval $-3 <$[Fe/H] < -1. The maximum in [X/Fe] is at lower metallicities than for the first peak elements (but higher than for the third peak), due to the fact that the *s*-process preferentially produces heavier neutron-capture elements when the number of Fe seeds is low (i.e., when the initial metallicity is low). This maximum is delayed in the K18+NuGrid model with respect to C15+N13 and C15+LC18, because more *s*-elements are removed from the Galaxy in stellar winds prior to the epoch of SNe Ia enrichment due to the higher mass loading factor in this model. The maximum value of [Ba/Fe] measured in young open cluster stars is higher than for La, to such an extent that it cannot currently be explained without invoking the need for an additional production mechanism of Ba at late Galactic times (D'Orazi et al., 2009; Magrini et al., 2018). As can be seen in Figure 2.8, the K18 models undergo a more efficient *s*-processing at the second peak than the C15 models; this is true across the complete metallicity range for $M_\star \leq 3M_\odot$ (see Figure A.1) and leads to vast overestimates of the second peak *s*-elements at $t_\odot$.

The third s-process peak (Pb): It is difficult to use GCE to constrain stellar sources of the strong *s*-component at early Galactic times because (i) there is a lack of low-metallicity abundance measurements for Pb; and (ii) low-metallicity observations are most affected by

the potentially large ($\sim$ 0.2 dex) NLTE corrections (Mashonkina et al., 2012). Nevertheless, it is clear from Figure 2.8 that LIMS stars are the dominant source of Pb in the Solar System, with the steep upturn in the GCE tracks in Figure 2.7 showing they come to dominate the Galactic production after [Fe/H] $\gtrsim -2$. This upturn occurs at earlier times than the equivalent GCE tracks for the first and second *s*-process peaks due to the higher neutron-to-seed ratio in low-metallicity LIMS. The peak in [Pb/Fe] for the C15+N13 and C15+LC18 models occurs at [Fe/H] ~ -1, which corresponds to the metallicity at which low-mass stars most efficiency produce Pb (Travaglio et al., 2001).

2.4.7 The *r*-process elements

The distinct signature of *r*-isotopes observed in the ejecta of the NSM responsible for the GW170817 gravitational wave event (Abbott et al., 2017) and the subsequent high-energy 'blue kilonova' (Evans et al., 2017) confirmed the long-held belief that these astrophysical phenomena contribute some amount toward the *main* *r*-process budget in the Galaxy. However, the presence of rare *r*-enhanced (i.e., [Eu/Fe] $> +1.0$) low-metallicity stars (e.g., Sneden et al., 2000; Hill et al., 2002; Barklem et al., 2005) cannot be explained in GCE models that consider NSMs as the only source of the *r*-process (Argast et al., 2004; Kobayashi et al., 2023), unless these events have delay-times several times shorter (i.e., of the order $\sim$ 1 Myr) than predicted by BPS models (Matteucci et al., 2014; Molero et al., 2021). Since the gas that formed these stars would have been enriched by only a small number of events, the universality of the *r*-process distribution across Galactic age can be determined by cross-comparing the abundances in these low-metallicity stars to the scaled solar values. Such studies suggest that, for those elements either belonging to or between the second and third peaks (i.e., the main *r*-process component), the *r*-process is indeed universal (Burris et al., 2000; Roederer et al., 2012). The convergence to a universal distribution for the main *r*-process in the observational data provides an unparalleled constraint for the necessary conditions in models of stellar nucleosynthesis (see discussion in Frebel, 2018). Despite this fact, the main astrophysical sites of the *r*-process remain under much scrutiny, with MRD SNe proposed as promising candidates due to the fact their inclusion in GCE models has allowed predictions to reproduce the *r*-enhanced abundances seen in metal poor stars (Wehmeyer et al., 2015; Côté et al.,

2019a).

The main r-process component (Eu, Gd, Dy, Yb): Without an r-process source contributing at low-metallicities, the GCE models underproduce relative to the stellar abundance data in the [Fe/H] $\lesssim -2$ regime. Due to the fact that the NSM yields of Rosswog et al. (2014) are not metallicity-dependent (reflecting the universality of the main r-process component), [r/Fe] steadily increases after [Fe/H] ~ -3, reaching a maximum at [Fe/H] ~ -1 corresponding to the time of significant Fe deposition in the ISM from SNe Ia. For comparison, Prantzos et al. (2018) assume r-process yields from massive stars, and so [r/Fe] evolves in a comparable way to [α/Fe], following the same convergence to [r/Fe] at [Fe/H] as in Figure 2.7. On the other hand, Kobayashi et al. (2020b) produce supersolar [Eu/Fe] at [Fe/H] $\lesssim -4$ by including an r-contribution from MRD SNe. In any case, Figure 2.8 shows that NSMs can account for $\sim 80\%$ of solar r-elements at $t_\odot$, which suggests that any contribution from additional sources would dominate only at low-metallicities.

2.5 The evolution of ^{26}Al in the Galaxy

Following its first detection by Mahoney et al. (1982), measurements of the 1.8 MeV emission line have established that the majority of the Galaxy's 2 to 3 $M_\odot$ of ^{26}Al is located in star-forming regions in the Galactic plane (Diehl et al., 1995). Since its half-life ($T_{1/2}$ = 0.717 Myr) is short relative to galactic timescales, the presence of live ^{26}Al is evidence for ongoing nucleosynthesis in the Milky Way. Whilst the detection of live ^{26}Al can be used to trace nucleosynthesis in the Galaxy today, the evidence of excess ^{26}Mg, the daughter of ^{26}Al, in several Ca-Al rich inclusions (CAIs), indicates that ^{26}Al was one of several short-lived radionuclides (SLRs) known to have been present in the early Solar System (ESS; Lee et al., 1977; Wasserburg et al., 2006). Another radioisotope known to have existed in the ESS is ^{60}Fe. Analogous to ^{26}Al, ^{60}Fe has a short half-life ($T_{1/2}$ = 2.62 Myr) and is produced by massive stars and their supernovae, thus making the ^{60}Fe/^{26}Al flux ratio an important tracer for massive star-forming regions Wang et al. (2020). However, the ^{60}Fe/^{26}Al flux ratio measured today indicates an abundance ratio 3 to 300 times higher than that inferred from meteorites. This problem is further compounded by theoretical core-collapse

supernovae yields, which currently overproduce ^{60}Fe relative to ^{26}Al even compared to the spectroscopic γ-ray observations (Sukhbold et al., 2016; Austin et al., 2017; Jones et al., 2019a). Unfortunately, this is not the only discrepancy between present day and ESS values. High precision measurements of the Mg content of meteorite chondrules suggests that ^{26}Al was distributed homogeneously in the ESS (Villeneuve et al., 2009), with a "canonical" ^{26}Al/^{27}Al ratio of $\sim 5 \times 10^{-5}$; this is an order of magnitude greater than the ratio observed today via γ-ray spectroscopy (8.4×10^{-6}; Diehl et al., 2006) and predicted by galactic chemical evolution (GCE) models (Huss et al., 2009; Côté et al., 2019b; Meyer & Clayton, 2000). The existence of a canonical value has been challenged however, with evidence of ^{26}Al/^{27}Al variations in several CAIs and chondrules, but it is currently unclear whether this variation probes an heterogeneous distribution of ^{26}Al in the cloud or different generations of meteoritic inclusions (Mishra & Chaussidon, 2014; Krot et al., 2012; Pignatale et al., 2019).

Regardless of whether the $\sim 5 \times 10^{-5}$ value for the ^{26}Al/^{27}Al ratio represents a canonical value or an upper limit for the spatial distribution in the Galactic disk, it still remains unclear how the ESS came to have an initial ^{26}Al abundance far exceeding the Galactic average. Using an analytical GCE framework, Huss et al. (2009) determined that massive stars, through both mass loss in winds and their supernovae, are the primary contributors of ^{26}Al in the interstellar medium. Whilst these stars present a likely origin site, there is ambiguity around the exact scenario responsible for the Solar System's enrichment. Furthermore, only single stars $\gtrsim 30 M_{\odot}$ could conceivably produce enough ^{26}Al in their winds to be considered as a possible candidate, although Brinkman et al. (2019) have shown that lower mass stars could achieve similar yields if they are part of a binary system. Another possible origin is asymptotic giant branch stars (Busso et al., 1999), however, this source seems unlikely because (1) they cannot produce the required ^{26}Al abundance without also overproducing several s-process SLRs (Vescovi et al., 2018); and (2) they are very long lived ($\sim$ 1 Gyr), so are unlikely to be found in close proximity to star-forming regions (Kastner & Myers, 1994). Since stellar enrichment events are discrete in time and space, local enhancements in the ^{26}Al abundance due to spatial inhomogoneities have also been considered (Côté et al., 2019c; Kaur & Sahijpal, 2019), however the former find the evolution of any given SLR is dependent on the time interval

between progenitor formation - a parameter which is currently poorly understood.

Given the high level of uncertainty in stellar yields, it is important to consider how these relate to isotopic abundance ratios at different times in the Galaxy's history. Considering firstly the ^{26}Al/^{27}Al ratio in the ESS, since ^{27}Al is stable, its abundance directly probes the complete star formation and gas flow histories of the Milky Way (see, e.g. Clayton, 1984), thus a GCE model is necessary to predict its abundance in the ESS. On the other hand, since ^{26}Al has such a short half-life, its ESS abundance is only affected by the time elapsed between the formation of the protosolar molecular cloud and the last stellar event that polluted it with ^{26}Al (Lugaro et al., 2018). The time of this last event gives an upper limit for the isolation time (T_{iso}) - the time between the last addition of stellar material into the molecular cloud and the formation of the first solids. Considering again the isotopic inventory of the ESS, a GCE simulation is not needed to interpret the ^{26}Al/^{60}Fe ratio, since both isotopes are very short-lived. Instead, their relative abundance depends on the specific mass of the star (or binary system) that synthesized them, as well as the isolation time. Furthermore, it is important to consider that ^{26}Al and ^{60}Fe decay with different half-lives and, since they are ejected synchronously by stochastic enrichment events, the ^{60}Fe/^{26}Al ratio is a factor of 7% higher than that predicted by the steady-state formula (Yagüe López et al., 2021b). The ^{26}Al/^{60}Fe signal measured today sums the contribution of all nearby stellar populations currently ejecting the isotopes, as opposed to probing a limited number of specific stellar mass(es), as in the ESS case. Since the flux ratio only traces recent nucleosynthesis events, a GCE simulation following the complete 13 Gyr history of the Galaxy is unnecessary. In this case, to accurately model the ^{26}Al/^{60}Fe ratio we need to know: the star formation rate of the Milky Way at the present time; the initial mass function, in order to work with stellar populations; the yields produced by stars with a range of masses and metallicites, reflecting the distribution in the solar neighbourhood; the population of stars in binary systems, and the effect binaries have on the yields. Comparing a 3D hydrodynamic simulated distribution of ^{26}Al to observed 1.8 MeV emission line flux maps, Pleintinger et al. (2019); Fujimoto et al. (2020) provide constraints on the Galaxy-wide distribution of ^{26}Al and studies like this could shed light on whether the Sun is a peculiar object in terms of its ^{26}Al and ^{60}Fe content. In any case, the fundamental input for any numerical prediction - whether they be GCE, ISM, or

single-source enrichment models - are the stellar yields.

3. Galactic Chemical Evolution of Radioactive Isotopes with an s-process Contribution

This Chapter contains work published in The Astrophysical Journal, Volume 924, Issue 1, id.10, 16 pp. as *"Galactic Chemical Evolution of Radioactive Isotopes with an s-process Contribution"* (Trueman et al., 2022). I was the principal contributor to this work in terms of research and writing of the article: I made all the GCE models, the figures, and led the analysis in the paper. Maria Lugaro mainly supervised my work in connection with the ESS observations. Suggestions and feedback for the paper were provided by Benoit Côté, Andrés Yagüe López, Jacqueline den Hartogh, Marco Pignatari, Benjámin Soós, Amanda Karakas, and Maria Lugaro.

3.1 Introduction

It has been inferred from analysis of meteoritic rocks and inclusions that many short-lived radionuclides (SLRs) with half-lives of $T_{1/2} \sim 0.1 - 100$ Myr were present in the early solar system (ESS; Dauphas & Chaussidon, 2011; Lugaro et al., 2018). These SLRs can be used as tracers of the local circumstances of the birth of the Sun and the history that led to them. In particular, SLRs offer the unique opportunity to probe the length of time that the protosolar gas was isolated from further stellar enrichment events in the Galaxy before the birth of the Sun - the so called, "isolation time" (see e.g. Wasserburg et al., 2006; Huss et al., 2009; Lugaro et al., 2014; Côté et al., 2019b). Furthermore, the *in situ* decay of ^{26}Al ($T_{1/2}$ = 0.72 Myr) provided an important energy source for the thermo-mechanical evolution of protoplanets (see, e.g., Lichtenberg et al., 2016). However, a self-consistent origin scenario that explains the abundances of of all SLRs in the ESS has yet to be found.

We investigate the ESS origin of three SLRs[1], ^{107}Pd ($T_{1/2}$ = 6.5 Myr), ^{135}Cs ($T_{1/2}$ = 2.3

[1]Despite the fact it is also made by the *s*-process, we do not study ^{205}Pb due to its poorly understood half-life in stellar interiors (Mowlavi et al., 1998).

Myr), and ^{182}Hf ($T_{1/2}$ = 8.90 Myr), which can be produced in astrophysical sites by two neutron capture processes (Burbidge et al., 1957): the *slow* (*s*)-process (see review by Käppeler et al., 2011), so called because the neutron capture rate is slow compared to the β-decay rate of unstable nuclei along the *s*-process path; and the *rapid* (*r*)-process (see review by Thielemann et al., 2011), where instead the timescale for neutron-capture is much shorter than the competing β-decay rate. The main site of production of the *s*-process isotopes in the mass range 90 < A < 208 are low- and intermediate-mass ($M \lesssim 8$ M$_\odot$) asymptotic giant branch (AGB) stars (Gallino et al., 1998; Busso et al., 1999; Goriely & Mowlavi, 2000; Herwig, 2005; Cristallo et al., 2009; Lugaro et al., 2012). These stars experience thermal convective instabilities triggered by recurrent He-burning episodes on top of a degenerate C-O core. During the relatively long interpulse phase ($\gtrsim 10^3$ years), the ^{13}C$(\alpha, n)^{16}$O neutron source reaction is activated. The nucleosynthesis products are subsequently mixed into the thermal convective instability region where a second neutron source, the ^{22}Ne$(\alpha, n)^{25}$Mg reaction, is marginally activated and plays a role in the production of several *s*-process isotopes. These products are then brought to the surface of the star in a convective mixing process called third dredge-up (TDU), from where they are then lost to the interstellar medium (ISM) via stellar winds (Karakas & Lattanzio, 2014, and references therein).

Two scenarios have been proposed to explain the origin of ^{107}Pd, ^{135}Cs, and ^{182}Hf in the ESS: (1) a nearby star that ejected its material into the protosolar nebula, and (2) Galactic inheritance from the local ISM. Considering first scenario (1), the idea that a nearby, low-mass AGB could have polluted the ESS was explored by Wasserburg et al. (1994) and Busso et al. (1999). The former found that such stars can readily provide a solution for the origin of several SLRs in the ESS, and that the production of *s*-isotopes is sensitive to the overall neutron exposure. However, as Busso et al. (1999) point out, the AGB models used in Wasserburg et al. (1994) incorrectly assumed that the ^{13}C$(\alpha, n)^{16}$O reaction takes place under convective rather than radiative conditions. More recent studies have looked in to an intermediate-mass AGB star as a potential candidate (Wasserburg et al., 2006, 2017; Vescovi et al., 2018), however, these stars produce, for example, too much ^{107}Pd relative to ^{26}Al to provide a self consistent solution. Core-collapse supernovae stars have also been considered as potential sources for

the origin of ^{107}Pd and ^{182}Hf (Meyer & Clayton, 2000, Lawson et al. in prep). However, a late addition of ejecta from a massive star into the forming solar nebula would significantly overproduce ^{53}Mn and ^{60}Fe if the dilution factor is calibrated to reproduce the necessary abundances for other SLRs (see, e.g. Wasserburg et al., 2006; Vescovi et al., 2018).

In scenario (2) the distribution of SLRs in the ESS reflects contributions from multiple stellar enrichment sources. In this case, the abundance of isotopes in the ISM at the time of the birth of the Sun ($t_\odot$) can be predicted using a galactic chemical evolution (GCE) code that considers contributions from a variety of stellar nucleosynthesis events (Travaglio et al., 1999, 2004; Huss et al., 2009; Prantzos et al., 2018, 2020; Côté et al., 2019b). To compare to the ESS data, we need to calculate the ratio of an SLR relative to a stable, or long-lived, reference isotope, which directly probes the complete star formation and gas flow histories of the Milky Way. The isolation time ($T_{\rm iso}$) is therefore the time taken for the radioactive-to-stable abundance ratio in the ISM at $t_\odot$ to reach the abundance ratio inferred for the earliest solids known to form in the ESS, assuming that the only change in the relative abundances of the two isotopes is due to the radioactive decay of the SLR.

The uncertainties associated with the modelling of the evolution of radioactive-to-stable isotopic ratios in the Galaxy were analysed quantitatively by Côté et al. (2019b) (hereafter Paper I). In Paper I the GCE framework used herein was first established: using observations of the Galactic disk to calibrate a two-zone GCE code, `OMEGA+`, a low, a best, and a high value of the radioactive-to-stable isotopic ratio in the ISM at $t_\odot$ were obtained with a total uncertainty of a factor of 3.6 between the high and low GCE setups. To quantify the uncertainty in the isotopic ratio, considering the fact that enrichment events are not continuous but discrete in time, Côté et al. (2019c) (hereafter Paper II) added Monte Carlo calculations to the GCE framework in order to sample appropriate delay-time distribution functions for different astrophysical sites. They recovered uncertainty factors for the abundance of an SLR in a given parcel of ISM matter at $t_\odot$ for several values of τ/γ, where τ is the mean life of the SLR ($\tau = T_{1/2}/\ln 2$) and γ is the interval of time between the formation of enrichment progenitor. If $\tau/\gamma \gtrsim 2$ (henceforth Regime I), the GCE description is valid and the error bar of the abundance of the SLR at $t_\odot$ remains below a factor of 0.8. If $\tau/\gamma \lesssim 0.3$ (henceforth Regime III), instead the

SLR probably originates from only one event, so it is not possible to determine the isolation time but only the time from the last event (see discussion in Lugaro et al., 2014, 2018). Yagüe López et al. (2021b) (hereafter Paper III) expanded this framework to analyse the ratio of two SLRs that are produced together by the same enrichment events. By exploring this last ratio, one can completely remove uncertainties associated with the GCE of the stable isotopes whilst simultaneously reducing the statistical uncertainty on the radioactive-to-radioactive ratio due to ISM heterogeneities to less than a factor of a half, assuming that Regime I holds for both SLRs.

The aim of this paper is to analyse ^{107}Pd, ^{135}Cs, and ^{182}Hf together in the framework described above. It is possible to do this because Lugaro et al. (2014) showed that ^{182}Hf has a substantial *s*-process component in the Galaxy, since the faster decay of ^{181}Hf at stellar temperatures, due to the existence of a 68 keV excited level and hampering ^{182}Hf production, was based on a wrong assignment (Rickey & Sheline, 1968), as already noted in Firestone (1991), and then confirmed by Bondarenko et al. (2002). Prior to this, it was found that the majority of ^{182}Hf, like ^{129}I ($T_{1/2}$ = 15.7 Myr), was mostly produced by the *r*-process leading to inconsistent isolation times from ^{182}Hf/^{180}Hf and ^{129}I/^{127}I (see, e.g., Ott & Kratz, 2008, and references therein). With the knowledge now that ^{182}Hf is also produced by the *s*-process in AGB stars, we can use the new methodology and framework presented in Papers I and II to re-investigate the SLRs with an *s*-process Galactic component.

3.2 Methods and models

Following the methodology of Paper I, we calibrate our GCE framework to recover a low, best, and high value for the radioactive-to-stable abundance ratio of ^{107}Pd/^{108}Pd, ^{135}Cs/^{133}Cs, and ^{182}Hf/^{180}Hf in the ISM at $t_{\odot}$. Paper I only considered the simplified case of a constant production ratio between an SLR and its reference isotope, while in this work we use mass- and metallicity-dependent stellar nucleosynthesis yields from two different sets of AGB models in our GCE framework. In addition, we use the uncertainties calculated in Papers II and III to account for the effects of ISM heterogeneities on the radioactive-to-stable and radioactive-to-radioactive abundance ratios at $t_{\odot}$. In this Section we give a brief description of our GCE

framework, the choice of stellar yields, and the calibration of our three different GCE setups.

3.2.1 The OMEGA+ GCE framework

We follow the evolution of SLRs in the Galaxy using the publicly available OMEGA+ GCE code[2] (Côté et al., 2018). This two-zone model is comprised of (1) a central star forming region, modelled using the OMEGA code (Côté et al., 2017), which simulates the chemical evolution of a cold gas reservoir as a function of time, and (2) a surrounding hot gas reservoir with no star formation. Following the nomenclature adopted in Côté et al. (2018), we refer to Region (1) as the galaxy and Region (2) as the circumgalactic medium (CGM).

At each timestep, the code creates a simple stellar population in the galaxy. All stars in a stellar population form at the same time and have the same initial metallicity - that of the ISM at that time - since they are assumed to have been born from the same parent gas cloud. The mass of the stellar population is proportional to the star formation rate (SFR) at that time. The SFR at any given time is directly proportional to the total mass of gas inside the galaxy, such that

$$\dot{M}_\star(t) = \frac{\epsilon_\star}{\tau_\star} M_{\rm gas} = f_\star M_{\rm gas}(t), \tag{3.1}$$

where $f_\star$ [yr^{-1}], represents the combination of the dimensionless star formation efficiency $\epsilon_\star$ and the star formation timescale $\tau_\star$. At each time step in the simulation, the SYGMA code (Ritter et al., 2018a) calculates the combined yield from all stellar populations in the galaxy. For a galaxy with N stellar populations formed by time t, each with their own initial mass, metallicity, and formation time (M_j, Z_j, and t_j respectively), the rate at which gas is returned to the ISM from stellar ejecta is given by

$$\dot{M}_{\rm ej}(t) = \sum_j \dot{M}_{\rm ej}(M_j, Z_j, t - t_j). \tag{3.2}$$

where $t - t_j$ is the current age of population j. The code includes the mass- and metallicity-dependent yields for low- and intermediate-mass stars (the progenitors of AGB stars), massive stars and their core-collapse supernovae, and SNe Ia. Additionally, it has the option to include

[2]https://github.com/becot85/JINAPyCEE

contributions from any number of user-defined additional sources. `OMEGA` is a one-zone GCE model, so the stellar ejecta is assumed to mix instantaneously and uniformly into the ISM.

The addition of the CGM as a one-zone extension to `OMEGA` allows the code to track the elements that are expelled from the galaxy by galactic outflows. Whilst galactic inflows introduce new, often metal poor gas into the galaxy, galactic outflows expel gas and heavy elements into the CGM. Considering the transfer of matter into and out of the galaxy, the gas locked inside stars ($M_\star$), and the gas returned to the ISM by stellar ejecta ($M_{\rm ej}$), the time dependence of the total mass ($M_{\rm gas}$) inside the galaxy can be expressed as

$$\dot{M}_{\rm gas}(t) = \dot{M}_{\rm inflow}(t) + \dot{M}_{\rm ej}(t) - \dot{M}_\star(t) - \dot{M}_{\rm outflow}(t). \tag{3.3}$$

The gas inflow and outflow rates can be controlled by user-defined inputs. In this work we apply the methodology from Chiappini et al. (1997) and assume two exponential gas inflow episodes described by

$$\dot{M}_{\rm inflow}\,(t) = A_1 \exp\left(\frac{-t}{\tau_1}\right) + A_2 \exp\left(\frac{t_{\rm max} - t}{\tau_2}\right), \tag{3.4}$$

where A_1 and A_2 are the normalization of the first and second infall, τ_1 and τ_2 are the timescales for mass accretion in the first and second infall episodes, and $t_{\rm max}$ is the time of maximum contribution of the second gas accretion episode which is assumed to be zero for the first episode. For all GCE setups, $\tau_1 = 0.68$ Gyr, $\tau_2 = 7.0$ Gyr and $t_{\rm max} = 1.0$ Gyr. The outflow rate is proportional to the SFR,

$$\dot{M}_{\rm outflow}\,(t) = \eta \dot{M}_\star(t), \tag{3.5}$$

where the the mass-loading factor, η, determines the magnitude of the outflow.

3.2.2 Stellar AGB yields

Low- and intermediate-mass stars ($\sim 0.8-8$ M$_\odot$) will evolve along the AGB stage of evolution after core H- and He-burning. Once the star has finished core H-burning, the core will contract and the star will begin burning H in a shell surrounding the He core - the outer layers of the star expand and it begins its climb up the red giant branch (RGB). During this phase, convective

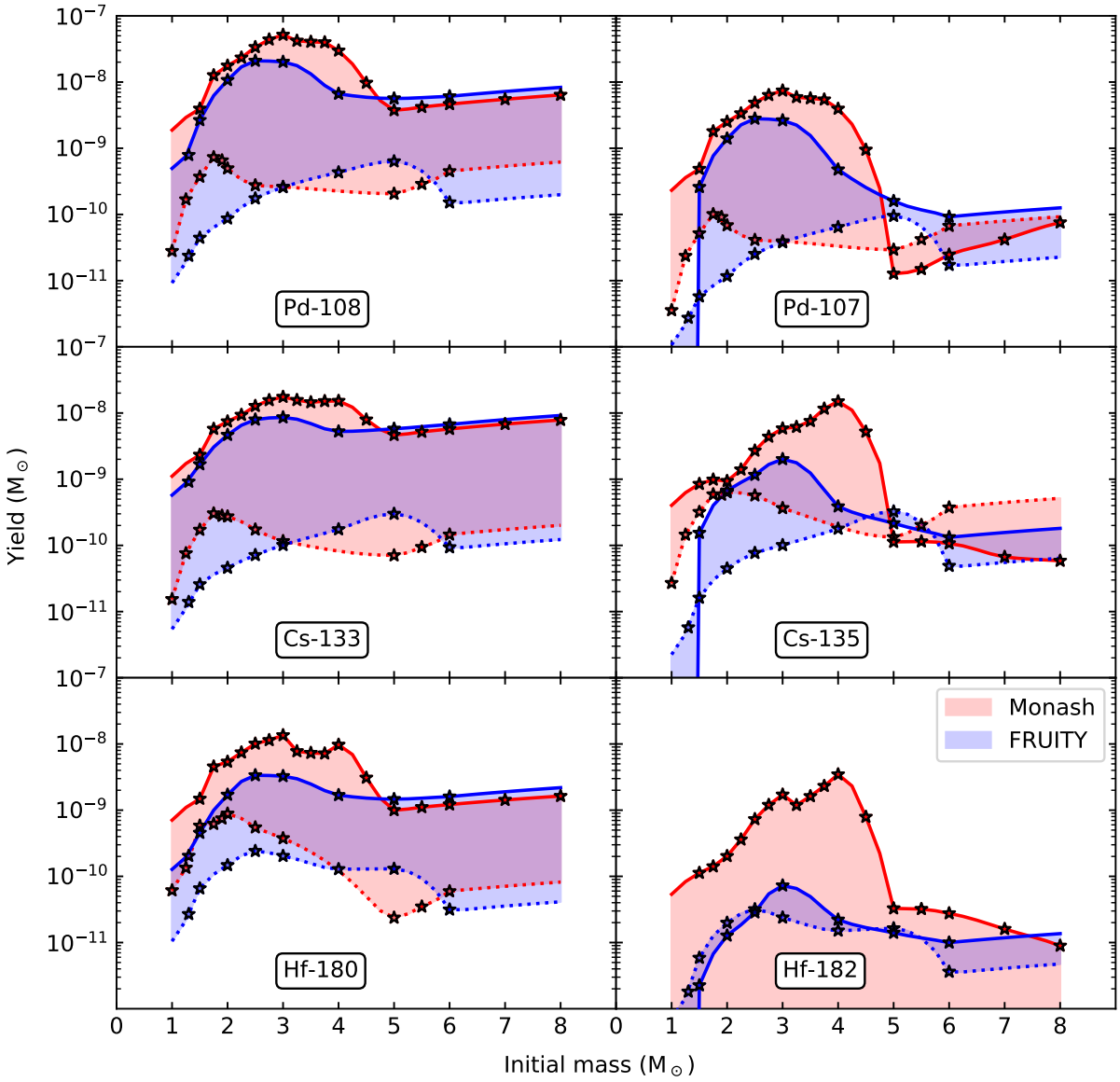

Figure 3.1: Predicted isotopic yields from the Monash (red) and FRUITY (blue) AGB stellar nucleosynthesis models. The yields from models of two metallicities (0.0001 and 0.014) are plotted as lines and star symbols as a function of initial stellar mass for the radioactive isotopes ^{107}Pd, ^{135}Cs, and ^{182}Hf, as well as their respective stable reference isotope. The shaded regions indicate the range of yields ejected by models with $0.0001 < Z < 0.014$. Yields with an initial mass marked by a star symbol are taken directly from a model, while the lines are obtained by their interpolation.

instabilities in the envelope trigger mixing processes that bring the products of partial H shell burning to the surface (first dredge-up), resulting in surface enhancements of N. Core He ignition marks the end of the RGB phase which, upon termination, leaves behind a CO core supported by electron degeneracy pressure. Surrounding the degenerate core, H- and He-burning continue in shells with a thin He-rich intershell region betwixt. Initially, the He-burning shell provides most of the energy generation for the star and it propagates outward in mass. Erstwhile, the convective envelope can move inward causing a second dredge-up event in LIMS stars more massive than $\sim 4M_{\odot}$, this time bringing to the surface products of complete H-burning.

Structurally, AGB stars are characterized by a degenerate C/O core surrounded by an inner He-burning shell, which is separated from an outer H-burning shell by a He-rich intershell region. The outermost layer of the star is an extended H-rich convective envelope which experiences mass loss via stellar winds. In the advanced stage of AGB evolution, the star undergoes recurrent He-burning flashes (or thermal pulses, TPs), at the base of the intershell (Herwig, 2005; Karakas & Lattanzio, 2014). Each TP releases a large amount of energy for a short period of time, which drives a convective region over the whole intershell. As the star expands, the temperature in the H-burning shell falls below that required to sustain nuclear fusion, and H burning switches off. Once the TP is extinguished, and before H burning starts again, the outer base of the convective envelope can reach down deeper into the star. The ashes of He burning can then be mixed into the envelope and brought to the surface, a process called third dredge-up (TDU). It is during this thermally-pulsing AGB phase that the two neutron source reactions, $^{13}\mathrm{C}(\alpha, n)^{16}\mathrm{O}$ and $^{22}\mathrm{Ne}(\alpha, n)^{25}\mathrm{Mg}$, are activated.

The $^{13}\mathrm{C}(\alpha, n)^{16}\mathrm{O}$ reaction dominates the production of the *s*-process isotopes in low-mass AGB stars and is activated during the periods of quiescent H-burning between each TP. Although the neutron densities rarely exceed $10^{7}\mathrm{cm}^{-3}$, the long timescales during the interpulse periods ($\sim 10^{4}$ years) means that the overall neutron exposure (essentially the neutron density integrated over time) is high. In order for enough neutrons to be released via the $^{12}\mathrm{C}(p, \gamma)^{13}\mathrm{N}(\beta^{+})^{13}\mathrm{C}$ reaction chain, at the deepest extent of the TDU a partial mixing zone (PMZ) forms where protons are mixed into the intershell from the convective envelope. This results in the formation of a thin ^{13}C-rich region at the top of the intershell, called the ^{13}C

"pocket". The formation of the PMZ is a long standing uncertainty in AGB nucleosynthesis models and a common consensus regarding its implementation in 1D stellar evolution models has yet to be reached (see Wagstaff et al., 2020, for further discussion). Proposed mixing mechanisms include, but are not limited to, diffusive mixing (Herwig et al., 1997; Cristallo et al., 2009), internal gravity waves (Denissenkov & Tout, 2003), convective boundary mixing (Battino et al., 2016), and magneto driven hydrodynamics (Trippella et al., 2016; Busso et al., 2021). Nevertheless, Buntain et al. (2017) demonstrated that the nature of the mixing function that creates the pocket in 1-D stellar models, once the size of the PMZ is defined, is generally a smaller source of uncertainty on the *s*-process nucleosynthesis than other uncertainties in stellar physics, like the treatment of convective boundaries.

During a TP, the ^{14}N in the H ashes is entirely consumed to make ^{22}Ne by the reaction chain $^{14}\mathrm{N}(\alpha,\gamma)^{18}\mathrm{F}(\beta,\nu)^{18}\mathrm{O}(\alpha,\gamma)^{22}\mathrm{Ne}$. In AGB stars with an initial mass $\gtrsim$ 3 $\mathrm{M}_\odot$ the temperatures are high enough during a TP to activate the $^{22}\mathrm{Ne}(\alpha,n)^{25}\mathrm{Mg}$ neutron source reaction. The resulting *s*-process takes place over a much shorter timescale ($\approx$ 10 years), but with higher neutron densities (up to $\sim 10^{11}\mathrm{cm}^{-3}$) than from the $^{13}\mathrm{C}(\alpha,n)^{16}\mathrm{O}$ neutron source. Overall, the time integrated neutron flux is lower from this secondary neutron burst, which prevents the production of *s*-nuclei beyond the Sr-peak[3]. However, the $^{22}\mathrm{Ne}(\alpha,n)^{25}\mathrm{Mg}$ plays a crucial role in the activation of branching points at unstable nuclei along the *s*-process path (Bisterzo et al., 2015). Branching point nuclei are so called because their rate of β-decay is comparable to the rate of neutron capture, thus the *s*-process can *branch* in two different ways. Of relevance here, are the branching points at ^{134}Cs ($T_{1/2}$ = 2.1 years) and ^{181}Hf ($T_{1/2}$ = 42.3 days), which lead to the production of ^{135}Cs and ^{182}Hf, respectively. The production of ^{135}Cs and ^{182}Hf therefore require the activation of both neutron sources: first, the $^{13}\mathrm{C}(\alpha,n)^{16}\mathrm{O}$ reaction is needed to produce the stable isotopes ^{133}Cs and ^{180}Hf, then the $^{22}\mathrm{Ne}(\alpha,n)^{25}\mathrm{Mg}$ reaction is needed to activate the ^{134}Cs and ^{181}Hf branching points. This condition is only met in AGB stars with initial mass $\sim 3-4$ $\mathrm{M}_\odot$, in which both neutron sources are activated relatively efficiently. AGB stars of lower masses do not activate the ^{22}Ne neutron source, while at higher masses the mixing leading to the formation of the ^{13}C pocket is inhibited by

[3]The solar *s*-process abundance distribution has three abundance peaks, which arise due to lower neutron capture cross-sections at the neutron magic numbers N = 50, 82, 126.

the pressure and density distribution in the very thin intershell (Cristallo et al., 2011), and the hot temperature at the base of the convective envelope at the time of the TDU (Goriely & Siess, 2004).

We model the GCE of the *s*-process SLRs using two sets of AGB nucleosynthesis yields: (1) Monash (Karakas et al., 2012; Fishlock et al., 2014; Karakas & Lugaro, 2016; Karakas et al., 2018) and (2) FRUITY (Cristallo et al., 2008, 2009, 2011, 2015a). We also considered yields from the NuGrid (Pignatari et al., 2016; Ritter et al., 2018b; Battino et al., 2019, 2021) and the S-process NUcleosynthesis Post-Processing code for ATon (`SNUPPAT`; Yagüe López et al., 2021a, accepted) set of AGB models. However, the range of masses and metallicities are more limited for these data sets, and as such the results are within the variations for Monash and FRUITY GCE setups. We therefore do not use these yields in our analysis.

Monash use a two-stage approach to solve for the nucleosynthesis yields, in order to reduce the computational cost. First, the stellar structure evolution is calculated with a limited reaction network, containing only the necessary reactions and isotopes so as to reasonably account for the energy generation in the star (Pignatari et al., 2016; Karakas & Lugaro, 2016). Second, the resulting temperature and density trajectory is post-processed with a reaction network containing many thousands of isotopes and reaction rates, in order to fully account for the full *s*-process flow up to Pb. The stellar structure is mapped out using a grid of zones, which describe the stellar interior by means of a series of concentric spherical shells so as to capture physical processes such as TDU and convection during the TP-AGB phase of evolution. In contrast, in the FRUITY models the above two stages are combined into one – the equations describing the complete nuclear network and physical processes are solved simultaneously, which is more realistic and makes the need for a post-processing stage redundant, however, the computational time is drastically increased.

For Monash, we included the mass- and metallicity-dependent yields for 82 stellar nucleosynthesis models, covering a mass range of 1.0 $M_\odot \leq M \leq 8$ $M_\odot$ for metallicities $0.0001 \leq Z \leq 0.03$. In these models the PMZ mixing profile is artificially inserted as an exponential profile and the mass of the ^{13}C pocket can be varied (for more details see Buntain et al., 2017). Where several models with a different size of the PMZ are available with the same initial mass and metallicity, we selected the model using the "standard" PMZ size as

defined in Karakas & Lugaro (2016).

For FRUITY, we included the yields from 82 stellar nucleosynthesis models, for masses and metallicities in the ranges 1.0 $M_\odot \leq M \leq 6\ M_\odot$ and $0.0001 \leq Z \leq 0.02$, respectively. To populate the FRUITY yield table for stars between 6 and 8 $M_\odot$ we use the same abundance pattern as for the highest mass model available (usually 6 $M_\odot$) at the desired metallicity. However, the total ejected mass for a star with initial mass between 6 and 8 $M_\odot$ is found by linearly extrapolating the ejected mass as a function of initial mass for all stellar models with the same initial metallicity. We only use the non-rotating models, as the effect of rotation is likely overestimated (Cseh et al., 2018; den Hartogh et al., 2019). For stars $M_\star > 12$ $M_\odot$, we used the yields from the NuGrid massive star models (Ritter et al., 2018b). To obtain the yields for stars $8 > M_\star > 12$ we apply the same technique used for estimating the $6 - 8$ $M_\odot$ FRUITY yields, but we instead use the yields of the 12 $M_\odot$ and re-scale them according to a linear fit of the total ejected mass as a function of stellar mass for the NuGrid massive star models. Massive stars eject large amounts of the $A < 90$ s-elements into the ISM following the activation of the ^{22}Ne$(\alpha, n)^{25}$Mg neutron source during He- and C-burning (see e.g., Pignatari et al., 2010, and references therein). However, they produce only very small amounts of the SLRs of interest here.

Prior to the ascent along the AGB branch, stars will lose some amount of their mass, particularly during the red giant branch (RGB) phase. For FRUITY, mass is lost at a rate given by the Reimers (1975) parameterization ($\eta = 0.4$), whereas Monash experience no mass loss during the RGB[4]. This difference of approach has little impact on the final yields for the higher mass models in the Monash and FRUITY yield sets, because the RGB lifetime is short enough that the star will not be able to lose an appreciable amount of its mass before TDU (Karakas et al., 2022). However, there is an appreciable mass-loss in the lowest mass models at higher metallicities for FRUITY, with the $1.3M_\odot$, $Z = 0.15$ model losing $> 15\%$ of its mass prior to the start of the AGB phase due to the longer central He burning lifetime. The mass-loss rate during the AGB phase is not well constrained, however, its parameterization is crucial for determining the length of time spent on the AGB. In Monash, two mass-loss

[4]The most recent models using the Monash code (Karakas et al., 2022) do in fact include mass-loss on the RGB for $M < 3M_\odot$, however, these yields are not used in this work.

laws are used depending on the initial mass of the star: for $M \geq 4M_{\odot}$ the prescription from Bloecker (1995) with $\eta = 0.02$ is used (see also Ventura et al., 2013), otherwise the mass-loss law from Vassiliadis & Wood (1993) is used. In Karakas et al. (2022), it is found that at high metallicities adopting the Bloecker (1995) mass-loss law rather than Vassiliadis & Wood (1993) leads to longer TP-AGB lifetimes and thus increased s-process yields. At lower metallicities, the reverse is true (Karakas, 2014). The mass-loss rate derived by Vassiliadis & Wood (1993) is a function of the pulsation period, and this formalism is adopted across the complete stellar grid by FRUITY with minor revisions to the mass-loss-period relation.

The mass-loss rate is also determined by the C/O ratio at the stellar surface due to changes in the effective temperature (Marigo, 2002). As more C is mixed to the surface of the star, the C/O ratio that is initially < 1 can become greater than unity. As the composition in the outer layers of the star becomes more C-rich, the opacity increase as more C-bearing molecules are formed. Consequently, the outer layers of the star expand and cool, and the mass-loss rate increases. In FRUITY, two opacity regimes are used depending on whether the composition of the star is scaled to the solar isotopic distribution, or whether there is an overabundance of α-isotopes relative to solar. Instead, Monash have a high- and a low-temperature opacity regime, with the low-temperature regime taking into account two different opacity prescriptions on a molecule-by-molecule basis. The implementation of this last is thought to be responsible for the large number of TPs seen in the $Z = 0.007$ models with hot bottom burning (Karakas et al., 2018).

The nucleosynthetic yields from AGB stars are very sensitive to the adopted mixing regime (Herwig, 2005). Both FRUITY and Monash adopt the mixing-length theory of convection (Böhm-Vitense, 1958), with a mixing-length free parameter set to $\alpha = 2.15$ and $\alpha = 1.86$, respectively. In general, models with a larger mixing-length parameter lead to a deeper penetration into the star by the convective envelope during third-dredge up (Boothroyd & Sackmann, 1988). During third-dredge up, a steep opacity gradient between the envelope and the H-free core materialises as the high opacity H-rich envelope penetrates the low opacity He-rich intershell, which in turn causes a large jump in the radiative gradient (Straniero et al., 2006). The treatment of convective boundary mixing is a large uncertainty in AGB models. In FRUITY, the convective instability is modeled by way of evaluating the average convective

velocity, which decreases exponentially with distance from the convective boundary due to the steep pressure gradient and causes a small ^{13}C pocket to form. In contrast, in Monash the position of the convective boundary is determined using an iterative process to solve numerically for the mixing at the radiative/convective interface until a stable location is found. The ^{13}C pocket is then formed by artificially mixing protons into the intershell at this boundary following an exponential function (Karakas et al., 2018). The ^{13}C pocket is included in all Monash models with $M \leq 4.5 M_{\odot}$ that experience third dredge-up, however, some FRUITY models beyond this mass do form a ^{13}C pocket, although the overall neutron exposure is negligible since the efficiency of the TDU is low.

Furthermore, the nuclear physics is different between the two yield sets, most notably for the SLRs of interest in this work is the choice of the reaction rate for the ^{181}Hf β-decay. FRUITY uses the FU11-Network (FUN) stellar evolution code (Straniero et al., 2006), for which β-decay rates are taken from Takahashi & Yokoi (1987), Monash instead adopts the β-decay rate from Lugaro et al. (2014) based on the experimental data of Bondarenko et al. (2002). The former includes a 68 keV excited level in ^{181}Hf, which significantly reduces the half-life in stellar interiors. The existence of this level was based on the wrong assignment of an observed band head in (d,p) by Rickey & Sheline (1968). This was superseded by Bondarenko et al. (2002), who found no evidence of such a state[5]. The absence of this state essentially removed the temperature dependence of the half-life. Using this updated reaction rate results in a significantly increased production of ^{182}Hf in AGB nucleosynthesis models (Lugaro et al., 2014).

Figure 3.1 shows the mass- and metallicity-dependent yields of Monash and FRUITY for the SLRs ^{107}Pd, ^{135}Cs, and ^{182}Hf, and their respective stable reference isotopes, ^{108}Pd, ^{133}Cs, and ^{180}Hf. The stellar yields represent the total mass of a given isotope ejected over the complete lifetime of the star. The stellar yields for two metallicities (0.0001 and 0.014) are plotted with lines and star symbols because they represent the extreme values for the initial compositions for which both Monash and FRUITY have yields available; the shaded regions indicate the range of yields ejected by the respective set of models between these two metallicities. We note that Monash has calculated yields for models with initial

[5]See also the latest two releases of the Nuclear Data Sheets for A=181 (Firestone, 1991; Wu, 2005).

metallicity 0.03 which are not shown in Figure 3.1, however, in our GCE framework stars with $Z > Z_{\odot} = 0.014$ (Asplund et al., 2009) are only born after $t_{\odot}$, so they do not contribute to the ESS SLR abundances. This is in contrast with observations of the solar neighbourhood age-metallicity distribution, which shows that stars older than the Sun with $Z > Z_{\odot}$ do exist, up to [Fe/H] $\sim$ +0.5. Therefore AGB stars with these metallicities may in fact have contributed to the SLR budget in the ESS and we will discuss this possibility in Section 3.3.4.

As previously mentioned, the ^{181}Hf decay rate is different in Monash and in FRUITY: the longer half-life of ^{181}Hf in the Monash models means it is more likely for ^{181}Hf to capture a neutron before decaying than in the FRUITY models. This is why there is a higher production of ^{182}Hf at Z= 0.014 in the Monash models, up to two orders of magnitude higher than FRUITY at $M \sim 4$ M$_{\odot}$. We note that the lowest metallicity Monash models do not include any ^{182}Hf[6], which is why there is no lower limit on the yields in this case. This has little impact on the final abundance of the isotope in the ESS because in our GCE framework low-metallicity stars are only born in the early Galaxy and subsequently all of the ^{182}Hf they may produce will have decayed by $t_{\odot}$.

A comparison of the yields from the 3 M$_{\odot}$, $Z = 0.014$ Monash and FRUITY models for the SLRs of interest and their respective reference isotopes is shown in Table 3.1. For sake of comparison, a 3 M$_{\odot}$ model is chosen since it represents the typical mass at which both the ^{13}C$(\alpha, n)^{16}$O and the ^{22}Ne$(\alpha, n)^{25}$Mg neutron source reactions are activated.

Comparing the absolute yields in Table 3.1, we can see that the Monash yields are higher for all the isotopes. In the case of the ^{107}Pd/^{108}Pd ratio, the models show good agreement. This is because the ^{107}Pd/^{108}Pd ratio is mostly determined by the inverse ratio of the neutron-capture cross sections of the two isotopes, since there are no branching points involved and the isotopes are far from neutron magic numbers. The *s*-process flux between the two Pd isotopes reaches the equilibrium defined by $N\sigma \simeq constant$, where N is the abundance and σ the neutron-capture cross section. The ^{135}Cs/^{133}Cs ratio is higher in Monash by about 50%. This difference is probably due to different nuclear input physics, as the decay rate of ^{134}Cs is constant in the Monash models but has a temperature dependency in the FRUITY models.

[6]The $Z = 0.0001$ models were published prior to the Lugaro et al. (2014) paper, and ^{181}Hf was not included in the network.

Table 3.1: Comparison between the yields (in notation where, e.g., 7.43e-09 represents 7.43×10^{-09}) from a 3 $M_{\odot}$, Z = 0.014 AGB model of Monash and FRUITY for ^{107}Pd, ^{135}Cs, and ^{182}Hf as well as their respective stable reference isotopes.

Isotope	Monash	FRUITY
^{107}Pd	7.43e-09	2.64e-09
^{108}Pd	5.17e-08	2.02e-08
^{133}Cs	1.75e-08	8.58e-09
^{135}Cs	5.83e-09	2.01e-09
^{180}Hf	1.35e-08	3.27e-09
^{182}Hf	1.71e-09	7.27e-11
Ratio		
^{107}Pd/^{108}Pd	1.44e-01	1.31e-01
^{135}Cs/^{133}Cs	3.33e-01	2.34e-01
^{182}Hf/^{180}Hf	1.27e-01	2.32e-02

The ^{182}Hf/^{180}Hf ratio instead is more than one order of magnitude lower in the FRUITY models than in Monash. This is due to the different ^{181}Hf β-decay rate used in the models.

3.2.3 GCE calibration

The calibration of our GCE simulation is performed as in Paper I. Using observations of the Galactic disk (Kubryk et al., 2015), three GCE setups are considered for each set of stellar yields to reproduce a high, low, and best fit value for the radioactive-to-stable abundance ratios in the ISM at $t_{\odot}$. For both sets of yields, these GCE setups represent three distinct simulations of the Milky Way's disk, each with their own chemical evolution history. Each model is paramaterized using current observations and their associated uncertainties of the SFR, gas inflow rate, supernovae rate, and total mass of gas in the Galaxy. All models reach solar metallicity (Z = 0.014) at the time of the birth of the Sun. We do not look at individual elements and isotopes to calibrate our GCE setups as it is beyond the scope of the paper to explore isotopes other than s-only, since these have contributions from several astrophysical sources for which we would need to explore different yields options. In any case, we note that

Table 3.2: Adopted values of parameters in our GCE framework for our low, best, and high fit models.

Quantity	Low	Best	High
A_1 [$M_\odot$ yr^{-1}]	91	46	0.5
A_2 [$M_\odot$ yr^{-1}]	2.9	5.4	10.0
$f_\star$ [$10^{-10}yr^{-1}$]	1.8	2.6	6.5
η	0.45	0.50	0.45

a similar `OMEGA+` GCE setup to those in this paper is used by Jones et al. (2019c) wherein they find good agreement with the solar abundances for several isotopes from Si to Nb. As can be seen in Figure 3.2, the low, best, and high reference models can reproduce well the general trends of APOGEE thin-disk stars in the [α/M] versus [M/H] diagram. However, the GCE tracks for yields that use NuGrid massive star models tend to underproduce [α/Fe] relative to observations and other massive star yield sets (see, e.g., [O/Fe] versus [Fe/H] in Figure 2.6), such that the high-α sequence is better reproduced by the C15+LC18 model from Section 2.4. The adopted values of A_1 and A_2; the star formation efficiency, $f_\star$; and the mass loading parameter, η, for each setup are shown in Table 3.2 (see Section 3.2.1 for a discussion of these parameters). Below, we give a brief summary of the reasoning behind our choice of the values for each parameter though we refer to Paper I for a more detailed explanation.

To increase the amount of stable isotopes in the ISM at $t_\odot$, and therefore obtain the low value of the radioactive-to-stable ratio, the first infall normalization parameter (A_1) is increased, whereas the second infall normalization parameter (A_2) is decreased. This increases the magnitude of the first gas infall episode and decreases the magnitude of the second, so that we reach the upper limit for the observed stellar mass in the Galaxy, whilst also reaching the lower limit for the observed inflow rate. By increasing the star formation process at earlier times, more stable isotopes are produced by $t_\odot$, however, the SLR abundances at $t_\odot$ remain mostly unchanged as they are more sensitive to the SFR rather than the total integrated star formation history (Côté et al., 2019b). For this reason, the high radioactive-to-stable GCE setup has a small A_1 and large A_2. Increasing the star formation efficiency means that more stable isotopes are locked inside stars, thus decreasing the gas-to-star ratio. Therefore, the

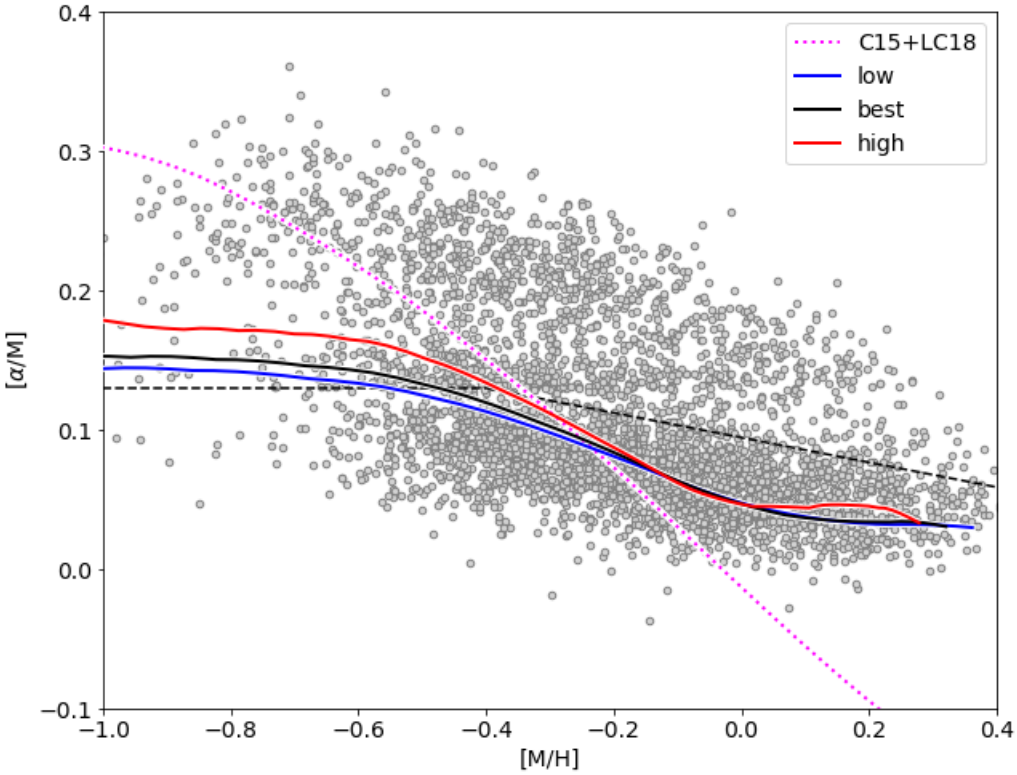

Figure 3.2: [α/M] versus [M/H] for the low, best, and high fit GCE models compared to APOGEE data included as part of the Sloan Digital Sky Survey's 12th data release. For comparison, the C15+LC18 model from Section 2.4 is also included. The data is selected according to the Gold sample criterion using the following constraints (i) $4000 < T_{\rm eff} < 5000$, (ii) S/N > 70, (iii) $0.5 \text{ dex} < \log g < 3.8$ dex, (iv) $\sigma(v_{\rm los}) \leq 1$ km s^{-1}, and (v) $\chi^2_{\rm ASCAP} < 10$ (we refer the reader to Anders et al. 2014 for a definition of these parameters). As in Figure 1.5, the dashed line delineates the high- and low-α sequences.

Table 3.3: Estimated percentage of ^{108}Pd, ^{133}Cs, and ^{180}Hf from the *s*- and *r*-process in the ISM at $t_\odot$. The roman and the italics numbers are calculated using Monash and FRUITY yields, respectively. The *s*-process contribution from AGB (main) and massive stars (weak) is shown separately.

Isotope	GCE	*s*-process		*r*-process
		main	weak	
^{108}Pd[7]	High	59, *90*	1	40, *09*
	Best	44, *60*	1	55, *39*
	Low	36, *46*	1	63, *53*
^{133}Cs	High	20, *37*	1	79, *62*
	Best	16, *25*	1	83, *74*
	Low	14, *21*	~ 0	86, *79*
^{180}Hf	High	84, *84*	1	15, *15*
	Best	85, *83*	1	14, *16*
	Low	88, *83*	~ 0	12, *17*

higher the star formation efficiency the higher the radioactive-to-stable abundance ratio at $t_\odot$. The value of η, which determines the magnitude of the Galactic outflows, is chosen to remove enough metals from the Galaxy in order to recover solar metallicity at $t_\odot$.

To see how well the GCE setups reproduce the solar *s*-isotopic distribution at $t_\odot$, in the top panels of Figure 3.3 we show the isotopic distribution in the ISM at $t_\odot$ of the *s*-only[8] stable nuclei: ^{70}Ge, ^{76}Se, ^{80,82}Kr, ^{86,87}Sr, ^{96}Mo, ^{100}Ru, ^{104}Pd, ^{110}Cd, ^{116}Sn, ^{122,123,124}Te ^{128,130}Xe, ^{134,136}Ba, ^{142}Nd, ^{148,150}Sm, ^{154}Gd, ^{160}Dy, ^{170}Yb, ^{176}Lu, ^{176}Hf, ^{186,187}Os, ^{192}Pt, ^{198}Hg, ^{204}Pb, as well as ^{208}Pb (not *s*-only) and the stable isotopes of interest here that have both an *s*- and *r*-process origin, ^{108}Pd, ^{133}Cs, and ^{180}Hf. All isotopes in Figure 3.3 are plotted relative to their present day solar values (Lodders et al., 2009). In general, the GCE setups using Monash yields overproduce the *s*-isotopes relative to solar, except for $A < 90$ which are mainly produced by massive stars. The GCE setups that use the FRUITY AGB yields produce less *s*-isotopes in the ISM at $t_\odot$ than Monash and thus obtain a better match with solar. Figure

[8]We note that ^{80}Kr and ^{86}Sr in particular may attribute an appreciable fraction of their ISM abundance to the *p*-process (Travaglio et al., 2015)

3.1 confirms that the FRUITY AGB yields for ^{107,108}Pd, ^{133,135}Cs, and ^{180,182}Hf are lower than their Monash counterparts, suggesting that the physical conditions in the Monash models lead to a more efficient *s*-process. Here we are not overly concerned with reproducing the absolute solar abundances for the *s*-isotopes, as we are instead more interested in relative abundance ratios. However, the stable reference isotopes ^{108}Pd, ^{133}Cs, and ^{180}Hf also have an *r*-process contribution in the ISM which we did not include in our GCE framework. This needs to be evaluated and taken into account when calculating the isotopic ratios of Pd, Cs, and Hf. To determine the *r*-process residual, we have to derive what fraction of the respective ESS abundance of the stable reference isotopes has an *s*-process origin once the *s*-only distribution is normalised relative to solar.

To normalise the distribution to the solar values we scale the abundances relative to that of the *s*-only isotope ^{150}Sm. The reason for this is twofold: first, due to the short half-lives of ^{149}Nd ($T_{1/2}$ = 1.73 hours) and ^{149}Pm ($T_{1/2}$ = 53.08 hours), the complete *s*-process flow proceeds through ^{150}Sm, regardless of whether or not the nearby branching points at ^{148}Pm and ^{147}Nd are activated (see e.g. Arlandini et al., 1999; Bisterzo et al., 2015); second, like other rare earth elements, the solar abundance of Sm is measured to a high precision.

We do not consider an *r*-process contribution for ^{107}Pd, ^{135}Cs, and ^{182}Hf, because the last *r*-process event has been inferred to have occurred at least 100 Myr before $t_\odot$ (Lugaro et al., 2014; Tsujimoto et al., 2017; Côté et al., 2021). This means that the SLRs would have significantly decayed in the local ISM from that event by $t_\odot$. Using the GCE setups normalised to ^{150}Sm, the *r*-process residual Y for a stable isotope produced both by the *s*- and *r*-process, is calculated as

$$Y_{\text{residual}} = 1 - (Y_{\text{MS}}/Y_\odot + Y_{\text{AGB}}/Y_\odot), \tag{3.6}$$

where the subscripts MS and AGB denote the ISM contribution in solar masses from massive and AGB stars respectively, and the subscript $\odot$ the solar abundance. The *s*-process yields from massive stars are included in the core-collapse supernovae yields (Ritter et al., 2018a) used as input for the GCE simulations. The yields from each type of stellar source are tracked independently in `OMEGA+`, which means we can see the relative contribution from each source

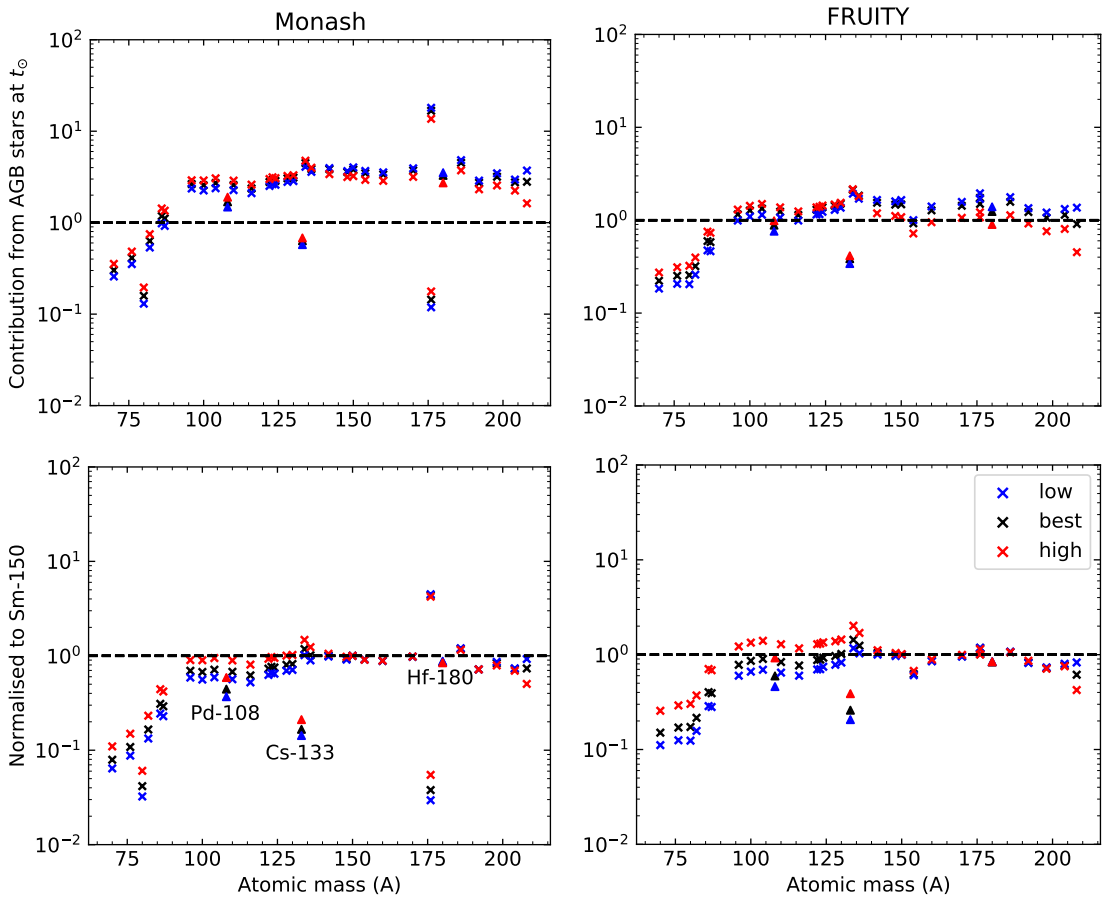

Figure 3.3: GCE production factors due to AGB stars for the stable *s*-only isotopes (marked by crosses) and ^{208}Pb (marked by a circle) in our low (blue), best (black), and high (red) Milky Way models (top panel) using the Monash and FRUITY yields, and then normalised to ^{150}Sm (bottom panel). The stable reference isotopes (^{108}Pd, ^{133}Cs, and ^{180}Hf) are marked by a triangle. Note that in the Monash models, not all the *s*-process branching points are properly implemented, which results in unrealistic predictions for some isotopes (e.g., ^{176}Lu and ^{176}Hf).

to the total mass of an isotope in the ISM. The relative *s*-process contribution from massive and AGB stars for the reference isotopes ^{108}Pd, ^{133}Cs, and ^{180}Hf in each GCE model are shown in Table 3.3.

The *r*-residuals of ^{180}Hf and ^{133}Cs are relatively unchanged for the two AGB data sets, with a 12% – 17% *r*-process contribution in the case of ^{180}Hf, and a 62 – 86% contribution for ^{133}Cs, which are consistent with those obtained by (Prantzos et al., 2020): 19% and 84%, respectively. However, the *r*-residual of ^{108}Pd is significantly affected by changes in the choice of GCE parameters, particular when using the FRUITY AGB yields. This can be explained by considering the fact that since ^{108}Pd is a first peak *s*-isotope, its production at higher metallicities is favoured relative to ^{133}Cs and ^{180}Hf which require a higher neutron-to-seed ratio (i.e., a higher ^{13}C/^{56}Fe ratio). By changing the GCE setup, we change the SFR and the evolution of metallicity in the Milky Way model, which consequently changes the relative weight of each metallicity (in the AGB yields) on the overall Solar System enrichment. In the high GCE setup the gas metallicity evolves the fastest (see Figures 6 and 7 in Paper I), which puts the most weight on high-Z AGB models and consequently the production of the first peak *s*-isotopes. Cristallo et al. (2015b) also observe an increase in the production of light *s*-isotopes, relative to heavier ones, in their GCE models that use an increased SFR.

Furthermore, when determining the *r*-residual of ^{108}Pd we must be also be mindful of the well known problem that, when considering contributions from only the *s*- and *r*-process, the abundances of the elements around the first *s*-process peak (Sr, Y, Zr, close to Pd) are underproduced compared to solar (Travaglio et al., 2004). For this reason, Travaglio et al. (2004) invoke an additional process, the *lighter element primary process* (LEPP), in order to account for the missing fraction of the abundances of these isotopes in the ISM; the existence of a LEPP is still the subject of much debate (see Section 3.4). When using the FRUITY yields Cristallo et al. (2015b) did not find this problem and this result is confirmed by our results (see the best and high GCE setups in the bottom right panel of Figure 3.3). However, a problem we encounter is that the setups that match the first *s*-process peak (i.e., the best and the high FRUITY setups and the high Monash setup) under-produce the third *s*-process peak, i.e. ^{208}Pb, by a factor of two (see also Travaglio et al., 2001).

The low FRUITY GCE setup and the low and best Monash setups instead produce sub-

solar abundances (i.e., below the dashed line in the bottom panel of Figure 3.3) for Sr, Y, Zr, while ^{208}Pb is closer to solar. Therefore, we would still need to invoke an additional contribution of the first *s*-process peak (e.g., a LEPP) in these models. We readdress this problem in Section 3.3.3 using for the first time the isotopic ratio ^{107}Pd/^{182}Hf.

3.3 Results

In this section, we present the evolution of the abundance ratios related to the SLRs of interest, assuming an homogeneous distribution of isotopes in the Galaxy (see Section 3.3.1.) Then, we derive the isolation times from each of these abundance ratios (see Section 3.3.2). We apply the statistical analysis in Papers II and III to calculate the uncertainties on the isolation time, $T_{\rm iso}$, due to the effects of heterogeneities on SLR abundances in the ISM assuming that $\tau/\gamma > 2$ (Regime I). In this Regime, the average length of time between the formation of enrichment progenitor γ is short enough that the SLR does not have time to completely decay in the ISM, so a GCE description is valid. In Section 3.3.3, we look at the predicted ^{107}Pd/^{182}Hf abundance ratio and use it to estimate the amount of ^{107}Pd in our GCE setups with a non *s*- or *r*-process origin. In Section 3.3.4 we consider instead the case where $\tau/\gamma \lesssim 0.3$ and then derive times from the last event and potential constraints on the nucleosynthesis in this last event.

3.3.1 Time evolution of the SLR ratios

In Figure 3.4 the time evolution of three radioactive-to-stable abundance ratios and the ratio of two SLRs, ^{107}Pd/^{182}Hf, are plotted for the high, low, and best fit GCE setups. These ratios take into consideration only the *s*-process contributions in the ISM. The dashed vertical line at 8.4 Gyr indicates $t_\odot$, corresponding to the time when $Z = Z_\odot = 0.014$. Prior to calculating $T_{\rm iso}$ from each ratio, we added the respective *r*-process residual from Table 3.3 to the reference isotope at $t_\odot$[9]. Recall that the GCE setups, represented by the coloured bands in the figure, represent unique solutions for the chemical evolution of the Milky Way. Each solution has its own star formation history and Galactic inflows and outflows, such that the width of each

[9]The residual is not added in Figure 3.4 since it applies only at $t_\odot$ specifically, not at all Galactic times.

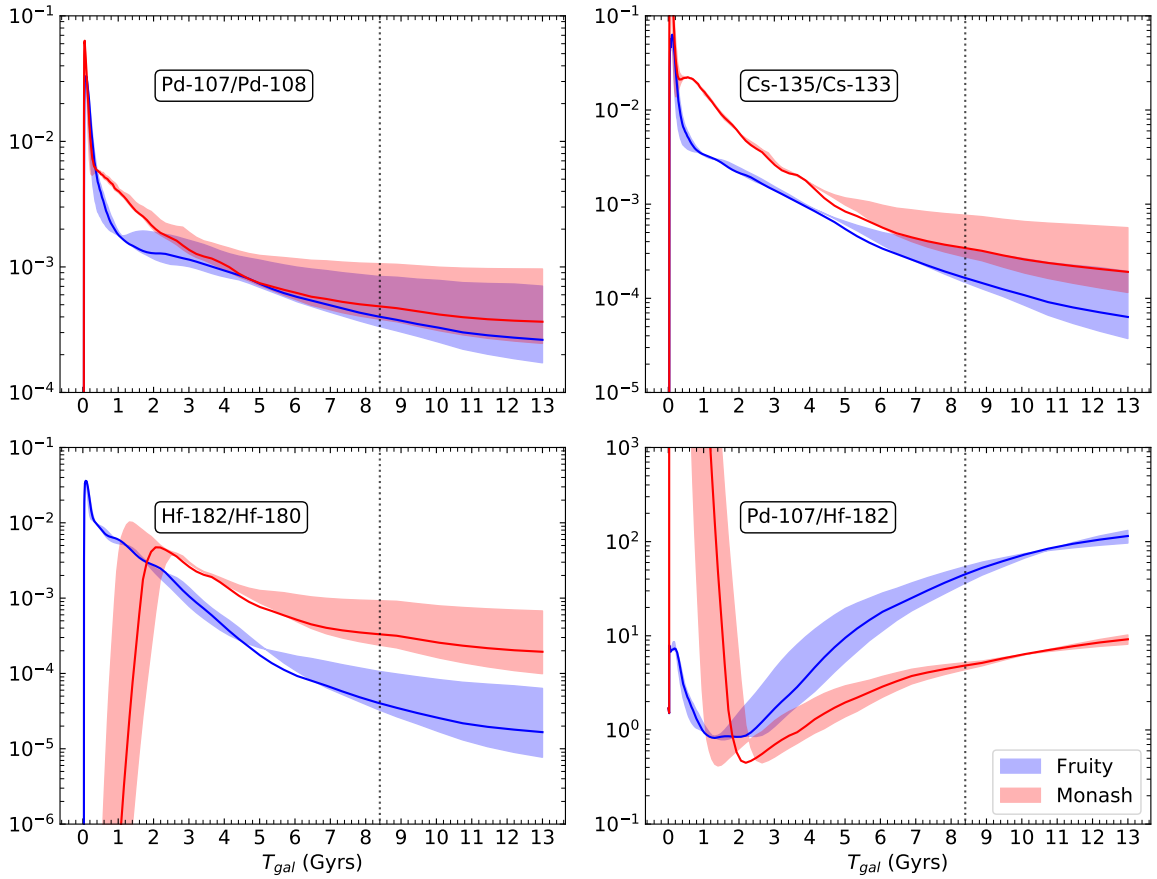

Figure 3.4: Evolution of the ^{107}Pd/^{108}Pd, ^{135}Cs/^{133}Cs, ^{182}Hf/^{180}Hf, and ^{107}Pd/^{182}Hf abundance ratios in the ISM as a function of Galactic time using Monash (red) and FRUITY (blue) ABG stellar yields. For each set of yields, the best (solid line), and high and low (extremities of the shaded region) GCE setups are plotted. The vertical dashed line is at $t_\odot$ = 8.4 Gyr. The ratios do not include the r-process residual for the stable isotope since the residual is calculated only at $t_\odot$.

colour band at $t_\odot$ = 8.4 Gyr represents the associated GCE uncertainties on the radioactive-to-stable abundance ratios in the ESS for each set of yields. However, they do not necessarily represent the upper and lower limits on the ISM ratio at earlier or later Galactic times. Since our low and high GCE setups are calibrated to minimise and maximise the ISM ratio at $t_\odot$, respectively, it would be incorrect, for example, to compare the abundance ratio from the best fit model of FRUITY with the abundance ratio from the low fit model of Monash, as they represent different Galaxies entirely.

The temporal evolution of the ^{107}Pd/^{108}Pd, ^{135}Cs/^{133}Cs, and ^{182}Hf/^{180}Hf ratios in Figure 3.4 are typical for SLRs in the ISM. The abundance ratio peaks at early galactic times, as the gas inflow rate and subsequently also the SFR peak then. When the SFR drops, the SLR

reaches a steady-state abundance in the ISM when its stellar production rate is balanced by its decay rate. The abundance of the stable isotope instead continues to rise and therefore the radioactive-to-stable abundance ratios decrease with time.

The evolution of the ^{107}Pd/^{108}Pd abundance ratio is very similar in the Monash and FRUITY GCE setups. This result reflects the similarity in the mass and metallicity dependent yields for the two Pd isotopes from the two sets of stellar models shown in Figure 3.1. The higher ^{135}Cs/^{133}Cs abundance ratio in the Monash setups is because the Monash stellar models produce more ^{135}Cs than FRUITY at the same initial metallicity (see Figure 3.1). However, this difference between the ^{135}Cs/^{133}Cs abundance ratios of the two data sets is reduced when the *r*-process residual of ^{133}Cs is added (as listed in Table 3.3), because the *r*-process residuals in each of the Monash GCE setups are higher than those for FRUITY.

Regarding the evolution of the ^{182}Hf/^{180}Hf abundance ratio, the production of ^{182}Hf is delayed for Monash with respect to FRUITY because this isotope is not included in the lowest metallicity Monash models. However, this has negligible consequence for the abundance ratio at $t_{\odot}$, since only the ^{182}Hf produced by the most recent events is potentially inherited by the ESS. The Monash abundance ratio at $t_{\odot}$ is almost an order of magnitude higher than FRUITY due to the significantly longer half-life (see Section 3.2.2) used for ^{181}Hf in the Monash models, which leads to a much larger production of ^{182}Hf.

In Figure 3.4 we also show the abundance evolution of ^{107}Pd relative to ^{182}Hf; the former is representative of the first *s*-process peak, whilst the latter of the second peak. Interestingly, although ^{107}Pd has a shorter half-life than ^{182}Hf, the ratio increases with time because ^{107}Pd is produced more than ^{182}Hf by higher metallicity ($Z \sim 0.014$) AGB stars in both sets of models. This result can be directly attributed to the fact that, unlike the iron peak *s*-process seeds (notably ^{56}Fe), ^{13}C is a primary neutron source, since it is produced inside the star starting from the initial H and He (see e.g. Gallino et al., 1998). Therefore, AGB stars with lower initial metallicities have a higher neutron-to-seed ratio (i.e., ^{13}C/^{56}Fe) and, consequently, produce more effectively nuclei beyond the first *s*-peak. Observations of Ba stars, the binary companion of AGB stars, confirm this trend (Cseh et al., 2018). The very high ^{107}Pd/^{182}Hf ratio in the FRUITY setups compared to Monash setups originates again from the higher ^{181}Hf β-decay rate used to calculate these models.

3.3.2 Derivation of the isolation times

For each abundance ratio plotted in Figure 3.4, $T_{\rm iso}$ is the time taken for the predicted ratio at $t_\odot$ to decay to the observed ESS value, assuming the ESS is not exposed to further stellar enrichment events. This is a reasonable assumption as the evolutionary stages of low-mass stars, the main *s*-process sources in the Galaxy, prior to the AGB phase have a long duration ($\sim$ 1 Gyr), however, star-forming regions typically live at most for a few tens of Myr. Therefore these regions would have dissolved by the time a low-mass star reaches the AGB. Also the probability of an AGB star encountering a star-forming region is extremely low (Kastner & Myers, 1994). We reiterate that the values for $T_{\rm iso}$ calculated using the low and high GCE setups represent the associated GCE uncertainty from observational constraints of the Milky Way disc.

Since `OMEGA` assumes a smooth and continuous enrichment process, we must determine the associated error on $T_{\rm iso}$ that arises when we instead consider that stellar additions are discrete in time.

Table 3.4 shows the values of $T_{\rm iso}$ calculated using the ratios from Figure 3.4 along with the error analysis of Paper II. Paper II determined that it is possible to define a statistical distribution for the evolution of an SLR if it falls in the $\tau/\gamma \gtrsim 2$ Regime (henceforth Regime I from Paper II). For an SLR in Regime I, the time between the formation of two progenitors γ is short enough to ensure that its minimum abundance at $t_\odot$ is always greater than zero. In Paper II, the SLR ISM abundance uncertainty was calculated with a Monte Carlo method as a function of γ and τ/γ for three box delay-time-distribution (DTD) functions, each with uniform probability as defined in Paper II. We choose the DTD function with the longest delay time, which applies in the case where the average time interval between the formation of a progenitor and subsequent ejection of material is approximately 5 Gyr. Since the parameter γ is poorly understood, we take the largest value of γ for each SLR, from the six available values in Paper II, whilst still remaining in Regime I (i.e. $\tau/\gamma \gtrsim 2$). This approach gives us the most conservative errors from the Monte Carlo Spread. Following this approach, we adopt a value of $\gamma = 3.16$ for ^{107}Pd and ^{182}Hf from Table 4 of Paper II. ^{135}Cs, instead, has a much lower $\tau = 3.3$, therefore, the maximum value that we can choose is $\gamma = 1$ in order to

Table 3.4: Isolation times $T_{\rm iso}$ calculated from the abundance ratios at $t_\odot$ from Figure 3.4 assuming that they fall into Regime I ($\tau/\gamma \gtrsim 2$). The ISM ratios are taken from Figure 3.4 with an additional r-process residual added to the stable isotopes according to Table 3.3. The uncertainty factors for the isolation times are calculated following the statistical analysis presented in Paper II. We do not calculate $T_{\rm iso}$ using the ^{107}Pd/^{182}Hf ratio, since a fraction of the Pd isotopes in the ESS may have a non s- or r-process origin (see Section 3.3.3), however, Hf does not. All τ, γ, and $T_{\rm iso}$ are given in Myr. The value of τ for ^{107}Pd/^{182}Hf represents the equivalent τ of the two SLRs, where $\tau_{\rm eq} = \tau_1\tau_2/(\tau_1 - \tau_2)$. The uncertainty factors for this ratio are taken from Paper III.

		^{107}Pd/^{108}Pd	^{135}Cs/^{133}Cs	^{182}Hf/^{180}Hf	^{107}Pd/^{182}Hf
ESS Ratio		6.6×10^{-5}	$< 2.8 \times 10^{-6}$ [10]	1.02×10^{-4}	4.25
τ		9.4	3.3	12.8	35.4
γ (adopted)		3.16	1.00	3.16	10.00
τ/γ		2.97	3.30	4.05	3.54
Uncertainty Factors		0.61, 1.39	0.63, 1.45	0.61, 1.39	0.73, 1.17
GCE Model		ISM Ratio			
Low	Monash	1.7×10^{-4}	5.2×10^{-5}	2.2×10^{-4}	4.37
	FRUITY	1.8×10^{-4}	4.0×10^{-5}	–	–
Best	Monash	2.5×10^{-4}	7.9×10^{-5}	3.1×10^{-4}	4.83
	FRUITY	2.7×10^{-4}	5.4×10^{-5}	–	–
High	Monash	7.3×10^{-4}	2.2×10^{-4}	8.6×10^{-4}	5.19
	FRUITY	7.7×10^{-4}	1.5×10^{-4}	–	–
		Isolation Time			
Low	Monash	9^{+3}_{-5}	$> 10^{+1}_{-1}$	10^{+4}_{-6}	–
	FRUITY	9^{+3}_{-5}	$> 9^{+1}_{-1}$	–	–
Best	Monash	13^{+3}_{-5}	$> 11^{+1}_{-1}$	14^{+4}_{-6}	–
	FRUITY	13^{+3}_{-5}	$> 10^{+1}_{-1}$	–	–
High	Monash	23^{+3}_{-5}	$> 14^{+1}_{-1}$	27^{+4}_{-6}	–
	FRUITY	23^{+3}_{-5}	$> 13^{+1}_{-1}$	–	–

fall into Regime I. In principle, γ should be consistent for all three SLRs given that they are ejected by the same stellar enrichment event, however, in this work the choice of γ is only relevant for determining the 68% confidence level.

From Table 3.4, the range of $T_{\rm iso}$ derived with the Monash *(FRUITY)* GCE setups are; low: 9 – 12 *(8–12)* Myr, best: 10 – 16 *(9–16)* Myr, high: 18 – 26 *(18–26)* Myr. In each GCE setup all $T_{\rm iso}$, when available, overlap within 1σ uncertainty, regardless of the adopted yields and isotopic ratios. The values from the FRUITY GCE setups are less well constrained since we cannot use the ^{182}Hf/^{180}Hf ratio in this case. The ^{107}Pd/^{108}Pd ratio in the ISM at $t_\odot$ shows remarkable agreement for Monash and FRUITY in the respective low, best, and high GCE setups. This is due to the fact this ratio depends mostly only on the ratio of the cross sections. Furthermore, the nuclear uncertainties for ^{107}Pd/^{108}Pd are very small. Monte Carlo sampling of a log-normal Gaussian following the methodology of Longland et al. (2010), gives a 1σ and 2σ uncertainty for the branching ratio of 12.4% and 26.8%, respectively; these are insignificant compared to the GCE uncertainties considered in this paper (i.e. for both sets of yields there is more than a factor of 2 difference in $T_{\rm iso}$ derived from the low and high GCE setups).

A conservative estimate for the nuclear uncertainty associated with the ^{182}Hf/^{180}Hf branching point can be estimated by considering the reaction rates that can maximise and minimise this ratio. The maximum ^{182}Hf/^{180}Hf ratio can be obtained by taking the upper limits of the ^{180}Hf(n,γ) and ^{181}Hf(n,γ) reaction rates, and the lower limits of the ^{181}Hf β-decay and ^{182}Hf(n,γ) rates, as this would maximise the ^{182}Hf and minimise the ^{180}Hf yields. Likewise, reversing the limits for the above reaction rates returns the minimum ^{182}Hf/^{180}Hf ratio. We tested the effects of changing the reaction rates to the above mentioned limits using the uncertainties reported by Rauscher et al. (2002) for the n,g rates, and by Lugaro et al. (2014) for the decay rate of ^{181}Hf (mostly coming from the presence of a state at 45 keV) using a Monash 3 M$_\odot$, $Z = 0.014$ AGB model. We found that the ^{182}Hf yield could be a factor of two lower than the presently adopted value. If we consider this most extreme scenario by applying a factor of two reduction to all the ^{182}Hf yields, the ^{182}Hf/^{180}Hf and ^{107}Pd/^{182}Hf ratios in the ISM at $t_\odot$ will be a factor of two lower and a factor of two higher, respectively. Given that $T_{\rm iso} = \tau(\ln r_\odot - \ln r_{\rm ESS})$ - where τ is the mean-life of the SLR, $r_\odot$ is the radioactive-to-stable

abundance ratio in the ISM at $t_{\odot}$, and $r_{\rm ESS}$ is the ESS ratio - then a reduction of factor two of the ^{182}Hf/^{180}Hf ratio in the ISM results in an $T_{\rm iso}$ derived from this ratio that is ≈ 9 Myr shorter than the respective times given in Table 3.4. If this were the case, no value of $T_{\rm iso}$ exists in the low and best Monash GCE setups that is consistent when derived using all three radioactive-to-stable ratios. However, for the high Monash GCE setup, $T_{\rm iso}$ would still be self-consistent in the range 18 – 22 Myr. Therefore, whilst highly unlikely, since a solution exists in the high GCE setup, such an extreme reduction in the ^{182}Hf/^{180}Hf ratio due to nuclear uncertainties is not entirely ruled out by our results. Despite the seemingly large nuclear uncertainty relating to the ^{182}Hf/^{180}Hf branching point, the method we apply above only gives us a maximum or minimum value of the ratio with no probability associated to it. To better understand the uncertainty associated with this branching ratio, it would be necessary to perform a statistical analysis to identify which combination of reaction rates are more or less likely.

3.3.3 The ^{107}Pd/^{182}Hf ratio

The ^{107}Pd/^{182}Hf ratio is interesting as it is indicative of the relative abundance ratio of isotopes prior to and beyond the second *s*-process peak at the neutron magic number $N = 82$. Several previous GCE studies that considered contributions from both *s*- and *r*-process sources appear to underproduce the *s*-process elements with $90 < A < 130$ relative to solar abundances (Travaglio et al., 1999, 2004; Bisterzo et al., 2014, 2017). Therefore, we might not be able to reliably use the ^{107}Pd/^{182}Hf ratio to determine $T_{\rm iso}$ since ^{107}Pd might be underproduced in our GCE framework. On the other hand, the GCE studies by Prantzos et al. (2018, 2020) find that the weak *s*-process in rotating massive stars provides a sufficient contribution to the $90 < A < 130$ *s*-isotopes, such that a LEPP is not needed to reproduce their solar abundances. ^{107}Pd and ^{182}Hf can provide fresh information on this issue because they only sample production in stars of around solar metallicity, as any abundance produced in the early Galaxy in low-metallicity objects would have decayed by the time of the formation of the Sun. We can quantitatively estimate to what extent (if at all) ^{107}Pd is underproduced in our GCE framework at $t_{\odot}$ by determining the ^{107}Pd/^{182}Hf ratio in the ISM at $t_{\odot}$ that is necessary to obtain a $T_{\rm iso}$ consistent with those calculated using the ^{107}Pd/^{108}Pd and ^{182}Hf/^{180}Hf ratios in Section 3.3.2. This method can provide us an independent constraint on the production of the

Table 3.5: Upper and lower limits for the isolation time, $T_{\rm iso}$; the ^{107}Pd/^{182}Hf ratio in the ISM at $t_\odot$ obtained by decaying back the ESS ratio (4.25) by $T_{\rm iso}$, $r_{\rm ISM}$; the ^{107}Pd deficit in the ISM at $t_\odot$, $f_{\rm Pd}$; and the ^{107}Pd/^{182}Hf production ratio, P derived using the results in Table 3.4 (see text for details).

	$T_{\rm iso}$ (Myr)	$r_{\rm ISM}$	$f_{\rm Pd}$	P
Low	4 – 12	4.77 – 6.00	9 – 38%	5.55 – 11.19
Best	8 – 16	5.34 – 6.73	11 – 39%	6.21 – 12.55
High	21 – 26	7.77 – 8.98	50 – 73%	9.04 – 16.75

first s-process peak in the Galaxy at the time of the formation of the Sun. Since we are using the ESS ratio of two SLRs, any “missing" component of ^{107}Pd cannot be from the r-process, as the last r-process event was over 100 Myr before $t_\odot$ (see Section 3.2.3). Furthermore, in order for the ^{107}Pd/^{108}Pd ratio to remain unchanged, any deficit of ^{107}Pd in our GCE setups corresponds to an identical deficit of ^{108}Pd.

We consider only the Monash GCE setups here as the FRUITY AGB models do not produce enough ^{182}Hf. In order to get the ^{107}Pd/^{182}Hf ratio in the ISM at $t_\odot$ that includes contributions from all production channels, henceforth $r_{\rm ISM}$, we decay the ESS ^{107}Pd/^{182}Hf ratio backwards in time (i.e., we reverse the radioactive decay process) by $T_{\rm iso}$. The ESS ^{107}Pd/^{182}Hf ratio inferred from meteoritic analysis is taken here to be 4.25 (Lugaro et al., 2018), and we use upper and lower limits for $T_{\rm iso}$ that are derived using the ^{107}Pd/^{108}Pd and ^{182}Hf/^{180}Hf ratios in Table 3.4. It follows, that for each of the low, best, and high Monash GCE setups the amount of ^{107}Pd missing in the ESS, $f_{\rm Pd}$, is

$$f_{\rm Pd} = \frac{r_{\rm ISM} - r_{\rm GCE}}{r_{\rm GCE}}, \tag{3.7}$$

where the denominator $r_{\rm GCE}$ is the respective ^{107}Pd/^{182}Hf ratio at $t_\odot$ predicted by the GCE framework given in Table 3.4.

Table 3.5 shows the upper and lower limits for $T_{\rm iso}$, the decayed back $r_{\rm ISM}$, and the estimated ^{107}Pd deficit in each of the low, best, and high Monash GCE setups. In the final column, we also calculate the upper and lower limits on the production ratio for ^{107}Pd/^{182}Hf,

$$P = r_{\rm ISM}\frac{\tau_{\rm Hf}}{\tau_{\rm Pd}}, \tag{3.8}$$

where $\tau_{\rm Pd}$ and $\tau_{\rm Hf}$ are the mean-life of ^{107}Pd and ^{182}Hf, respectively.

Assuming that we are in Regime I, that is $\tau/\gamma \gtrsim 2$ (see Section 3.3.2), we can determine the minimum and maximum values of P within a 68% confidence level that are consistent with the upper and lower limits for $r_\odot$. By applying the relevant uncertainty factors from the fifth row of Table 3.4, the maximum and minimum values for P are given by,

$$P_{\rm max} = \frac{r_{\rm ISM,max}}{0.73}\frac{\tau_{\rm Hf}}{\tau_{\rm Pd}}, \tag{3.9}$$

and

$$P_{\rm min} = \frac{r_{\rm ISM,min}}{1.17}\frac{\tau_{\rm Hf}}{\tau_{\rm Pd}}, \tag{3.10}$$

where we have used the subscripts *min* and *max* to denote the upper and lower limits on our range of $r_{\rm ISM}$ values in Table 3.5.

From Table 3.5, we can see that as $T_{\rm iso}$ increases (i.e., going from the low to high GCE setups) the more ^{107}Pd is underproduced relative to the inferred ESS value. Our results for $f_{\rm Pd}$ in the low and best GCE setups are consistent with both Travaglio et al. (2004) and Bisterzo et al. (2014), wherein the former find that the solar abundances of Sr, Y, and Zr show deficits of 8%, 18%, and 18%, respectively and the latter conclude an additional production channel contributes $\sim$ 25% towards the solar abundances of the $90 < A < 130$ s-isotopes. We note however, that the ^{182}Hf yield could be up to a factor of two lower than the presently adopted value due to the nuclear uncertainties associated with the ^{182}Hf/^{180}Hf branching point, which means that the ^{107}Pd/^{182}Hf ratio would increase by a factor of two. If this were indeed the case then the predicted ^{107}Pd/^{182}Hf ratio would be higher than $r_{\rm ISM}$ for all GCE setups. In particular, if we consider the high Monash GCE setup - the only setup for which a self-consistent solution exists for all three radioactive-to-stable ratios assuming that the ^{182}Hf yield is a factor of two lower (see Section 3.3.2) - then the GCE predicted ^{107}Pd/^{182}Hf ratio is $27-50$% higher than $r_{\rm ISM}$. In fact, if the ^{182}Hf yield is 50% lower than the adopted value, then the predicted ^{107}Pd/^{182}Hf ratio at $t_\odot$ is 7.79, which corresponds to a $T_{\rm iso}$ of 21 Myr; this is self-consistent with the range of $T_{\rm iso}$ found in Section 3.3.2 and therefore demonstrates

that the possible deficit of the $90 < A < 130$ s-isotopes depends also on the nuclear physics uncertainties associated with the ^{182}Hf/^{180}Hf branching point.

3.3.4 Derivation of the time from last event

The results reported so far apply to the specific case of Regime I of Paper II, when $\tau/\gamma \gtrsim 2$, where γ is the time interval between the birth of the progenitor of each AGB star that contributed to the composition of the ESS (which is analogous to the average time interval δ between additions from different AGB stars into the same parcel of ISM gas). Given that τ = 9.4 Myr and 12.8 Myr for ^{107}Pd and ^{182}Hf, respectively, Regime I requires that $\gamma \lesssim 5$ Myr. However, we also need to consider the possibility that γ is much larger than this value since we do not know a priori the value of γ for s-process AGB sources.

Referring back to the Regimes discussed in Paper II, in particular, if $\tau/\gamma \lesssim 0.3$ (henceforth Regime III), i.e., in the case of ^{107}Pd and ^{182}Hf if $\gamma \gtrsim 30$ Myr, the ESS abundances of these SLRs are dominated by the last nucleosynthetic enrichment event that added s-process elements to the ESS. In this case we cannot derive a $T_{\rm iso}$ because the length of time between successive enrichment events is long enough that the SLR can completely decay from the ISM. We can calculate instead the time that elapsed between the last event that added these SLRs to the ESS matter and the formation of the first solids in the ESS, $T_{\rm LE}$. As an example, the ^{107}Pd/^{108}Pd abundance ratio following the last event (Wasserburg et al., 2006; Lugaro et al., 2018) is given by (Côté et al., 2021),

$$\frac{^{107}\mathrm{Pd}}{^{108}\mathrm{Pd}} = K \left(\frac{Y_{^{107}\mathrm{Pd}}}{Y_{^{108}\mathrm{Pd}}}\right)\left(\frac{\langle\delta\rangle}{T_{\rm gal}}\right), \tag{3.11}$$

where δ is a free parameter with average time $\gamma \gtrsim 30$ Myr, $T_{\rm gal}$ the age of the Galaxy up to the formation of the Sun (8.4 Gyr), and $Y_{^{107}\mathrm{Pd}}/Y_{^{108}\mathrm{Pd}}$ is the production factor in the AGB last event, where we used the stellar yields from Monash models of metallicity 0.007, 0.01, 0.014, and 0.03 reported in Table 3.6. Finally, K is a free parameter implemented in the analytical GCE solutions of Clayton (1984) to account for different choices of the gas inflow rate, where $1 < K < 3$ is found to provide the best fit to the observational data (Clayton, 1988). It is therefore necessary to include this multiplication factor in the steady-state formula

if primordial gas is assumed to flow into the Galaxy. Following the results in Paper I, we adopt herein a multiplication factor of $K = 2.3$, which is consistent also with the value of $K = 2.7$ recovered by Dauphas et al. (2003).

For the isotopic ratios of interest here, we needed to add to this estimate the r-process component of the stable reference isotopes, ^{108}Pd and ^{180}Hf. Using the component from the Monash models as reported in Table 3.3 results in a decrease of the radioactive-to-stable ratio, and therefore of the corresponding $T_{\rm LE}$ by $5 - 9$ Myr and $1.5 - 2$ Myr, when using ^{107}Pd and ^{182}Hf, respectively. Table 3.6 shows the models for which it is possible to derive self-consistent $T_{\rm LE}$ using ^{107}Pd and ^{182}Hf; Figure 3.5 shows three example cases from Table 3.6 for the metallicity $Z = 0.03$ of the trend of $T_{\rm LE}$ as a function of the free parameter δ. The top panel shows an example case in which a self-consistent $T_{\rm LE}$ can be found within ESS and mean life uncertainties in the region of δ where the blue and orange bands overlap. The middle and bottom panel instead show cases where there is no overlap because the $T_{\rm LE}$ derived from ^{182}Hf is always higher than from ^{107}Pd. Overall, it is possible for models in the mass range between 2 and 3 $M_\odot$ to obtain self-consistent $T_{\rm LE}$. The upper limit of the ESS ^{135}Cs/^{133}Cs ratio reported in Table 3.4 is also generally consistent with the values of $T_{\rm LE}$. For example, for the 3 $M_\odot$, $Z = 0.014$ (high K) model $T_{\rm LE}$ is > 21 Myr, which is consistent with the interval $29 - 41$ Myr derived from the other two SLRs.

When we consider the ^{107}Pd/^{182}Hf ratio, we can find a $T_{\rm LE}$ consistent with the ^{107}Pd/^{108}Pd and ^{107}Pd/^{182}Hf ratios for the 2 $M_\odot$, $Z = 0.01$ model. To match exactly the ^{107}Pd/^{182}Hf production factor given in Column 5 for this model, we find that the time from the last event to formation of the solids in the ESS is 25.5 Myr. This result is particularly interesting since a 2 $M_\odot$ star is the most common type of AGB star with TDU at this metallicity and they are also the most likely candidates for the parent stars of presolar SiC grains (Cristallo et al., 2020). Therefore, this model well represents the last AGB source to have added s-process elements to the ESS. Instead, at $Z = 0.007$, for the 2.1 $M_\odot$ model, the predicted ^{107}Pd/^{182}Hf ratio in Column 5 of Table 3.6 is even lower than the ESS ratio. This is because at this metallicity the production of the elements beyond the second s-process peak (like Hf) is favoured relative to those between the first and second s-process peaks (like Pd). For the higher metallicities, $Z = 0.014$ and $Z = 0.03$, we found the reverse problem: the predicted ^{107}Pd/^{182}Hf ratio needs

more time to decay to its ESS value than allowed by the $T_{\rm LE}$ calculated on the basis of the radioactive-to-stable ratios.

In summary, when comparing the time intervals derived using Regime I or Regime III, we find an overall consistency, as expected from our mathematical framework. In fact, $T_{\rm LE}$ is always longer than $T_{\rm iso}$ because the equation used to calculate the radioactive-to-stable ratio after the last event in Regime III (Equation 3.11) differs from the steady-state equation used to calculate the ratio in Regime I (see Equation 1 in Paper I) in that instead of τ the ratio is proportional to δ. In Regime III by definition δ is larger than τ, therefore, the ratio is higher and the time is longer. Furthermore, the shorter the δ the closer is $T_{\rm LE}$ to $T_{\rm iso}$. The main difference between the two Regimes is that in Regime I we need to invoke an extra source of Pd, while in Regime III we can identify an AGB star of 2 $M_\odot$ and $Z = 0.01$ to have potentially been the last to contribute to the Solar System *s*-process elements.

3.4 Discussion

For the low, best, and high GCE setups, $T_{\rm iso}$ is consistent for the Monash and FRUITY yields in the ranges 9 – 12 Myr, 10 – 16 Myr, and 18 – 26 Myr, respectively. Comparing these values of $T_{\rm iso}$ to those in Paper I (see their Table 2) calculated using ^{107}Pd and ^{182}Hf (^{135}Cs was not considered), we find that the times here are shorter by more than a factor of two. The main reason for this is that we did not include here an *r*-process source for the SLRs, since the last *r*-process event occurred more than 100 Myr before the formation of the Sun (Côté et al., 2021). We only consider the *r*-process component for the stable reference isotopes using the *r*-process residuals. Similarly, in Paper II an *r*-process source for the SLRs was not included, however, constant production ratios (as in Paper I) were used instead of the more realistic stellar nucleosynthesis yields we use in this work. Our isolation times are also shorter than those reported in Paper II (see their Table 4) by roughly 5 Myr in the case of ^{182}Hf, but agree for ^{107}Pd. The discrepancy between these results can be attributed to the fact that the ^{182}Hf/^{180}Hf ratio is extremely sensitive to the stellar mass and metallicity, unlike ^{107}Pd/^{108}Pd which mostly depends on the neutron-capture cross section ratio.

In Section 3.3.3, we found that an extra contribution to ^{107}Pd is needed to recover a $T_{\rm iso}$

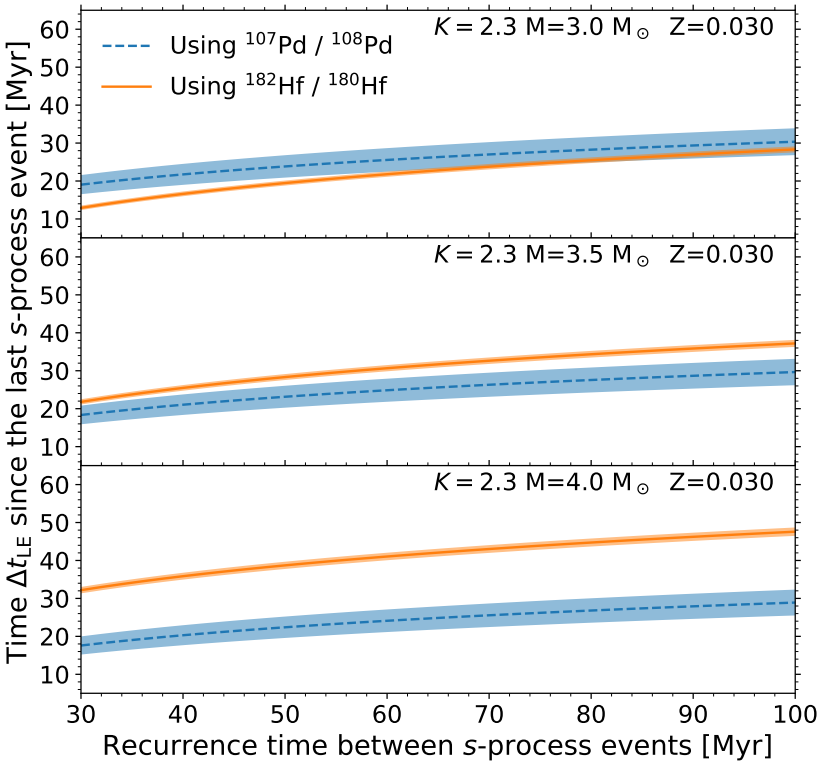

Figure 3.5: Time elapsed from the last AGB *s*-process event to the formation of the first solids in the ESS as a function of the free parameter δ, the recurrent time interval between *s*-process contributing events. Three stellar AGB models 3, 3.5, and 4 $M_\odot$, at $Z = 0.03$ are selected as examples, using the best GCE ($K = 2.3$). The error bars include the uncertainties on the ESS values and on the mean lives of the two isotopes. For the 3 $M_\odot$ model it is possible to derive several self-consistent solutions, where the blue and the orange bands overlap, depending on the value of the recurrence time (δ) on the x-axis.

Table 3.6: Production factors of AGB Monash models of metallicities representative of the metallicity of stars that were present in the solar neighbourhood 4.6 Gyr ago (Casagrande et al., 2011; Nissen et al., 2020). For four of the eleven models of mass between 2 and 3 $M_\odot$ it is possible to derive a range of self-consistent values of T_{LE}, reported in Column 6, with the corresponding Galaxy model (i.e. value of K) indicated in brackets. Column 6 reports the $^{107}Pd/^{182}Hf$ ratio predicted by decaying back the ESS value of 4.25 by the corresponding T_{LE} range, to be compared to the same ratio as derived directly from the models.

Z	M($M_\odot$)	$^{107}Pd/^{108}Pd$	$^{182}Hf/^{180}Hf$	$^{107}Pd/^{182}Hf$	T_{LE} (Myr)	$(^{107}Pd/^{182}Hf)_{decay}$
0.007	2.1	0.14	0.07	3.01	15 - 22 (low)	6.49 - 7.91
					19 - 30 (best)	7.27 - 9.92
					31 - 46 (high)	10.20 - 15.60
	2.5	0.14	0.11	2.45	no solution	
	3	0.13	0.23	1.21	no solution	
0.01	2	0.14	0.05	8.73	12 - 26 (low)	5.96 - 8.85
					17 - 31 (best)	6.87 - 10.20
					26 - 42 (high)	8.86 - 13.90
	3	0.14	0.14	5.61	no solution	
0.014	2	0.14	0.03	26.9	36 (high)	11.7
	3	0.14	0.12	7.62	no solution	
	4	0.13	0.34	2.09	no solution	
0.03	3	0.14	0.04	27.4	17 - 25 (low)	6.87 - 8.61
					22 - 29 (best)	7.91 - 9.64
					29 - 41 (high)	9.64 - 13.5
	3.5	0.13	0.08	18.4	no solution	
	4	0.12	0.18	8.45	no solution	

from the ^{107}Pd/^{182}Hf ratio that is consistent with the values obtained using the ^{107}Pd and ^{182}Hf radioactive-to-stable abundance ratios. Alternatively, the ^{107}Pd/^{182}Hf ratio in the ISM at $t_{\odot}$ could be increased by reducing the production of ^{182}Hf via a less efficient activation of the ^{181}Hf branching point. However, this second solution would remove the current agreement on the $T_{\rm iso}$ derived using the ^{107}Pd/^{108}Pd and ^{182}Hf/^{180}Hf ratios with the Monash models. Therefore, we need to invoke an extra source for the production of the first *s*-peak elements like ^{107}Pd in the Solar System. An additional process, often referred to as the lighter element primary process (LEPP) has been postulated to play a role in the production of isotopes at and around the first *s*-peak (Travaglio et al., 2004; Bisterzo et al., 2014, 2017) and the amount of ^{107}Pd that is "missing" in our low and best Monash GCE setups is consistent with the LEPP contribution invoked by both Travaglio et al. (2004) and Bisterzo et al. (2014).

The LEPP and the different nucleosynthesis processes possibly contributing to the process have been a matter of discussion (see e.g. Montes et al., 2007; Qian & Wasserburg, 2007; Farouqi et al., 2010; Arcones & Montes, 2011, and references therein). Also, the need of a LEPP to reproduce the solar abundances has been questioned, particularly when considering the FRUITY models (e.g. Cristallo et al., 2015b). Indeed our GCE models show that the FRUITY models produce more first peak *s*-process elements than the Monash models (Figure 3.3), however, in this case ^{208}Pb is underproduced. Using FRUITY AGB yields, Prantzos et al. (2018, 2020) were able to resolve this issue by including in their GCE model rotating massive star yields from Limongi & Chieffi (2018) which provide an additional contribution to the first peak *s*-isotopes. Since the GCE models of Prantzos et al. (2018, 2020) also reproduce well the third *s*-process peak (including ^{208}Pb), this suggests that the existence of a possible deficit of the first *s*-process peak may be a consequence of the choice of yields as well as the GCE model. However, it must be considered that like AGB stellar yields, the yields for rotating massive stars also have uncertainties and the significant variations obtained between different sets of models are not surprising. Among other things, this may be due to the different approaches used to implement the rotation mechanism in one-dimensional models and to the efficiency of rotation in affecting the stellar structure at different metallicities. In Brinkman et al. (2021) the authors show that on the lower mass-end of massive stars ($10 - 35$ M$_{\odot}$),

the rotating models of Limongi & Chieffi (2018) show features that are not present in other rotating massive star yields. On the other hand, Rizzuti et al. (2019) found that their GCE model can best reproduce the observed *s*-process abundances in the Milky Way when using the rotating massive star yields of Frischknecht et al. (2016) or, in the case of the Limongi & Chieffi (2018) yields, if they assume that only the stars at the lowest metallicity slowly rotate. The uncertainties coming from GCE, including the different assumptions adopted by Rizzuti et al. (2019) and Prantzos et al. (2018, 2020) concerning the metallicity dependence of the rotational velocity distribution for rotating massive stars, must be taken into account mean that it not yet possible to derive effective constraints between different stellar sets. Additionally, as discussed by Pignatari et al. (2008) and Frischknecht et al. (2016), the *s*-process production in rotating massive stars is highly affected by nuclear uncertainties (e.g., by α capture rates on ^{22}Ne and ^{17}O). It is evident that the effective contribution of fast rotating massive stars to GCE is still a matter of debate, and therefore we believe that the existence of a LEPP is still an open question.

A potential solution to the missing ^{107}Pd may be found by considering an enhanced contribution to the solar abundances of the *s*-process elements from AGB stars of a higher metallicity than those that were assumed to contribute to the ESS in this work. For example, the effect of stellar migration could have moved higher metallicity AGB stars from the inner region of the Galaxy to the location of the formation of the Sun (Wielen et al., 1996; Minchev et al., 2013, 2014; Kubryk et al., 2015; Cristallo et al., 2020). These stars could potentially have increased the abundances of the first *s*-peak elements and of s-process isotopes in the mass region between Sr and the second *s*-process peak in the ESS, without contributing any additional iron. We cannot model this processes in our code, but to test if this solution would work qualitatively we calibrated a best fit GCE setup using the Monash yields that reached $Z = 0.018$ (instead of 0.014) at $t_{\odot}$. The isolation times derived from this test model using the radioactive-to-stable ratios were of the order of 12 Myr, and the ^{107}Pd/^{182}Hf ratio at $t_{\odot}$ is 7.8 which, when decayed to the ESS value, results in an isolation time of 30 Myr. Therefore, in principle it would be possible to find a self-consistent solution with a model run calibrating the solar Z somewhere in-between 0.014 and 0.018. This alternative solution for the LEPP in the Solar System needs to be investigated with more sophisticated GCE models, considering

the balance between the first and third *s*-process peak, and the fact that metal-rich AGB stars may contribute to the chemical enrichment history of the Sun. Furthermore, the abundances of all elements between the first and the second *s*-process peaks will need to be reproduced consistently.

Another potential solution to the missing ^{107}Pd is to consider a longer delay ($\gtrsim$ 4 Gyr) between the first and second infall episodes, as in the revised two-infall model of Grisoni et al. (2017). In this scenario the delay is long enough to allow the ISM to reach super-solar metallicity prior to the second infall, such that metal-rich AGB stars that formed during the first infall could have contributed material to the presolar matter. Indeed, as discussed in Section 1.2.3, the revised two-infall model proposed by Spitoni et al. (2019) can simultaneously reproduce the age-metallicity relation and the high- and low-α sequences for the APOKASC sample from Silva Aguirre et al. (2018) and the age dichotomy of solar twin stars found by Nissen et al. (2020). We hope to test this scenario in future work.

Overall, our analysis can provide new, independent, accurate, and precise constraints in the form of the ESS ^{107}Pd/^{182}Hf ratio to the open question of the production of the first *s*-process peak elements in the Milky Way disk. However, before we can make robust conclusions it will be necessary to analyse the ^{107}Pd/^{182}Hf ratio also using FRUITY yields, but with an updated ^{181}Hf decay rate. Since our results only apply to the solar abundances, however, they cannot be used to infer whether a missing contribution of the first peak *s*-isotopes was already active in the early Galaxy.

3.5 Conclusion

In this work, we investigated the origin of ^{107}Pd, ^{135}Cs, and ^{182}Hf in the ESS using the `OMEGA+` GCE code. We calculate timescales relevant for the birth of the Sun by comparing our predicted radioactive-to-stable abundance ratios in the ISM at $t_\odot$ to isotopic abundance ratios in primitive meteorites. We simulate three Milky Way setups for each of two sets of mass and metallicity dependent theoretical AGB yields (Monash and FRUITY), so that our timescales account for uncertainties due to GCE and stellar nucleosynthesis modelling. At $t_\odot$, the uncertainty factors for the abundance of an SLR in the ISM depends on the ratio of its

mean-life, τ, to the average length of time between the birth of the progenitor of the AGB stars that contributed to the ESS, γ. Since the latter is poorly constrained, we calculate timescales for two different cases of τ/γ. The main results are:

- If $\tau/\gamma \gtrsim 2$ (Regime I), we calculate an isolation time, $T_{\rm iso}$, between 9 and 26 Myr. This range is self-consistent for all radioactive-to-stable abundance ratios investigated in this work and takes into account a 1σ uncertainty due to the effects of ISM heterogeneities on the radioactive-to-stable ratio at $t_{\odot}$.

- Assuming that we are in Regime I, the predicted ^{107}Pd/^{182}Hf ratio indicates that $9-73\%$ of ^{107,108}Pd in the ESS is missing from our GCE setups. If the nuclear physics inputs we used here will be confirmed by future experiments and theory, we postulate two potential solutions to this problem: (1) an additional stellar production mechanism for the first *s*-peak isotopes, such as a *lighter element primary process*; or (2) an enhanced contribution of the first *s*-peak isotopes to the solar abundances from higher metallicity stars that migrated from the inner disk of the Galaxy. We find also a solution in the high GCE setup by considering the nuclear physics uncertainties associated with the ^{182}Hf/^{180}Hf branching point.

- If $\tau/\gamma \lesssim 0.3$ (Regime III), we find that for the Monash models in the range $2-3$ M$_{\odot}$ at $Z = 0.007$, 0.014, and 0.03 the time from the last event, $T_{\rm LE}$, is self-consistent for all radioactive-to-stable ratios explored in this work. Furthermore, we identify a single Monash model (2 M$_{\odot}$, $Z = 0.01$) for which $T_{\rm LE} = 25.5$ Myr is a self-consistent solution which takes into account also the ^{107}Pd/^{182}Hf ratio. Importantly, this solution exists without the need to invoke an extra Pd source in the Galaxy.

The methodology presented in this work can be used to follow the evolution of the radioactive-to-stable abundance ratio for any SLR in the ISM, for which stellar nucleosynthesis yields for a range of masses and metallicity are available, in order to better understand the birth environment of the Sun. In future work we would like to include the yields from the rotating massive star models of Limongi & Chieffi (2018) in our GCE framework, to see whether we reach the same conclusion as Prantzos et al. (2018, 2020): that an additional

contribution of the $A < 90$ s-isotopes in the ESS is not needed, owing to the increased weak s-process in rotating massive star models. Also, a better treatment of the r-process sources in the Galaxy in our calculations should be implemented and models of transport of radioactive nuclei in the ISM are needed to better asses the value of γ for the s-process.

Furthermore, as we have shown here, our approach can help us clarify the production mechanism and stellar sources in the Galaxy, and it could also be applied to constrain nuclear physic properties. An example of this is the case of ^{205}Pb (with a τ of 25 Myr), which is produced by the s-process in AGB stars and known to be present in the ESS (although the evidence is weak and awaits confirmation). However, the isotope's electron-capture rate is strongly temperature and density dependent and its variations are not well determined in stellar environments (Mowlavi et al., 1998). Future work could consider this isotope and constrain its nuclear properties by comparing $T_{\rm iso}$ derived using the ^{205}Pb/^{204}Pb ratio to those derived here.

3.6 Acknowledgements

We are thankful to the referee for helping to improve the manuscript through their constructive comments and suggestions. We thank also Blanka Világos for helping to test several important reaction rates using the Monash models and Claudia Travaglio for discussion. This research is supported by the ERC Consolidator Grant (Hungary) programme (Project RADIOSTAR, G.A. n. 724560). We thank the ChETEC COST Action (CA16117), supported by the European Cooperation in Science and Technology, the ChETEC-INFRA project funded from the European Union's Horizon 2020 research and innovation programme under grant agreement No 101008324, and the IReNA network supported by NSF AccelNet. TT and MP acknowledge significant support to NuGrid from STFC (through the University of Hull's Consolidated Grant ST/R000840/1) and ongoing access to `viper`, the University of Hull High Performance Computing Facility. BC and MP are grateful for support from the National Science Foundation (NSF, USA) under grant No. PHY-1430152 (JINA Center for the Evolution of the Elements), and from the "Lendulet-2014" Program of the Hungarian Academy of Sciences (Hungary). AK was supported by the Australian Research Council Centre of

Excellence for All Sky Astrophysics in 3 Dimensions (ASTRO 3D), through project number CE170100013.

4. Galactic Chemical Evolution of the Fe-group Elements with Different Type Ia SN Progenitor

This Chapter contains work submitted to The Monthly Notices of the Royal Astronomical Society as *"The Type Ia Supernovae history of the Milky Way with Galactic Chemical Evolution Models"*. I was the principal contributor to this work in terms of research and writing: I made all the GCE models, the figures and led the analysis and the discussion included in the paper. Suggestions and feedback were provided during the analysis and paper preparation by Marco Pignatari, James Keegans, Benoit Côté, and Brad Gibson.

4.1 Introduction

Type Ia supernovae (SNe Ia) are some of the most luminous events in the Universe. They are also appreciated as important beacons of knowledge in the fields of both galactic evolution and cosmology. On a galactic scale, they play a pivotal role in the chemical evolution of Fe and several of its neighbouring elements (Fe-peak elements) in the interstellar medium (ISM; Matteucci, 2021). On a cosmological scale, SNe Ia can be used as standardizable candles for measuring distances due to the correlation between their peak luminosity and light-curve width (the Phillips Relation; Phillips, 1993), and they were also credited with helping in the discovery of dark energy and the associated expansion of the Universe (Riess et al., 1998; Perlmutter et al., 1999). The fact that the identity of the progenitor and the explosion mechanism for SNe Ia remains unresolved [1] has consequences for these observations.

Some observational clues regarding the origin of SNe Ia are the absence of hydrogen and helium absorption lines in their spectra, as well as the production of large amounts ($\sim 0.6 M_{\odot}$) of radioactive ^{56}Ni in the central regions; the decay of which is responsible for the sharp maxima in their light curves. The discovery of various sub-classes of SNe Ia that deviate spectroscopically from the characteristic 'normal' explosions that follow the

[1] The so called "progenitor problem" (Maoz & Mannucci, 2012)

Phillips Relation have fueled the notion that more than one progenitor channel could lead to SNe Ia (see, e.g. Taubenberger, 2017). Furthermore, the fact that SNe Ia are observed in both galaxies undergoing active star formation as well as quiescent lenticular and elliptical galaxies suggests the existence of two distinct populations of SN Ia progenitor that explode over different timescales (Scannapieco & Bildsten, 2005; Mannucci et al., 2006).

There is a consensus at least that SNe Ia originate in binary systems in which a carbon-oxygen (CO) WD accretes material from its stellar companion. As the WD grows in mass its central temperature rises due to compressional heating, eventually triggering a thermonuclear explosion. A number of potential explosion mechanisms have been proposed, depending on whether material is donated from a non-degenerate star (single-degenerate scenario; Whelan & Iben, 1973) or another WD (double-degenerate scenario; Iben & Tutukov, 1984), and whether the mass of the exploding WD is close to or below the Chandrasekhar mass $M_{\rm ch} \sim 1.4 M_{\odot}$.

The relative frequency of SNe Ia events in a population of stars from the single-degenerate and double-degenerate scenarios can be estimated with binary population synthesis (BPS) codes (Belczynski et al., 2008; Ruiter et al., 2011; Temmink et al., 2020), although simplifying assumptions regarding the treatment of otherwise computationally intensive physical processes can lead to substantial differences in the predicted SNe Ia rates for different BPS codes (Toonen et al., 2014). There are valid arguments favouring the double-degenerate scenario and the sub-$M_{\rm Ch}$ SNe Ia explosions from the theoretical point of view, due to the difficulty in forming a $M_{\rm Ch}$ progenitor within the single-degenerate scenario (e.g. Denissenkov et al., 2017; Battino et al., 2020) and the lack of ionizing UV-radiation in extra-galactic observations (e.g. Woods & Gilfanov, 2013; Johansson et al., 2016). However, at present it is unclear which binary configuration(s) may contribute to the SNe Ia that are observed in Nature (see, e.g. discussions in Hillebrandt et al., 2013).

Given the uncertainty regarding both the physical progenitor system and the explosion mechanism, a wealth of SNe Ia yields have been calculated using detailed stellar nucleosynthesis models covering a large parameter space of initial conditions (for recent reviews regarding these different progenitor conditions, we refer the reader to Livio & Mazzali, 2018; Soker, 2019; Ruiter, 2020). Whilst the majority of SNe Ia have little variation in their spectroscopic and photometric features, their yields are chemically diverse and are particularly

sensitive to both the density (mass) of the WD and the explosion mechanism. The yields are also metallicity dependent, as the metallicity of the zero age main sequence progenitor star determines the electron fraction (Y_e) during NSE in near-$M_{\rm Ch}$ WD, and the neutron-excess during α-rich freeze-out in sub-$M_{\rm Ch}$ WD (Gronow et al., 2021b). These nucleosynthesis yields are the cornerstone of Galactic Chemical Evolution (GCE) models that aim to reproduce stellar abundances derived from spectroscopy.

The W7 model of Iwamoto et al. (1999) has historically been the SNe Ia yield of choice for GCE models of the solar neighbourhood, due to its close fit to SNe Ia spectra and light curves, as well as the fact it provides a reasonable fit to the elemental ratios measured in stars. These last include the increase of [Mn/Fe] and decrease in [α/Fe] after [Fe/H] ~ -1, which is a consequence of the delayed enrichment from SNe Ia in the ISM with respect to that of massive stars and core-collapse supernovae (CC-SNe; Minchev et al., 2013; Snaith et al., 2015). However, the yields for the W7 model are indicative only of a 1D pure deflagration explosion in a near-$M_{\rm Ch}$ WD, and the reaction network includes outdated electron capture rates that leads to over-estimations of [Ni/Fe] with respect to solar. The deflagration of a near-$M_{\rm Ch}$ WD is now considered the favoured explosion mechanism of the SN .Iax sub-class of SNe Ia that make up only a small percentage of the total SNe Ia rate (Foley et al., 2013).

In regards to 'normal' SNe Ia, a large number of GCE studies have looked to constrain the relative fraction of SNe Ia that have either a sub- or near-$M_{\rm Ch}$ progenitor (see, e.g. Seitenzahl et al., 2013b; Kobayashi et al., 2020a; de los Reyes et al., 2020; Palla, 2021; Sanders et al., 2021; Eitner et al., 2022). These studies commonly use Mn, or Ni, or both as tracer elements for WD mass, since they are produced during nuclear statistical equilibrium (NSE) at high densities (Seitenzahl & Townsley, 2017; Lach et al., 2020; Keegans, 2022); this condition is only met in near-$M_{\rm Ch}$ WD, therefore at least some fraction of the SNe Ia that exploded in the past must have been of near-$M_{\rm Ch}$ origin in order to reach solar [Mn/Fe] and [Ni/Fe] (Seitenzahl et al., 2013b; Kobayashi et al., 2020a). However, the sub/near progenitor ratio is far from settled. In particular, GCE models predict different estimates for the required fraction of sub-$M_{\rm Ch}$ progenitor depending on the specific mixing and fallback parameters of the core-collapse supernovae yields (see, e.g. Gronow et al., 2021b). Recently this issue was addressed by Eitner et al. (2022), who applied a scaling factor to two sets of CC-SNe yields (one

rotating and one non-rotating) in order to account for the underestimation of [Mn/Fe] in the GCE models at lower metallicities when compared to non-local thermodynamic equilibrium (NLTE) observations. Others have also argued for an enhanced Mn production in CC-SNe at lower metallicities in order to better fit the observational data (Sanders et al., 2021).

In this work we compare GCE predicted abundances of the Fe-peak elements (Ti, Cr, V, Co, Mn, and Ni) to observational measurements in stars in order to constrain SNe Ia explosion mechanisms in the Galaxy. We extend the scope of this investigation to elements other than the commonly used SNe Ia progenitor tracers Mn and Ni, because (i) recently it has been shown that Cr and V could potentially be used to probe the explosion pattern of sub-$M_{\rm Ch}$ SNe Ia (Leung & Nomoto, 2020; Palla, 2021) and (ii) the Fe-peak elements are made together in stellar ejecta and therefore their production will be connected. The GCE framework is calibrated for two sets of massive star yields, one including the effects of rotation, and GCE calculations are made for several SNe Ia yields covering a range of potential explosion mechanisms. Where they are deemed necessary, NLTE abundance estimates are assumed.

The paper is arranged as follows. In Section 4.2 we describe the SNe Ia yields that are investigated in this work, followed by a description of the GCE code in Section 4.3. In Section 4.4 we compare the predicted GCE of the Fe-peak elements for each of the SNe Ia yields to observational measurements in stars, we discuss also the differences between the GCE models with rotating and non-rotating massive star yields. GCE models with a combination of SNe Ia yields are considered in Section 4.5, and a statistical test is used to determine the respective fraction of SNe Ia from the sub- and near-$M_{\rm Ch}$ progenitor channels that best fits the data. Finally, in Section 4.6 we offer a discussion of the results and our concluding remarks.

4.2 The SNe Ia yields

We investigate the GCE of SNe Ia in the Milky Way by considering the yields for nucleosynthesis models which cover a range of progenitor masses and explosion mechanisms. For deflagration-to-detonation transition (DDT) explosions of near-$M_{\rm Ch}$ progenitor we include the yields from Seitenzahl et al. (2013a), Leung & Nomoto (2018), and Townsley et al. (2016). The yields for pure deflagration (PDf) models are taken from Iwamoto et al. (1999), Kromer

et al. (2015) and Fink et al. (2014). In terms of sub-$M_{\rm Ch}$ progenitor, pure detonation (PDt) yields are taken from the models of Pakmor et al. (2012) and Sim et al. (2010), while we use the double-detonation (DD) yields of Gronow et al. (2021b), Leung & Nomoto (2020), and Shen et al. (2018). Below we give a brief description of the main characteristics for each of the SNe Ia models. Following this Section, the models are labeled according to the following naming convention: (1) shorthand reference, (2) explosion mechanism, (3) progenitor mass in $M_{\odot}$, (4) He shell mass in $M_{\odot}$ (DD models only), with (1), (2), (3) and, where appropriate, (4) all separated by an underscore. As an example, the $1.40M_{\odot}$, deflagration-to-detonation transition model of Townsley et al. (2016) is labeled T16_DDT_M1.40.

Figure 4.1 shows the elemental yields relative to Fe for all models investigated in this work. Where yields have been calculated for several WD progenitors with different initial metallicities, only yields for the solar metallicity model are shown. The intermediate mass elements (IMEs) show a clear odd-even effect, with even-Z elements produced more efficiently (e.g., Prantzos, 2008; Pagel, 2009). In Figure 4.1 there is an increase in the elemental yields of the Fe-group elements starting with Ti, which is often classified as an α-element like O or Si, but from a nucleosynthesis point of view should be classified as an Fe-group element (Woosley & Weaver, 1995).

4.2.1 Deflagration-to-detonation transition (DDT) models

In order for near-$M_{\rm Ch}$ progenitors to produce the abundances of intermediate mass elements (e.g. Ne, Mg, Si, S, and Ca) that are observed in the spectra of SNe Ia, prior to detonation the fuel density must decrease prior to detonation, else the subsequent thermonuclear runaway will only produce isotopes at and around the Fe peak (Arnett, 1969; Steinmetz et al., 1992). The necessary expansion of the fuel occurs due to the energy released during a subsonic propagation of the combustion front at the onset of C-burning (Röpke, 2007). After some time, once the fuel density falls below $\sim 10^7$g cm^{-3}, the subsonic deflagration of the combustion front transitions into a supersonic detonation which produces enough nuclear energy to unbind the WD. These explosions are also often referred to as delayed-detonations, due to the period of pre-expansion of the fuel prior to detonation.

In Seitenzahl et al. (2013a), a three-dimensional hydrodynamic code is used to calculate

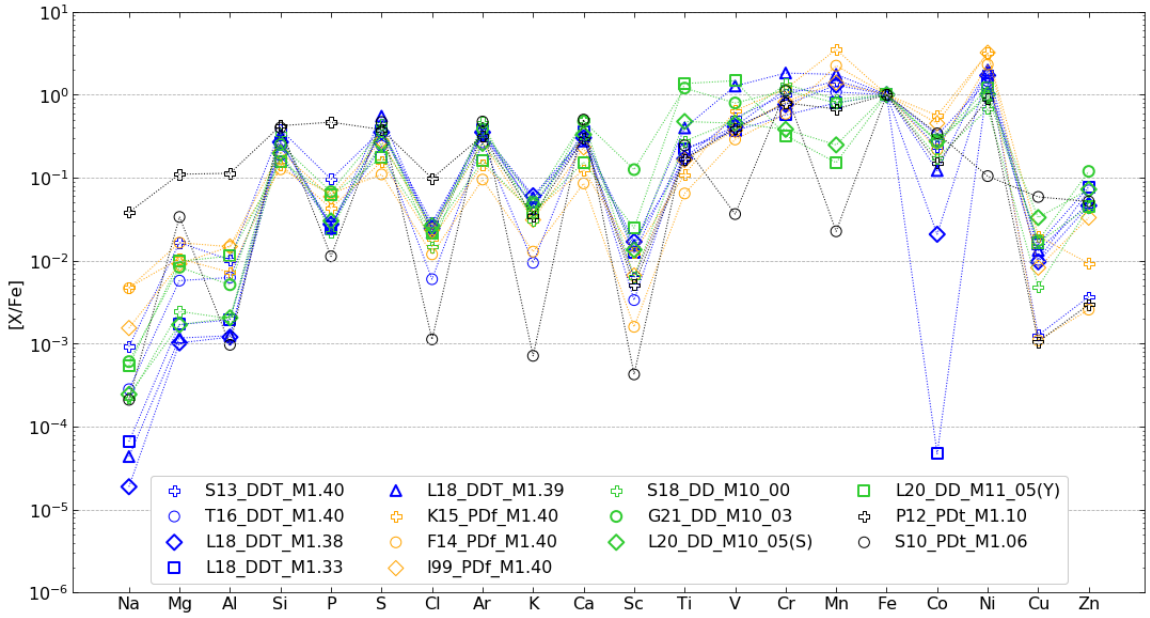

Figure 4.1: Elemental yields normalized to Fe with respect to solar ratios (Asplund et al., 2009) for the SNe Ia models investigated in this work: DDT (blue), PDf (orange), DD (green), PDt (black). The models shown are based on an explosion of a WD progenitor with $Z = Z_{\odot}$.

yields for 14 models covering a parameter space of 11 different ignition scenarios. The ignition geometry of the deflagration is determined by the arrangement of the various numbers of spherical ignition kernels (ranging from 1 to 1600), where a higher number of kernels results in a higher degree of spherical symmetry. The ignition setup determines the strength of deflagration and the extent to which fuel can expand prior to the detonation. In this work, we use the model with 100 ignition kernels with a central density of $\rho_c = 2.9 \times 10^9$g cm^{-3}, henceforth S13_DDT_M1.40. This model is post-processed by Seitenzahl et al. (2013a) at four different metallicities by reducing the ^{22}Ne mass fraction to 0.01, 0.1, and 0.5 of the solar value ($M_{\mathrm{Ne},\odot} = 0.025$).

Using a two-dimensional hydrodynamic code, Leung & Nomoto (2018) calculate chemical yields resulting from DDT explosions in near-M_{Ch} WDs. However, the authors note that the WD mass is extended down to $\sim 1.30 M_{\odot}$ which could more closely resemble a sub-M_{Ch} explosion. SNe Ia yields are calculated by post-processing the explosions of WD progenitor covering a large range of model parameters, such as central density, metallicity, and flame shape. Herein, we use the yields from the benchmark model with $\rho_c = 3 \times 10^9$g cm^{-3} and $M_{WD} = 1.38 M_{\odot}$ at 7 different metallicities ($Z = 0, 0.1, 0.5, 1, 2, 3, 5\ Z_{\odot}$), hereafter

L18_DDT_M1.38. Yields are also calculated at these metallicities for models with initial masses of $1.33 M_{\odot}$ and $1.39 M_{\odot}$, corresponding to central densities of $\rho_c = 1 \times 10^9$g cm^{-3} and $\rho_c = 5 \times 10^9$g cm^{-3} respectively. The L18_DDT_M1.33 and L18_DDT_M1.39 models present an excellent opportunity to explore the impact that central density/initial mass of the progenitor has on the GCE of the Fe-group elements.

Finally, we include the DDT model of Townsley et al. (2016) with updated yields from Keegans (2022). The yields are calculated by post-processing the trajectories of the Townsley et al. (2016) model with an extended reaction network of over 5000 isotopes and 75,000 reactions. The model, hereafter T16_DDT_M1.40, uses an artificially thickened reaction front in order for a cell in the computational grid to consist of both unburned and burned material. A reconstruction of the temperature-density history of these cells is then performed to approximate the passing of a fluid element through a reaction front of realistic size (Townsley et al., 2016). The detonation is triggered by inserting a hot spot into the WD progenitor, with a central density at ignition of $\rho_c = 2 \times 10^9$g cm^{-3}.

4.2.2 Pure deflagration (PDf) models

In contrast to the DDT scenario, if a detonation is not triggered and the combustion front only proceeds as deflagration then the nuclear energy released is insufficient to fully unbind the WD, leaving behind a bound remnant. Since in this regime the flame front propagates outwards at subsonic speeds, material further from the centre of the WD will have time to expand before being burnt and will therefore be synthesised mostly into intermediate mass elements (Röpke et al., 2007). Conversely, fuel near the centre will be burnt at higher densities producing mostly Fe-peak nuclei. The speed of the flame front determines the relative ratio of intermediate-mass to Fe-peak elements, with faster flame speeds producing relatively more of the last. In recent years, pure deflagration explosions have been proposed as potential candidates to explain the subluminous Type Iax (SNe Iax) supernovae (Jha, 2017). This class of SNe are thought to have short delay times since they are not readily observed in elliptical type galaxies (Foley et al., 2009; Valenti et al., 2009).

The most widely used SNe Ia nucleosynthesis yields in GCE models of the Milky Way are those of Iwamoto et al. (1999), hereafter I99_PDf_M1.40, based on the W7 pure deflagration

model of Nomoto et al. (1984). The progenitor WD is constructed from a mass grid of 200 zones within an implicit Lagrangian hydrodynamics code, using reaction network data from Thielemann et al. (1996). The explosion is modelled starting from a WD of mass $M = 1M_{\odot}$, which grows by accreting H-rich material at a steady rate of $\dot{M}_H = 4 \times 10^{-8} M_{\odot} \mathrm{y}^{-1}$ until carbon is ignited at a central density of $\rho_c = 2.5 \times 10^9$ g cm^{-3}. Following this, the convective core undergoes thermonuclear runaway at $T_c \approx 8 \times 10^8$ K and $\rho_c = 2.12 \times 10^9$ g cm^{-3}, with a laminar flame propagation speed of $10\% - 30\%$ of the sound speed, which results in a significant overproduction of ^{58}Ni due to the fast burning front producing too much material in the range $Y_e = 0.47 - 0.485$. This can be partially solved by reducing the metallicity of the zero-age main sequence progenitor from [Fe/H] = 0 to [Fe/H] = -1 (see Figure 6 in Thielemann et al., 2003). Recently, the W7 model was post-processed by Leung & Nomoto (2018) with updated nuclear reaction network and electron capture rates; these revised yields provide a much better match with [Ni/Fe] at solar metallicity (Palla, 2021).

As in Seitenzahl et al. (2013a), Fink et al. (2014) perform three-dimensional hydrodynamical simulations of an exploding WD for different numbers of ignition kernels. Although they use the same initial conditions as the former, the combustion front never becomes supersonic. As is the case for the DDT simulations in Seitenzahl et al. (2013a), we use the yields from the model with 100 ignition kernels, hereafter F14_PDf_M1.40, in our GCE analysis.

Kromer et al. (2015) simulate the explosion of a $1.4M_{\odot}$ hybrid WD with $\rho_c = 2.9 \times 10^9$g cm^{-3} following an off-centre deflagration, hereafter K15_PDf_M1.40. The WD has a so-called “hybrid" structure, comprising a CO core surrounded by an ONe mantle, and is formed as a late evolutionary stage of super asymptotic giant branch stars (Denissenkov et al., 2013). The abrupt change in the composition profile of these stars is thought to lead to lower ^{56}Ni yields, and as such they are postulated to be a potential progenitor scenario for the faintest SNe Iax, such as SN 2008ha.

4.2.3 Double-detonation (DD) models

The DD progenitor system involves the accretion of He-rich material onto the surface of a sub-M_{Ch} WD from its binary companion via Roche-lobe overflow (Woosley & Weaver, 1994; Livne & Arnett, 1995). The companion can be either a helium-burning star, a helium WD,

or hybrid WD, with the single-degenerate channel giving rise to short delay times (Ruiter et al., 2011). Regardless of whether the binary system is single- or double-degenerate, the detonation of CO material in the core of the WD is triggered by a preliminary He-shell detonation due to the compressional heating of the accreted material onto its surface.

In Gronow et al. (2021a), yields are calculated resulting from the DD explosions of WD progenitor with core masses from $0.8M_{\odot}$ to $1.1M_{\odot}$ and shell mass between $0.02M_{\odot}$ and $0.1M_{\odot}$. The temperature and density of the hydrodynamic simulations are mapped out by 2 million tracer particles with a reaction network of $\sim$ 30 key isotopes. The explosion is then postprocessed with an extended nuclear network to obtain yields for a primary WD progenitor with initial metallicity equal to solar. The work of Gronow et al. (2021b) extends the yield set to explosions from progenitor of initial metallicities of 0.01, 0.1 and $3Z_{\odot}$. In this work, we consider the yields from the M10_03 ($1M_{\odot}$ core with $0.03M_{\odot}$ shell mass) model at all metallicities, hereafter G21_DD_M10_03, since the authors claim that this model best matches the solar values of Ti, V, and Cr.

The DD explosions of sub-$M_{\rm Ch}$ WD simulated in Leung & Nomoto (2020) are based on the same two dimensional hydrodynamic code used in Leung & Nomoto (2018). Again, yields are calculated for a large parameter space of initial conditions including metallicity, mass, and the geometry of the He detonation (bubble, spherical, ring). Metallicity-dependent yields are calculated for three “benchmark" models (one for each detonation trigger) that have the smallest He shell, whilst also being able to eject $\sim 0.6M_{\odot}$ ^{56}Ni in line with most ‘normal’ SNe Ia observations. From these, we include the benchmark models with a ring (Y) and spherical (S) He detonation configuration. In a Y-type detonation, the He detonation is initiated as a ring around the rotation axis of the WD, whereas in an S-type detonation the He detonation is spherical and takes place 50 Km above the He/CO interface. Henceforth, we refer to these models as L20_DD_M11_05(Y) and L20_DD_M10_05(S), respectively. We choose to include these two benchmark models because they have an identical He envelope mass $M_{He} = 0.05M_{\odot}$, as opposed to $M_{He} = 0.1M_{\odot}$ for the bubble He detonation, therefore they offer a more direct probe of the effect of He detonation pattern, rather than M_{He}, on the GCE of the Fe-group elements. The effect of M_{He} on the GCE can be seen by comparing the models of Leung & Nomoto (2020) to, for example, G21_DD_M10_03 which has $M_{He} = 0.03$

instead.

The final set of DD yields investigated in this work are based on post-processing of the $1.0 M_{\odot}$ model in Shen et al. (2018), hereafter S18_DD_M10_00. The classification of this model as a DD detonation is somewhat tenuous, since the explosion is based on a “bare" C/O WD with no He shell - the explosion is representative of a double-detonation of a CO WD resulting from the rapid accretion of material from a low-mass He WD companion (see also Shen & Moore, 2014). The detonation in the core is ignited artificially by inserting a hot spot of $\sim 2 \times 10^9$ at its core. For the purposes of this work we consider this model representative of a dynamically driven double detonation, where the He detonation triggers the C detonation but that the ashes of the latter dominate the yields since the He shell mass is negligible. We include in our GCE updated yields from Keegans (2022), calculated by post-processing the S18_DD_M10_00 model using the same nuclear reaction network as for the T16_DDT_M1.40 and M19_PDt_M0.80 models in this work.

4.2.4 Pure detonation (PDt) models

Sub-$M_{\rm Ch}$ WDs are proposed to explode as PDt if there is no helium-rich outer shell. A problem with most DD explosion models is the tendency to overproduce ^{56}Ni due to the He-shell detonation prior to core detonation. However, whilst the absence of such a He-shell in theory produces light curves and spectra that can better match observations, it presents a new problem as to how the core detonation is triggered. One such solution is the violent merger of two WDs due to loss of angular momentum, which can nullify the need for a preliminary surface detonation of He in order to trigger a carbon detonation in the core. In this case, the material accreted onto the primary is rich in C+O rather than He which could lead to brief periods of C ignition on the WD surface. These class of SNe Ia would appear less luminous than those sub-$M_{\rm Ch}$ progenitor that experienced a He detonation, since in the latter large amounts of ^{56}Ni are produced during burning in the He shell.

Pakmor et al. (2012) model the explosion resulting from the violent merger of two WDs with masses 0.9 and 1.1 $M_{\odot}$, hereafter P12_PDt_VM. The binary system is evolved beginning with the coalescence of the stars and the subsequent detonation is triggered due to the heating and compression of material at the surface of the primary, which causes hot spots to form

deeper inside the star. The nucleosynthesis is calculated by post processing the temperature and density profile recorded by 10^6 tracer particles.

Although the violent merger (VM) scenario is a plausible site for PDt progenitor, the resulting mass of the WD remnant could exceed $M_{\rm Ch}$ in the case where the mass ratio of the merging WDs is $<\sim 0.8$ (Pakmor et al., 2011; Sato et al., 2016) leading to an accretion-induced collapse (AIC) of the WD remnant to a neutron star (see e.g., Liu & Wang, 2020). The exact physical conditions that determine whether a merging binary system of two CO WDs results in an AIC or VM are still not fully clear. Therefore, it is not uncommon for models of PDt SNe Ia explosions to remove the ambiguity surrounding the detonation trigger and instead concern themselves only with the timeframe starting from core detonation. This latter approach is adopted by Sim et al. (2010), who use one-dimensional hydrostatic models to explore PD explosions in WDs with masses from 0.97 to 1.15 $M_\odot$. The models consider only the explosion in a numerical context without consideration of the underlying trigger for the detonation. In this work, we use the yields from the 1.06 $M_\odot$ C+O WD model, hereafter S10_PDt_M1.06, since its light curve is in good agreement with observations. We choose not to use the 1.06 $M_\odot$ C+O+Ne WD with higher initial Ne composition as this model produces a higher abundance of Fe-group elements but comparatively less intermediate mass elements.

4.3 The GCE code

We use the `OMEGA+` GCE code (Côté et al., 2017, 2018) to model the evolution of chemical abundances in the Galaxy. The GCE framework is calibrated based on the Milky Way's disk and takes into account present day observational estimates for the star formation rate (SFR; $M_\star$), the gas infall rate, supernovae rates, and the total mass of gas ($M_{\rm gas}$) in the Galaxy. `OMEGA+` is a two-zone model comprised of a central cold gas reservoir with active star formation that contains all stellar populations in the Galaxy; this is encompassed by a hot gas reservoir devoid of star formation and stellar populations. These zones are referred to henceforth as the "galaxy" and the "circumgalactic medium" respectively, and gas can circulate between the two zones via galactic inflows and outflows. The change in the total mass of gas in the Galaxy ($M_{\rm gas}$) at time t is

$$\dot{M}_{\rm gas}(t) = \dot{M}_{\rm inflow}(t) + \dot{M}_{\rm ej}(t) - \dot{M}_{\star}(t) - \dot{M}_{\rm outflow}(t), \tag{4.1}$$

where the terms on the right-hand side of the equation are, from left to right, the gas inflow rate into the Galaxy from the circumgalactic medium, the rate at which gas is returned to the ISM from stellar ejecta, the star formation rate (SFR), and the rate of gas outflow from the Galaxy into the circumgalactic medium due to stellar feedback. Below we describe each of these four terms in more detail.

Beginning firstly with the gas inflow rate ($\dot{M}_{\rm inflow}$), for all of our GCE calculations in this work we assume that the formation of the Milk Way disc can be attributed to two distinct infall episodes. In this two infall model, the gas inflow rate ($\dot{M}_{\rm inflow}$) is given by (Chiappini et al., 1997)

$$\dot{M}_{\rm inflow}\,(t) = A_1 \exp\left(\frac{-t}{\tau_1}\right) + A_2 \exp\left(\frac{t_{\rm max} - t}{\tau_2}\right), \tag{4.2}$$

where each exponential term describes a separate infall episode. The second infall is delayed by $t_{\rm max} = 1.0$ Gyr with respect to the first and occurs over a much longer timescale: $\tau 1 \simeq 0.7$ Gyr for the first infall compared to $\tau_2 \simeq 7$ Gyr for the second. The normalization constants A_1 and A_2 are chosen so as to best reproduce the current estimated mass of gas in the Milky Way ($9.2 \pm 5.3\ M_{\odot} \times 10^9$) as derived by Kubryk et al. (2015)[2]. For comparison, the final mass of gas predicted by the low, best, and high GCE models is 1.36×10^{10}, 7.19×10^9, and $3.16 \times 10^9\ M_{\odot}$, respectively.

Mechanical energy released from CCSNe can propel gas out of the Galaxy into the CGM. Since these galactic outflows are driven by stellar feedback, the outflow rate $\dot{M}_{\rm outflow}$ is proportional to the SFR, such that

$$\dot{M}_{\rm outflow}(t) = \eta \dot{M}_{\star}(t). \tag{4.3}$$

The SFR ($\dot{M}_{\star}$) is a linear function of $M_{\rm gas}$,

$$\dot{M}_{\star}(t) = f_{\star} M_{\rm gas}(t), \tag{4.4}$$

[2]Since the Galaxy component is modelled as a single zone, this value is a summation of the current mass of gas in the disk and the bulge components.

where $f_\star$ represents the star formation efficiency in units of $[\mathrm{yr}^{-1}]$. At each timestep, the `OMEGA` code converts some amount of the gas in the Galaxy into a simple stellar population (SSP). The mass of the SSP is determined by the current star formation rate and the distribution of stellar masses it contains is based on the chosen initial mass function (IMF); in this work we adopt the IMF of Kroupa et al. (1993). All stars in a given SSP are assumed to be born simultaneously with a chemical composition identical to that of the gas reservoir at that time. However, the stars in an SSP will eject their yields into the ISM over different timescales depending on the specific delay-time distribution function. The Stellar Yields for Galactic Modeling Applications (SYGMA; Ritter et al., 2018a) module is called by `OMEGA` at each timestep to calculate the composition of the stellar ejecta from all SSPs in the system based on the mass- and metallicity-dependent stellar yields being used.

In this work we include in our GCE framework the yields of low- and intermediate-mass stars (LIMS) and massive stars, together with the SNe Ia yields described in Section 4.2. The LIMS yields of Cristallo et al. (2015a) are used in all of our GCE calculations, however, we perform two sets of independent GCE calculations using the massive star yields of Limongi & Chieffi (2018) (hereafter LC18) and Nomoto et al. (2013) (hereafter N13). For LC18, the yields are weighted according to a metallicity-dependent function of the rotational velocity as derived by Prantzos et al. (2018), and we include in the IMF massive stars up to $100M_\odot$, however, stars more massive than $25M_\odot$ are assumed to collapse to a black hole and thus contribute to chemical enrichment only by virtue of their winds (i.e., set R in Limongi & Chieffi, 2018). For N13, we assume that some amount of stars with $M \geq 20M_\odot$ end as hypernovae (explosion energy $\geq 10^{52}$ erg) with a rate that is a function of the metallicity (Kobayashi & Nakasato, 2011). However, the upper limit for the IMF is restricted to $50M_\odot$ so that $Z = Z_\odot = 0.014$ at the time of the birth of the Sun (see also Gronow et al., 2021b, where the same upper mass limit is applied). The transition mass between LIMS and massive stars is set to $8M_\odot$ (see, e.g. Karakas & Lattanzio, 2014). We choose to run GCE calculations for both sets of massive star yields because in Gronow et al. (2021b) it was found that the choice of massive star yields has large implications for the relative contributions from sub- and near-M_{Ch} SNe Ia progenitor toward the solar Mn abundance.

We adopt a fiducial delay-time distribution (DTD) for SNe Ia of the form $t^{-1.07}$ as derived by Maoz et al. (2012). This DTD is normalised so that $\sim 10^{-3}$ SNe form per stellar mass in a SSP, which is to the same order of magnitude as rates derived from observations (for comparison, a compilation of observed Galactic SNe Ia rates are given in Table 5 of Côté et al., 2016). A power law form for the DTD is expected for double degenerate systems in which the delay time is dominated by the merger timescale, assuming the distribution for the orbital separation S of binary stars follows $f(S)dS \sim S^{-1}$ (see Ruiter et al., 2009). Indeed, a power law DTD with exponent ≈ -1 has also been found to have the best fit to the observed SNe Ia rate in Nature (Totani et al., 2008; Maoz et al., 2012). On the other hand, delay times for single degenerate systems will depend mostly on the evolutionary timescale of the donor (Ruiter et al., 2009). However, Matteucci et al. (2009) demonstrated that DTDs calculated using either single or double degenerate scenarios lead to a very similar chemical evolution of [O/Fe] vs [Fe/H]. Similarly, we find negligible difference for the GCE of Fe-group elements when using instead the DTD calculated by Ruiter et al. (2014) for a WD accreting from a non-degenerate companion.

4.4 Results

4.4.1 The chemical evolution of the iron-group elements in the Milky Way

Figure 4.2 shows the evolution of [Ti, V, Cr, Mn, Co, Ni/Fe] versus [Fe/H] for the Milky Way disc as predicted by our GCE model with N13 massive star yields. For comparison, Figure 4.3 shows the same but for LC18 massive star yields. The top (bottom) panel includes SNe Ia yields from near (sub)-$M_{\rm Ch}$ WD progenitor and the lines are colour coded according to the explosion mechanism: DDT (blue), PDf (orange), DD (green), and PDt (black). The GCE code is calibrated to reach [Fe/H] ≈ 0 at the time of the birth of the Sun ($t_\odot = 8.6$ Gyr) based on global properties of the Milk Way's disk (e.g., star formation rate, gas inflow rate, mass of gas, etc.) and current estimates for supernovae rates (both SNe Ia and CC-SNe). However, due to the fact a bound remnant remains following the PDf explosions of F14_PDf_M1.40 and K15_PDf_M1.40, less material is ejected from these SNe Ia and so the associated GCE tracks never reach solar [Fe/H]. In addition to the GCE predictions that include an SNe Ia

contribution, we show with a grey line the evolution of [X/Fe] but with no contribution of X from SNe Ia (i.e. only the contribution from massive stars). The [O/Fe] vs [Fe/H] evolution is also plotted as an example of an α element that receives no contribution from SNe Ia. Below, we describe the GCE of each element in detail.

4.4.1.1 Titanium

Regardless of whether massive star yields are taken from N13 or LC18, the GCE predictions underproduce [Ti/Fe] relative to observations, at least prior to SNe Ia enrichment in the ISM; this is a known phenomena of GCE models (see, e.g. Kobayashi et al., 2006; Hughes et al., 2008; Romano et al., 2010; Mishenina et al., 2017; Kobayashi et al., 2020b).

In both Figures 4.2 & 4.3, all DDT models (blue lines) initially exhibit a steady decrease in [Ti/Fe] with [Fe/H], with only the L18_DDT_M1.39 model plateauing at [Fe/H] ~ -0.5. The PDF models (orange lines) all behave slightly differently: K15_PDf_M1.40 increases with the rise becoming more gradual with [Fe/H], I99_PDf_M1.40 decreases almost linearly with metallicity, F14_PDf_M1.40 rises at first before decreasing. The PDt models (black lines) show a similar trend to the DDT models. There is a large spread in [Ti/Fe] for the DD models (green lines), with both G21_DD_M10_03 and L20_DD_M11_05(Y) reaching nearly solar, whereas S18_DD_M10_00 and L20_DD_M11_05(S) decrease and plateau, respectively. At [Fe/H] = 0 there is a $\sim$ 0.3 dex difference in [Ti/Fe] for L20_DD_M11_05(Y) and S18_DD_M10_00. The discrepancies between the DD models for Ti can be explained by considering the fact that the most abundant isotope of Ti in the ejecta of these models, irrespective of the metallicity of the progenitor, is ^{48}Ti. At higher temperatures ($>$ 8 GK) ^{48}Ti is directly produced, however, at lower temperatures the largest contribution is from the decay of ^{48}Cr (Keegans, 2022). Since this radiogenic contribution will depend strongly on the burning that takes place during He detonation, the production of Ti will be higher for models with larger $M_{\rm He}$. This explains why L20_DD_M11_05(Y) can produce supersolar amounts of Ti, and why the bare (i.e. no He shell) CO WD model S18_DD_M10_00 behaves so similar to the PDt models for this element.

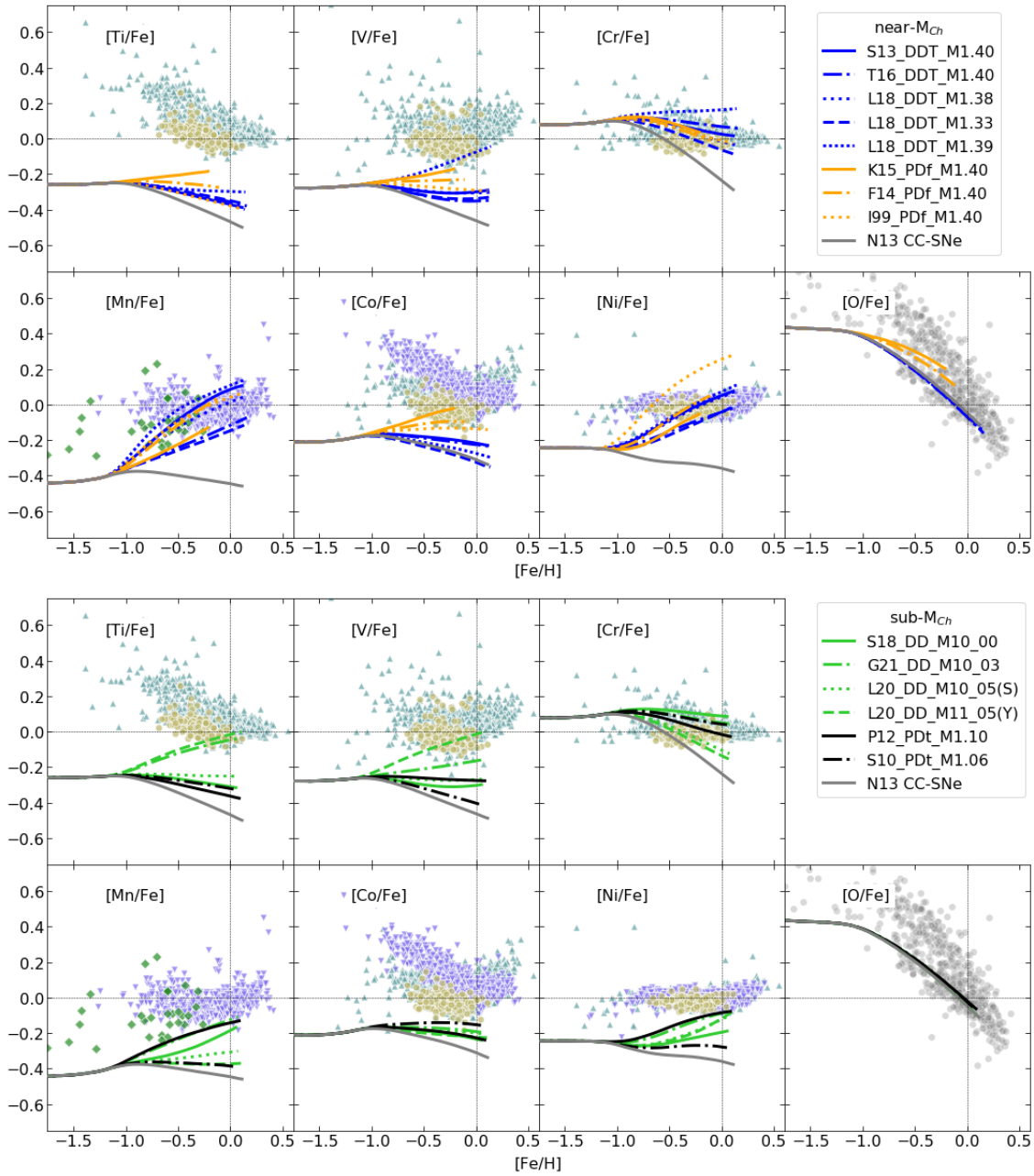

Figure 4.2: Predicted evolution of [X/Fe] as a function of [Fe/H] in the Milky Way's disk for the Fe-peak elements with N13 CC-SNe yields. The [O/Fe] versus [Fe/H] evolution is also plotted as an example of an α element that receives no contribution from SNe Ia. The top and bottom panels show GCE predictions with sub- and near-$M_{\rm Ch}$ SNe Ia yields, respectively. The lines are colour coded according to the explosion mechanism (see text), where the grey line shows the evolution of [X/Fe] with no contribution from SNe Ia (i.e., assuming only a contribution to X from CC-SNe). Observational data are from Adibekyan et al. (2012) (blue-green triangles), Bensby et al. (2014); Battistini & Bensby (2015) (NLTE corrected; upside down purple triangles), Reddy et al. (2003) (gold circles), Eitner et al. (2020) (NLTE corrected; green diamonds), and Bensby et al. (2014) (grey circles).

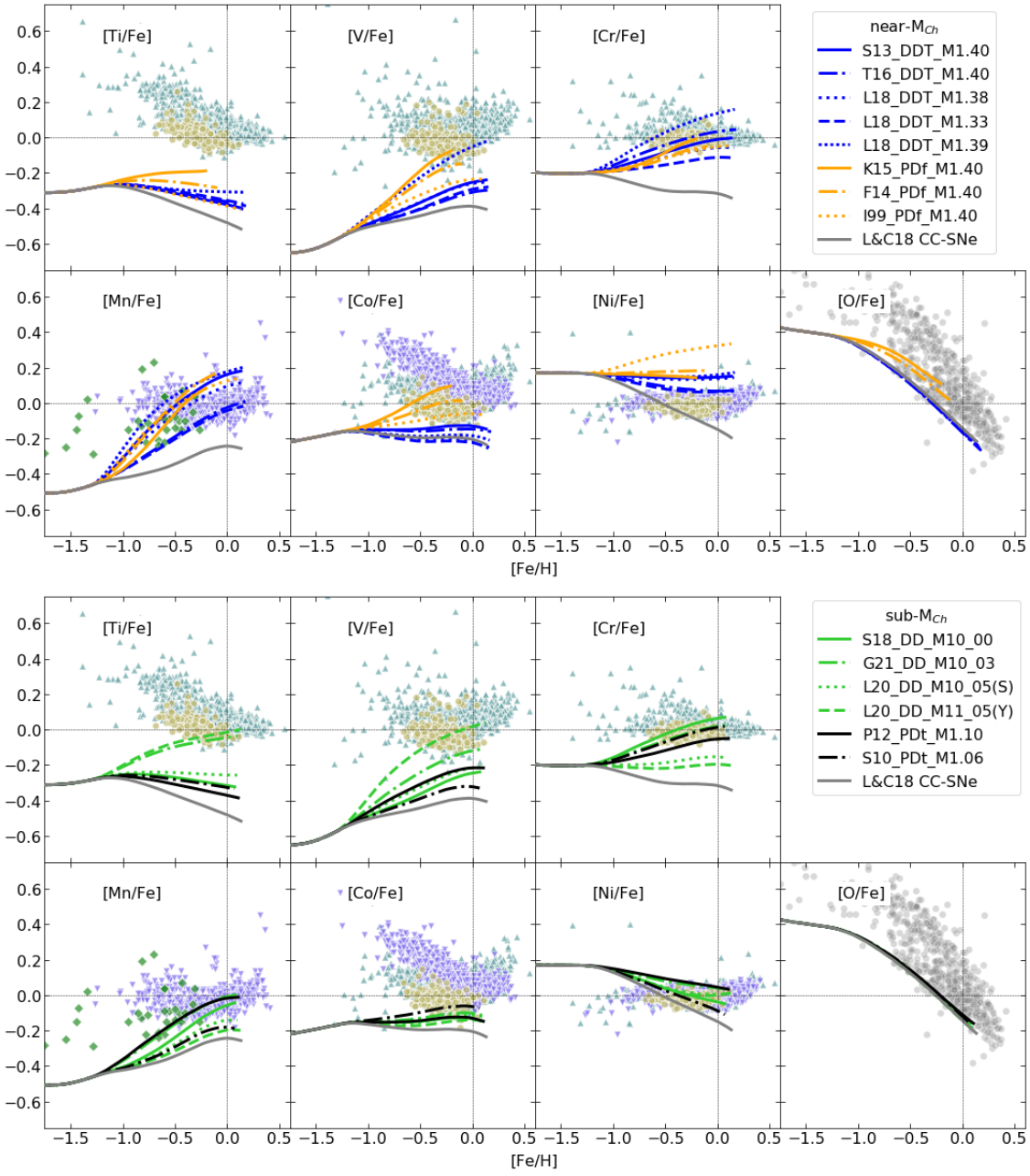

Figure 4.3: Same as Figure 4.2 but for LC18 CC-SNe yields.

4.4.1.2 Vanadium

Much like for Ti, GCE models have historically underproduced V with respect to observations, particularly at low metallicities (see, e.g. Timmes et al., 1995; Goswami & Prantzos, 2000; Romano et al., 2010; Prantzos et al., 2018; Côté et al., 2020). Furthermore, the predicted GCE of [V/Fe] depends crucially on the choice of massive star yields, with the V contribution from LC18 (Figure 4.3) being ~ 0.2 dex lower than for N13 (Figure 4.2). This means that there is a much steeper increase of [V/Fe] in Figure 4.3 after [Fe/H] ~ -1.5. For N13 massive star yields, the evolution of [V/Fe] vs [Fe/H] mirrors that very closely of [Ti/Fe] for the respective SNe Ia models. However, there are some key differences, most obviously for the Leung & Nomoto (2018) models of different central density, with a difference of ~ 0.4 dex between the high and low density models at [Fe/H] = 0. This is because at higher central densities the electron fraction in the core is lower, which results in a reduced production of ^{56}Fe since there is less ^{56}Ni in NSE (Leung & Nomoto, 2018). Furthermore, a larger amount of fuel in the L18_DDT_M1.39 ($\rho_c = 5 \times 10^9$g cm^{-3}) model is burnt during deflagration than in the L18_DDT_M1.33 ($\rho_c = 1 \times 10^9$g cm^{-3}), which increases the production of V.

Another difference in the evolution of [V/Fe] and [Ti/Fe] in Figure 4.2 is that all near-$M_{\rm Ch}$ predictions of [V/Fe] have an upward trend by the end of the GCE simulation as opposed to a flat, or even decreasing, trend as seen for Ti. This is because at higher initial metallicity the electron fraction is lower, which increases the production of ^{51}V through the low temperature contribution of the radioactive ^{51}Cr (Keegans, 2022). However, this upward trend is not seen in Figure 4.3 and in fact the lines begin to flatten due to the reduced V contribution after [Fe/H] = 0 from the higher metallicity LC18 massive stars.

Analogous to [Ti/Fe], despite the fact L20_DD_M10_05(S) has a He shell of the same size as L20_DD_M11_05(Y), it contributes much less toward V enrichment. This suggests that these lighter Fe-elements could be used to probe the geometry of the He detonation. This same conclusion was reached by Palla (2021) when they compared the GCE of [V/Fe] for both the Leung & Nomoto (2020) models with spherical and bubble He detonation triggers. They also find that models with a spherical detonation seed underproduce the light Fe-group elements compared to models with an aspherical He detonation.

4.4.1.3 Chromium

Much like for V, in Figures 4.2 and 4.3 we see disparities between Cr production for the GCE calculations made using the two sets of massive star yields - there is a ~ 0.3 dex higher [Cr/Fe] abundance at [Fe/H] < -1.5 for the GCE predictions using N13 massive star yields. Despite this, the majority of SNe Ia yields, irrespective of the choice of massive star yields, are in good agreement with the observational data.

In Figure 4.2, the onset of SNe Ia enrichment is met by an almost linear drop in [Cr/Fe] with increasing [Fe/H]. Neither the detonation mechanism nor the mass of the WD progenitor seem to have a pronounced effect on the rate of decrease. In Figure 4.3, the predicted [Cr/Fe] increases and then begins to plateau once [Fe/H] ~ -0.5. The flattening of the trend with metallicity is most pronounced for sub-$M_{\rm Ch}$ progenitor.

In contrast to the evolution of Ti and V, there is a negligible difference in the Cr evolution for models with different He detonation geometries (i.e. models L20_DD_M11_05(Y) and L20_DD_M10_05(S)). In fact these models underproduce Cr compared to the two other DD models, S18_DD_M10_00 and G21_DD_M10_03, which initially suggests that a prominent production channel of Cr that is included in the reaction networks of Keegans (2022)[3] and Gronow et al. (2021a) is absent in the reaction network of Leung & Nomoto (2020). However, Palla (2021) find that Cr production is increased for the Leung & Nomoto (2020) benchmark model with aspherical detonation pattern, resulting in super-solar abundances of [Cr/Fe] - the S-type detonation produces sub-solar abundances as found in this work. In Palla (2021) the aspherical yields are taken from the Leung & Nomoto (2020) benchmark model with X-type He detonation, which has a He shell twice as massive (i.e. $M_{\rm He} = 0.1 M_{\odot}$) as those of L20_DD_M11_05(S) and L20_DD_M11_05(Y) used in this work. The significance of the He shell detonation on Cr production is called into question however, when we consider that the S18_DD_M10_00 model with no He shell, as well as all PDt models, can produce [Cr/Fe] values that agree well with the observational data.

The complexity of Cr production can be somewhat explained by considering that although

[3]We remind that the yields for S18_DD_M10_00 are updated in Keegans (2022) by post-processing the model with a more extensive network

Cr has four stable isotopes (^{50,52,53,43}Cr), the solar abundance of this element comes almost entirely from the contribution of ^{52}Cr ($\sim$ 84% of solar). The bulk of ^{52}Cr production, regardless of progenitor mass, is as the radiogenic ^{52}Fe at intermediate temperatures $\sim 5-6$ GK during incomplete Si burning (Iwamoto et al., 1999; Keegans, 2022). This means that the Cr yield has very little dependency on the initial metallicity of the progenitor. Instead, Cr production is sensitive to conditions affecting nucleosynthesis during the explosion (Keegans, 2022). This is particularly true when we compare [Cr/Fe] for L18_DDT_M1.33, L18_DDT_M1.38 and L18_DDT_M1.39, which have different central densities. At higher metallicities, the high density model leads to an overproduction relative to solar, whereas [Cr/Fe] is underproduced by the low density model. Finally, we note that all PDf models produce [Cr/Fe] that is consistent with observations.

4.4.1.4 Manganese

A key feature of Mn production in SNe Ia is its dependency on progenitor mass. For this reason, the [Mn/Fe] ratio has been used extensively as a tool to constrain the number of WD progenitor in the Galaxy of either a sub-$M_{\rm Ch}$ or near-$M_{\rm Ch}$ origin.

The only stable isotope of Mn is ^{55}Mn, which is predominantly made as the radioactive ^{55}Co during deflagration and freeze-out from NSE, assuming small mass fractions of ^{4}He (Seitenzahl et al., 2013b). At densities below $\rho \sim 2\times10^{8}$g cm^{-3}, ^{55}Co is destroyed via the reaction ^{55}Co(p,γ)^{56}Ni, which leads to a lower production of Mn from sub-$M_{\rm Ch}$ progenitor. In Figures 4.2 and 4.3 supersolar [Mn/Fe] is obtained for GCE models with pure deflagration explosions or SNe Ia with prolonged periods of burning with subsonic propagation of the flame front, such as the L18_DDT_M1.39 model with higher central density. The ejected mass of Mn also increases with metallicity, since at higher metallicities ^{55}Fe is more readily produced at temperatures of $3-4$ GK (Keegans, 2022). This metallicity dependency is more pronounced for sub-$M_{\rm Ch}$ progenitor than for near-$M_{\rm Ch}$.

In terms of the CC-SNe yields, on average the rotational yields of LC18 produce more Mn than the non-rotating yields of N13, particularly in the mass range $M \lesssim 20M_{\odot}$. This means that in Figure 4.3, the sub-$M_{\rm Ch}$ progenitor models S18_DD_M10_00, G21_DD_M10_03,

and P12_PDt_VM produce enough Mn to reach the solar value, however, in Figure 4.2, no sub-$M_{\rm Ch}$ model reaches within 0.2 dex of solar. There is also a distinct upward trend in [Mn/Fe] at higher metallicities for the DD models in Figure 4.2, but instead the trend flattens in Figure 4.3; this is a consequence of the amount of Mn ejected by the higher metallicity models in the respective CC-SNe yield sets (see also Figure 8 in Gronow et al., 2021b). The [Mn/Fe] data at [Fe/H] $\gtrsim 0$ also appears to have a slight upward trend, which is more in line with the GCE using N13.

The majority of Mn abundance data is based on local thermodynamic equilibrium (LTE) analysis of Mn I and Mn II lines. However, there is an increasing amount of evidence that suggests Mn I lines in particular are strongly affected by non-LTE (NLTE) effects (Bergemann et al., 2019). Applying NLTE corrections to a sample of 42 stars, Eitner et al. (2020) showed that the [Mn/Fe] trend is relatively flat and close to the solar value at all metallicities, rather than highly sub-solar at low metallicites if LTE is assumed. For comparison, we include the NLTE corrected data for [Mn/Fe] from Eitner et al. (2020) in Figures 4.2 and 4.3. At low metallicites, the GCE predictions in both Fig 4.2 & 4.3 do not well fit the NLTE data since [Mn/Fe] is underproduced by the twos sets of CC-SNe yields. Indeed, it has been demonstrated that a better match between GCE predictions and NLTE data at low metallicities can be obtained assuming an enhanced production of Mn from CC-SNe (Palla, 2021; Sanders et al., 2021; Eitner et al., 2022). These papers also predict up to 80% of SNe Ia progenitors to be sub-$M_{\rm Ch}$, which is a much higher percentage than GCE analyses that assume instead LTE Mn measurements (e.g., Kobayashi et al., 2020b, predict < 25% Mn contribution from sub-$M_{\rm Ch}$ progenitor). However, in order to to remain self-consistent, if the Mn yield is artificially increased then considerations must also be made regarding changes in the yields of other elements that are produced in the same region and by the same nucleosynthesis process as Mn.

Despite the fact that Mn production is sensitive to progenitor mass, the constraining potential of [Mn/Fe] is limited by uncertainties surrounding its production in CC-SNe and tension regarding LTE and NLTE measurements (Bergemann & Gehren, 2008; Bergemann et al., 2019; Lomaeva et al., 2019). The GCE predictions herein also confirm that using different CC-SNe yields could significantly alter the needed fraction of sub-$M_{\rm Ch}$ progenitor

to reproduce solar [Mn/Fe]. Furthermore, this fraction is also dependent on the SNe Ia yields, as in Figures 4.2 & 4.3 there is a $\sim$ 0.3 dex difference in [Mn/Fe] at [Fe/H] = 0 for L20_DD_M11_05(Y) and G21_DD_M10_03, despite the fact these models are both based on a double-detonation explosion of a sub-$M_{\rm Ch}$ WD. Likewise, there is a $\sim$ 0.2 dex difference between the pure detonation models P12_PDt_VM and S10_PDt_M1.06 at the end of the simulation. These results confirm differences in Mn production for SNe Ia models with the same explosion mechanism, a result that would not significantly change even if we were to consider a unique DTD for each progenitor scenario.

Another important consideration is the extent of the contribution toward Galactic Mn from SNe Iax. The deflagration models can produce supersolar [Mn/Fe], leading to [Mn/Fe] $\sim$ 0.2 in Figure 4.3. This subclass of SNe Ia could occur with a rate of up to $\sim$ 30% of the classical SNe Ia rate (Srivastav et al., 2022), which could further reduce the necessary fraction of sub-$M_{\rm Ch}$ progenitor. Population synthesis simulations of He-rich accretion in the single-degenerate scenario predict that the majority of SNe Iax should explode in the order of $\sim 10^7$ years (Eitner et al., 2022). A prompt enrichment of supersolar [Mn/Fe] from SNe Iax could go someway in helping to account for the higher [Mn/Fe] data at low metallacities when accounting for NLTE corrections (Kobayashi et al., 2015).

4.4.1.5 Cobalt

The majority of Co in the Galaxy is made by CC-SNe, with a contribution of $\sim$ 20% from SNe Ia at [Fe/H] = 0. In both Figures 4.2 & 4.3 the [Co/Fe] = -0.2 at [Fe/H] = -1.5, which indicates that there is little difference in Co production from N13 and LC18 at lower metallicities.

After [Fe/H] = -1.5 the [Co/Fe] for N13 CC-SNe decreases linearly with metallicity, whereas LC18 CC-SNe decreases until [Fe/H] $\sim$ -1.5, then plateaus until around solar metallicity before decreasing again. Quantitatively, the GCE predictions in Figures 4.2 and 4.3 that include contributions from SNe Ia also follow these general trends, respectively.

Like Mn, Co also has only one stable isotope, ^{59}Co. This isotope is primarily produced by two radiogenic decay channels, from ^{59}Ni and ^{59}Cu, that each dominate at different

temperatures depending on the mass of the progenitor (Keegans, 2022). The Co yield has an increasing trend with metallicity in lower mass SNe Ia models but remains relatively flat at higher masses. Figures 4.2 & 4.3 show that PDf models produce higher [Co/Fe] than all other explosion types. However, although the [Co/Fe] ratio is higher for PDf explosions than others, the absolute yield is low and so they contribute only marginally toward the overall Co inventory when more than one SNe explosion channel is considered. In general, sub-$M_{\rm Ch}$ SNe Ia lead to higher [Co/Fe] than near-$M_{\rm Ch}$, at least when PDf models are not considered.

4.4.1.6 Nickel

Much like Mn, Ni has also been hailed as a diagnostic of WD progenitor mass (Kirby et al., 2019; Kobayashi et al., 2020a; Blondin et al., 2022). Unlike Mn, however, Ni has five stable isotopes ^{58,60,61,62,64}Ni, with ^{58}Ni constituting the largest fraction of the element in terms of both SNe Ia yields and the solar composition (Blondin et al., 2022). ^{58}Ni is mostly synthesised during NSE at temperatures $\gtrsim$ 5 GK (Brachwitz et al., 2000; Blondin et al., 2022; Keegans, 2022). In terms of SNe Ia modeling, the metallicity of the progenitor and, by extension, the resulting electron fraction (Y_e) is often fine tuned by adjusting the ^{22}Ne mass fraction in the pre-explosion material. A WD that evolved from a higher metallicity main sequence star will have a higher ^{22}Ne mass fraction and, since ^{22}Ne is neutron rich, subsequently a lower Y_e. However, the central density of the WD during the explosive burning of material affects the electron chemical potential (Brachwitz et al., 2000). This means that WD with higher central densities (i.e., near-$M_{\rm Ch}$ SNe Ia) have increased Fermi energy and thus enhanced electron-capture rates, which leads to a reduction in Y_e and results in a more efficient production of neutron-rich isotopes (Blondin et al., 2022). The speed of propagation of the flame front during deflagration in near-$M_{\rm Ch}$ also determines the amount of ^{58}Ni that is synthesised, as a slower flame speed means that the outer layers of the core have more time to expand before being incinerated. Therefore, slower flame speeds lead to a decrease in the electron-capture rate as a function of radius in the central core, and consequently a reduction in the ^{58}Ni yield. In summary, the Ni yield i) increases with the density (mass) of the WD progenitor, ii) increases in deflagration models with a faster flame front (e.g., the I99_PDf_M1.40 model),

iii) has a greater metallicity dependency in sub-$M_{\rm Ch}$ models, due to the fact that there is no initial deflagration to allow the Y_e to decrease.

There are large differences in the evolution of [Ni/Fe] for N13 and LC18, with the former having a highly subsolar ratio at [Fe/H] compared to [Ni/Fe] $\simeq 0.2$ for the latter. In CC-SNe, Ni (as ^{58}Ni) is mostly synthesised during explosive Si burning inside the innermost regions of the star, and thus the parameterization of the mixing and fallback determines the amount of Ni that can escape the remnant by being mixed into the ejected material (Limongi & Chieffi, 2018). For stars in the mass range $13 < M < 25 M_{\odot}$ of the set R yields of LC18 the inner border of the mixed region is calibrated such that [Ni/Fe] = 0.2, whereas for N13 with HNe the mixing and fallback parameters are chosen to give the largest [Zn/Fe], which requires a shallower mass cut and thus a lower [Ni/Fe] yield (Nomoto et al., 2006). Close to the onset of SNe Ia enrichment at [Fe/H] ~ -1, the [Ni/Fe] for both N13 and LC18 CC-SNe decreases, leading to [Ni/Fe] $\simeq -0.4$ and [Ni/Fe] $\simeq -0.1$ at [Fe/H] = 0, respectively. This 0.3 dex difference in [Ni/Fe] for the two sets of CC-SNe yields results in markedly different GCE tracks for this ratio in Figures 4.2 and 4.3.

In Figure 4.2, there is a steep increase in [Ni/fe] for all near-$M_{\rm Ch}$ models after [Fe/H] $\gtrsim -1$, with no clear difference in the rate of increase between the PDf models of F14_PDf_M1.40 and K15_PDf_M1.40 and the DDT models. An exception, however, is I99_PDf_M1.40 which increases faster than the others and reaches highly subsolar [Ni/Fe]. The W7 model of I99_PDf_M1.40 has been, and indeed still is, adopted by many GCE models, and as such its tendency to grossly overestimate Galactic Ni has been well documented. For all other near-$M_{\rm Ch}$ models there is good agreement with the observational data, with a slight under or overestimation of [Ni/Fe] relative to solar for L18_DDT_M1.33 and L18_DDT_M1.39, respectively.

For the sub-$M_{\rm Ch}$ models in Figure 4.2, the GCE tracks show different behaviours for each of the SNe Ia yields: P12_PDt_VM and G21_DD_M10_03 initially increase, though less rapidly than for near-$M_{\rm Ch}$, before reaching a plateau of [Ni/Fe] ~ -0.1 at [Fe/H] $\simeq 0$; S18_DD_M10_00, L20_DD(S), and L20_DD(Y) remain relatively flat until [Fe/H] ~ -0.5 when they increase; S10_PDt_M1.06 stays constant until [Fe/H] ~ 0 and then decreases, following a similar trend as for N13 CC-SNe. All sub-$M_{\rm Ch}$ models in Figure 4.2 produce

subsolar [Ni/Fe] at [Fe/H] = 0.

In Figure 4.3, since the GCE tracks with LC18 have supersolar [Ni/Fe] for [Fe/H] $\lesssim -1$, an increase in [Ni/Fe] is only seen for I99_PDf_M1.40. Due to the decrease in [Ni/Fe] from LC18 CC-SNe after [Fe/H] ~ 1, the GCE tracks for S13_DDT_M1.40 and L18_DDT_M1.33 also decrease from [Ni/Fe] $\simeq 0.2$ to [Ni/Fe] $\simeq 0.1$ at [Fe/H] = 0. The remaining near-$M_{\rm Ch}$ models have GCE tracks that remain relatively flat, resulting in [Ni/Fe] $\simeq 0.2$ at [Fe/H] = 0.

There is less variation in the chemical evolution patterns of the sub-$M_{\rm Ch}$ models in Figure 4.3, as Ni production is lower than for near-$M_{\rm Ch}$ the GCE is more heavily influenced by the sharp decrease in [Ni/Fe] production from LC18 CC-SNe in the [Fe/H] $\gtrsim -1.0$ regime. Despite this, all sub-$M_{\rm Ch}$ models in this Figure have good agreement with the observational data and lie within 0.1 dex of solar at [Fe/H] = 0.

4.4.2 The evolution of Cr and Mn relative to Ni

In this Section we compare [Cr/Fe] and [Mn/Fe] versus [Ni/Fe] for each of the GCE models in Figures 4.2 and 4.3. The Cr to Ni relationship is interesting due to the respective way these elements are synthesised during the SNe Ia explosion - the bulk of Cr production is mostly primary and at intermediate temperatures, whereas the majority of stable Ni is produced at higher explosive temperature peaks during NSE and is therefore dependent on the mass of the WD progenitor star (see relevant Sections above for further detail). Furthermore, there are large discrepancies between the production of both elements in N13 and LC18 CC-SNe models, with the former having supersolar Cr and subsolar Ni at [Fe/H] < -1.0, whereas the reverse is true in the latter.

Figure 4.4 (top panel) shows the evolution of [Cr/Fe] with respect to [Ni/Fe] for each of the SNe Ia yields investigated in this work. The thick and thin lines indicate GCE calculations made with N13 and LC18, respectively. Only the GCE starting from the time of first SNe Ia enrichment is shown, i.e. from [Fe/H] $\gtrsim -1.0$. The positions of the cyan and magenta stars on each line indicate the time at which the Galaxy is 3 Gyr and 8.6 Gyr old respectively, where the last is taken to be the age of the Galaxy at the time of the birth of the Sun, $t_{\odot}$.

There is a > 0.3 dex difference in both [Cr/Fe] and [Ni/Fe] between N13 and LC18 GCE models at the time of first SNe Ia enrichment. This leads to two profoundly different chemical

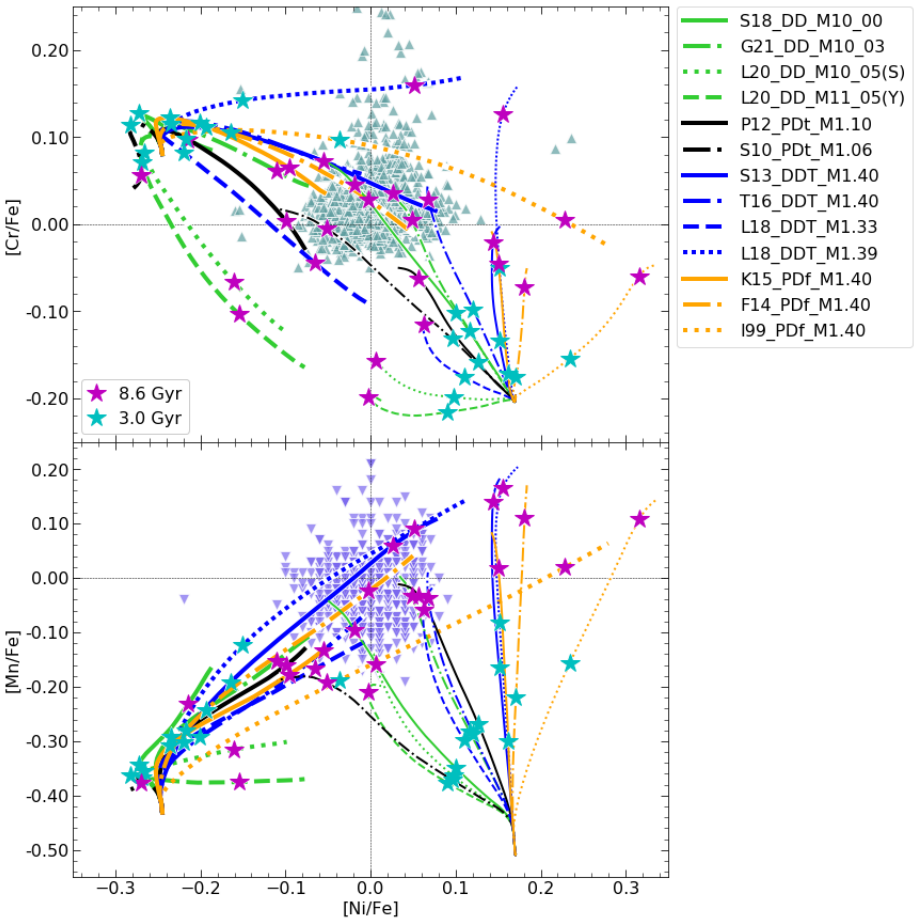

Figure 4.4: Predicted evolution of [Cr/Fe] (top panel) and [Mn/Fe] (bottom panel) versus [Ni/Fe] for different SNe Ia yields. Thick lines are GCE predictions made with N13, whereas thin lines use LC18. The GCE tracks are plotted from the time of first SNe Ia enrichment. The positions of the cyan and purple stars along the GCE tracks indicate a Galactic time of 3.0 Gyr and 8.6 Gyr, respectively, where the last is taken to be the age of the Galaxy at the time of the birth of the Sun. Observational data are colour coded according to Figures 4.2 and 4.3.

evolution tracks for each SNe Ia model, depending on the choice of massive star yields. In general, the N13 GCE models better fit the observational data in the [Cr/Fe] versus [Ni/Fe] plane, due to the fact that the majority of the observational data is at supersolar [Cr/Fe]. Furthermore, since the [Cr/Fe] from N13 massive stars is supersolar, after 3 Gyr the scatter in [Cr/Fe] between different N13 GCE models is $\lesssim 0.1$ dex. On the other hand, after the same amount of time there is a larger scatter for the LC18 GCE models, owing to the fact that the massive star yields produce instead subsolar [Cr/Fe] and therefore the Cr that is ejected by SNe Ia constitutes a greater fraction of the total amount of Cr in the Galaxy. For the N13 models at $t_{\odot}$, there appears to be a correlation between [Ni/Fe] and [Cr/Fe], with models with higher [Ni/Fe] also having higher [Cr/Fe]. An obvious exception is S10_PDt_M1.06, which has subsolar [Ni/Fe] but supersolar [Cr/Fe]; Figure 4.1 shows that this model exhibits a particularly strong odd-even effect up to Fe, beyond which the production of higher mass Fe-group elements is inhibited by the relatively low core density ($\rho_c = 4.15 \times 10^7$). However, due to the supersolar [Ni/Fe] for LC18 massive star yields, this model results in only a slightly subsolar [Ni/Fe] value at $t_{\odot}$ and agrees well with the observational data. In contrast, the PDf models produce highly supersolar [Ni/Fe] due to increased electron-capture rates during deflagration; this results in a fast evolution toward the solar value for N13 GCE tracks, with I99_PDf_M1.40 having [Ni/Fe] within 0.05 dex of the solar value at $t_{\rm gal} = 3$ Gyr. However, since the LC18 massive star yields lead to supersolar [Ni/Fe] prior to SNe Ia enrichment, there is a much less rapid increase in [Ni/Fe] for the PDf models, with K15_PDf_M1.40 actually slightly decreasing with time.

The bottom panel of Figure 4.4 shows the same GCE tracks as in the top panel, but for [Mn/Fe] versus [Ni/Fe]. The evolution of Mn and Ni are compared as they are the most commonly used elements to constrain the sub/near-$M_{\rm Ch}$ SNe Ia ratio.

The observations for [Ni/Fe] occupy a range of values from ~ -0.1 to ~ 0.1 dex, with an almost symmetrical distribution about [Ni/Fe] = 0, whereas there are more data at subsolar [Mn/Fe] values within the range ~ -0.2 to ~ 0.1. Comparing the GCE predictions (for both N13 and LC18) at $t_{\rm gal} = 3$ Gyr and $t_{\rm gal} = t_{\odot}$, there is a positive, almost linear relationship between [Ni/Fe] and [Mn/Fe] due to the fact that the production of both Mn and Ni depends on the density of the WD progenitor - this is evident when comparing the yields for these

elements between different SNe Ia models in Figure 4.1. Furthermore, both ratios increase with metallicity of the progenitor (see Figure 24 in Kobayashi et al., 2020a). For N13, several near-$M_{\rm Ch}$ SNe Ia are able to simultaneously reproduce the [Mn/Fe] and [Ni/Fe] ratios, however, all sub-$M_{\rm Ch}$ SNe Ia produce too little Mn and Ni. On the other hand, the best agreement to the data for the LC18 GCE models is found when using sub-$M_{\rm Ch}$ SNe Ia yields, whereas the near-$M_{\rm Ch}$ SNe Ia overproduce both elements (with the exception of the T16_DDT_M1.40 and L18_DDT_M1.33 models which reach [Mn/Fe] ≈ -0.05 at $t_\odot$ and overproduce [Ni/Fe] by $\lesssim 0.1$ dex).

4.5 Parameter study of yield combinations

In this Section we test the goodness of fit for GCE models that include contributions from a combination of different SNe Ia yields, in order to make predictions about the fraction of sub- and near-$M_{\rm Ch}$ SNe Ia in the Galaxy.

Iterating through all sub- and near-$M_{\rm Ch}$ yields (except PDf explosions) in Section 4.2, we calculate GCE models using all possible sub- and near-$M_{\rm Ch}$ SNe Ia yield combinations with different fractional contributions of each. For each of the $\sim$ 1200 GCE models, we perform a χ^2 test in order to quantify the yield combinations and relative fraction of sub/near-$M_{\rm Ch}$ that best predict the observational data.

For a given GCE model, the χ^2 test is calculated as

$$\chi^2 = \frac{1}{N}\sum_{i=1}^{N}\left(\frac{P_i - O_i}{\sigma_{O_i}}\right)^2, \tag{4.5}$$

where the sum is taken over the number of observational data points N that have [Fe/H] ≥ -1 (such that the calculation is only performed from the time of first SNe Ia enrichment). For a given observational measurement with $N = i$, the least-squares is calculated as the difference in [X/Fe] between the observational data O_i and the GCE model prediction P_i, where O_i and P_i have the same [Fe/H]. The denominator σ_{O_i} is the summation of the uncertainty in [X/Fe] and [Fe/H] that is associated with star O_i. Since the resolution of the GCE calculation is limited by the number of timesteps, some observational data will have [Fe/H] values that do not correspond exactly to the calculated [Fe/H] of the Galaxy at any given timestep. In this

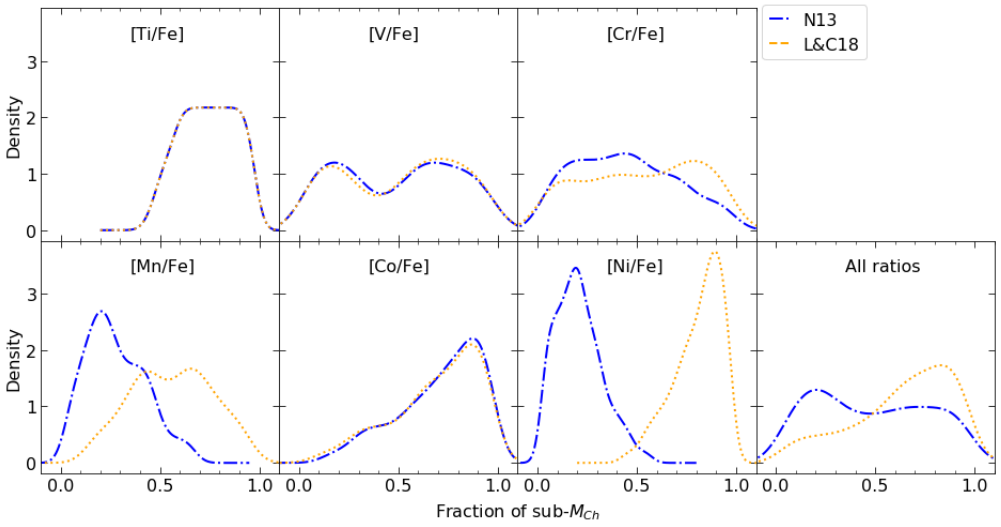

Figure 4.5: Probability density function of GCE models with a χ^2 score in the 84$^{\text{th}}$ percentile, as a function of the fractional contribution from sub-M_{Ch} SNe Ia in those GCE models (see text for details). The dashed blue and solid orange lines are for GCE models with N13 and LC18 massive star yields, respectively.

instance, P_i is calculated as $Fn([\text{Fe/H}_{O_n})$, where O_n is one such observational data point and the function Fn is derived by overfitting a cubic interpolation onto the GCE model.

In order to place constraints on the relative fraction of sub/near-M_{Ch} progenitor, for each element and for each set of massive star yields we consider the GCE models with a χ^2 score in the upper 84$^{\text{th}}$ percentile. The GCE tracks for models with a combination of sub- and near-M_{Ch} yields are shown in Appendix B. Figure 4.5 shows the 84$^{\text{th}}$ percentile kernel density estimations (KDE) for each element as a function of the sub-M_{Ch} fraction f_{sub} in the GCE models. The density of the KDE at fraction f_{sub} indicates the relative number of GCE models in the 84$^{\text{th}}$ percentile with f_{sub} sub-M_{Ch} yields and $1 - f_{\text{sub}}$ near-M_{Ch} yields. The KDE is normalised such that $\int \text{density}(f_{\text{sub}}) df_{\text{sub}} = 1$, where the integral is taken over all fractions f_{sub}. The blue and orange lines indicate KDEs calculated for GCE models with N13 or LC18 massive star yields, respectively. The bottom right panel shows the spread of the sub-M_{Ch} fraction in the GCE models summed for all [X/Fe] ratios.

Further to examining the spread of f_{sub} in the best fit GCE models, for each element we investigate the number of GCE models in the 84$^{\text{th}}$ percentile based on the specific choice of SNe Ia yields. Figure 4.6 shows a histogram of the number of GCE models in the 84$^{\text{th}}$ percentile based on the choice of sub-M_{Ch} (top panel) and near-M_{Ch} yields (bottom panel).

By examining Figures 4.5 and 4.6 in tandem, we can see the sub/near-$M_{\rm Ch}$ ratios and SNe Ia models that provide the best fit to the observational data and how much the choice of massive star yields can affect the constraining capabilities of such GCE tests.

In Figure 4.5 the KDE for [Ti/Fe] is identical for both N13 and LC18 GCE models. The KDE shows that nearly all GCE models in the 84$^{\rm th}$ percentile have a > 0.5 fraction of sub-$M_{\rm Ch}$ yields which, when examining Figure 4.6, are exclusively from the L20_DD_M10_05(S) and G21_DD_M10_03 sub-$M_{\rm Ch}$ models. Since all GCE models in this percentile use only one of two sub-$M_{\rm Ch}$ yields, the peak of the KDE is relatively flat and extends between $0.6 < f_{\rm sub} < 1$. Since L20_DD_M10_05(Y) and G21_DD_M10_03 are required to obtain a good fit, Figure 4.6 (bottom panel) shows that there is an almost even distribution of the adopted near-$M_{\rm Ch}$ yields in the best-fitting GCE models. Our results for Ti agree with Palla (2021), who reason that a significant contribution from DD SNe Ia explosions with aspherical He detonation (i.e. non S-type) are required to match solar Ti. We also find that GCE models using G21_DD_M10_03 lead to similar χ^2 values to those of L20_DD_M11_05(Y). The reason for this is unclear, however, in Gronow et al. (2021b) the authors note that increasing the contribution of G21_DD_M10_03 in their GCE calculations so as to match solar Mn, would lead to an overestimation of the Ti yield. Regardless, Ti production favours a dominant $f_{\rm sub}$ in the Galaxy.

Similar to Ti, the KDE for [V/Fe] is identical for N13 and LC18 GCE models. However, the KDE covers a wider range of $f_{\rm sub}$ than Ti and has a distinct double-peak shape, with symmetry about $f \simeq 0.5$. Looking at Figure 4.6, the double-peak feature of the KDE is clearly an artifact of the fact that there are two best-fitting SNe Ia yields that dominate the 84$^{\rm th}$ percentile: L20_DD_M11_05(Y) for sub-$M_{\rm Ch}$ and L18_DDT_M1.39 for near-$M_{\rm Ch}$. The strong binarity of $f_{\rm sub}$ for the best fitting GCE models indicates that this ratio is not a good determinant for the fraction of sub-$M_{\rm Ch}$ in the Galaxy.

The KDE for [Cr/Fe] has subtle differences depending on the choice of massive star yields, however, in both cases the distribution is relatively low and flat. For N13, the distribution is shifted slightly in favour of a higher contribution from near-$M_{\rm Ch}$, whereas for LC18 the opposite is true. A wide distribution indicates that there are a range of $f_{\rm sub}$ that fit the observational data to an almost equal degree. By virtue of being the models that produce

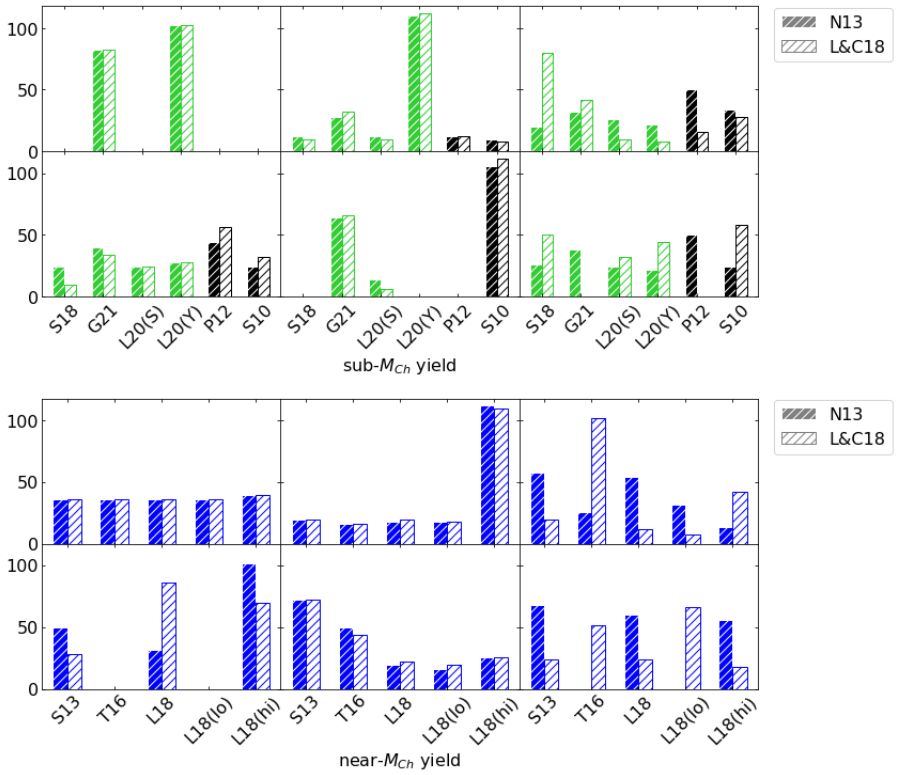

Figure 4.6: Number of of sub-$M_{\rm Ch}$ (top panel) and near-$M_{\rm Ch}$ (bottom panel) SNe Ia yields that are used by N13 and LC18 GCE models with a χ^2 score in the 84$^{\rm th}$ percentile. The colors indicate the explosion mechanism, as in Figures 4.2 and 4.3. The panels are arranged according to the elemental ratios shown in Figure 4.5.

the highest amount of Cr, the S18_DD_M10_00 and T16_DDT_M1.40 yields are the most common among GCE models in the 84$^{\text{th}}$ percentile for LC18. This suggests that Cr production in SNe Ia is sensitive to the choice of reaction network rather than progenitor mass, since we remind that for these models we take the updated yields from Keegans (2022).

The differences in Figure 4.5 are more apparent for Mn. For N13, the distribution peaks at $f_{\text{sub}} \simeq 0.2$, with very few GCE models with $f_{\text{sub}} > 0.5$ having a χ^2 in the upper 84$^{\text{th}}$ percentile. In contrast, for LC18 the distribution covers a broader range of fractions, with the highest number density in the range $0.4 < f_{\text{sub}} < 0.7$. This disparity is to be expected, since Mn production is enhanced in LC18 relative to N13, less near-M_{Ch} progenitor are necessary to obtain a good fit to the observational data. Furthermore, even for the N13 GCE models, at least some fraction of sub-M_{Ch} SNe Ia is favoured in order to not overproduce [Mn/Fe] at solar and higher metallicities. For comparison to other work, the peak fraction of $f_{\text{sub}} \simeq 0.2$ for N13 GCE models agrees with Kobayashi et al. (2020a), who conclude that sub-M_{Ch} must contribute up to $\sim 25\%$ of SNe Ia chemical enrichment. The massive star yields used therein are also similar to N13, however, they only use LTE abundances for Mn. Using similar massive star yields, Palla (2021) find that they can best fit MnII LTE and Mn NLTE data with a GCE model that has a 25% contribution from sub-M_{Ch}. On the other hand, Eitner et al. (2022) find that a higher fraction ($\sim 60\%$) of sub-M_{Ch} SNe Ia can reproduce the NLTE data, even when using the N13 yields. Therein they consider unique DTDs for different explosion mechanisms based on a binary population synthesis code, and also apply a scaling factor to the massive star yields to better reproduce NLTE data in the [Fe/H] $\lesssim 2.5$ regime. Their results are more in line with the $0.4 < f_{\text{sub}} < 0.7$ range we find for the maximum density in the 84$^{\text{th}}$ percentile KDE for LC18.

In Sections 4.3 and 4.4.2, it was found that GCE models with PDf SNe Ia yields lead to supersolar [Mn/Fe]. However, these explosions eject too little ^{56}Ni to be considered 'normal' SNe Ia, and are instead the leading candidate to explain the subluminous .Iax subclass (*c.f.* Karambelkar et al., 2022). Binary population synthesis models have shown that .Iax can have delay times much shorter than typical SNe Ia, leading to a prompt enhancement of [Mn/Fe] in the Galaxy. To test whether a prompt contribution from .Iax can help correct for the [Mn/Fe] deficit predicted by GCE models when compared to NLTE observations, we run additional

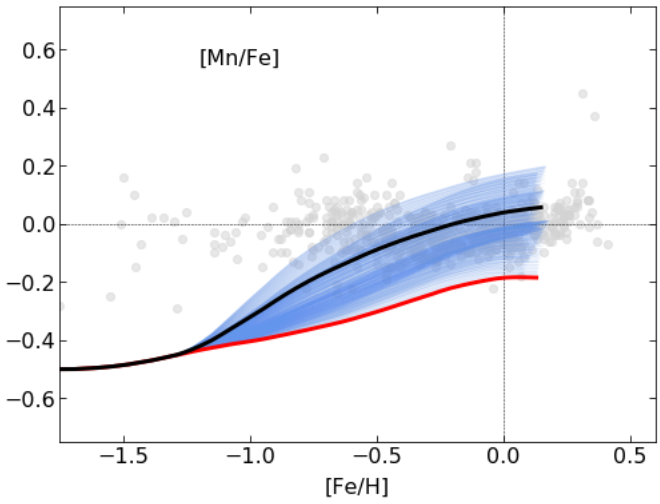

Figure 4.7: GCE model predictions for [Mn/Fe] with LC18 massive star yields with a combination of sub- and near-$M_{\rm Ch}$ SNe Ia, including also a 20% contribution from faint SNe .Iax. The best and worst fitting predictions as calculated by the χ^2 test are shown by the black and red lines, respectively. Observational data are the same as in Figures 4.2 and 4.3.

GCE models that take into account also a contribution from .Iax SNe Ia. In these models we assume that SNe .Iax explode at a rate of 20% of normal SNe Ia, such that the total SNe Ia rate is 1.56×10^{-3} $M_{\odot}^{-1}$, and their delay time distribution peaks sharply at $\sim$ 100 Myr (see, e.g. Liu et al. (2015)). Since low-luminosity .Iax make up the bulk of the total .Iax rate (Srivastav et al., 2022), we use the yields from the K15_PDf_M1.40 model, which is shown to have good agreement to the subluminous SN 2008ha.

The [Mn/Fe] versus [Fe/H] for GCE models including a 20% prompt contribution from SNe .Iax are shown in Figure 4.7, where the best and worst fitting models to the observational data are shown by the black and red lines, respectively. There are negligible differences in [Mn/Fe] at [Fe/H] < -1 for Figures 4.7 and 4.3, this is also confirmed by our statistical test which shows identical $f_{\rm sub}$ for GCE models with and without a contribution from SNe .Iax. Therefore, we claim that SNe .Iax events are both too rare and eject too little Mn to affect the evolution of [Mn/Fe], even at earlier Galactic times. This result is in agreement with Eitner et al. (2022), who find that unless the .Iax rate is unrealistically high ($\gtrsim$ 70% of the total SNe rate), the amount of Mn ejected by each event is too low to significantly affect the GCE of [Mn/Fe].

For Mn, it is important to consider also the choice of near-$M_{\rm Ch}$ SNe Ia yields used in

the GCE calculations, as L18_DDT_M1.39 (for LC18) or T16_DDT_M1.40 (for N13) are adopted by a large number of GCE models in the 84$^{\text{th}}$ percentile. Only a small number of the best-fitting GCE models use S13_DDT_M1.40, whereas none of the best-fitting GCE models use L18_DDT_M1.38 or L18_DDT_M1.33. The choice of sub-M_{Ch} SNe Ia yields are of lesser importance, though P12_PDt_VM and to a lesser extent G21_DD_M10_03 are favoured by both N13 and LC18 due to the fact they provide a slightly better fit to the observational data than other sub-M_{Ch} yields at [Fe/H] ~ -1 (see Figures 4.2 and 4.3).

For [Co/Fe], the distribution is again near identical for N13 and LC18, with a strong correlation between the goodness of fit of the GCE model and a higher f_{sub}. Figure 4.6 shows that the majority of sub-M_{Ch} yields in the 84$^{\text{th}}$ percentile are G21_DD_M10_03 and S10_PDt_M1.06, with a more varied distribution for near-M_{Ch} yields.

The largest difference in f_{sub} between N13 and LC18 GCE models is for [Ni/Fe]. Figure 4.5 shows that both probability density distributions have well-defined peaks - at $f_{\text{sub}} \simeq 0.2$ for N13 and $f_{\text{sub}} \simeq 0.9$ for LC18 - with comparatively few models in each distribution having $f_{\text{sub}} \sim 0.5$. This result is particularly troubling, because it calls into question the validity of using [Ni/Fe] to constrain SNe Ia while a large uncertainty is associated with the Ni yield from massive stars. Since [Ni/Fe] is supersolar for LC18 at [Fe/H] < 1 (we remind this is due to the choice of mixing and fallback which determines the position of the mass cut), a higher f_{sub} is favoured since sub-M_{Ch} SNe Ia have lower [Ni/Fe] than near-M_{Ch}. On the other hand, the [Ni/Fe] plateau prior to SNe Ia enrichment for N13 GCE models is sub-solar, therefore a higher number of near-M_{Ch} SNe Ia are required in order to fit the observational data. In both cases, the sharp peak of the KDE in Figure 4.5 indicates that f_{sub} is more important for reproducing the observational data than the specific SNe Ia yields. This is confirmed in Figure 4.6, since no one sub- or near-M_{Ch} yield dominates in the best-fitting GCE models.

Finally, in Figure 4.5 we plot the distribution of f_{sub} in GCE models across all ratios combined. In general, the Fe-peak elements are better fit for LC18 GCE models by a higher f_{sub}, whereas the distribution of f_{sub} is more evenly distributed (though is slightly weighted in favour of $f_{\text{sub}} < 0.5$) for N13 GCE models. The most important elemental ratio for determining f_{sub} is [Ni/Fe], as indicated by the sharply peaked KDE and the relatively even spread of SNe Ia models in Figure 4.6.

4.6 Discussion and Conclusion

In this work, we investigated the GCE of the Fe-peak elements (Ti, V, Cr, Mn, Co, and Ni) using yields from four different SNe Ia explosion mechanisms and two sets of massive star yields: N13 (non-rotating) and LC18 (rotating). We compare our GCE predictions to spectroscopic measurements in stars and describe the results by analysing the nucleosynthesis conditions that are required to produce each element during the explosion. In particular, we consider how the predicted evolution depends on the mass of the WD progenitor and the choice of massive star yields. We calculate GCE models that include contributions from both sub- and near-$M_{\rm Ch}$ SNe Ia, including a suite of GCE models that take into account a 20% contribution from the faint .Iax subclass. For each element, a statistical test is used to score the models based on the goodness of fit to the stellar data, and a probability density estimation is made over the fraction of sub-$M_{\rm Ch}$ SNe Ia for N13 and LC18 GCE models with a χ^2 score in the $84^{\rm th}$ percentile. These are cross-compared with the distribution of SNe Ia yields that are used in the best-fitting GCE models to help constrain the relative fraction of sub- and near-$M_{\rm Ch}$ SNe Ia in the Galaxy.

We show that the present uncertainties and large variations affecting the yields of the Fe-peak elements in CC-SN yields do not allow the use of GCE simulations alone to constrain the populations of SNe Ia progenitors in the Milky Way disk. If we use CC-SN yields by LC18, the GCE models better reproduce the observations using a sub-$M_{\rm Ch}$ fraction ($f_{\rm sub}$) $\gtrsim$ 0.5. In particular, we obtain a best match for [Mn/Fe] with $0.4 \lesssim f_{\rm sub} \lesssim 0.7$, and $f_{\rm sub} \approx 0.9$ for [Co/Fe] and [Ni/Fe], with no strong constraints from [V/Fe]. If we use N13, we obtain contradicting indications from different elements: the [Ti/Fe] and [Co/Fe] are best fit by high $f_{\rm sub}$, while [Cr/Fe], [Mn/Fe] and [Ni/Fe] are best fit by low $f_{\rm sub}$ values (with $f_{\rm sub} \approx 0.2$ for [Ni/Fe]). Therefore, GCE results need to be used carefully to infer about the contribution from different SNIa populations, and for these applications they should be used together with other independent theoretical and observational indicators. Additionally, we also show that all available Fe-peak elements should be considered in the GCE analysis, since misleading results can be obtained by only using single elemental ratios (e.g., [Mn/Fe] or [Ni/Fe]), which may not be representative of the overall behavior of the Fe-peak elements themselves.

Further results are summarised below.

- The GCE of [Mn/Fe] and [Ni/Fe] after [Fe/H] ~ -1 are sensitive to the relative fraction of SNe Ia in the Galaxy from the sub- and near-$M_{\rm Ch}$ WD progenitor channels. However, the inter-channel explosion mechanisms (i.e., whether DDT or PDF yields are used for near-$M_{\rm Ch}$, or DD or PDt for sub-$M_{\rm Ch}$) do not significantly change the GCE of either element.

- We have shown that the fraction of sub-$M_{\rm Ch}$ SNe Ia ($f_{\rm sub}$) that best fit the [Ni/Fe] spectroscopic data depends on the choice of massive star yields. The GCE models that use N13 require a higher fraction of near-$M_{\rm Ch}$ SNe Ia than those that use LC18 - for [Ni/Fe] the probability density function of the best-fitting GCE models peaks at $f_{\rm sub} \simeq 0.2$ (N13) and $f_{\rm sub} \simeq 0.9$ (LC18). However, the position of the mass cut in CC-SNe models determined by the mixing and fallback scheme is the largest source of uncertainty for GCE predictions of [Ni/Fe]. Therefore, at present this abundance ratio cannot reliably be used in GCE studies to constrain SNe Ia explosion mechanisms.

- Despite the fact they produce supersolar [Mn/Fe], an additional prompt enrichment of SNe .Iax results in a negligible increase of [Mn/Fe] at low metallicities. This is because their absolute yields are too low and they are too few in number to counterbalance the [Mn/Fe] deficit from massive stars compared to NLTE abundance measurements in the [Fe/H] $\lesssim -1$ regime.

- In terms of explosion mechanisms that lead to 'normal' SNe Ia (i.e., classifying PDf explosions as the .Iax sub-class), sub-$M_{\rm Ch}$ SNe Ia typically lead to ~ 0.1 dex higher [Co/Fe] than near-$M_{\rm Ch}$ SNe Ia at [Fe/H] = 0. Both N13 and LC18 massive star yields have a decreasing [Co/Fe] trend with metallicity after [Fe/H] ~ -1, which means that the majority of best-fitting GCE models have $f_{\rm sub} \simeq 0.8 - 0.9$. However, it is important to consider that the 0.1 dex difference in [Co/Fe] from sub- and near-$M_{\rm Ch}$ GCE models at solar metallicity might be smaller than the typical error associated with observational measurements of [Co/Fe]. This, combined with the fact that the majority of Co in the Galaxy is from CC-SNe, means that [Co/Fe] cannot reliably be used to determine $f_{\rm sub}$.

- At lower metallicities, the choice of massive star yields is significant for the GCE of V and Cr. At [Fe/H] $\lesssim -1$ the non-rotating massive star yields of N13 are ~ 0.3 dex higher for [Cr/Fe] than for the rotating massive star yields of LC18. For N13, the [V/Fe] plateaus at low metallcities before decreasing after [Fe/H] $\gtrsim -0.1$, whereas for LC18 the metallicity is highly subsolar at low metallicities before increasing with metallicity. However, for [V/Fe] only the sub-$M_{\rm Ch}$ model L20_DD_M11_05(S) and the near-$M_{\rm Ch}$ L18_DDT_M1.39 model can reach solar.

- For [Ti/Fe], despite the systematic underproduction in this ratio for the GCE models at lower metallicities, both the L20_DD_M11_05(Y) model with ring He detonation and G21_DD_M10_03 model lead to predicted values within 0.1 dex of solar. In comparison, the L20_DD_M10_05 model with spherical He detonation leads to [Ti/Fe] $\simeq -0.3$ at [Fe/H] = 0. Similarly, of the sub-$M_{\rm Ch}$ models, only L20_DD_M11_05(Y) can reproduce solar [V/Fe]. In terms of the other Fe-peak elements, the L20_DD_M11_05(Y) model is unremarkable from other DD and PDt models, which suggests that at least some fraction of sub-$M_{\rm Ch}$ SNe Ia have an aspherical He detonation pattern. This notion was also proposed by Palla (2021), wherein they investigated the Leung & Nomoto (2020) benchmark model with bubble He explosion geometry.

Acknowledgements

This work made use of the Heidelberg Supernova Model Archive (HESMA), `https://hesma.h-its.org`. We are grateful to Ashley Ruiter for providing SNe Ia delay-time data to compare with our fiducial rate. TT, MP, and BKG acknowledge the support of STFC (through the University of Hull's Consolidated Grant ST/R000840/1) and ongoing access to `viper`, the University of Hull High Performance Computing Facility. BC, MP, and BKG thank the National Science Foundation (NSF, USA) under grant No. PHY-1430152 (JINA Center for the Evolution of the Elements). BKG and MP acknowledge the support of the European Union's Horizon 2020 research and innovation programme (ChETEC-INFRA – Project no. 101008324). MP thanks the "Lendulet-2014" Program of the Hungarian Academy of Sciences (Hungary) and the ERC Consolidator Grant (Hungary) funding scheme (Project

RADIOSTAR, G.A. n. 724560).

Data Availability

The data generated for this article will be shared on reasonable request to the corresponding author.

5. Discussion and conclusions

In this thesis we have demonstrated how chemical evolution models can be used to constrain both the timescales of events in the early Solar System and the SN Ia history of the Galaxy. By using several different mass- and metallicity-dependent stellar yield sets, our results account for variations in the GCE due to differences in the choice of input physics between stellar modelling groups. In this Chapter the main results of this thesis are summarised, and some relevant future research areas are then discussed.

5.1 GCE with short-lived radionulcides: radiometric determination of timescales in the early solar system

Short-lived radionuclides (SLRs) with half-lives of the order of a few Myr are important tools for measuring the timescales of events predating the birth of the Sun. To this end, in Chapter 3 we use the `OMEGA+` GCE code to predict the evolution of the radioactive-to-stable abundance ratio for three SLRs (^{107}Pd, ^{135}Cs, and ^{182}Hf) in the ISM. The GCE predicted ratios at the time of the birth of the Sun are then decayed to the early Solar System (ESS) ratios inferred from meteorites, and the time taken for the decay is a measure of the length of time that the parcel of ESS matter was isolated from further stellar enrichment events, or the "isolation time". In order to account for nuclear physics uncertainties, two sets of mass- and metallicity-dependent AGB yields are considered in the GCE calculations (FRUITY and Monash), since these are the primary astrophysical production sites for the three SLRs of interest. Only the Monash yields are considered for the isolation time calculations using Hf, since the FRUITY models assume an outdated stellar decay rate for ^{181}Hf.

In Paper II (Côté et al., 2019c) it was found that the uncertainty factors for SLR abundances in the ISM depend on the ratio τ/γ, where τ is the mean life of the SLR and γ is the average recurrence time for enrichment events. If $\tau/\gamma \gtrsim 2$ (Regime I), the SLR does not have time to completely decay in the ISM before it is replenished, eventually reaching a steady-state abundance that can be properly quantified with statistical confidence levels. In Regime I,

the derived isolation times are self-consistent between 9 and 26 Myr for both sets of AGB yields. Furthermore, using the ^{107}Pd/^{182}Hf ratio we determine that ^{107}Pd is potentially underproduced relative to ^{182}Hf, which may indicate that a production site of the first peak *s*-elements is "missing"' from our GCE models – this is in qualitative agreement with other GCE studies that have claimed that an as-yet unidentified lighter element primary process (LEPP) is required to correctly predict the solar *s*-distribution of isotopes at and around the first *s*-peak (Travaglio et al., 2004; Bisterzo et al., 2014, 2017). Recently, Cseh et al. (2022) found that four stars from a sample of 28 Ba-enhanced stars were overabundant in first *s*-peak isotopes compared to model predictions – this could indicate that these stars are hosts of a LEPP-like process, however, future nucleosynthesis and GCE studies would be required to confirm the viability of this.

If instead $\tau/\gamma \lesssim 0.3$ (Regime III), then the SLR has enough time to significantly decay before it is replenished, such that its ISM abundance does not accumulate to a steady state value but is instead largely dominated by the stochastic nature of stellar enrichment events. In Regime III, since the SLR could have completely decayed from the ISM, it is possible to calculate only the time from the formation of the Solar System and the last *s*-process enrichment event, rather than the isolation time. For the Monash yields, a self-consistent solution for all abundance ratios is found for the $2M_{\odot}$, $Z = 0.01$ AGB model and a time from the last event of 25.5 Myr.

5.2 GCE with different Type Ia supernova explosion mechanisms: constraining SNe Ia progenitors in the Milky Way

Thermonuclear explosions of CO white dwarfs (WDs) as type Ia supernova (SNe Ia) play a significant role in the chemical evolution of the Milky Way. However, a long standing and as yet unresolved problem of modern astrophysics concerns the identity of their progenitor. It is possible to use GCE to help constrain potential progenitor scenarios because SNe Ia nucleosynthesis yields, in particular the Fe-peak elements, depend on the explosion mechanism. In Chapter 4, predicted abundance ratios calculated using the `OMEGA+` GCE code for four different SNe Ia explosion mechanisms are compared to stellar spectroscopic measurements. Considerations are made regarding differences in the GCE depending on whether

the WD progenitor is sub-Chandrasekhar or near-Chandrasekhar at the time of explosion. Furthermore, the GCE framework is calibrated for two sets of massive star yields in order to asses the implications of rotation on the relative contribution from CC-SNe toward the Fe-peak elements. The fraction of sub-$M_{\rm Ch}$ ($f_{\rm sub}$) that best fit the spectroscopic data for GCE models with rotating CC-SNe is $0.4 \lesssim f_{\rm sub} \lesssim 0.7$ and $f_{\rm sub} \approx 0.9$ for [Mn/Fe] and [Ni/Fe], respectively. This range for $f_{\rm sub}$ is in agreement with the results of Eitner et al. (2022), who find that the best fit to the data is obtained by GCE models with $f_{\rm sub} \sim 60\%$. If, however, rotation-induced effects are not included then the best-fitting models have $f_{\rm sub} \sim 0.2$ for both [Mn/Fe] and [Ni/Fe], which is in agreement with the upper limit of 25% contribution from sub-$M_{\rm Ch}$ found for the GCE models of Kobayashi et al. (2020a). The large disparity in $f_{\rm sub}$ found in this work between GCE models that use rotating and non-rotating massive star yields suggests that GCE is not a robust constraint of SNe Ia progenitor. In particular, the results depend on the choice of CC-SNe yield set used for the GCE calculations, where still large uncertainties do exist, even without considering the impact of rotation (see, e.g. Romano et al., 2010; Mollá et al., 2015). Furthermore, the GCE models do not well reproduce the [Mn/Fe] data at [Fe/H] $\lesssim -1$, even if a prompt enrichment from SNe .Iax is considered. Also, Ti, V, and Co are not well fit by any yield combinations, however, [Co/Fe] slightly favours a higher sub/near-$M_{\rm Ch}$ ratio irrespective of whether or not the CC-SNe yields take into account rotation.

5.3 Future work

5.3.1 Inhomogeneous GCE models

In the `OMEGA+` GCE code the Galaxy component is modeled as a single zone with homogeneous chemical composition. As such, the work in this thesis considers only the temporal evolution of the chemical abundances in the Milky Way. A natural progression of the work herein would be to investigate spatial variations in the ISM abundances through the use of inhomogeneous GCE models. In regards to the research areas discussed in this thesis, some avenues of future work that could be explored by transitioning to multi-dimensional GCE models are given below.

The effect of stellar migration: It was discussed in Section 1.2.2.1 that the migration of stars from their birth radii is an important dynamical process for understanding the flattening of the radial metallicity gradient in the Galactic disk. Chemodynamical simulations have shown that there is a tendency for the outwardly migrating stellar populations (i.e., moving to larger radii than their birth radii) to be comprised of mostly metal-rich stars, with typical timescales of migration of the order $\sim$ 5 Gyr (Vincenzo & Kobayashi, 2020). This mechanism could therefore reasonably allow for a $Z = 0.014 - 0.018$ metallicity AGB star to be at the location of the formation of the Sun, leading to local enhancements of elements between the first and second s-peaks, thus providing a solution to the relative underproduction of ^{107}Pd compared to other s-process SLRs in the ESS (see Section 3.4). However, the net effect of stellar migration on the abundances of SLRs in the ESS has not yet been investigated, which would only be feasible with inhomogeneous GCE models. Such future studies could help constrain the role of dynamical processes on the distribution of SLRs in the Galaxy, and could perhaps shed light on whether the material that formed the ESS is peculiar in terms of its stellar enrichment history.

Another compelling direction of research relating to stellar migration is its role in the Galactic SNe Ia rate. In particular, due to the long delay-times of SNe Ia (see Section 2.3.3.1), radial migration could transport SNe Ia progenitor far from their birth sites prior to explosion (Johnson et al., 2021). This could have important implications for the radial distribution of the Fe-peak elements, particularly for those elements whose production is most affected by the initial metallicity of the progenitor (i.e., Mn). Therefore, the relative abundances of the Fe-peak elements could, in conjunction with the [α/Fe]-[Fe/H] abundance pattern, provide an observational constraint for radial migration in inhomogeneous GCE models.

Propagation of SLRs in the ISM: One of the main sources of uncertainty limiting the predictive capabilities of short-lived radioisotope dating as a tool for probing events in the ESS is the parameter γ. This parameter is difficult to measure empirically because it depends on (i) the *average* recurrence time between stellar enrichment events, which are intrinsically stochastic in nature; and (ii) the dilution factor of ejected material into the ISM, which depends on the speed and distances involved with the transportation. Considerations were made regarding

(i) in the times derived in Chapter 3, however, for (ii) it was assumed that the dilution factor is constant for isotopes produced by the same enrichment event. In regards to this last assumption, the longer the length of time between the ejection of material and its mixing into the ISM, the more the radioactive-to-stable abundance ratio will decrease from its initial value. In order to properly determine (ii), it is necessary to consider the propagation mechanisms of SLRs in the Galaxy using an inhomogeneous GCE code. Recently, Wehmeyer et al. (2023) investigated the role of supernovae driven transportation, finding that CC-SNe are the dominant mode of transportation for SLRs produced by several different astrophysical sites. However, the effect of additional propagation mechanisms such as diffusive mixing, superbubbles, and Galactic outflows were not considered, and these offer important avenues of future research for understanding the origin of SLRs in the ESS.

Astrophysical sites of the r-process: Whilst it has been confirmed observationally that NSMs are sites of the r-process in the Galaxy, the current paradigm is that they are not the *only* source of these elements (Wehmeyer et al., 2015; Côté et al., 2019b; Kobayashi et al., 2023), however, see also Shen et al. (2015). This is primarily because their associated delay-times recovered from BPS models are too long to explain the origin of metal-poor stars that are enhanced in the r-process element Eu (see, e.g. Argast et al., 2004). At the early Galactic times that these stars formed (i.e., [Fe/H] < -2.5), the stochastic nature of stellar enrichment means that local pockets of gas may exhibit large scatter in [X/Fe] compared to the global ISM composition. This is particularly relevant for an element such as Eu, since r-process events are rare and they eject large amounts of material. The scatter in [Eu/Fe] at low metallicities cannot be reproduced by 1-dimensional models that inherently assume the instantaneous mixing approximation. Instead, the spatial resolution afforded by inhomogeneous models appears necessary in the pursuit of identifying the first Galactic r-sources (Wehmeyer et al., 2015). Recently, post-processed nucleosynthesis yields from 3D hydrodynamic models of magnetorotationally driven supernovae have been calculated (Reichert et al., 2023), and they offer an exciting opportunity for GCE models to re-evaluate whether these extreme SNe could be the dominant astrophysical r-process sources.

5.3.2 Refinements to current techniques

Isotopic tracers of SNe Ia progenitor mass: Following a similar approach to the work in Chapter 4, it may be possible to constrain SNe Ia progenitor based on isotopic, rather than elemental, abundance ratios. In particular, the production of the isotopes ^{54}Cr, ^{58}Fe, and ^{64}Ni are sensitive to the electron-fraction in the core of the WD progenitor (Seitenzahl et al., 2013a; Keegans, 2022), and thus they could be used to constrain the sub/near-$M_{\rm Ch}$ SN Ia fraction in the Milky Way. Initial results indicate that, of these isotopes, ^{54}Cr has the highest constraining potential because (i) $\sim$ 50% of the solar abundance is from SNe Ia; and (ii) its production in massive stars is relatively unchanged between rotating and non-rotating models (J. Keegans 2023, private communication).

Another isotope of interest produced by SNe Ia, and also partly by CC-SNe, is the SLR ^{53}Mn ($\tau_{1/2}$ = 3.7 Myr). This radionuclide is known to have been present in the gas that collapsed to form the ESS, however, its origin is still ambiguous. Due to the long delay-times of SNe Ia, it seems likely that $\tau/\gamma \lesssim 0.3$ (i.e. Regime III described in Chapter 3), where we remind that τ is the isotopes mean life and γ the average time between enrichment events, and that the ESS abundance of ^{53}Mn is determined by the last stellar enrichment event that added it to the protosolar nebula. On the other hand, since ^{53}Mn is produced also by CC-SNe over short timescales, it may never completely decay from the ISM and therefore its ESS abundance could have been inherited from the galactic background. It may be possible to disentangle these origin scenario using a GCE models to follow, for example, the ^{53}Mn/^{60}Fe abundance ratio, since ^{60}Fe is only produced by CC-SNe.

Markov Chain Monte Carlo (MCMC) fitting methods for GCE applications: It is sometimes stated derisively that GCE models are calibrated to reproduce observed trends based on a large number of free parameters. This is problematic only if no consideration is made in regards to the likelihood or confidence levels associated with the values of these parameters. So long as enough walkers are used and the code is allowed to reach convergence, an MCMC calculation will find the best set of parameters to fit the data (Brooks et al., 2011). In addition, the confidence level of each parameter can be quantified based on the frequency of walkers at each position in the parameter space during the exploratory calculation. This technique

has been applied for several decades in different areas of astrophysics, such as ultraviolet emission spectra (Kashyap & Drake, 1998), cosmology (Lewis & Bridle, 2002), and galaxy clustering (Jullo et al., 2007). The use of MCMC fitting methods in GCE is more novel, however, with examples of its application including the works of Côté et al. (2017) to find the best-fitting GCE model to Sculptor data, and Spitoni et al. (2020) to derive the delay time between gas infall episodes in the two-infall model based on APOKASC (APOGEE + Kepler Astroseismology Science Consortium; Silva Aguirre et al., 2018) data.

Bibliography

Abbott B. P., et al., 2017, , 119, 161101

Adibekyan V. Z., Santos N. C., Sousa S. G., Israelian G., 2011, A&A, 535, L11

Adibekyan V. Z., Sousa S. G., Santos N. C., Delgado Mena E., González Hernández J. I., Israelian G., Mayor M., Khachatryan G., 2012, A&A, 545, A32

Aliotta M., et al., 2022, Journal of Physics G Nuclear Physics, 49, 010501

Allende Prieto C., Lambert D. L., Asplund M., 2001, ApJL, 556, L63

Anders E., Grevesse N., 1989, , 53, 197

Anders F., et al., 2014, A&A, 564, A115

Anders F., et al., 2017, A&A, 600, A70

Andrews B. H., Weinberg D. H., Schönrich R., Johnson J. A., 2017, ApJ, 835, 224

Antoja T., et al., 2018, Nature, 561, 360

Arcones A., Montes F., 2011, ApJ, 731, 5

Arellano-Córdova K. Z., Esteban C., García-Rojas J., Méndez-Delgado J. E., 2020, MNRAS, 496, 1051

Arellano-Córdova K. Z., Esteban C., García-Rojas J., Méndez-Delgado J. E., 2021, MNRAS, 502, 225

Argast D., Samland M., Thielemann F. K., Qian Y. Z., 2004, A&A, 416, 997

Arlandini C., Käppeler F., Wisshak K., Gallino R., Lugaro M., Busso M., Straniero O., 1999, ApJ, 525, 886

Arnett W. D., 1969, ApJ, 157, 1369

Arnett D., 1996, Supernovae and Nucleosynthesis: An Investigation of the History of Matter from the Big Bang to the Present

Arnett W. D., Thielemann F. K., 1985, ApJ, 295, 589

Asplund M., Grevesse N., Sauval A. J., Scott P., 2009, ARA&A, 47, 481

Asplund M., Amarsi A. M., Grevesse N., 2021, A&A, 653, A141

Athanassoula E., 2005, MNRAS, 358, 1477

Audouze J., Tinsley B. M., 1976, ARA&A, 14, 43

Austin S. M., West C., Heger A., 2017, ApJL, 839, L9

Baade W., 1944, ApJ, 100, 137

Baade W., 1946, PASP, 58, 249

Banerjee S., Kroupa P., 2012, A&A, 547, A23

Barbuy B., Chiappini C., Gerhard O., 2018, ARA&A, 56, 223

Barklem P. S., et al., 2005, A&A, 439, 129

Bassini L., Feldmann R., Gensior J., Hayward C. C., Faucher-Giguère C. A., Cenci E., Liang L., Bernardini M., 2022, arXiv e-prints, p. arXiv:2211.08423

Bastian N., Covey K. R., Meyer M. R., 2010, ARA&A, 48, 339

Battino U., et al., 2016, ApJ, 827, 30

Battino U., et al., 2019, MNRAS, 489, 1082

Battino U., Pignatari M., Travaglio C., Lederer-Woods C., Denissenkov P., Herwig F., Thielemann F., Rauscher T., 2020, MNRAS, 497, 4981

Battino U., Lederer-Woods C., Cseh B., Denissenkov P., Herwig F., 2021, Universe, 7, 25

Battistini C., Bensby T., 2015, A&A, 577, A9

Bedell M., et al., 2018, ApJ, 865, 68

Beers T. C., Drilling J. S., Rossi S., Chiba M., Rhee J., Führmeister B., Norris J. E., von Hippel T., 2002, AJ, 124, 931

Behroozi P. S., Wechsler R. H., Conroy C., 2013, ApJ, 770, 57

Belczynski K., Kalogera V., Rasio F. A., Taam R. E., Zezas A., Bulik T., Maccarone T. J., Ivanova N., 2008, ApJS, 174, 223

Belfiore F., Vincenzo F., Maiolino R., Matteucci F., 2019, MNRAS, 487, 456

Bellardini M. A., Wetzel A., Loebman S. R., Faucher-Giguère C.-A., Ma X., Feldmann R., 2021, MNRAS, 505, 4586

Belokurov V., Erkal D., Evans N. W., Koposov S. E., Deason A. J., 2018, MNRAS, 478, 611

Belokurov V., Sanders J. L., Fattahi A., Smith M. C., Deason A. J., Evans N. W., Grand R. J. J., 2020, MNRAS, 494, 3880

Bennett M. E., et al., 2012, MNRAS, 420, 3047

Bensby T., Feltzing S., Oey M. S., 2014, A&A, 562, A71

Bensby T., et al., 2017, A&A, 605, A89

Berg D. A., Erb D. K., Henry R. B. C., Skillman E. D., McQuinn K. B. W., 2019, ApJ, 874, 93

Bergemann M., Gehren T., 2008, A&A, 492, 823

Bergemann M., et al., 2014, A&A, 565, A89

Bergemann M., et al., 2019, A&A, 631, A80

Berman L., 1935, ApJ, 81, 369

Binney J., Gerhard O., Spergel D., 1997, MNRAS, 288, 365

Bird J. C., Kazantzidis S., Weinberg D. H., Guedes J., Callegari S., Mayer L., Madau P., 2013, ApJ, 773, 43

Bisterzo S., Gallino R., Straniero O., Cristallo S., Käppeler F., 2011, MNRAS, 418, 284

Bisterzo S., Travaglio C., Gallino R., Wiescher M., Käppeler F., 2014, ApJ, 787, 10

Bisterzo S., et al., 2015, MNRAS, 449, 506

Bisterzo S., Travaglio C., Wiescher M., Käppeler F., Gallino R., 2017, ApJ, 835, 97

Bland-Hawthorn J., Gerhard O., 2016, ARA&A, 54, 529

Bland-Hawthorn J., et al., 2019, MNRAS, 486, 1167

Blitz L., Spergel D. N., 1991, ApJ, 379, 631

Bloecker T., 1995, A&A, 297, 727

Blondin S., Bravo E., Timmes F. X., Dessart L., Hillier D. J., 2022, A&A, 660, A96

Blumenthal G. R., Faber S. M., Primack J. R., Rees M. J., 1984, Nature, 311, 517

Boardman N., et al., 2020, MNRAS, 498, 4943

Böhm-Vitense E., 1958, , 46, 108

Bondarenko V., et al., 2002, , 709, 3

Boothroyd A. I., Sackmann I. J., 1988, ApJ, 328, 671

Bovy J., 2015, ApJS, 216, 29

Bovy J., Rix H.-W., Hogg D. W., 2012, ApJ, 751, 131

Bovy J., Rix H.-W., Schlafly E. F., Nidever D. L., Holtzman J. A., Shetrone M., Beers T. C., 2016, ApJ, 823, 30

Bovy J., Leung H. W., Hunt J. A. S., Mackereth J. T., García-Hernández D. A., Roman-Lopes A., 2019, MNRAS, 490, 4740

Brachwitz F., et al., 2000, ApJ, 536, 934

Brinkman H. E., Doherty C. L., Pols O. R., Li E. T., Côté B., Lugaro M., 2019, ApJ, 884, 38

Brinkman H. E., den Hartogh J. W., Doherty C. L., Pignatari M., Lugaro M., 2021, arXiv e-prints, p. arXiv:2109.05842

Bromm V., Larson R. B., 2004, ARA&A, 42, 79

Brooks S., Gelman A., Jones G., Meng X.-L., 2011, Handbook of Markov Chain Monte Carlo. CRC press

Bullock J. S., Kravtsov A. V., Weinberg D. H., 2001, ApJ, 548, 33

Buntain J. F., Doherty C. L., Lugaro M., Lattanzio J. C., Stancliffe R. J., Karakas A. I., 2017, MNRAS, 471, 824

Burbidge E. M., Burbidge G. R., Fowler W. A., Hoyle F., 1957, Reviews of Modern Physics, 29, 547

Burkert A., Hensler G., 1988, A&A, 199, 131

Burris D. L., Pilachowski C. A., Armandroff T. E., Sneden C., Cowan J. J., Roe H., 2000, ApJ, 544, 302

Busso M., Gallino R., Wasserburg G. J., 1999, ARA&A, 37, 239

Busso M., Gallino R., Lambert D. L., Travaglio C., Smith V. V., 2001, ApJ, 557, 802

Busso M., Vescovi D., Palmerini S., Cristallo S., Antonuccio-Delogu V., 2021, ApJ, 908, 55

Cabrera-Lavers A., Hammersley P. L., González-Fernández C., López-Corredoira M., Garzón F., Mahoney T. J., 2007, A&A, 465, 825

Calabrò A., et al., 2022, A&A, 667, A117

Calura F., Pipino A., Chiappini C., Matteucci F., Maiolino R., 2009, A&A, 504, 373

Cameron A. G. W., 1957, PASP, 69, 201

Carollo D., et al., 2007, Nature, 450, 1020

Carollo D., et al., 2010, ApJ, 712, 692

Carr C., Johnston K. V., Laporte C. F. P., Ness M. K., 2022, MNRAS, 516, 5067

Carrillo A., Ness M. K., Hawkins K., Sanderson R. E., Wang K., Wetzel A., Bellardini M. A., 2023, ApJ, 942, 35

Casagrande L., Schönrich R., Asplund M., Cassisi S., Ramírez I., Meléndez J., Bensby T., Feltzing S., 2011, A&A, 530, A138

Caselli P., Ceccarelli C., 2012, , 20, 56

Caswell J. L., Haynes R. F., 1987, A&A, 171, 261

Cautun M., et al., 2020, MNRAS, 494, 4291

Cavichia O., Mollá M., Costa R. D. D., Maciel W. J., 2014, MNRAS, 437, 3688

Cayrel R., et al., 2004, A&A, 416, 1117

Cescutti G., Chiappini C., 2013, arXiv e-prints, p. arXiv:1301.1908

Cescutti G., Matteucci F., François P., Chiappini C., 2007, A&A, 462, 943

Cescutti G., Matteucci F., Lanfranchi G. A., McWilliam A., 2008, A&A, 491, 401

Chabrier G., 2003, PASP, 115, 763

Chabrier G., 2005, in Corbelli E., Palla F., Zinnecker H., eds, Astrophysics and Space Science Library Vol. 327, The Initial Mass Function 50 Years Later. p. 41 (arXiv:astro-ph/0409465), doi:10.1007/978-1-4020-3407-7_5

Chamberlain J. W., Aller L. H., 1951, ApJ, 114, 52

Cheng J. Y., et al., 2012, ApJ, 746, 149

Chevalier R. A., 1976, Nature, 260, 689

Chiappini C., Matteucci F., Gratton R., 1997, ApJ, 477, 765

Chiappini C., Matteucci F., Romano D., 2001, ApJ, 554, 1044

Chiappini C., Hirschi R., Meynet G., Ekström S., Maeder A., Matteucci F., 2006, A&A, 449, L27

Chiba M., Beers T. C., 2000, AJ, 119, 2843

Chieffi A., Limongi M., Straniero O., 1998, ApJ, 502, 737

Childress M. J., Wolf C., Zahid H. J., 2014, MNRAS, 445, 1898

Chiosi C., 1980, A&A, 83, 206

Chisholm J., Tremonti C. A., Leitherer C., Chen Y., Wofford A., Lundgren B., 2015, ApJ, 811, 149

Chisholm J., Tremonti C., Leitherer C., 2018, MNRAS, 481, 1690

Clayton D. D., 1982, , 23, 174

Clayton D. D., 1984, ApJ, 285, 411

Clayton D. D., 1988, MNRAS, 234, 1

Clegg R. E. S., Lambert D. L., Tomkin J., 1981, ApJ, 250, 262

Cohen J. G., Christlieb N., Thompson I., McWilliam A., Shectman S., Reimers D., Wisotzki L., Kirby E., 2013, ApJ, 778, 56

Colavitti E., Cescutti G., Matteucci F., Murante G., 2009, A&A, 496, 429

Côté B., Ritter C., O'Shea B. W., Herwig F., Pignatari M., Jones S., Fryer C. L., 2016, ApJ, 824, 82

Côté B., O'Shea B. W., Ritter C., Herwig F., Venn K. A., 2017, ApJ, 835, 128

Côté B., Silvia D. W., O'Shea B. W., Smith B., Wise J. H., 2018, ApJ, 859, 67

Côté B., et al., 2019a, ApJ, 875, 106

Côté B., Lugaro M., Reifarth R., Pignatari M., Világos B., Yagüe A., Gibson B. K., 2019b, ApJ, 878, 156

Côté B., Yagüe A., Világos B., Lugaro M., 2019c, ApJ, 887, 213

Côté B., Jones S., Herwig F., Pignatari M., 2020, ApJ, 892, 57

Côté B., et al., 2021, Science, 371, 945

Couch R. G., Schmiedekamp A. B., Arnett W. D., 1974, ApJ, 190, 95

Cowan J. J., Sneden C., Lawler J. E., Aprahamian A., Wiescher M., Langanke K., Martínez-Pinedo G., Thielemann F.-K., 2021, Reviews of Modern Physics, 93, 015002

Cristallo S., Straniero O., Lederer M. T., 2008, in O'Shea B. W., Heger A., eds, American Institute of Physics Conference Series Vol. 990, First Stars III. pp 320–324, doi:10.1063/1.2905571

Cristallo S., Straniero O., Gallino R., Piersanti L., Domínguez I., Lederer M. T., 2009, ApJ, 696, 797

Cristallo S., et al., 2011, ApJS, 197, 17

Cristallo S., Straniero O., Piersanti L., Gobrecht D., 2015a, ApJS, 219, 40

Cristallo S., Abia C., Straniero O., Piersanti L., 2015b, ApJ, 801, 53

Cristallo S., Nanni A., Cescutti G., Minchev I., Liu N., Vescovi D., Gobrecht D., Piersanti L., 2020, A&A, 644, A8

Crowther P. A., 2007, ARA&A, 45, 177

Cseh B., et al., 2018, A&A, 620, A146

Cseh B., et al., 2022, A&A, 660, A128

Curti M., et al., 2023, MNRAS, 518, 425

Cyburt R. H., Fields B. D., Olive K. A., Yeh T.-H., 2016, Reviews of Modern Physics, 88, 015004

D'Antona F., Matteucci F., 1991, A&A, 248, 62

D'Orazi V., Magrini L., Randich S., Galli D., Busso M., Sestito P., 2009, ApJL, 693, L31

Dalcanton J. J., Bernstein R. A., 2002, AJ, 124, 1328

Dame T. M., Hartmann D., Thaddeus P., 2001, ApJ, 547, 792

Dauphas N., Chaussidon M., 2011, Annual Review of Earth and Planetary Sciences, 39, 351

Dauphas N., Rauscher T., Marty B., Reisberg L., 2003, , 719, C287

Davé R., Finlator K., Oppenheimer B. D., 2011, MNRAS, 416, 1354

Davis M., Efstathiou G., Frenk C. S., White S. D. M., 1985, ApJ, 292, 371

De Young D. S., 1978, ApJ, 223, 47

Deason A. J., Belokurov V., Sanders J. L., 2019, MNRAS, 490, 3426

Dekel A., et al., 2009, Nature, 457, 451

Delgado Mena E., et al., 2019, A&A, 624, A78

Delgado Mena E., Adibekyan V., Santos N. C., Tsantaki M., González Hernández J. I., Sousa S. G., Bertrán de Lis S., 2021, A&A, 655, A99

Denissenkov P. A., Tout C. A., 2003, MNRAS, 340, 722

Denissenkov P. A., Herwig F., Truran J. W., Paxton B., 2013, ApJ, 772, 37

Denissenkov P. A., et al., 2014, MNRAS, 442, 2058

Denissenkov P. A., Herwig F., Battino U., Ritter C., Pignatari M., Jones S., Paxton B., 2017, ApJL, 834, L10

Di Matteo P., et al., 2014, A&A, 567, A122

Diehl R., et al., 1995, A&A, 298, 445

Diehl R., et al., 2006, Nature, 439, 45

Doherty C. L., Gil-Pons P., Siess L., Lattanzio J. C., 2017, , 34, e056

Dominik M., Belczynski K., Fryer C., Holz D. E., Berti E., Bulik T., Mandel I., O'Shaughnessy R., 2012, ApJ, 759, 52

Donor J., et al., 2020, AJ, 159, 199

Edmunds M. G., 1990, MNRAS, 246, 678

Edvardsson B., Andersen J., Gustafsson B., Lambert D. L., Nissen P. E., Tomkin J., 1993, A&A, 275, 101

Eggen O. J., Lynden-Bell D., Sandage A. R., 1962, ApJ, 136, 748

Eitner P., Bergemann M., Hansen C. J., Cescutti G., Seitenzahl I. R., Larsen S., Plez B., 2020, A&A, 635, A38

Eitner P., Bergemann M., Ruiter A. J., Seitenzahl I. R., Gent M. R., Côté B., 2022, arXiv e-prints, p. arXiv:2206.10258

Ellison S. L., Patton D. R., Simard L., McConnachie A. W., 2008, ApJL, 672, L107

Esteban C., García-Rojas J., 2018, MNRAS, 478, 2315

Esteban C., Méndez-Delgado J. E., García-Rojas J., Arellano-Córdova K. Z., 2022, ApJ, 931, 92

Evans P. A., et al., 2017, Science, 358, 1565

Faber S. M., 1973, ApJ, 179, 731

Fabian A. C., 2012, ARA&A, 50, 455

Farouqi K., Kratz K. L., Pfeiffer B., Rauscher T., Thielemann F. K., Truran J. W., 2010, ApJ, 712, 1359

Feldmann R., 2015, MNRAS, 449, 3274

Feltzing S., Gonzalez G., 2001, A&A, 367, 253

Feuillet D. K., et al., 2018, MNRAS, 477, 2326

Fink M., Röpke F. K., Hillebrandt W., Seitenzahl I. R., Sim S. A., Kromer M., 2010, A&A, 514, A53

Fink M., et al., 2014, MNRAS, 438, 1762

Finlator K., Davé R., 2008, MNRAS, 385, 2181

Firestone R. B., 1991, Nuclear Data Sheets, 62, 101,103

Fishlock C. K., Karakas A. I., Lugaro M., Yong D., 2014, ApJ, 797, 44

Foley R. J., et al., 2009, AJ, 138, 376

Foley R. J., et al., 2013, ApJ, 767, 57

Fowler W. A., Hoyle F., 1964, ApJS, 9, 201

2017, Gas Accretion onto Galaxies Astrophysics and Space Science Library Vol. 430, doi:10.1007/978-3-319-52512-9.

François P., Matteucci F., Cayrel R., Spite M., Spite F., Chiappini C., 2004, A&A, 421, 613

Francois P., 1986, A&A, 160, 264

Francois P., Matteucci F., 1993, A&A, 280, 136

Frebel A., 2018, Annual Review of Nuclear and Particle Science, 68, 237

Frebel A., Simon J. D., Geha M., Willman B., 2010, ApJ, 708, 560

Freeman K., Bland-Hawthorn J., 2002, ARA&A, 40, 487

Freeman K., et al., 2013, MNRAS, 428, 3660

Friaça A. C. S., Barbuy B., 2017, A&A, 598, A121

Frischknecht U., et al., 2016, MNRAS, 456, 1803

Fuhrmann K., 1998, A&A, 338, 161

Fujimoto Y., Krumholz M. R., Inutsuka S.-i., 2020, MNRAS, 497, 2442

Gallino R., Arlandini C., Busso M., Lugaro M., Travaglio C., Straniero O., Chieffi A., Limongi M., 1998, ApJ, 497, 388

Gandhi P. J., Wetzel A., Hopkins P. F., Shappee B. J., Wheeler C., Faucher-Giguère C.-A., 2022, MNRAS, 516, 1941

Garnett D. R., Shields G. A., Skillman E. D., Sagan S. P., Dufour R. J., 1997, ApJ, 489, 63

Genzel R., et al., 2010, MNRAS, 407, 2091

Georgelin Y. M., Georgelin Y. P., 1976, A&A, 49, 57

Gibson B. K., Pilkington K., Brook C. B., Stinson G. S., Bailin J., 2013, A&A, 554, A47

Gilmore G., Reid N., 1983, MNRAS, 202, 1025

Gilmore G., et al., 2012, The Messenger, 147, 25

Goldschmidt V., 1938, Verteilungsgestze der Elemente IX. Die Mengenverha tnisse der Elemente und der Atom-Arten.

Gonzalez O. A., et al., 2015, A&A, 584, A46

Goriely S., Mowlavi N., 2000, A&A, 362, 599

Goriely S., Siess L., 2004, A&A, 421, L25

Goswami A., Prantzos N., 2000, A&A, 359, 191

Gratton R. G., Sneden C., 1988, A&A, 204, 193

Gratton R. G., Carretta E., Claudi R., Lucatello S., Barbieri M., 2003, A&A, 404, 187

Gray C. M., 1974, Nature, 251, 495

Greggio L., Renzini A., 1983, , 54, 311

Grevesse N., Noels A., 1993, in Prantzos N., Vangioni-Flam E., Casse M., eds, Origin and Evolution of the Elements. pp 15–25

Grimmett J. J., Karakas A. I., Heger A., Müller B., West C., 2020, MNRAS, 496, 4987

Grisoni V., Spitoni E., Matteucci F., Recio-Blanco A., de Laverny P., Hayden M., Mikolaitis Ŝ., Worley C. C., 2017, MNRAS, 472, 3637

Grisoni V., Spitoni E., Matteucci F., 2018, MNRAS, 481, 2570

Grisoni V., Matteucci F., Romano D., Fu X., 2019, MNRAS, 489, 3539

Gronow S., Collins C. E., Sim S. A., Röpke F. K., 2021a, A&A, 649, A155

Gronow S., Côté B., Lach F., Seitenzahl I. R., Collins C. E., Sim S. A., Röpke F. K., 2021b, A&A, 656, A94

Han Z.-W., Ge H.-W., Chen X.-F., Chen H.-L., 2020, Research in Astronomy and Astrophysics, 20, 161

Harkins W. D., 1917, The Evolution of the Elements and the Stability of Complex Atoms. I. A New Periodic System Which Shows a Relation Between the Abundance of the Elements and the Structure of the Nuclei of Atoms., doi:10.1021/ja02250a002, https://doi.org/10.1021/ja02250a002

Hartwick F. D. A., 1987, The Structure of the Galactic Halo. Springer Netherlands, Dordrecht, pp 281–290, doi:10.1007/978-94-009-3925-7_12, https://doi.org/10.1007/978-94-009-3925-7_12

Hayakawa T., Fukui Y., 2022, arXiv e-prints, p. arXiv:2208.13406

Hayden M. R., et al., 2014, AJ, 147, 116

Hayden M. R., et al., 2015, ApJ, 808, 132

Hayden M. R., et al., 2020, arXiv e-prints, p. arXiv:2011.13745

Hayes C. R., et al., 2018, ApJ, 852, 49

Haywood M., Di Matteo P., Lehnert M. D., Katz D., Gómez A., 2013, A&A, 560, A109

Haywood M., Di Matteo P., Lehnert M. D., Snaith O., Khoperskov S., Gómez A., 2018, ApJ, 863, 113

Heckman T. M., Armus L., Miley G. K., 1990, ApJS, 74, 833

Heger A., Fryer C. L., Woosley S. E., Langer N., Hartmann D. H., 2003, ApJ, 591, 288

Helmi A., 2020, ARA&A, 58, 205

Helmi A., White S. D. M., de Zeeuw P. T., Zhao H., 1999, Nature, 402, 53

Helmi A., Babusiaux C., Koppelman H. H., Massari D., Veljanoski J., Brown A. G. A., 2018, Nature, 563, 85

Herwig F., 2005, ARA&A, 43, 435

Herwig F., Bloecker T., Schoenberner D., El Eid M., 1997, A&A, 324, L81

Hill V., 2001, Astrophysics and Space Science Supplement, 277, 137

Hill V., et al., 2002, A&A, 387, 560

Hillebrandt W., Kromer M., Röpke F. K., Ruiter A. J., 2013, Frontiers of Physics, 8, 116

Hinkel N. R., Timmes F. X., Young P. A., Pagano M. D., Turnbull M. C., 2014, AJ, 148, 54

Hirai Y., Saitoh T. R., Ishimaru Y., Wanajo S., 2018, ApJ, 855, 63

Hirschi R., 2007, A&A, 461, 571

Ho I. T., Kudritzki R.-P., Kewley L. J., Zahid H. J., Dopita M. A., Bresolin F., Rupke D. S. N., 2015, MNRAS, 448, 2030

Hopkins A. M., 2018, , 35, e039

Hou L. G., Han J. L., 2014, A&A, 569, A125

Howard W. M., Arnett W. D., Clayton D. D., Woosley S. E., 1972, ApJ, 175, 201

Hoyle F., 1946, MNRAS, 106, 343

Hoyle F., Fowler W. A., 1960, ApJ, 132, 565

Hughes G. L., Gibson B. K., Carigi L., Sánchez-Blázquez P., Chavez J. M., Lambert D. L., 2008, MNRAS, 390, 1710

Hulsbosch A. N. M., 1978, A&A, 66, L5

Huss G. R., Meyer B. S., Srinivasan G., Goswami J. N., Sahijpal S., 2009, , 73, 4922

Ibata R. A., Gilmore G., Irwin M. J., 1994, Nature, 370, 194

Iben I. J., Tutukov A. V., 1984, ApJS, 54, 335

Iliadis C., 2007, Nuclear Physics of Stars, doi:10.1002/9783527692668.

Ireland T., 1996, Journal of the Royal Society of Western Australia, 79 Pt 1, 43

Ishigaki M. N., Chiba M., Aoki W., 2012, ApJ, 753, 64

Ishigaki M. N., Aoki W., Chiba M., 2013, ApJ, 771, 67

Iwamoto K., Brachwitz F., Nomoto K., Kishimoto N., Umeda H., Hix W. R., Thielemann F.-K., 1999, ApJS, 125, 439

Jacobson H. R., et al., 2015, ApJ, 807, 171

Janes K. A., 1979, ApJS, 39, 135

Jeffries R. D., 2012, in Reylé C., Charbonnel C., Schultheis M., eds, EAS Publications Series Vol. 57, EAS Publications Series. pp 45–89 (arXiv:1205.2966), doi:10.1051/eas/1257002

Jerkstrand A., et al., 2015, ApJ, 807, 110

Jeřábková T., Hasani Zonoozi A., Kroupa P., Beccari G., Yan Z., Vazdekis A., Zhang Z. Y., 2018, A&A, 620, A39

Jha S. W., 2017, in Alsabti A. W., Murdin P., eds, , Handbook of Supernovae. p. 375, doi:10.1007/978-3-319-21846-5_42

Johansson J., Woods T. E., Gilfanov M., Sarzi M., Chen Y.-M., Oh K., 2016, MNRAS, 461, 4505

Johnson J. W., et al., 2021, MNRAS, 508, 4484

Johnson C. I., et al., 2022, MNRAS, 515, 1469

Jones S., et al., 2013, ApJ, 772, 150

Jones S., Ritter C., Herwig F., Fryer C., Pignatari M., Bertolli M. G., Paxton B., 2016, MNRAS, 455, 3848

Jones S. W., et al., 2019a, MNRAS, 485, 4287

Jones S., et al., 2019b, A&A, 622, A74

Jones S., Côté B., Röpke F. K., Wanajo S., 2019c, ApJ, 882, 170

José J., Hernanz M., 1998, ApJ, 494, 680

José J., Hernanz M., Amari S., Lodders K., Zinner E., 2004, ApJ, 612, 414

Jullo E., Kneib J. P., Limousin M., Elíasdóttir Á., Marshall P. J., Verdugo T., 2007, New Journal of Physics, 9, 447

Jurić M., et al., 2008, ApJ, 673, 864

Kaeppeler F., Gallino R., Busso M., Picchio G., Raiteri C. M., 1990, ApJ, 354, 630

Kaeppeler F., et al., 1994, ApJ, 437, 396

Käppeler F., Gallino R., Bisterzo S., Aoki W., 2011, Reviews of Modern Physics, 83, 157

Karakas A. I., 2010, MNRAS, 403, 1413

Karakas A. I., 2014, MNRAS, 445, 347

Karakas A. I., Lattanzio J. C., 2014, , 31, e030

Karakas A. I., Lugaro M., 2016, ApJ, 825, 26

Karakas A. I., García-Hernández D. A., Lugaro M., 2012, ApJ, 751, 8

Karakas A. I., Lugaro M., Carlos M., Cseh B., Kamath D., García-Hernández D. A., 2018, MNRAS, 477, 421

Karakas A. I., Cinquegrana G., Joyce M., 2022, MNRAS, 509, 4430

Karambelkar V., et al., 2022, in American Astronomical Society Meeting Abstracts. p. 317.07

Kashyap V., Drake J. J., 1998, ApJ, 503, 450

Kastner J. H., Myers P. C., 1994, ApJ, 421, 605

Kaur T., Sahijpal S., 2019, MNRAS, 490, 1620

Keegans J., 2022, Thesis

Kemp A. J., Karakas A. I., Casey A. R., Kobayashi C., Izzard R. G., 2022, MNRAS, 509, 1175

Kennicutt Robert C. J., 1998, ApJ, 498, 541

Kennicutt R. C., Evans N. J., 2012, ARA&A, 50, 531

Kereš D., Katz N., Weinberg D. H., Davé R., 2005, MNRAS, 363, 2

Kereš D., Katz N., Fardal M., Davé R., Weinberg D. H., 2009, MNRAS, 395, 160

Kewley L. J., Ellison S. L., 2008, ApJ, 681, 1183

Kinugawa T., Takeda H., Tanikawa A., Yamaguchi H., 2022, ApJ, 938, 52

Kirby E. N., et al., 2019, ApJ, 881, 45

Kobayashi C., Nakasato N., 2011, ApJ, 729, 16

Kobayashi C., Umeda H., Nomoto K., Tominaga N., Ohkubo T., 2006, ApJ, 653, 1145

Kobayashi C., Nomoto K., Hachisu I., 2015, ApJL, 804, L24

Kobayashi C., Leung S.-C., Nomoto K., 2020a, ApJ, 895, 138

Kobayashi C., Karakas A. I., Lugaro M., 2020b, ApJ, 900, 179

Kobayashi C., et al., 2023, ApJL, 943, L12

Koppelman H. H., Helmi A., Massari D., Price-Whelan A. M., Starkenburg T. K., 2019, A&A, 631, L9

Köppen J., Weidner C., Kroupa P., 2007, MNRAS, 375, 673

Kromer M., et al., 2015, MNRAS, 450, 3045

Kromer M., Ohlmann S., Röpke F. K., 2017, , 88, 312

Krot A. N., et al., 2012, , 47, 1948

Kroupa P., 2001, MNRAS, 322, 231

Kroupa P., 2002, Science, 295, 82

Kroupa P., Tout C. A., Gilmore G., 1993, MNRAS, 262, 545

Kroupa P., Weidner C., Pflamm-Altenburg J., Thies I., Dabringhausen J., Marks M., Maschberger T., 2013, in Oswalt T. D., Gilmore G., eds, , Vol. 5, Planets, Stars and Stellar Systems. Volume 5: Galactic Structure and Stellar Populations. p. 115, doi:10.1007/978-94-007-5612-0_4

Kubryk M., Prantzos N., Athanassoula E., 2015, A&A, 580, A126

Lacey C. G., Fall S. M., 1985, ApJ, 290, 154

Lach F., Röpke F. K., Seitenzahl I. R., Coté B., Gronow S., Ruiter A. J., 2020, A&A, 644, A118

Lamb S. A., Howard W. M., Truran J. W., Iben I. J., 1977, ApJ, 217, 213

Larson R. B., 1972, Nature Physical Science, 236, 7

Larson R. B., 1974, MNRAS, 169, 229

Larson R. B., 1976, MNRAS, 176, 31

Larson R. B., 1991, in Lambert D. L., ed., Astronomical Society of the Pacific Conference Series Vol. 20, Frontiers of Stellar Evolution. p. 571

Lee T., Papanastassiou D. A., Wasserburg G. J., 1977, ApJL, 211, L107

Lee Y. S., et al., 2011, ApJ, 738, 187

Lehner N., Howk J. C., Marasco A., Fraternali F., 2022, MNRAS, 513, 3228

Lequeux J., Peimbert M., Rayo J. F., Serrano A., Torres-Peimbert S., 1979, A&A, 80, 155

Leung S.-C., Nomoto K., 2018, ApJ, 861, 143

Leung S.-C., Nomoto K., 2020, ApJ, 888, 80

Leung S.-C., Nomoto K., 2021, arXiv e-prints, p. arXiv:2111.14795

Lewis A., Bridle S., 2002, , 66, 103511

Li W., Chornock R., Leaman J., Filippenko A. V., Poznanski D., Wang X., Ganeshalingam M., Mannucci F., 2011, MNRAS, 412, 1473

Lian J., Thomas D., Maraston C., 2018, MNRAS, 481, 4000

Lian J., et al., 2022, MNRAS, 513, 4130

Lichtenberg T., Golabek G. J., Gerya T. V., Meyer M. R., 2016, , 274, 350

Licquia T. C., Newman J. A., 2015, ApJ, 806, 96

Lilly S. J., Carollo C. M., Pipino A., Renzini A., Peng Y., 2013, ApJ, 772, 119

Limongi M., Chieffi A., 2006, ApJ, 647, 483

Limongi M., Chieffi A., 2018, ApJS, 237, 13

Liu D., Wang B., 2020, MNRAS, 494, 3422

Liu Z.-W., Moriya T. J., Stancliffe R. J., Wang B., 2015, A&A, 574, A12

Livio M., Mazzali P., 2018, , 736, 1

Livne E., Arnett D., 1995, ApJ, 452, 62

Lodders K., 2003, ApJ, 591, 1220

Lodders K., 2019, arXiv e-prints, p. arXiv:1912.00844

Lodders K., Palme H., Gail H. P., 2009, Landolt Börnstein, 4B, 712

Lomaeva M., Jönsson H., Ryde N., Schultheis M., Thorsbro B., 2019, A&A, 625, A141

Longland R., Iliadis C., Champagne A. E., Newton J. R., Ugalde C., Coc A., Fitzgerald R., 2010, , 841, 1

López-Corredoira M., Cabrera-Lavers A., Gerhard O. E., 2005, A&A, 439, 107

Luck R. E., 2018, AJ, 156, 171

Lugaro M., Herwig F., Lattanzio J. C., Gallino R., Straniero O., 2003, ApJ, 586, 1305

Lugaro M., Karakas A. I., Stancliffe R. J., Rijs C., 2012, ApJ, 747, 2

Lugaro M., et al., 2014, Science, 345, 650

Lugaro M., Ott U., Kereszturi Á., 2018, Progress in Particle and Nuclear Physics, 102, 1

Lütticke R., Dettmar R.-J., Pohlen M., 2000, , 145, 405

Luyten W. J., 1968, MNRAS, 139, 221

Lynden-Bell D., 1975, Vistas in Astronomy, 19, 299

Mac Low M.-M., Ferrara A., 1999, ApJ, 513, 142

Maciel W. J., Costa R. D. D., Uchida M. M. M., 2003, A&A, 397, 667

Mackereth J. T., et al., 2017, MNRAS, 471, 3057

Mackereth J. T., et al., 2019, MNRAS, 482, 3426

Maeda K., 2022, arXiv e-prints, p. arXiv:2210.00326

Maeder A., Meynet G., Ekström S., Georgy C., 2009, Communications in Asteroseismology, 158, 72

Magkotsios G., Timmes F. X., Hungerford A. L., Fryer C. L., Young P. A., Wiescher M., 2010, ApJS, 191, 66

Magrini L., Coccato L., Stanghellini L., Casasola V., Galli D., 2016, A&A, 588, A91

Magrini L., et al., 2018, A&A, 617, A106

Mahoney W. A., Ling J. C., Jacobson A. S., Lingenfelter R. E., 1982, ApJ, 262, 742

Maiolino R., Mannucci F., 2019, , 27, 3

Majewski S. R., et al., 2017, AJ, 154, 94

Mannucci F., Della Valle M., Panagia N., Cappellaro E., Cresci G., Maiolino R., Petrosian A., Turatto M., 2005, A&A, 433, 807

Mannucci F., Della Valle M., Panagia N., 2006, MNRAS, 370, 773

Mannucci F., Cresci G., Maiolino R., Marconi A., Gnerucci A., 2010, MNRAS, 408, 2115

Maoz D., Mannucci F., 2012, Publications of the Astronomical Society of Australia, 29, 447–465

Maoz D., Mannucci F., Brandt T. D., 2012, MNRAS, 426, 3282

Maoz D., Mannucci F., Nelemans G., 2014, ARA&A, 52, 107

Marasco A., Fraternali F., Lehner N., Howk J. C., 2022, MNRAS, 515, 4176

Marconi G., Matteucci F., Tosi M., 1994, MNRAS, 270, 35

Marigo P., 2002, A&A, 387, 507

Marks M., Kroupa P., Dabringhausen J., Pawlowski M. S., 2012, MNRAS, 422, 2246

Mashonkina L., Ryabtsev A., Frebel A., 2012, A&A, 540, A98

Massari D., Koppelman H. H., Helmi A., 2019, A&A, 630, L4

Mathews W. G., Baker J. C., 1971, ApJ, 170, 241

Matteucci F., 2012, Chemical Evolution of Galaxies, doi:10.1007/978-3-642-22491-1.

Matteucci F., 2021, , 29, 5

Matteucci F., Brocato E., 1990, ApJ, 365, 539

Matteucci F., Francois P., 1989, MNRAS, 239, 885

Matteucci F., Greggio L., 1986, A&A, 154, 279

Matteucci F., Spitoni E., Recchi S., Valiante R., 2009, A&A, 501, 531

Matteucci F., Romano D., Arcones A., Korobkin O., Rosswog S., 2014, MNRAS, 438, 2177

McCall M. L., Rybski P. M., Shields G. A., 1985, ApJS, 57, 1

McClure R. D., van den Bergh S., 1968, AJ, 73, 313

McCully C., et al., 2014, Nature, 512, 54

McKee C. F., Ostriker E. C., 2007, ARA&A, 45, 565

McMillan P. J., 2011, MNRAS, 414, 2446

McSween J. H. Y., Huss G. R., 2010, Cosmochemistry. Cambridge University Press, doi:10.1017/CBO9780511804502

McWilliam A., Zoccali M., 2010, ApJ, 724, 1491

McWilliam A., Rich R. M., Smecker-Hane T. A., 2003, ApJL, 592, L21

Meneguzzi M., Audouze J., Reeves H., 1971, A&A, 15, 337

Merrill P. W., 1952, ApJ, 116, 21

Meyer B. S., Clayton D. D., 2000, , 92, 133

Meynet G., Arnould M., 2000, A&A, 355, 176

Meynet G., Ekström S., Maeder A., 2006, A&A, 447, 623

Miglio A., et al., 2021, A&A, 645, A85

Miles B. J., Townsley D. M., Shen K. J., Timmes F. X., Moore K., 2019, ApJ, 871, 154

Miller G. E., Scalo J. M., 1979, ApJS, 41, 513

Minchev I., Chiappini C., Martig M., 2013, A&A, 558, A9

Minchev I., Chiappini C., Martig M., 2014, A&A, 572, A92

Minchev I., Steinmetz M., Chiappini C., Martig M., Anders F., Matijevic G., de Jong R. S., 2017, ApJ, 834, 27

Minchev I., et al., 2018, MNRAS, 481, 1645

Mirabel I. F., Morras R., 1984, ApJ, 279, 86

Mishenina T., et al., 2017, MNRAS, 469, 4378

Mishra R. K., Chaussidon M., 2014, Earth and Planetary Science Letters, 390, 318

Mitchell P. D., Schaye J., Bower R. G., Crain R. A., 2020, MNRAS, 494, 3971

Moe M., Kratter K. M., Badenes C., 2019, ApJ, 875, 61

Molaro P., Izzo L., Bonifacio P., Hernanz M., Selvelli P., della Valle M., 2020, MNRAS, 492, 4975

Molero M., Simonetti P., Matteucci F., della Valle M., 2021, MNRAS, 500, 1071

Mollá M., Cavichia O., Gavilán M., Gibson B. K., 2015, MNRAS, 451, 3693

Mollá M., Díaz Á. I., Cavichia O., Gibson B. K., Maciel W. J., Costa R. D. D., Ascasibar Y., Few C. G., 2019, MNRAS, 482, 3071

Montes F., et al., 2007, ApJ, 671, 1685

Mor R., Robin A. C., Figueras F., Roca-Fàbrega S., Luri X., 2019, A&A, 624, L1

Morgan W. W., Sharpless S., Osterbrock D., 1952, AJ, 57, 3

Mowlavi N., Goriely S., Arnould M., 1998, A&A, 330, 206

Muñoz-Mateos J. C., Boissier S., Gil de Paz A., Zamorano J., Kennicutt R. C. J., Moustakas J., Prantzos N., Gallego J., 2011, ApJ, 731, 10

Muratov A. L., Kereš D., Faucher-Giguère C.-A., Hopkins P. F., Quataert E., Murray N., 2015, MNRAS, 454, 2691

Murray N., Quataert E., Thompson T. A., 2005, ApJ, 618, 569

Myeong G. C., Vasiliev E., Iorio G., Evans N. W., Belokurov V., 2019, MNRAS, 488, 1235

Naab T., Ostriker J. P., 2006, MNRAS, 366, 899

Naidu R. P., Conroy C., Bonaca A., Johnson B. D., Ting Y.-S., Caldwell N., Zaritsky D., Cargile P. A., 2020, ApJ, 901, 48

Nataf D. M., Udalski A., Gould A., Fouqué P., Stanek K. Z., 2010, ApJL, 721, L28

Nelson D., Vogelsberger M., Genel S., Sijacki D., Kereš D., Springel V., Hernquist L., 2013, MNRAS, 429, 3353

Ness M., Lang D., 2016, AJ, 152, 14

Ness M., et al., 2013, MNRAS, 432, 2092

Ness M. K., Johnston K. V., Blancato K., Rix H. W., Beane A., Bird J. C., Hawkins K., 2019, ApJ, 883, 177

Netopil M., Paunzen E., Heiter U., Soubiran C., 2016, A&A, 585, A150

Nishimura N., Sawai H., Takiwaki T., Yamada S., Thielemann F. K., 2017, ApJL, 836, L21

Nissen P. E., 2015, A&A, 579, A52

Nissen P. E., Schuster W. J., 2010, A&A, 511, L10

Nissen P. E., Silva Aguirre V., Christensen-Dalsgaard J., Collet R., Grundahl F., Slumstrup D., 2017, A&A, 608, A112

Nissen P. E., Christensen-Dalsgaard J., Mosumgaard J. R., Silva Aguirre V., Spitoni E., Verma K., 2020, A&A, 640, A81

Nomoto K., Leung S.-C., 2017, in Alsabti A. W., Murdin P., eds, , Handbook of Supernovae. p. 483, doi:10.1007/978-3-319-21846-5_118

Nomoto K., Thielemann F. K., Yokoi K., 1984, ApJ, 286, 644

Nomoto K., Tominaga N., Umeda H., Kobayashi C., Maeda K., 2006, , 777, 424

Nomoto K., Kobayashi C., Tominaga N., 2013, ARA&A, 51, 457

Nordström B., et al., 2004, A&A, 418, 989

Oddo G., 1914, Zeitschrift für anorganische Chemie, 87, 253

Offner S. S. R., Clark P. C., Hennebelle P., Bastian N., Bate M. R., Hopkins P. F., Moraux E., Whitworth A. P., 2014, in Beuther H., Klessen R. S., Dullemond C. P., Henning T., eds, Protostars and Planets VI. p. 53 (arXiv:1312.5326), doi:10.2458/azu_uapress_9780816531240-ch003

Oh S., Kroupa P., 2016, A&A, 590, A107

Onodera M., et al., 2016, ApJ, 822, 42

Oort J. H., 1966, , 18, 421

Oort J. H., 1970, A&A, 7, 381

Oort J. H., Kerr F. J., Westerhout G., 1958, MNRAS, 118, 379

Oppenheimer B. D., Davé R., 2008, MNRAS, 387, 577

Oppenheimer B. D., Davé R., Kereš D., Fardal M., Katz N., Kollmeier J. A., Weinberg D. H., 2010, MNRAS, 406, 2325

Ott U., Kratz K.-L., 2008, , 52, 396

Pagel B. E. J., 1992, in Barbuy B., Renzini A., eds, Vol. 149, The Stellar Populations of Galaxies. p. 133

Pagel B. E. J., 1997, Nucleosynthesis and Chemical Evolution of Galaxies

Pagel B. E. J., 2009, Nucleosynthesis and Chemical Evolution of Galaxies

Pagel B. E. J., Patchett B. E., 1975, MNRAS, 172, 13

Pakmor R., Hachinger S., Röpke F. K., Hillebrandt W., 2011, A&A, 528, A117

Pakmor R., Kromer M., Taubenberger S., Sim S. A., Röpke F. K., Hillebrandt W., 2012, ApJL, 747, L10

Palla M., 2021, MNRAS, 503, 3216

Palla M., Matteucci F., Spitoni E., Vincenzo F., Grisoni V., 2020, MNRAS, 498, 1710

Palme H., Lodders K., Jones A., 2014, in Davis A. M., ed., , Vol. 2, Planets, Asteriods, Comets and The Solar System. pp 15–36

Pancino E., Carrera R., Rossetti E., Gallart C., 2010, A&A, 511, A56

Pandya V., et al., 2021, MNRAS, 508, 2979

Payne C. H., 1925, PhD thesis, RADCLIFFE COLLEGE.

Peeples M. S., Shankar F., 2011, MNRAS, 417, 2962

Peimbert M., 1979, in Burton W. B., ed., Vol. 84, The Large-Scale Characteristics of the Galaxy. p. 307

Perlmutter S., et al., 1999, ApJ, 517, 565

Phillips M. M., 1993, ApJL, 413, L105

Pignatale F. C., Jacquet E., Chaussidon M., Charnoz S., 2019, ApJ, 884, 31

Pignatari M., Gallino R., Meynet G., Hirschi R., Herwig F., Wiescher M., 2008, ApJL, 687, L95

Pignatari M., Gallino R., Heil M., Wiescher M., Käppeler F., Herwig F., Bisterzo S., 2010, ApJ, 710, 1557

Pignatari M., et al., 2013, ApJ, 762, 31

Pignatari M., et al., 2016, ApJS, 225, 24

Pilyugin L. S., 1993, A&A, 277, 42

Pleintinger M. M. M., Siegert T., Diehl R., Fujimoto Y., Greiner J., Krause M. G. H., Krumholz M. R., 2019, A&A, 632, A73

Portail M., Gerhard O., Wegg C., Ness M., 2017, MNRAS, 465, 1621

Portinari L., Chiosi C., 2000, A&A, 355, 929

Pouteau Y., et al., 2022, A&A, 664, A26

Prantzos N., 1998, in Friedli D., Edmunds M., Robert C., Drissen L., eds, Astronomical Society of the Pacific Conference Series Vol. 147, Abundance Profiles: Diagnostic Tools for Galaxy History. p. 171

Prantzos N., 2008, in Charbonnel C., Zahn J. P., eds, EAS Publications Series Vol. 32, EAS Publications Series. pp 311–356 (arXiv:0709.0833), doi:10.1051/eas:0832009

Prantzos N., Abia C., Limongi M., Chieffi A., Cristallo S., 2018, MNRAS, 476, 3432

Prantzos N., Abia C., Cristallo S., Limongi M., Chieffi A., 2020, MNRAS, 491, 1832

Qian Y. Z., Wasserburg G. J., 2007, , 442, 237

Quirk W. J., Tinsley B. M., 1973, ApJ, 179, 69

Raiteri C. M., Busso M., Gallino R., Picchio G., 1991, ApJ, 371, 665

Rattenbury N. J., Mao S., Sumi T., Smith M. C., 2007, MNRAS, 378, 1064

Rauscher T., Heger A., Hoffman R. D., Woosley S. E., 2002, ApJ, 576, 323

Rebassa-Mansergas A., et al., 2016, MNRAS, 463, 1137

Recio-Blanco A., et al., 2022, arXiv e-prints, p. arXiv:2206.05541

Reddy B. E., Tomkin J., Lambert D. L., Allende Prieto C., 2003, MNRAS, 340, 304

Reddy B. E., Lambert D. L., Allende Prieto C., 2006, MNRAS, 367, 1329

Reeves H., Fowler W. A., Hoyle F., 1970, Nature, 226, 727

Reggiani H., Meléndez J., Kobayashi C., Karakas A., Placco V., 2017, A&A, 608, A46

Reichert M., Obergaulinger M., Aloy M. Á., Gabler M., Arcones A., Thielemann F. K., 2023, MNRAS, 518, 1557

Reid I. N., et al., 1999, ApJ, 521, 613

Reid I. N., Gizis J. E., Hawley S. L., 2002, AJ, 124, 2721

Reimers D., 1975, in , Problems in stellar atmospheres and envelopes.. pp 229–256

Rich R. M., 1990, ApJ, 362, 604

Rickey F. A., Sheline R. K., 1968, Physical Review, 170, 1157

Riess A. G., et al., 1998, AJ, 116, 1009

Ritter C., Côté B., Herwig F., Navarro J. F., Fryer C. L., 2018a, ApJS, 237, 42

Ritter C., Herwig F., Jones S., Pignatari M., Fryer C., Hirschi R., 2018b, MNRAS, 480, 538

Rizzuti F., Cescutti G., Matteucci F., Chieffi A., Hirschi R., Limongi M., 2019, MNRAS, 489, 5244

Robin A. C., et al., 2022, arXiv e-prints, p. arXiv:2208.13827

Roederer I. U., et al., 2012, ApJS, 203, 27

Roederer I. U., Preston G. W., Thompson I. B., Shectman S. A., Sneden C., Burley G. S., Kelson D. D., 2014, AJ, 147, 136

Rojas-Arriagada A., et al., 2014, A&A, 569, A103

Rojas-Arriagada A., et al., 2020, MNRAS, 499, 1037

Romano D., 2022, arXiv e-prints, p. arXiv:2210.04350

Romano D., Matteucci F., Salucci P., Chiappini C., 2000, ApJ, 539, 235

Romano D., Chiappini C., Matteucci F., Tosi M., 2005, A&A, 430, 491

Romano D., Tosi M., Chiappini C., Matteucci F., 2006, MNRAS, 369, 295

Romano D., Karakas A. I., Tosi M., Matteucci F., 2010, A&A, 522, A32

Romano D., Franchini M., Grisoni V., Spitoni E., Matteucci F., Morossi C., 2020, A&A, 639, A37

Rood H. J., 1969, ApJ, 158, 657

Röpke F. K., 2007, ApJ, 668, 1103

Röpke F. K., Hillebrandt W., Schmidt W., Niemeyer J. C., Blinnikov S. I., Mazzali P. A., 2007, ApJ, 668, 1132

Rosswog S., Korobkin O., Arcones A., Thielemann F. K., Piran T., 2014, MNRAS, 439, 744

Rosswog S., Sollerman J., Feindt U., Goobar A., Korobkin O., Wollaeger R., Fremling C., Kasliwal M. M., 2018, A&A, 615, A132

Roškar R., Debattista V. P., Quinn T. R., Stinson G. S., Wadsley J., 2008, ApJL, 684, L79

Rudolph A. L., Fich M., Bell G. R., Norsen T., Simpson J. P., Haas M. R., Erickson E. F., 2006, ApJS, 162, 346

Ruiter A. J., 2020, IAU Symposium, 357, 1

Ruiter A. J., Belczynski K., Fryer C., 2009, ApJ, 699, 2026

Ruiter A. J., Belczynski K., Sim S. A., Hillebrandt W., Fryer C. L., Fink M., Kromer M., 2011, MNRAS, 417, 408

Ruiter A. J., Belczynski K., Sim S. A., Seitenzahl I. R., Kwiatkowski D., 2014, MNRAS, 440, L101

Ruiz-Lara T., Matsuno T., Lövdal S. S., Helmi A., Dodd E., Koppelman H. H., 2022, A&A, 665, A58

Russell H. N., 1929, ApJ, 70, 11

Sahlholdt C. L., Feltzing S., Feuillet D. K., 2022, MNRAS, 510, 4669

Sakuma K., Hidaka H., Yoneda S., 2020, Geochemical Journal, 54, 393

Sales-Silva J. V., et al., 2022, ApJ, 926, 154

Salpeter E. E., 1952, ApJ, 115, 326

Salpeter E. E., 1955, ApJ, 121, 161

Samland M., Hensler G., Theis C., 1997, ApJ, 476, 544

Sánchez S. F., et al., 2012, A&A, 546, A2

Sánchez S. F., et al., 2014, A&A, 563, A49

Sancisi R., Fraternali F., Oosterloo T., van der Hulst T., 2008, , 15, 189

Sanders R. L., et al., 2018, ApJ, 858, 99

Sanders J. L., Belokurov V., Man K. T. F., 2021, MNRAS, 506, 4321

Sato Y., Nakasato N., Tanikawa A., Nomoto K., Maeda K., Hachisu I., 2016, ApJ, 821, 67

Scalo J. M., 1986, , 11, 1

Scannapieco E., Bildsten L., 2005, ApJL, 629, L85

Scannapieco C., Tissera P. B., White S. D. M., Springel V., 2006, MNRAS, 371, 1125

Schaye J., et al., 2010, MNRAS, 402, 1536

Schmidt M., 1959, ApJ, 129, 243

Schmidt M., 1963, ApJ, 137, 758

Schneider F. R. N., et al., 2018, Science, 359, 69

Schönrich R., McMillan P. J., 2017, MNRAS, 467, 1154

Schönrich R., Asplund M., Casagrande L., 2011, MNRAS, 415, 3807

Schramm D. N., Tinsley B. M., 1974, ApJ, 193, 151

Schuster W. J., Moreno E., Nissen P. E., Pichardo B., 2012, A&A, 538, A21

Searle L., Sargent W. L. W., 1972, ApJ, 173, 25

Searle L., Zinn R., 1978, ApJ, 225, 357

Seeger P. A., Fowler W. A., Clayton D. D., 1965, ApJS, 11, 121

Seitenzahl I. R., Townsley D. M., 2017, in Alsabti A. W., Murdin P., eds, , Handbook of Supernovae. p. 1955, doi:10.1007/978-3-319-21846-5_87

Seitenzahl I. R., et al., 2013a, MNRAS, 429, 1156

Seitenzahl I. R., Cescutti G., Röpke F. K., Ruiter A. J., Pakmor R., 2013b, A&A, 559, L5

Sellwood J. A., Binney J. J., 2002, MNRAS, 336, 785

Shapiro P. R., Field G. B., 1976, ApJ, 205, 762

Sharda P., Krumholz M. R., 2022, MNRAS, 509, 1959

Sharma S., et al., 2022, MNRAS, 510, 734

Shaver P. A., McGee R. X., Newton L. M., Danks A. C., Pottasch S. R., 1983, MNRAS, 204, 53

Shen K. J., Moore K., 2014, ApJ, 797, 46

Shen S., Wadsley J., Stinson G., 2010, MNRAS, 407, 1581

Shen S., Cooke R. J., Ramirez-Ruiz E., Madau P., Mayer L., Guedes J., 2015, ApJ, 807, 115

Shen K. J., Kasen D., Miles B. J., Townsley D. M., 2018, ApJ, 854, 52

Siess L., 2006, A&A, 448, 717

Silva Aguirre V., et al., 2018, MNRAS, 475, 5487

Sim S. A., Röpke F. K., Hillebrandt W., Kromer M., Pakmor R., Fink M., Ruiter A. J., Seitenzahl I. R., 2010, ApJL, 714, L52

Smith H. E., 1975, ApJ, 199, 591

Snaith O., Haywood M., Di Matteo P., Lehnert M. D., Combes F., Katz D., Gómez A., 2015, A&A, 578, A87

Sneden C., Lambert D. L., Whitaker R. W., 1979, ApJ, 234, 964

Sneden C., Cowan J. J., Ivans I. I., Fuller G. M., Burles S., Beers T. C., Lawler J. E., 2000, ApJL, 533, L139

Soderblom D. R., 2010, ARA&A, 48, 581

Sofue Y., Honma M., Omodaka T., 2009, PASJ, 61, 227

Soker N., 2019, , 87, 101535

Somerville R. S., Davé R., 2015, ARA&A, 53, 51

Spitoni E., Matteucci F., 2011, A&A, 531, A72

Spitoni E., Calura F., Matteucci F., Recchi S., 2010, A&A, 514, A73

Spitoni E., Matteucci F., Marcon-Uchida M. M., 2013, A&A, 551, A123

Spitoni E., Romano D., Matteucci F., Ciotti L., 2015, ApJ, 802, 129

Spitoni E., Vincenzo F., Matteucci F., 2017, A&A, 599, A6

Spitoni E., Matteucci F., Jönsson H., Ryde N., Romano D., 2018, A&A, 612, A16

Spitoni E., Silva Aguirre V., Matteucci F., Calura F., Grisoni V., 2019, A&A, 623, A60

Spitoni E., Verma K., Silva Aguirre V., Calura F., 2020, A&A, 635, A58

Spitoni E., et al., 2021, A&A, 647, A73

Spitoni E., et al., 2022, arXiv e-prints, p. arXiv:2206.12436

Srivastav S., et al., 2022, MNRAS, 511, 2708

Stanek K. Z., Mateo M., Udalski A., Szymanski M., Kaluzny J., Kubiak M., 1994, ApJL, 429, L73

Stanek K. Z., Udalski A., SzymaŃski M., KałuŻny J., Kubiak Z. M., Mateo M., KrzemiŃski W., 1997, ApJ, 477, 163

Stanghellini L., Haywood M., 2018, ApJ, 862, 45

Steigman G., Romano D., Tosi M., 2007, MNRAS, 378, 576

Steinmetz M., Muller E., Hillebrandt W., 1992, A&A, 254, 177

Steinmetz M., et al., 2006, AJ, 132, 1645

Straniero O., Gallino R., Busso M., Chiefei A., Raiteri C. M., Limongi M., Salaris M., 1995, ApJL, 440, L85

Straniero O., Gallino R., Cristallo S., 2006, , 777, 311

Suess H. E., Urey H. C., 1956, Reviews of Modern Physics, 28, 53

Sukhbold T., Ertl T., Woosley S. E., Brown J. M., Janka H. T., 2016, ApJ, 821, 38

Susa H., Hasegawa K., Tominaga N., 2014, ApJ, 792, 32

Takahashi K., Yokoi K., 1987, Atomic Data and Nuclear Data Tables, 36, 375

Talbot Raymond J. J., 1974, ApJ, 189, 209

Talbot Raymond J. J., Arnett W. D., 1971, ApJ, 170, 409

Talbot Raymond J. J., Arnett W. D., 1973, ApJ, 186, 69

Taubenberger S., 2017, in Alsabti A. W., Murdin P., eds, , Handbook of Supernovae. p. 317, doi:10.1007/978-3-319-21846-5_37

Temmink K. D., Toonen S., Zapartas E., Justham S., Gänsicke B. T., 2020, A&A, 636, A31

The L. S., El Eid M. F., Meyer B. S., 2000, ApJ, 533, 998

Theis C., Burkert A., Hensler G., 1992, A&A, 265, 465

Thielemann F. K., Arnett W. D., 1985, ApJ, 295, 604

Thielemann F. K., Nomoto K., Yokoi K., 1986, A&A, 158, 17

Thielemann F.-K., Nomoto K., Hashimoto M.-A., 1996, ApJ, 460, 408

Thielemann F. K., et al., 2003, in Hillebrandt W., Leibundgut B., eds, From Twilight to Highlight: The Physics of Supernovae. p. 331, doi:10.1007/10828549_46

Thielemann F. K., et al., 2011, Progress in Particle and Nuclear Physics, 66, 346

Thies I., Kroupa P., 2007, ApJ, 671, 767

Timmes F. X., Woosley S. E., Weaver T. A., 1995, ApJS, 98, 617

Tinsley B. M., 1977, ApJ, 216, 548

Tinsley B. M., 1979, ApJ, 229, 1046

Tinsley B. M., 1980, , 5, 287

Tinsley B. M., 1981, ApJ, 250, 758

Toonen S., Claeys J. S. W., Mennekens N., Ruiter A. J., 2014, A&A, 562, A14

Tosi M., 1982, ApJ, 254, 699

Tosi M., 1988, A&A, 197, 33

Totani T., Morokuma T., Oda T., Doi M., Yasuda N., 2008, PASJ, 60, 1327

Townsley D. M., Miles B. J., Timmes F. X., Calder A. C., Brown E. F., 2016, ApJS, 225, 3

Travaglio C., Galli D., Gallino R., Busso M., Ferrini F., Straniero O., 1999, ApJ, 521, 691

Travaglio C., Gallino R., Busso M., Gratton R., 2001, ApJ, 549, 346

Travaglio C., Gallino R., Arnone E., Cowan J., Jordan F., Sneden C., 2004, ApJ, 601, 864

Travaglio C., Gallino R., Rauscher T., Röpke F. K., Hillebrandt W., 2015, ApJ, 799, 54

Tremonti C. A., et al., 2004, ApJ, 613, 898

Trippella O., Busso M., Palmerini S., Maiorca E., Nucci M. C., 2016, ApJ, 818, 125

Trueman T. C. L., Côté B., Yagüe López A., den Hartogh J., Pignatari M., Soós B., Karakas A. I., Lugaro M., 2022, ApJ, 924, 10

Truran J. W., 1981, A&A, 97, 391

Truran J. W., Cameron A. G. W., 1971, , 14, 179

Tsujimoto T., Yokoyama T., Bekki K., 2017, ApJL, 835, L3

Twarog B. A., 1980, ApJ, 242, 242

Urey H. C., 1954, ApJS, 1, 147

Valenti S., et al., 2009, Nature, 459, 674

Valenti E., et al., 2016, A&A, 587, L6

Vasini A., Matteucci F., Spitoni E., 2022, MNRAS, 517, 4256

Vassiliadis E., Wood P. R., 1993, ApJ, 413, 641

Veilleux S., Cecil G., Bland-Hawthorn J., 2005, ARA&A, 43, 769

Ventura P., Di Criscienzo M., Carini R., D'Antona F., 2013, MNRAS, 431, 3642

Vescovi D., et al., 2018, ApJ, 863, 115

Vickers J. J., Shen J., Li Z.-Y., 2021, ApJ, 922, 189

Vigroux L., Audouze J., Lequeux J., 1976, A&A, 52, 1

Villeneuve J., Chaussidon M., Libourel G., 2009, Science, 325, 985

Vincenzo F., Kobayashi C., 2018, MNRAS, 478, 155

Vincenzo F., Kobayashi C., 2020, MNRAS, 496, 80

Vincenzo F., Matteucci F., Belfiore F., Maiolino R., 2016a, MNRAS, 455, 4183

Vincenzo F., Belfiore F., Maiolino R., Matteucci F., Ventura P., 2016b, MNRAS, 458, 3466

Visvanathan N., Sandage A., 1977, ApJ, 216, 214

Vogelsberger M., et al., 2014, MNRAS, 444, 1518

Wagstaff G., Miller Bertolami M. M., Weiss A., 2020, MNRAS, 493, 4748

Wakker B. P., 2001, ApJS, 136, 463

Wakker B. P., van Woerden H., Gibson B. K., 1999, in Gibson B. K., Putman M. E., eds, Astronomical Society of the Pacific Conference Series Vol. 166, Stromlo Workshop on High-Velocity Clouds. p. 311

Wang W., et al., 2020, ApJ, 889, 169

Wasserburg G. J., Busso M., Gallino R., Raiteri C. M., 1994, ApJ, 424, 412

Wasserburg G. J., Busso M., Gallino R., Nollett K. M., 2006, , 777, 5

Wasserburg G. J., Karakas A. I., Lugaro M., 2017, ApJ, 836, 126

Wehmeyer B., Pignatari M., Thielemann F. K., 2015, MNRAS, 452, 1970

Wehmeyer B., Fröhlich C., Côté B., Pignatari M., Thielemann F. K., 2019, MNRAS, 487, 1745

Wehmeyer B., López A. Y., Côté B., K. Pető M., Kobayashi C., Lugaro M., 2023, ApJ, 944, 121

Weiland J. L., et al., 1994, ApJL, 425, L81

Whelan J., Iben Icko J., 1973, ApJ, 186, 1007

White S. D. M., Frenk C. S., 1991, ApJ, 379, 52

White S. D. M., Rees M. J., 1978, MNRAS, 183, 341

Wielen R., 1974, Highlights of Astronomy, 3, 395

Wielen R., Fuchs B., Dettbarn C., 1996, A&A, 314, 438

Wiersma R. P. C., Schaye J., Theuns T., Dalla Vecchia C., Tornatore L., 2009, MNRAS, 399, 574

Wiescher M., Görres J., Uberseder E., Imbriani G., Pignatari M., 2010, Annual Review of Nuclear and Particle Science, 60, 381

Wiklind T., et al., 2019, ApJ, 878, 83

Womack K. A., Vincenzo F., Gibson B. K., Côté B., Pignatari M., Brinkman H. E., Ventura P., Karakas A., 2023, MNRAS, 518, 1543

Woods T. E., Gilfanov M., 2013, MNRAS, 432, 1640

Woosley S. E., Weaver T. A., 1994, ApJ, 423, 371

Woosley S. E., Weaver T. A., 1995, ApJS, 101, 181

Woosley S. E., Heger A., Weaver T. A., 2002, Reviews of Modern Physics, 74, 1015

Wu S. C., 2005, Nuclear Data Sheets, 106, 367

Wylie S. M., Gerhard O. E., Ness M. K., Clarke J. P., Freeman K. C., Bland-Hawthorn J., 2021, A&A, 653, A143

Yagüe López A., García-Hernández D. A., Ventura P., Doherty C. L., den Hartogh J. W., Jones S. W., Lugaro M., 2021a, arXiv e-prints, p. arXiv:2110.08035

Yagüe López A., Côté B., Lugaro M., 2021b, ApJ, 915, 128

Yanny B., et al., 2009, AJ, 137, 4377

Yong D., et al., 2013, ApJ, 762, 26

Zhang Z.-Y., Romano D., Ivison R. J., Papadopoulos P. P., Matteucci F., 2018, Nature, 558, 260

Zoccali M., Valenti E., 2016, , 33, e025

Zoccali M., et al., 2003, A&A, 399, 931

Zoccali M., Hill V., Lecureur A., Barbuy B., Renzini A., Minniti D., Gómez A., Ortolani S., 2008, A&A, 486, 177

Zoccali M., et al., 2014, A&A, 562, A66

Zoccali M., et al., 2017, A&A, 599, A12

de Castro D. B., Pereira C. B., Roig F., Jilinski E., Drake N. A., Chavero C., Sales Silva J. V., 2016, MNRAS, 459, 4299

de Laverny P., Recio-Blanco A., Worley C. C., De Pascale M., Hill V., Bijaoui A., 2013, The Messenger, 153, 18

de los Reyes M. A. C., Kirby E. N., Seitenzahl I. R., Shen K. J., 2020, ApJ, 891, 85

den Hartogh J. W., Hirschi R., Lugaro M., Doherty C. L., Battino U., Herwig F., Pignatari M., Eggenberger P., 2019, A&A, 629, A123

van Woerden H., Wakker B. P., 2004, in van Woerden H., Wakker B. P., Schwarz U. J., de Boer K. S., eds, Astrophysics and Space Science Library Vol. 312, High Velocity Clouds. p. 195, doi:10.1007/1-4020-2579-3_10

van de Voort F., Schaye J., Booth C. M., Haas M. R., Dalla Vecchia C., 2011, MNRAS, 414, 2458

van den Bergh S., 1958, AJ, 63, 492

van den Bergh S., 1962, AJ, 67, 486

A. Comparison of stellar nucleosynthesis yields and GCE model constraints used in this thesis

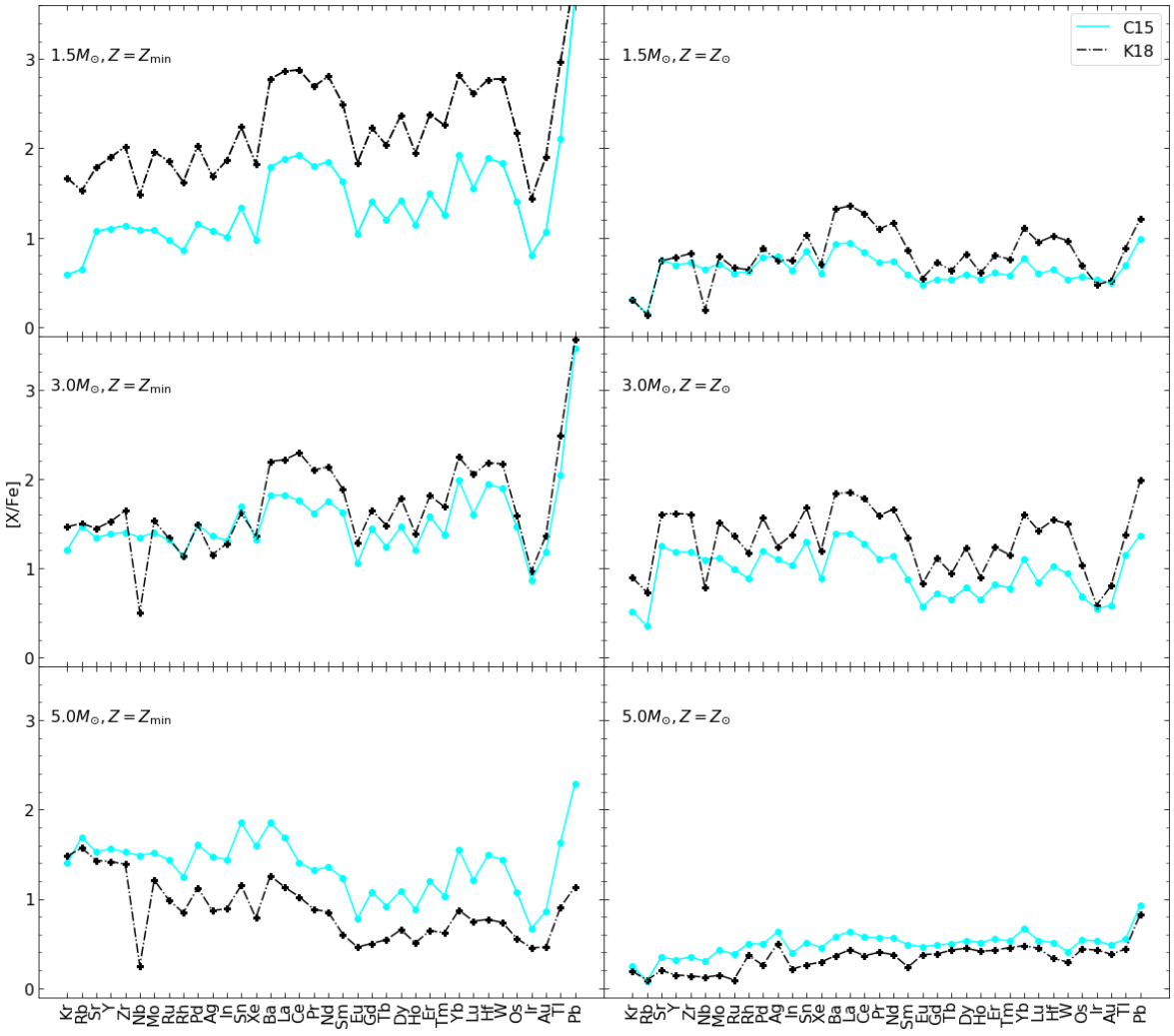

Figure A.1: Comparison of yields for elements from Kr to Pb for the LIMS models of FRUITY (C15; solid blue line) and Monash (K18; dashed black line). From top-to-bottom, the panels show yields for the 1.5, 3.0, and 5.0 $M_\odot$ models at both the lowest calculated metallicity (left panels) and solar metallicity (right panels).

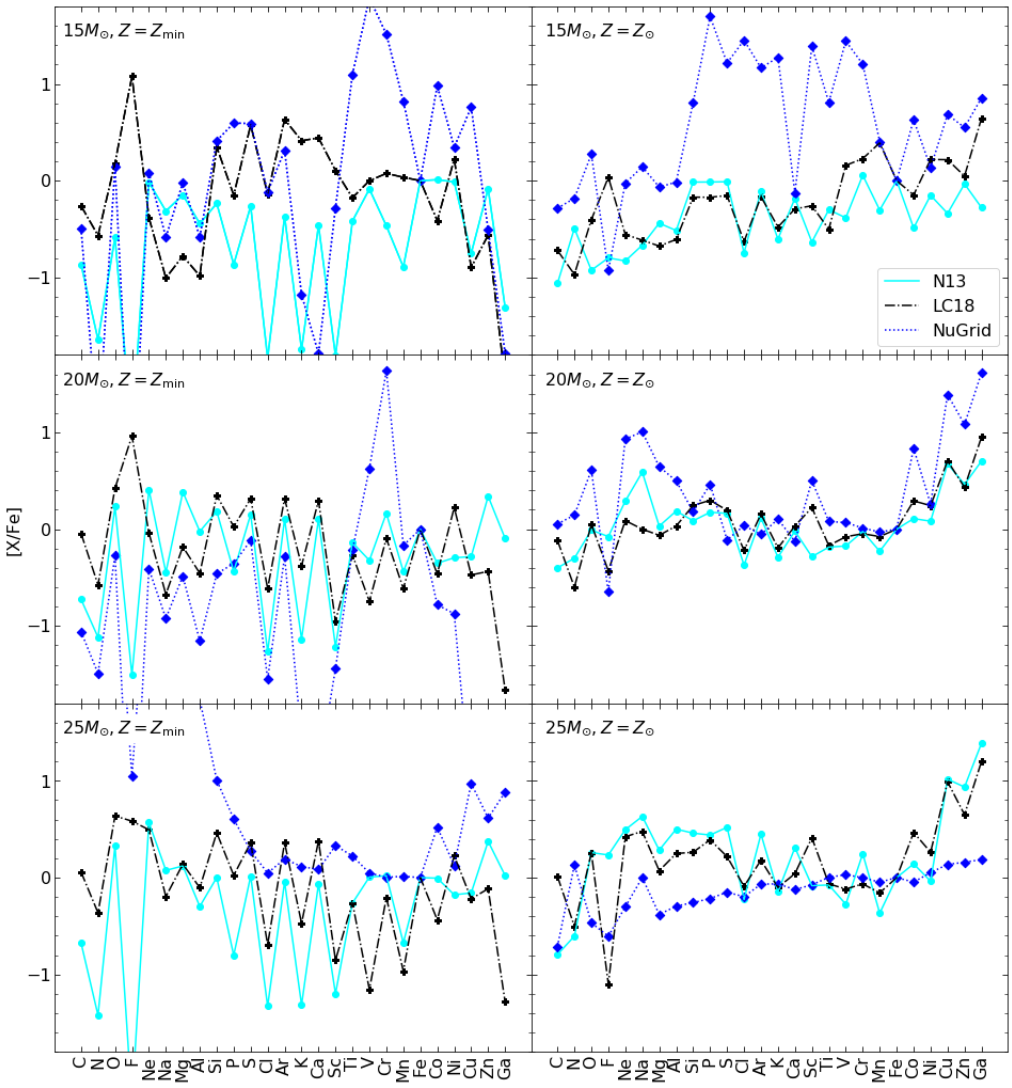

Figure A.2: Comparison of yields for elements from C to Ga for the massive star models of N13 Nomoto et al. 2013 (solid light-blue line), Limongi & Chieffi 2018 (dashed black line), and NuGrid collaboration (dotted dark-blue line). From top-to-bottom, the panels show yields for the 15, 20, and 25 $M_\odot$ models at both the lowest calculated metallicity (left panels) and solar metallicity (right panels).

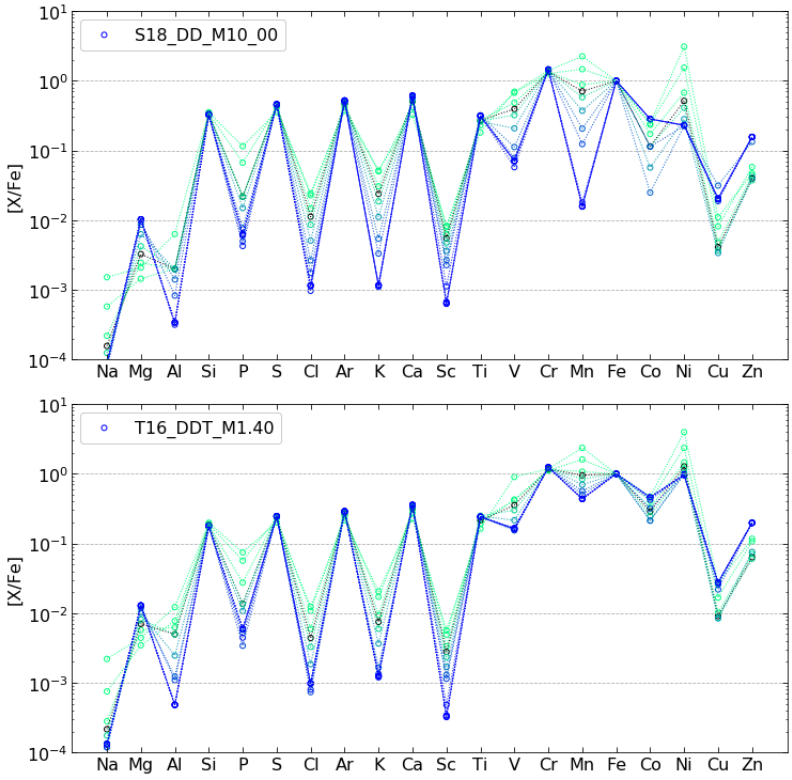

Figure A.3: Comparison of yields for elements from Na to Zn for the SNe Ia models of Shen et al. 2018 (S18_DD_M10_00; top panel) and Townsley et al. 2016 (T16_DDT_M1.40; bottom panel), where both models are post-processed by Keegans (2022). Lines with a darker shade of blue are for lower metallicity models, whereas lighter shades are higher metallicities. The yields for solar metallicity are shown by black circles interconnected by a black dotted line.

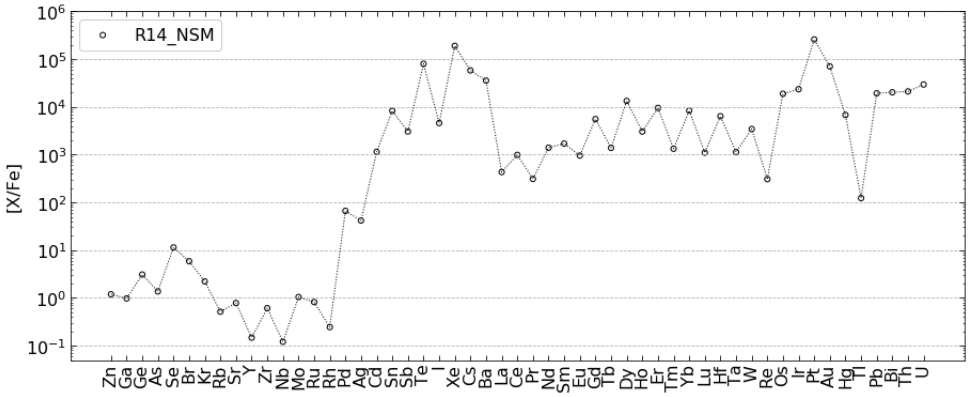

Figure A.4: Neutron star merger yields from Rosswog et al. (2014).

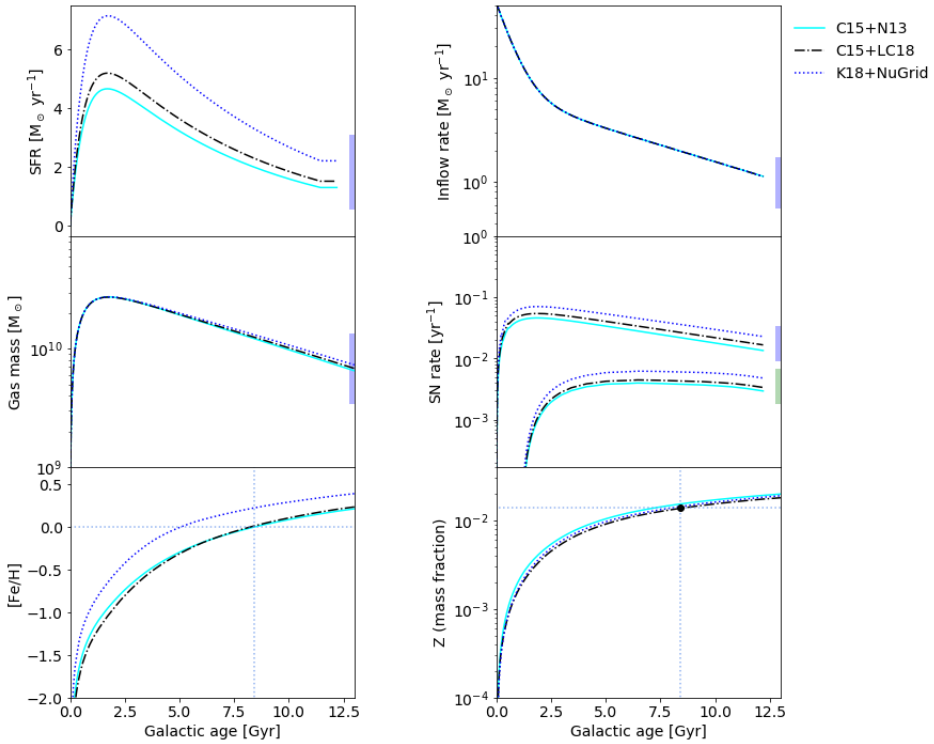

Figure A.5: Evolution of the star formation rate (top-left panel), mass of gas (middle left panel), [Fe/H] (bottom left panel), inflow rate (top right panel), core-collapse supernovae (top lines) and Type Ia supernovae rates (both middle right panel), and global metallicity of the gas (bottom right panel) for the three Milky-Way models used in Section 2.4. The blue bands at 13 Gyr indicate the current observational constraints for each parameter as derived by Kubryk et al. (2015), and the intersecting dotted lines in the two bottom panels are at the solar values.

B. Galactic chemical evolution models with SNe Ia yield combinations

Figure B.1 & B.2 show the predicted chemical evolution of the Fe-peak elements for each of the $\sim$ 1200 GCE models calculated using a combination of the sub- and near-$M_{\rm Ch}$ yields investigated in Chapter 4 (except for PDf explosions). Each GCE track is color coded based on the goodness of fit to the observational data according to the χ^2 test described by Equation 4.5.

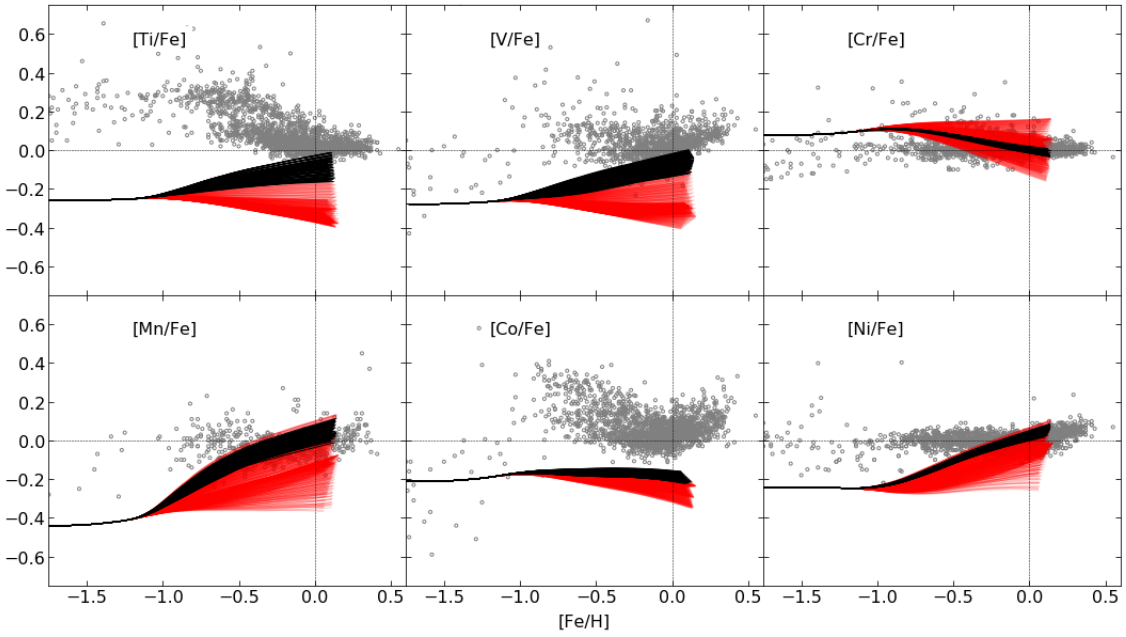

Figure B.1: GCE tracks for N13 CC-SNe yields with SNe Ia yield combinations (see Section 4.5 for details) with no contribution from SNe .Iax. The GCE tracks with black lines indicate the models that have a χ^2 score in 84th percentile. Observational data is the same as in Figure 4.2 & 4.3.

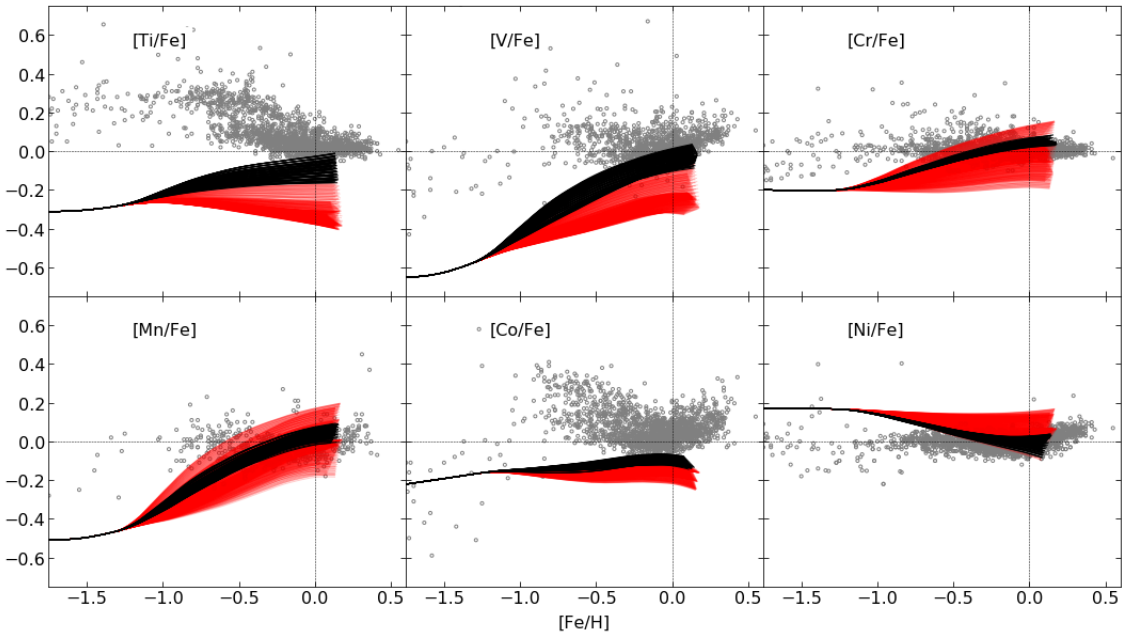

Figure B.2: Same as Figure B.1, but for LC18 CC-SNe yields.